The University Of Sheffield.

Simulation of Impedance Spectroscopy in Electroceramics Using a Finite Element Method

By

James Peter Heath

A thesis submitted in partial fulfilment of the requirements for the degree of Doctor of Philosophy

Supervised by

Dr. Julian Dean
Prof. Derek C. Sinclair
Prof. John H. Harding

The University of Sheffield
Faculty of Engineering
Department of Material Science and Engineering

July 2017

Contents

Acknowledgements

It amuses me greatly to look back at origins of this work, which was born from a hastily constructed (but ultimately successful) funding application for a second year undergraduate research project. A final year research project and PhD followed. I wish to express my gratitude to Julian Dean for that initial investment and many opportunities that came after. He has been a great advocate and a mentor. I have also been lucky enough to have also had the input of Derek Sinclair and John Harding into my work. They are both proverbial fountains of knowledge. Many thanks to both of them for all their feedback, advice and for making time in their schedules for myself. I could not have asked for a better supervisory team.

In the Materials department, in the most severe cases, modellers are quarantined to the H7 office. To all past and present inmates, you have been great company over the years. Perhaps the students who come after us will find that missing electrical wiring and seafood? I must also voice my appreciation for my drinking buddies in the greater ceramics group for helping me regain my sanity every Friday and to all my friends now scattered throughout the country who's nattering never fails to put a smile on my face.

For material support I gratefully acknowledge the Engineering and Physical Sciences Research Council for funding my PhD and the department of Material Science and Engineering (at Sheffield) for rubber stamping my DTA scholarship. *Someone* had to pay for all that beer and curry. I am also grateful for travel grants generously provided by the Worshipful Company of Armourers and Braisiers and the Institute of Materials, Minerals and Mining.

Finally, it is my parents' fault I turned out the way I did. Discussions of world around us with my mother and going to my father's work to see the robots have undoubtedly shaped the path I would tread. Thank you both for your love and encouragement.

Dedicated to the memory of Mary Elizabeth Lattey (1928-2016). For all your love and support throughout my education.

Abstract

Currently the electronic industry has a market demand for over a billion multi layer ceramic capacitors per annum. Electrical characterisation of the electroceramic component of these devices is required for optimisation of existing materials and to aid material discovery. Impedance spectroscopy is a technique that is commonly used to characterise the electrical properties of electroceramics. Experimental data is analysed using an equivalent circuit (usually some combination of resistors and capacitors connected in series and/or in parallel) to extract resistances and capacitances for specific components of a microstructure, e.g. bulk (grains), core-shell grains and grain boundaries. The ability to extract this information depends on the use of an appropriate equivalent circuit and on how to analyse the impedance data. Here an investigation of how the physical microstructure of an electroceramic can affect its impedance response using finite element modelling (FEM) is presented. By using a simulation-based approach the simulator can use the same methodology that would be used experimentally to obtain information on different microstructural components with prior knowledge of what the values should be, since the simulator has defined them. By comparing the values extracted to those originally inputted into the simulation allows the accuracy of the data analysis methods used to extract information to be evaluated and under what conditions these methods can be applied. The results presented in this thesis (chapters four to six) are divided into three studies.

Chapter four considers the characterisation of core-shell grain microstructures by estimating core and shell volume fractions from the core to shell capacitance ratio. FEM simulation of the impedance response of a core-shell microstructure allows the capacitance ratio of the core and shell to be obtained from the electric modulus formalism. Several microstructures were considered: a nested cube; nested truncated octahedra; and a series layer model (SLM). The first two microstructures are approximations for a core-shell grain and were simulated using FEM. The layer model is an idealised case that can be solved analytically and with FEM for validation purposes. Here the relative permittivity of the core and shell regions is fixed at a value of 100 and the core has a conductivity three orders of magnitude greater than the shell. As the core volume fraction decreases, the core volume fraction extracted from the SLM is always accurate but becomes increasing inaccurate for the other models. This discrepancy agrees with the results of effective medium theory proving that our conclusions are physically reasonable. Plots of the electrical microstructure using a stream tracer method to view current flow showed increased heterogeneity in the current density in the core and shell. A quantitative study of the electrical microstructure showed the formation of conduction pathways through the parallel shell and increased curvature of the pathways through the core as the core volume fraction decreased. The electrical microstructure no longer resembled the physical microstructure, making extraction of volume ratios increasingly unreliable. Only for core volume fractions of 0.7 or greater could the core volume fraction be extracted from capacitance ratios with errors of less than 25%.

Chapter five also considers the extraction of volume fractions from core-shell grains and other idealised microstructures. Here the conductivity of the core and shell regions is fixed and the permittivity of the core is greater than the shell.

The impedance responses of an encased model, SLM and a parallel layer model (PLM) are simulated. The response of the encased model is shown to be more similar to the SLM than the PLM, implying serial connectivity in the encased model. Due to the difference in permittivity in the core and shell regions, the core volume fraction could not be obtained from capacitance ratios but only from resistance ratios obtained from the impedance formalism. The core-shell volume fractions of the encased model and SLM were varied and then extracted using resistance ratios. Similar trends to chapter four were observed, in chapter five, where the volume fraction could be accurately obtained for the SLM from resistance ratios for all input volume fractions. For the encased model, the error when extracting the core volume from resistance ratios increased as the core volume fraction decreased. Again, this error was in excess of 25% when the core volume fraction was less than 0.7. Finally, a stream tracer investigation of electrical microstructure revealed heterogeneous current density in the encased model caused by the formation of capacitive pathways through the microstructure.

Chapter six examines the case where the microstructure is fixed and the material properties are varied. An encased model with a core volume fraction of 0.8 was chosen as it had been shown in the previous chapters that larger core volume fractions minimised the effects of conduction and capacitive pathways through the parallel shell but was still comparable to the volume fractions of core-shell microstructures in the literature. The core conductivity and relative permittivity was fixed at 0.1 mSm^{-1} and 2000, respectively. The shell conductivity was varied from 0.1 mSm^{-1} to 0.1 μSm^{-1} and the relative permittivity from 2000 to 10. One hundred combinations over a range of shell properties was simulated. The resultant spectra were then fitted with three equivalent circuits where the fits were compared to find the best equivalent circuit using all four impedance formalisms. The first circuit was based upon a SLM with the same material properties and volume fractions inputted into the encased model. The second was called the series brick layer model (SBLM) and based on the encased model but neglecting the contribution of the parallel shell region. The third circuit was called the parallel brick layer model (PBLM) which included a separate resistor capacitor branch for the parallel shell region. The SLM provided a poor fit for all encased simulations with errors between ±34 to ±163%. The SBLM and PBLM provided better fits to the encased simualtions with errors from ±0.7 to ±20% and from ±0.55 to ±20%, respectively. Analysis showed that the SBLM provided the best fit when both the conductivty and the permittivity values of the core and shell were more than an order of magnitude different. The PBLM was best when either the shell conductivty or permititvty was within an order of magnitude of the core values. Finally, the best equivalent circuit for a given set of shell material properties was used to extract values of conductivity and permittivity (for both the core and shell) in all four impedance formalisms. The accuracy of the extracted values was calculated with respect to the input values for the simulation. This allowed the most reliable form of data analysis (i.e. formalism) for extracting conductivity and permittivity values for a given combination of material properties to be established. The accuracy of the most reliable formalism was mapped out for every material property combination. This optimal methodology was used to show the best case accuracy that could be achieved for extracting intrisic material properties from a core shell microstructure as the shell properties were systematically varied.

Chapter 1: Introduction and Theory

In this chapter the motivation for the study of electroceramics will be discussed in the context of the dielectric ceramics considered in this project. Firstly the applications, industrial requirements and environmental challenges facing these materials will be reviewed. Then the mathematics needed to describe impedance will be derived and converted into the four impedance formalisms (impedance, electric modulus, admittance and complex capacitance). Comparison of the formalisms will give an overview of under what circumstances each formalism should be used. Finally the strengths and limitations of impedance spectroscopy will be discussed.

1.1. Motivation

1.1.1. Ceramics for Dielectric Applications

Within this study, the primary concern is impedance spectroscopy of dielectric ceramics. There is a large group of ceramic materials called electroceramics (sometimes functional oxides) that dielectric ceramics belong to. Broadly speaking electroceramics do something useful when we allow an electric current to flow through them: a piezoelectric will actuate; and a ferroelectric will become polarised[1].

The results in this work can be applied to a variety of electrical composite materials. However, due to our emphasis on dielectric ceramics and impedance spectroscopy, the assumptions behind the simulations discussed in this thesis are more specific:

- The frequency range considered is from mHz to MHz. Therefore induction effects can be neglected.
- Ferroelectric domains are not included explicitly in calculations as simulation methods that include these are computationally demanding[2].
- Materials that have a high permittivity due to ferroelectric domains are simply assigned a higher value of permittivity (ε_r)
- The permittivity is assumed to be isotropic.

Dielectric materials inhibit the flow of electric current. This makes them useful for electrical insulation but if the dielectric material is used to block current so that charge builds up at a conductor-dielectric interface, we have a capacitor or a device that can store charge. A simple implementation of this is the parallel plate capacitor (see fig. 1).

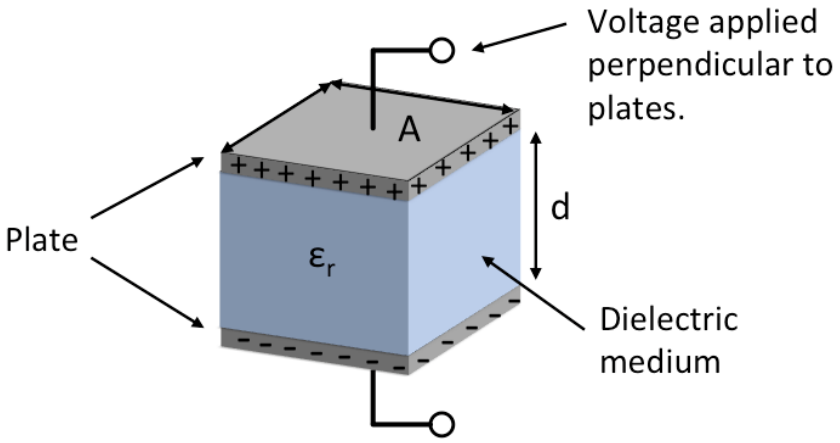

Fig. 1. *Schematic of a parallel plate capacitor where d is the plate separation in m, A is the area of the plates in m^2 and ε_r is the relative permittivity of the dielectric medium (dimensionless).*

The capacitance (C) of a parallel plate capacitor can be calculated as:

$$C = \frac{\varepsilon_r \varepsilon_0 A}{d} \qquad (1.1)$$

where ε_0 is the permittivity of free space in Fm^{-1}. If the classic parallel plate capacitor is used, the value of ε_r will be roughly one, as only air will be present between the plates. If a higher capacitance is desired for given capacitor dimensions, a dielectric medium with a higher ε_r should be considered. Ferroelectric materials that exhibit domain structures can have very high values of the permittivity. Currently barium titanate (BT) is the material of choice for XR7-type capacitors[3] which will be discussed in more depth later in this chapter. Another approach would be to use a material that has a microstructure with the internal barrier layer capacitor (IBLC) effect. These materials allow space charge to migrate through conductive or semi-conductive regions and build up on more resistive 'barrier' components. Calcium copper titanate (CCTO) has an IBLC type microstructure, made up of semi conducting cores surrounded by resistive shells[4]. IBLC microstructures can give very large value of ε_r but this is offset by frequency dependent permittivity, high dielectric loss and low breakdown voltages.

To improve components such as capacitors it is vital to understand the dielectric properties of the material used for the dielectric medium. Impedance spectroscopy is a powerful tool for the electrical characterisation of materials and how it achieves this shall be detailed in the impedance section of this chapter. First we must consider the motivation for materials discovery and hence electrical characterisation required for dielectric materials.

1.1.2. Demand of Electronics and the Environment

In the modern world, we are surrounded by consumer electronics. A drive towards miniaturisation pushes the limits of what materials can achieve in terms of devices meeting their specifications. Higher performance, energy efficiency and reliability whilst reducing weight are highly desirable. Materials chemists can attack this

problem by optimising the composition of materials for improved properties, whilst materials scientists and process engineers can optimise microstructure for the same purpose. Unfortunately, to get the best performance from materials often requires the use of highly toxic and/or expensive additives. Their use is thus inhibited by increased awareness of and legislation on their environmental effects. A good example of this is the piezoelectric material lead zirconate titanate (PZT). This material offers some of the best properties in its class but contains poisonous lead. Alternative materials are being developed but have not displaced PZT's dominant position in the market[5].

Many key materials used in the electronics industry have their properties enhanced by doping with small concentrations of rare earth elements (REE). Despite the name 'rare earth' these elements are fairly abundant in the Earth's crust but rarely concentrated in economically extractable deposits. Geo-political issues plague the global supply of rare earth elements. The few deposits that are used commercially are mostly concentrated in China but due to export restrictions there are plans to open new mines in other parts of the world[6]. It would be desirable to reduce the dependence on REEs, to do so requires optimisation of device microstructure and hence the methods used to characterise them.

1.1.3. Multi Layer Ceramic Capacitors

The connection of REEs to this work is their use for creating core-shell microstructured barium titanate, which is used industrially as a dielectric in multi layer ceramic capacitors (MLCCs). These are lamellar devices, composed of alternating layers of ceramic dielectric and nickel electrode layers. This configuration (see fig. 2) gives a high surface area (of electrode) to volume (of the device) ratio and hence a high capacitance to volume ratio. This is required to allow for a large network of capacitors to be placed on printed circuit boards for current smoothing and decoupling alternating and direct current signals. A common application of this is to give a clean electric signal that microprocessors require to function (see fig. 2). Given that many millions of microprocessors are sold every year and that hundreds of capacitors are required for each of them to function, the global market for capacitors is of the order of billions of units sold per annum[3].

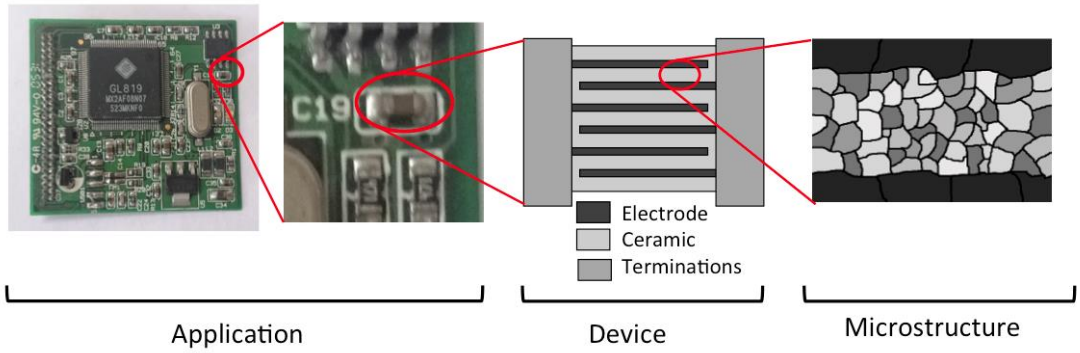

Fig. 2. *Application of multi-layer ceramic capacitors on a printed circuit board with device schematic and microstructure.*

Doping BT used for MLCCs with rare REE achieves two goals. Firstly it significantly improves the reliability of the device - the mechanism is not currently

understood but is the subject of much curiosity[3]. As previously mentioned, the second use of REE doping in BT is to form a core-shell microstructure[7]. As the ceramic is sintered segregation of the various dopants occurs, leading to a microstructure that can be roughly approximated as grains consisting of a core of pure (undoped) BT surrounded by a shell of dopant-rich BT[8].

The core-shell microstructure is also useful as it extends the temperature range in which a capacitor can operate to specification. Pure BT has a sharp peak in permittivity at its Curie temperature at 120°C as it undergoes a transition from a tetragonal to a cubic crystal structure. The Curie temperature for the dopant-rich shell is at a lower temperature and has a smaller but broader peak. The combination of the sharp core-BT peak and broad shell peak gives BT a more temperature-stable capacitance (see fig. 3). This is important for meeting industry standards. REE doped BT is typically used for XR7 rated capacitors. Here the capacitance must be within 15% of the room temperature capacitance over a temperature range of -55 to 125 °C.

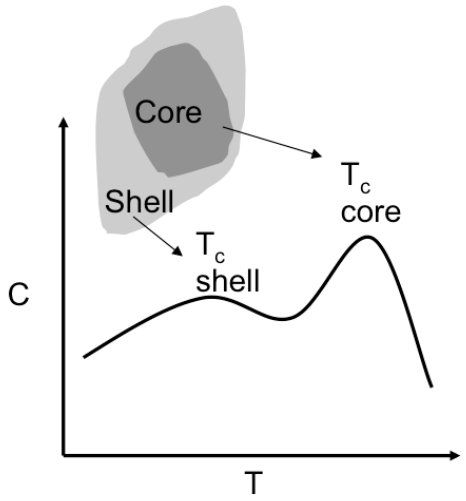

Fig. 3. *Schematic of a core-shell grain structure and the resulting capacitance/temperature profile produced.*

1.2. Theory of Impedance Spectroscopy

1.2.1. Basic Theory

Broadly speaking, impedance can be considered as the AC analogue to DC resistance. The key difference between the two is that impedance includes a phase difference between the current and voltage. When a sinusoidal voltage is applied, the induced current sinusoid may not take its maximum value at the same time. This phase difference is expressed as an angle in radians. The phase difference is defined here as θ instead of the usual Φ because Φ is used later for the potential and the lower case ϕ for the volume fraction. The measurement of impedance requires the value of θ in addition to the maxima of the current and voltage sinusoids (I_{max} and V_{max} respectively, see fig. 4).

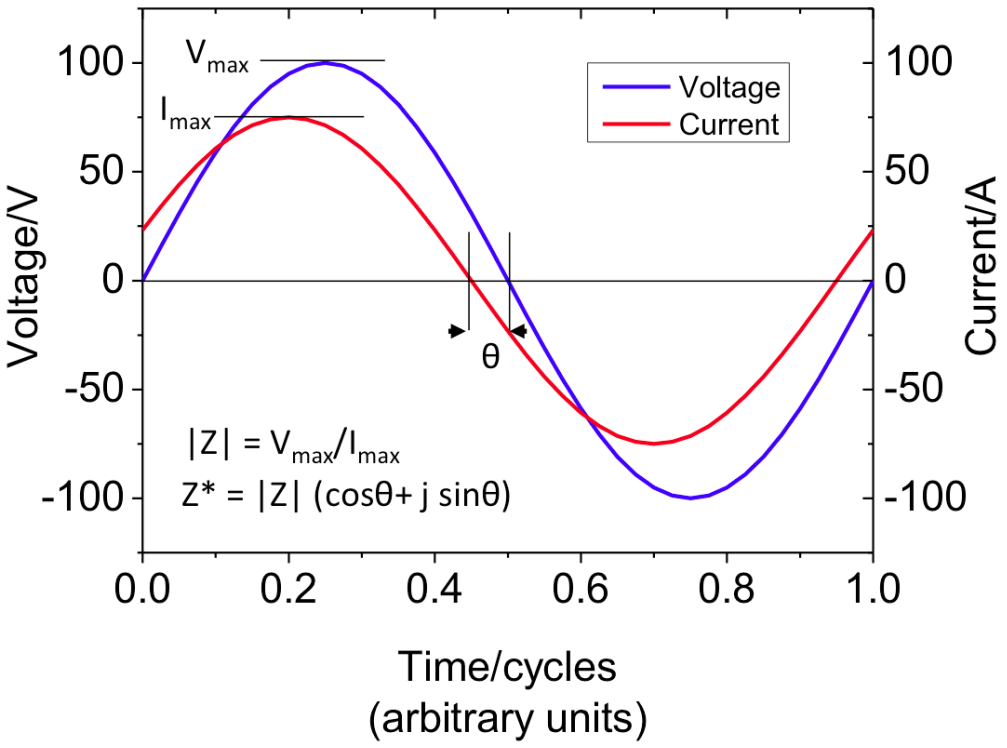

Fig. 4. *Relationship between the phase and magnitude of current/voltage sinusoids and impedance.*

The value of θ varies depending on the properties of the medium that has an AC signal applied to it. The electrical properties of a material comprise (or are a combination of) transport, polarisation and magnetic processes. These can be considered as resistive, capacitive and inductive processes, respectively. Let us consider the ideal electrical response of a pure resistor, capacitor and inductor. When an AC voltage $V(t)$ is applied to any component, it is defined as:

$$V(t) = V_{max}\sin(\omega t) \tag{1.2}$$

where ω is the angular frequency in radians per second (ω=2πf), where f is the frequency in Hz) and t is time in seconds. For a pure resistor of resistance R, the time dependent current $I(t)$ is always directly proportional to $V(t)$ as it follows Ohm's law:

$$I(t) = \frac{V_{max}}{R}\sin(\omega t) \tag{1.3}$$

As $I(t)$ has the same proportionality to frequency and time as $V(t)$ there can be no phase difference between $I(t)$ and $V(t)$. Hence at all frequencies the impedance of a resistor can be calculated by dividing equation (1.2) by (1.3):

$$Z^* = \frac{V(t)}{I(t)} = \mathrm{R} \tag{1.4}$$

Hence the impedance of a resistor is real and takes the value of the resistor's resistance at all frequencies.

The AC current in a capacitor is proportional to the rate of change of $V(t)$ and the capacitance of the capacitor. Differentiating equation (1.2) with respect to time and multiplication by the capacitance gives:

$$I(t) = C\left(\frac{dV(t)}{dt}\right) = \omega C V_{max}\cos(\omega t) \tag{1.5}$$

As sin(x) = cos(x-90), equation (1.5) can be re-written showing that $I(t)$ is -90° out of phase with $V(t)$. The phase difference is easier to handle by rewriting the sinusoidal function as a complex exponential using:

$$V_{max}\sin(\omega t) = V_{max} Im(e^{j\omega t}) \tag{1.6}$$

where e is Euler's number, using the relation:

$$e^{jt} = \cos(t) + j.\sin(t)$$

$$\therefore \mathrm{Im}(e^{jt}) = \sin(t) \tag{1.7}$$

Substitute equation (1.7) into (1.5):

$$I(t) = C\left(\frac{d(V_{max} Im(e^{j\omega t}))}{dt}\right) = C V_{max} Im(j\omega e^{j\omega t}) \tag{1.8}$$

Using Ohm's law divide equation (1.6) by (1.8):

$$\frac{V(t)}{I(t)} = \frac{V_{max} Im(e^{j\omega t})}{C V_{max} Im(j\omega e^{j\omega t})} \tag{1.9}$$

Take a factor of Im(jω) from the denominator and cancel like terms:

$$\frac{V(t)}{I(t)} = \frac{1}{Im(j\omega).C} \tag{1.10}$$

Im(jω) is simply jω, then multiply equation (1.10) by j over j:

$$\frac{V(t)}{I(t)} = \frac{1}{j\omega C}.\frac{j}{j}$$

$$Z^* = \frac{V(t)}{I(t)} = -\frac{j}{\omega C} \tag{1.11}$$

Here the impedance of a pure capacitor has only an imaginary component that is inversely proportional to the product of ω and capacitance.

Finally, for completeness, an inductor induces a voltage $V(t)$ when a sinusoidal current $I(t)$ passes through it:

$$I(t) = I_{max}\sin(\omega t) \tag{1.12}$$

The voltage is proportional to the rate of change of current passing through the inductor of inductance L:

$$V(t) = L\left(\frac{dI(t)}{dt}\right) = L\left(\frac{d(I_{max}\sin(\omega t))}{dt}\right) \tag{1.13}$$

$$V(t) = L\left(\frac{dI(t)}{dt}\right) = \omega L I_{max}\cos(\omega t) \tag{1.14}$$

Similar to the capacitor, the cosine indicates the current and voltage are out of phase for an inductor. Here $I(t)$ is +90° out of phase with $V(t)$. Again we will rewrite equation (1.12) as a complex exponential and substitute it into equation (1.13):

$$V(t) = L\left(\frac{dI(t)}{dt}\right) = L\left(\frac{d(I_{max}Im(e^{j\omega t}))}{dt}\right)$$

$$V(t) = LI_{max}Im(j\omega e^{j\omega t}) \tag{1.15}$$

Using Ohm's law, divide equation (1.15) by (1.12) written as complex exponentials to give an expression for the impedance:

$$Z^* = \frac{V(t)}{I(t)} = \frac{LI_{max}Im(j\omega e^{j\omega t})}{I_{max}Im(e^{j\omega t})} \tag{1.16}$$

Take a factor of Im($j\omega$) from the numerator and cancel like terms:

$$Z^* = Im(j\omega)L$$

As the imaginary component of Im($j\omega$) is $j\omega$:

$$Z^* = j\omega L \tag{1.16}$$

Here the impedance of an inductor has only an imaginary component that is proportional to ωL.

Real materials are effectively a combination of resistive, capacitive and inductive processes. From equations (1.2) to (1.16) it is easy to see that the electrical response of a material can be highly frequency dependent. As stated previously, here we are concerned with dielectric ceramics, where inductance is negligible and resistance and capacitance are the main contributors to the ceramic's electrical response over our considered frequency range. The interplay between capacitance and resistance has significance when interpreting impedance data. Within a microstructure different microstructural components (bulk, grain

boundaries, secondary phases *etc.*) all have resistances and capacitances associated with them. If we multiply the resistance and capacitance we have a time constant (τ) with units of seconds:

$$\tau = RC \tag{1.17}$$

Taking the inverse of equation (1.17) gives a quantity with units of inverse seconds (or Hz). This is frequency and is represented as an angular frequency, where ω has units of rads^{-1} and f is the frequency in Hz. Rearranging (1.17) gives:

$$\omega_{max} = \frac{1}{\tau} = \frac{1}{RC}$$

$$\omega_{max} RC = 1 \tag{1.18}$$

The angular frequency is denoted ω_{max} as it represents an angular frequency where the real and imaginary components of impedance have the same value. Removing the factor of 2π gives f_{max}, which is the characteristic relaxation frequency or Debye frequency of an RC circuit. This relationship is a useful result for understanding impedance spectroscopy.

The frequency dependent electrical behaviour of basic circuit elements not only illustrates where the electronic behaviour of materials comes from but also allows us to model it. Once a material's impedance spectrum has been measured, the data must be related back to the physical process occurring within the material. Typically this is achieved by constructing an equivalent circuit. This circuit contains basic elements that represent different parts of the material.

Using the example of a polycrystalline ceramic with resistive grain boundaries, a feasible equivalent circuit may contain two resistors. One resistor with a higher resistance than the other could represent the grain boundary and the less resistive resistor could represent the bulk. From equation (1.4) the impedance of a resistor is frequency independent; hence we would not be able to distinguish between the two resistors as frequency varies. While our assignment of bulk and grain boundary resistances is correct we must not neglect the capacitances.

Assuming the relative permittivity of the grain boundary and bulk is the same and the ceramic has micron-sized grains, it would be expected from equation (1.1) that, as the grain boundary is much thinner than the bulk, the grain boundary would have a higher capacitance than the bulk. As the capacitance and resistance of the grain boundary is greater than the bulk, from equation (1.18) the relaxation frequency of the grain boundary should be lower than the bulk. If the relaxation frequencies have sufficient separation (time constants varying by greater than two orders of magnitude) then there will be a distinct response from the bulk and the grain boundary regions in the ceramic's impedance spectra. Indeed a popular equivalent circuit for polycrystalline ceramics is two parallel capacitors and resistors connected in series[9]. The development of this equivalent circuit is detailed in the next chapter.

1.2.2. Derivation of Impedance Formalisms and Equivalent Circuits

Here we will derive the impedance response of some common equivalent circuits demonstrating how we use the impedance of resistors and capacitors derived in equations (1.2) to (1.16) in combination. A summary of the impedance of a resistor, capacitor and inductor is given in equations (1.19) to (1.21):

$$Z^* = R \tag{1.19}$$

$$Z^* = -\frac{j}{\omega C} \tag{1.20}$$

$$Z^* = \omega L \tag{1.21}$$

Impedance data can be viewed in several formalisms (see table. 1). It will be shown how the transformations of impedance weight different connectivity (whether circuits are connected in series or parallel) and magnitudes of resistance or capacitance differently.

Formalism	Symbol	Relation to Z*
Impedance	Z*	Z*
Admittance	Y*	$(Z^*)^{-1}$
Electric modulus	M*	$j\omega Z^*$
Complex capacitance	E*	$(j\omega Z^*)^{-1}$

Table. 1. *List of complex formalisms where j is the square root of minus one and ω is the angular frequency ($\omega=2\pi f$)[10]. E* and M* are absolute formalisms, multiplication of the Z* term by the cell capacitance (C_0) will give relative values.*

First consider a resistor and capacitor connected in series (see fig 5); this will be referred to as circuit one:

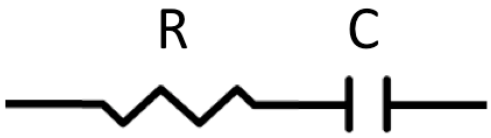

Fig. 5. *Equivalent circuit consisting of a resistor and capacitor connected in series.*

First we will derive Z* for circuit one. As impedances add in series, add equations (1.19) and (1.20):

$$Z^* = R - \frac{j}{\omega C} \tag{1.22}$$

From (1.22) the real component of Z^* (Z') takes the values of R (see fig. 6A) and the imaginary component is inversely proportional to ωC (see fig 6B). Plotting Z^* in the Nyquist format (real versus imaginary component) gives a straight line of $Z'=R$ with frequency increasing towards the real axis (see fig. 6C).

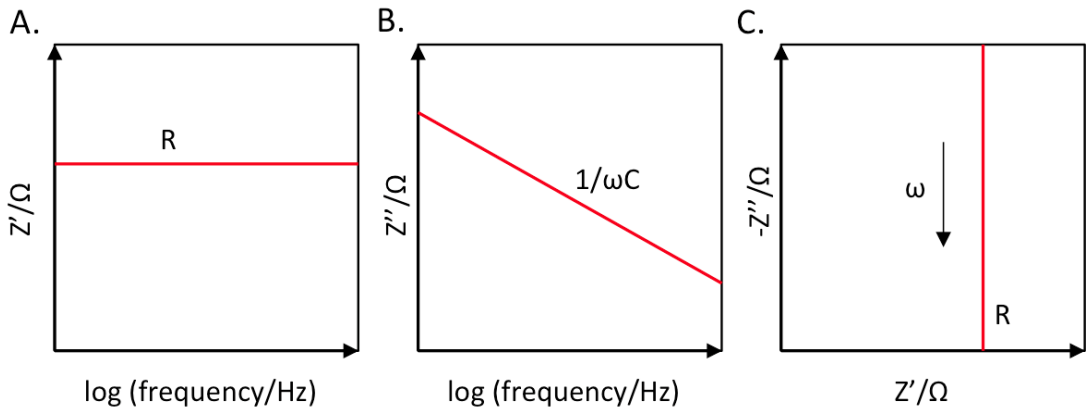

Fig. 6. *Schematics of (A) Z' versus frequency, (B) Z'' versus frequency and (C) Z'' versus Z' for a resistor and capacitor connected in series.*

Now transform Z^* into M^*. From table (1) multiply (1.22) by $j\omega$:

$$M^* = j\omega R - \frac{\omega j^2}{\omega C}$$

$$M^* = C^{-1} + j\omega R \qquad (1.23)$$

From (1.23) the real component of M* (M') takes the values of 1/C (see fig. 7A) and the imaginary component is proportional to ωR (see fig 7B). Plotting M* in the Nyquist format (M'' versus M') gives a straight line of Z'=1/C with frequency increasing away from the real axis (see fig. 7C).

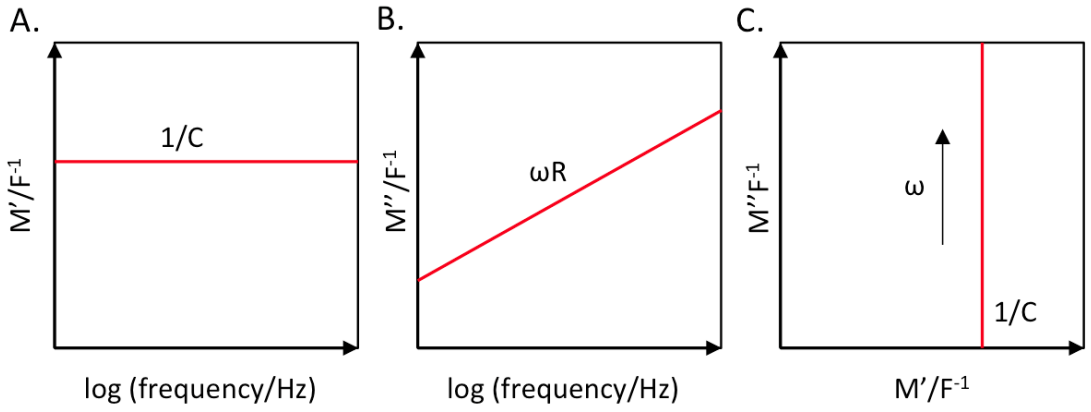

Fig. 7. *Schematics of (A) M' versus frequency, (B) M'' versus frequency and (C) M'' versus M' for a resistor and capacitor connected in series.*

Transform Z* into Y*. From table one, take the inverse of equation (1.22):

$$Y^* = \frac{1}{R - \frac{j}{\omega C}} \qquad (1.24)$$

Multiply top and bottom of equation (1.24) by ωC:

$$Y^* = \frac{\omega C}{R\omega C - j} \tag{1.25}$$

Multiply top and bottom of equation (1.25) by its complex conjugate to remove *j* from the denominator:

$$Y^* = \frac{\omega C}{R\omega C - j} \cdot \frac{R\omega C + j}{R\omega C + j}$$

$$Y^* = \frac{R(\omega C)^2 + j\omega C}{(R\omega C)^2 + 1} \tag{1.26}$$

Split into real and imaginary parts and multiply by R over R:

$$Y^* = \frac{R}{R} \cdot \left(\frac{R(\omega C)^2}{(R\omega C)^2 + 1} + \frac{j\omega C}{(R\omega C)^2 + 1} \right)$$

$$Y^* = \frac{1}{R} \cdot \frac{(R\omega C)^2}{(R\omega C)^2 + 1} + \frac{1}{R} \cdot \frac{j\omega RC}{(R\omega C)^2 + 1} \tag{1.27}$$

Consider the frequency limits of the real part (Y') of equation (1.27):

$$Y' = \frac{1}{R} \cdot \frac{(R\omega C)^2}{(R\omega C)^2 + 1} \tag{1.28}$$

Low frequency: $\omega \to 0$

$$Y' \to \frac{1}{R} \cdot \frac{(0)^2}{(0)^2 + 1}$$

$$Y' \to 0$$

High frequency: $\omega \to \infty$

$$Y' \to \frac{1}{R} \cdot \frac{(\infty)^2}{(\infty)^2 + 1}$$

$$Y' \to \frac{1}{R}$$

Plotting Y' as a function of frequency (logarithmic scale), Y' increases with frequency until it reaches $\sim 1/R$ and then plateaus (see fig. 8).

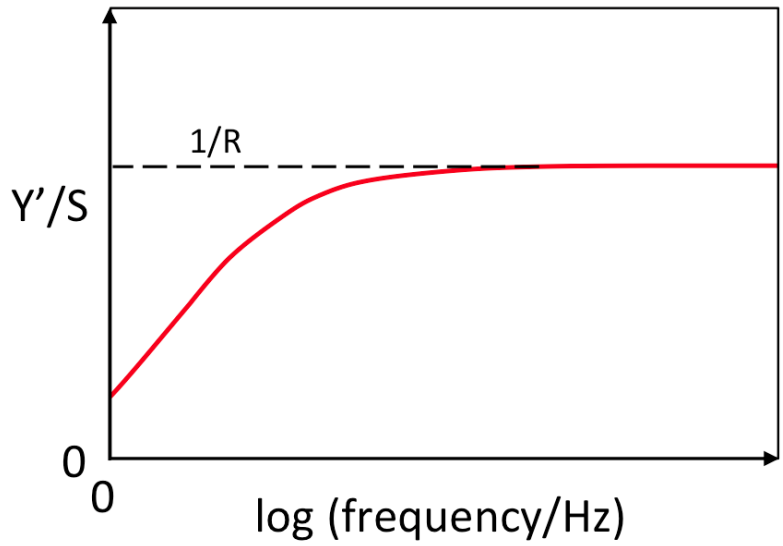

Fig. 8. *Schematic of the relation of Y' versus frequency for a resistor and capacitor in series with intercepts.*

Consider the frequency limits of the imaginary part (*Y''*) of equation (1.27):

$$Y'' = \frac{1}{R}.\frac{\omega RC}{(R\omega C)^2 + 1} \qquad (1.29)$$

Low frequency: $\omega \to 0$

$$Y'' \to \frac{1}{R}.\frac{(0)}{(0)^2 + 1}$$

$$Y'' \to 0$$

High frequency: $\omega \to \infty$

$$Y'' \to \frac{1}{R}.\frac{(\infty)}{(\infty)^2 + 1}$$

$$Y'' \to 0$$

Equation (1.29) contains a Debye function, at the Debye frequency when $\omega RC = 1$:

At Debye frequency: $\omega RC = 1$

$$Y'' = \frac{1}{R}.\frac{(1)}{(1)^2 + 1}$$

$$Y'' = \frac{1}{2R}$$

Considering the frequency limits and Debye function of (1.29) gives a single peak of height $1/2R$ at f_{max} when *Y''* is plotted as function of frequency (see fig. 9).

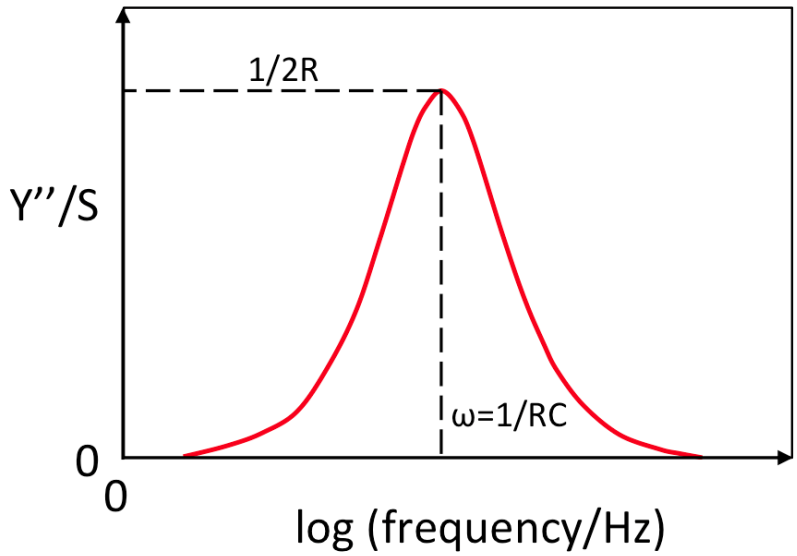

Fig. 9. *Schematic of the relation for Y'' versus frequency for a resistor and capacitor in series with intercepts.*

Plotting *Y*'' versus *Y*' (a Nyquist plot) gives a semicircle of height $1/2R$ and width $1/R$ with frequency increasing away from the origin (see fig. 10). The top of the semicircle coincides with f_{max} where $\omega RC = 1$.

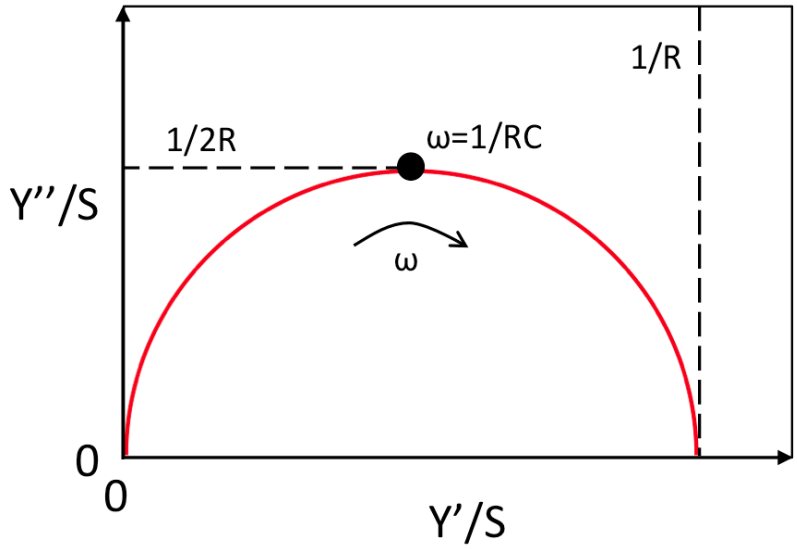

Fig. 10. *Schematic of a Nyquist plot for Y* (Y'' versus Y') with intercepts for a resistor and capacitor in series.*

Finally transforming *M** to *E**. From table (1) and equation (1.23):

$$E^* = (M^*)^{-1} = \frac{1}{(C^{-1} + j\omega R)} \tag{1.30}$$

Remove j from the denominator by taking the complex conjugate of the denominator and multiplying top and bottom by it:

$$E^* = \frac{1}{(C^{-1} + j\omega R)} . \frac{(C^{-1} - j\omega R)}{(C^{-1} - j\omega R)}$$

$$E^* = \frac{C^{-1} - j\omega R}{C^{-2} + (\omega R)^2} \tag{1.31}$$

Split into real and imaginary component and multiply top and bottom by C^2:

$$E^* = \left(\frac{C^{-1}}{C^{-2} + (\omega R)^2} - \frac{j\omega R}{C^{-2} + (\omega R)^2}\right).\frac{C^2}{C^2}$$

$$E^* = \frac{C}{1 + (\omega RC)^2} - \frac{j\omega RC^2}{1 + (\omega RC)^2} \tag{1.32}$$

Rewrite (1.32) in a more convenient form for spotting the Debye function:

$$E^* = C.\frac{1}{1 + (\omega RC)^2} - jC.\frac{\omega RC}{1 + (\omega RC)^2} \tag{1.33}$$

First consider the frequency limits of the real component (E') of (1.33):

$$E' = C.\frac{1}{1 + (\omega RC)^2} \tag{1.34}$$

Low frequency: $\omega \to 0$

$$E' \to C.\frac{1}{1 + (0)^2}$$

$$E' \to C$$

High frequency: $\omega \to \infty$

$$E' \to C.\frac{1}{1 + (\infty)^2}$$

$$E' \to 0$$

We plot E' as a function of frequency (logarithmic scale). Initially E' has a plateau with a value of C, then decreases to zero as frequency increases (see fig. 11).

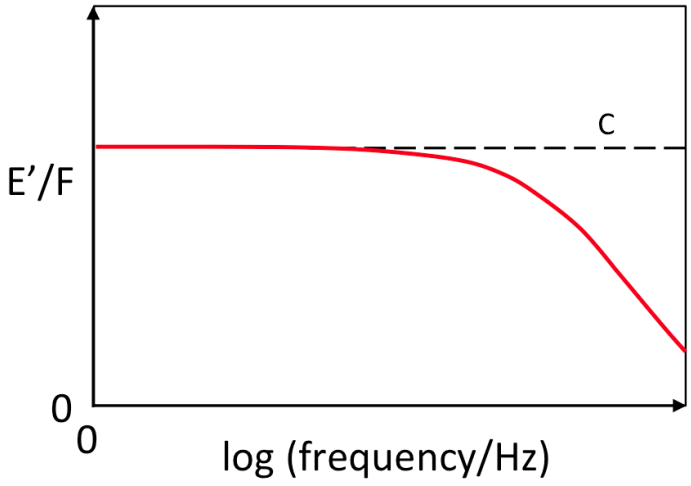

Fig. 11. *Schematic of the relation for E' versus frequency for a resistor and capacitor in series with intercepts.*

Consider the frequency limits of the imaginary part (E'') of equation (1.33):

$$E'' = C.\frac{\omega RC}{1 + (\omega RC)^2} \qquad (1.35)$$

Low frequency: $\omega \to 0$

$$E'' \to C.\frac{(0)}{1 + (0)^2}$$

$$E' \to 0$$

High frequency: $\omega \to \infty$

$$E'' \to C.\frac{(\infty)}{1 + (\infty)^2}$$

$$E'' \to 0$$

Equation (1.35) contains a Debye function, at the Debye frequency when $\omega RC = 1$:

At Debye frequency: $\omega RC = 1$

$$E'' = C.\frac{(1)}{1 + (1)^2}$$

$$E'' = \frac{C}{2}$$

Considering the frequency limits and Debye function of (1.35) gives a single peak of height $C/2$ at f_{max} when E'' is plotted as function of frequency (see fig. 12).

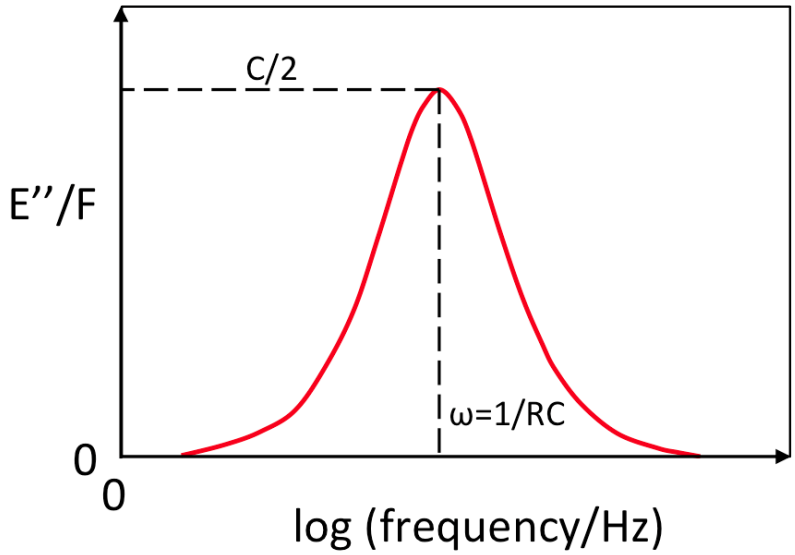

Fig. 12. *Schematic of the relation for E'' versus frequency for a resistor and capacitor in series with intercepts.*

Plotting E' versus E'' (a Nyquist plot) gives a semicircle of height $C/2$ and width C with frequency decreasing away from the origin (see fig. 13). The top of the semicircle coincides with f_{max} where $\omega RC = 1$.

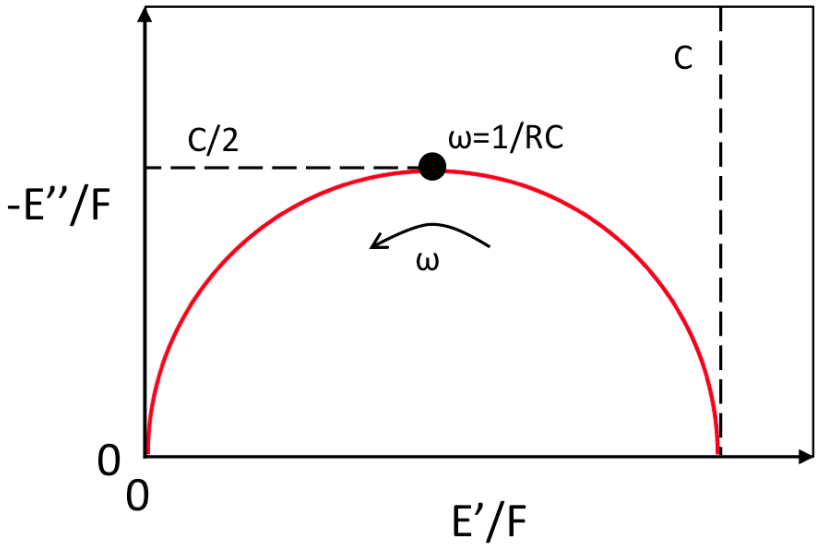

Fig. 13. *Schematic of a Nyquist plot for E* (E'' versus E') with intercepts for a resistor and capacitor in series.*

Next we will consider a resistor and capacitor connected in parallel (see fig. 14). This configuration will be referred to as circuit two:

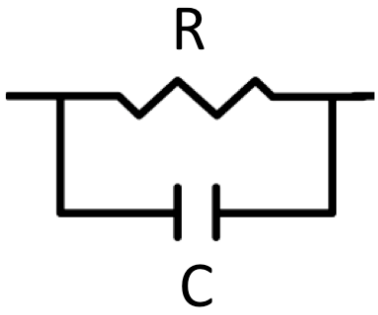

Fig. 14. *Equivalent circuit consisting of a resistor and a capacitor connected in parallel.*

As *Y** and *E** add in parallel we find these formalisms have simpler solutions for a resistor and a capacitor connected in parallel than for the serial case.

Consider Y*: as admittance adds in parallel, take the inverse of equations (1.19) and (1.20) and add them. Then multiply the imaginary part by *j* over *j* to remove *j* from the denominator:

$$Y^* = \frac{1}{R} - \frac{\omega C}{j} \cdot \frac{j}{j}$$

$$Y^* = \frac{1}{R} + j\omega C \qquad (1.36)$$

From (1.36) the real component of *Y** (*Y*') takes the values of $1/R$ (see fig. 15A) and the imaginary component (*Y*'') is proportional to ωC (see fig 15B). Plotting *Z** in the Nyquist format (real versus imaginary component) gives a straight line of $Y'=1/R$ with frequency increasing away from the real axis (see fig. 15C).

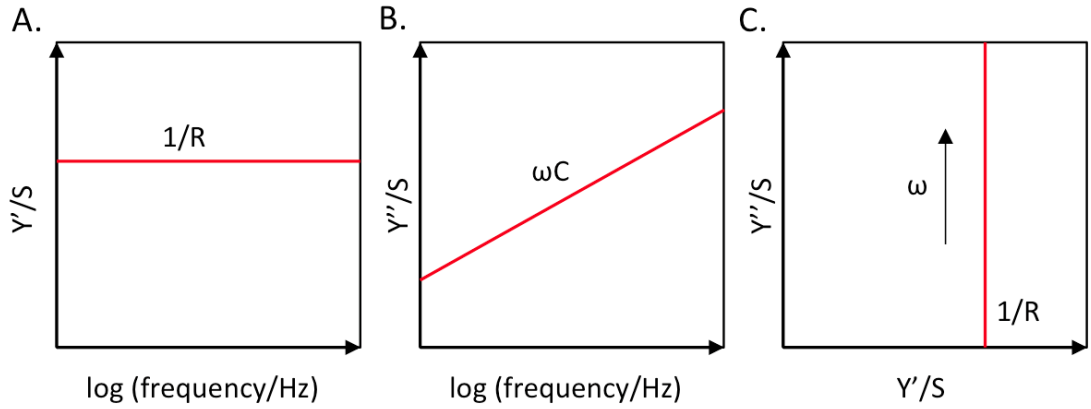

Fig. 15. *Schematics of (A) Y' versus frequency, (B) Y'' versus frequency and (C) Y'' versus Y' for a resistor and capacitor connected in parallel.*

Consider E^*: from table one, multiply equation (1.36) by $1/j\omega$ and multiply the imaginary part by j over j to remove j from the denominator:

$$E^* = \frac{Y^*}{\mathrm{j}\omega} = \frac{j}{j}.\frac{1}{R\mathrm{j}\omega} + \frac{\cancel{j\omega}C}{\cancel{j\omega}}$$

$$E^* = C - \frac{j}{\omega R} \qquad (1.37)$$

From (1.37) the real component of E^* (E') takes the values of C (see fig. 16A) and the imaginary component (E'') is inversely proportional to ωR (see fig 16B). Plotting Z^* in the Nyquist format (imaginary versus real component) gives a straight line of $E'=C$ with frequency decreasing away from the real axis (see fig. 16C).

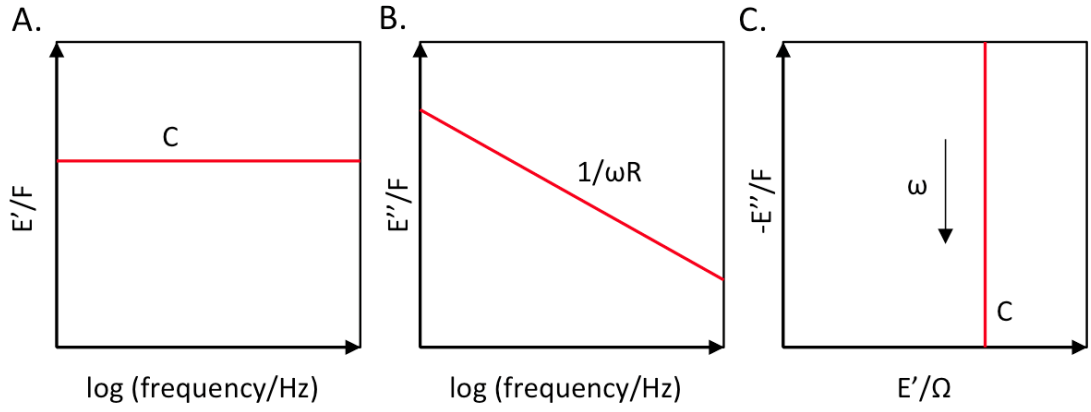

Fig. 16. *Schematics of (A) E' versus frequency, (B) E'' versus frequency and (C) E'' versus E' for a resistor and capacitor connected in parallel.*

Conversely Z^* and M^* have more complicated solutions for the parallel case.

Consider Z^*: Take the inverse of equation (1.36) and multiply by R over R:

$$Z^* = (Y^*)^{-1} = \frac{R}{R} . \frac{1}{\frac{1}{R} + j\omega C}$$

$$Z^* = \frac{R}{1 + j\omega RC} \tag{1.38}$$

Multiply top and bottom by the complex conjugate of the denominator to remove *j* from the denominator:

$$Z^* = \frac{R}{1 + j\omega RC} . \frac{1 - j\omega RC}{1 - j\omega RC}$$

$$Z^* = \frac{R - j\omega R^2 C}{1 + (\omega RC)^2} \tag{1.39}$$

Rearrange to isolate the real and imaginary component and to reveal a Debye function in the latter:

$$Z^* = R . \frac{1}{1 + (\omega RC)^2} - jR . \frac{\omega RC}{1 + (\omega RC)^2} \tag{1.40}$$

Consider the frequency limits of the real part (*Z'*) of (1.40):

$$Z' = R . \frac{1}{1 + (\omega RC)^2} \tag{1.41}$$

Low frequency: $\omega \to 0$

$$Z' \to R . \frac{1}{1 + (0)^2}$$

$$Z' \to R$$

High frequency: $\omega \to \infty$

$$Z' \to R . \frac{1}{1 + (\infty)^2}$$

$$Z' \to 0$$

Plotting *Z'* as a function of frequency (logarithmic scale), initially *Z'* has a plateau with a value of *R* then decreases to zero as frequency increases (see fig. 17).

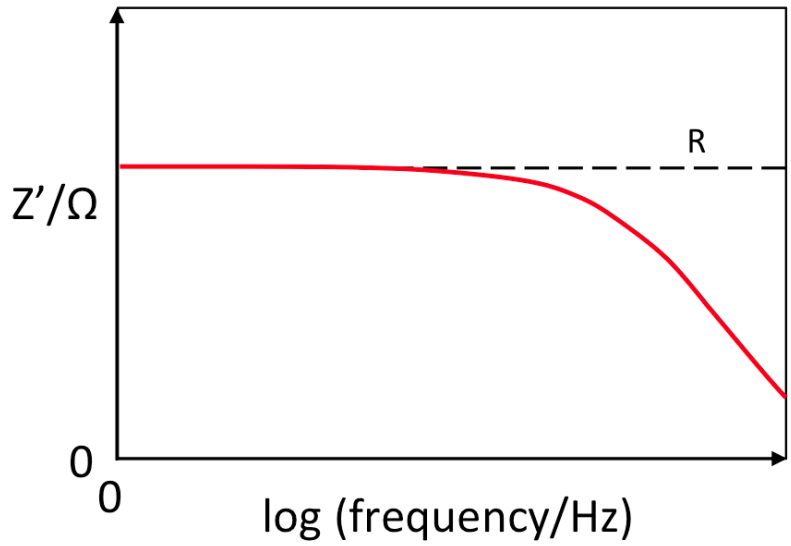

Fig. 17. *Schematic of the relation for Z' versus frequency for a resistor and capacitor in parallel with intercepts.*

Consider the frequency limits of the imaginary part (Z'') of equation (1.40):

$$Z'' = R.\frac{\omega RC}{1 + (\omega RC)^2} \tag{1.42}$$

Low frequency: $\omega \to 0$

$$Z'' \to R.\frac{(0)}{1 + (0)^2}$$

$$Z'' \to 0$$

High frequency: $\omega \to \infty$

$$Z'' \to R.\frac{(\infty)}{1 + (\infty)^2}$$

$$Z'' \to 0$$

Equation (1.43) contains a Debye function, at the Debye frequency when $\omega RC = 1$:

At Debye frequency: $\omega RC = 1$

$$Z'' = R.\frac{(1)}{1 + (1)^2}$$

$$Z'' = \frac{R}{2}$$

Considering the frequency limits and Debye function of (1.42) gives a single peak of height $R/2$ at f_{max} when Z'' is plotted against frequency (see fig. 18).

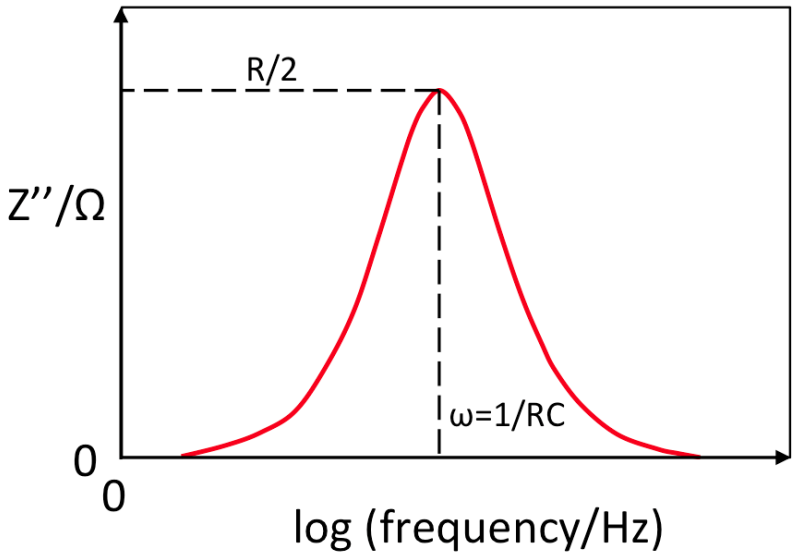

Fig. 18. *Schematic of the relation for Z'' versus frequency for a resistor and capacitor in parallel with intercepts.*

Plotting Z' versus Z'' (a Nyquist plot) gives a semicircle of height $R/2$ and width R with frequency decreasing away from the origin (see fig. 19). The top of the semicircle coincides with f_{max} where $\omega RC = 1$.

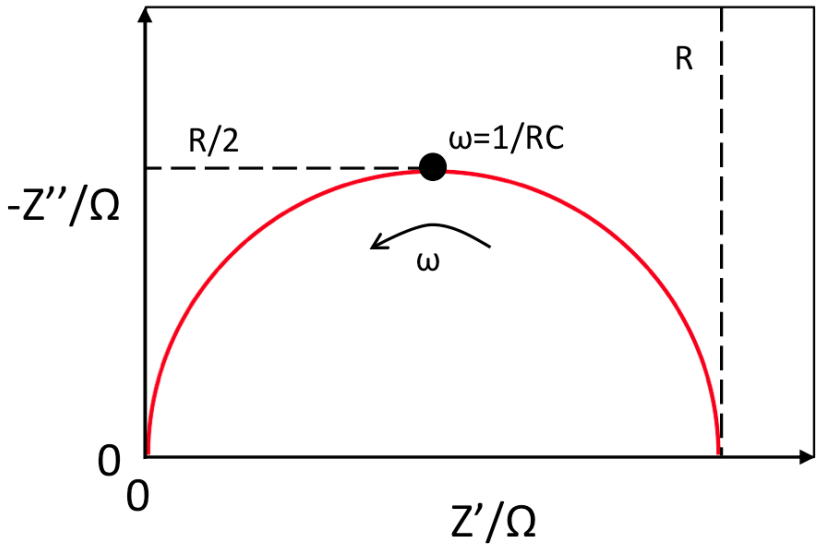

Fig. 19. *Schematic of a Nyquist plot of Z* (Z'' versus Z') with intercepts for a resistor and capacitor in series.*

Consider M^*: from table (1) multiply equation (1.42) by $j\omega$:

$$M^* = j\omega Z^* = j\omega\left(R.\frac{1}{1+(\omega RC)^2} - jR.\frac{\omega RC}{1+(\omega RC)^2}\right)$$

$$M^* = j\omega R.\frac{1}{1+(\omega RC)^2} - j^2 R\omega.\frac{\omega RC}{1+(\omega RC)^2}$$

$$M^* = R\omega.\frac{\omega RC}{1+(\omega RC)^2} + j\omega R.\frac{1}{1+(\omega RC)^2}$$

$$M^* = \frac{\omega^2 R^2 C}{1+(\omega RC)^2} + j.\frac{\omega R}{1+(\omega RC)^2} \quad (1.43)$$

Multiply (1.43) by C over C then rearrange to reveal a Debye function in the imaginary component:

$$M^* = \frac{C}{C}.\frac{\omega^2 R^2 C}{1+(\omega RC)^2} + j\frac{C}{C}.\frac{\omega R}{1+(\omega RC)^2}$$

$$M^* = \frac{1}{C}.\frac{\omega^2 R^2 C^2}{1+(\omega RC)^2} + j\frac{1}{C}.\frac{\omega RC}{1+(\omega RC)^2} \quad (1.44)$$

Consider the frequency limits of the real component (M') of equation (1.44):

$$M' = \frac{1}{C}.\frac{\omega^2 R^2 C^2}{1+(\omega RC)^2} \quad (1.45)$$

Low frequency: $\omega \to 0$

$$M' \to \frac{1}{C}.\frac{(0)}{1+(0)^2}$$

$$M' \to 0$$

High frequency: $\omega \to \infty$

$$M' \to \frac{1}{C}.\frac{(\infty)^2}{1+(\infty)^2}$$

$$Z' \to \frac{1}{C}$$

Plotting M' as a function of frequency (logarithmic scale), M' increases with frequency until it reaches $\sim 1/C$ and then plateaus (see fig. 20).

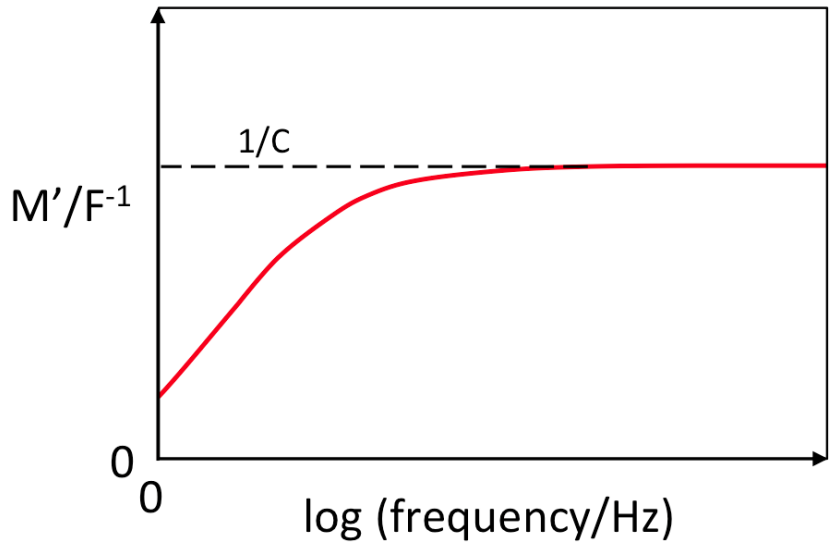

Fig. 20. *Schematic of the relation for M' versus frequency for a resistor and capacitor in parallel with intercepts.*

Consider the frequency limits of the imaginary part (M'') of equation (1.44):

$$M'' = \frac{1}{C} \cdot \frac{\omega RC}{1 + (\omega RC)^2} \tag{1.46}$$

Low frequency: $\omega \to 0$

$$M'' \to \frac{1}{C} \cdot \frac{(0)}{1 + (0)^2}$$

$$M'' \to 0$$

High frequency: $\omega \to \infty$

$$M'' \to \frac{1}{C} \cdot \frac{(\infty)}{1 + (\infty)^2}$$

$$M'' \to 0$$

Equation (1.46) contains a Debye function, at the Debye frequency when $\omega RC = 1$:

At Debye frequency: $\omega RC = 1$

$$M'' = \frac{1}{C} \cdot \frac{(1)}{1 + (1)^2}$$

$$Z'' = \frac{1}{2C}$$

Considering the frequency limits and Debye function of (1.46) gives a single peak of height $1/2C$ at f_{max} when M'' is plotted against frequency (see fig. 21). The full width half maximum of the peak is 1.14 decades of frequency.

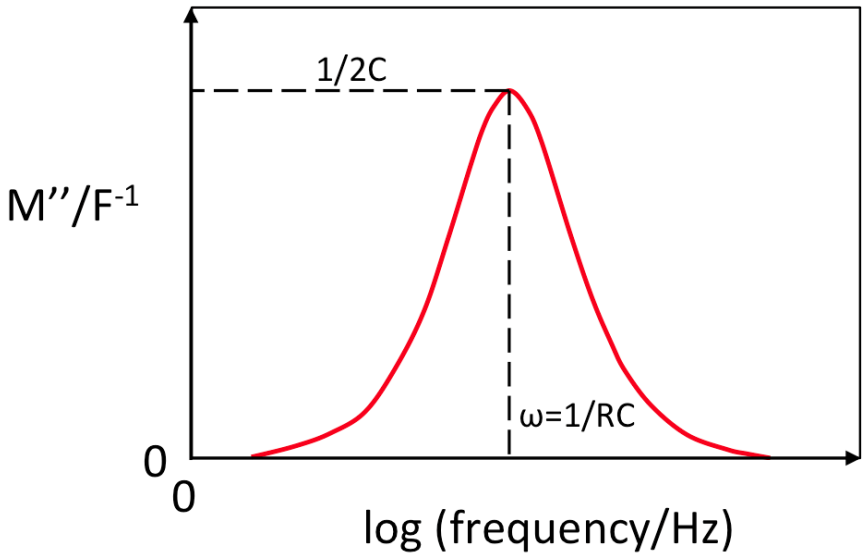

Fig. 21. *Schematic of the relation for M'' versus frequency for a resistor and capacitor in parallel with intercepts.*

Plotting *M*' versus *M*'' (a Nyquist plot) gives a semicircle of height $1/2C$ and width $1/C$ with frequency increasing away from the origin (see fig. 22). The top of the semicircle coincides with f_{max} where $\omega RC = 1$.

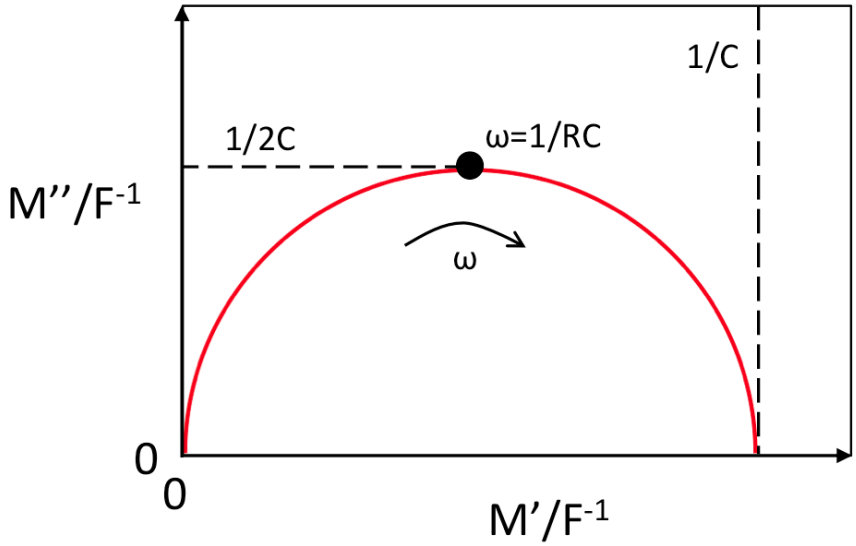

Fig. 22. *Schematic of a Nyquist plot of M* (M'' versus M') with intercepts for a resistor and capacitor in series.*

Finally we will consider the impedance response of two parallel resistors and capacitors connected in series (see fig. 23). This circuit will be referred to as circuit three.

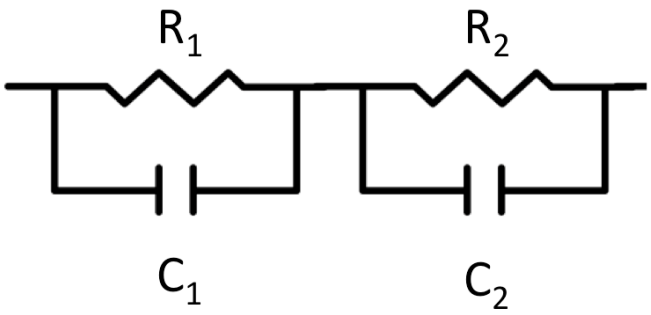

Fig. 23. *Schematic of two parallel resistor capacitor elements connected in series.*

The impedance response of circuit three is derived in a similar manner to circuits one and two but the derivations are significantly longer. The reader is directed to appendix (A.1) for the full derivations. For the purpose of consistency when showing the relations between the real and imaginary components versus frequency it is assumed that $R_2 >> R_1$ and $C_2 >> C_1$. The final equations are given below:

Consider Z^*:

$$Z^* = \frac{R_1 - j\omega R_1^2 C_1}{1 + (\omega R_1 C_1)^2} + \frac{R_2 - j\omega R_2^2 C_2}{1 + (\omega R_2 C_2)^2} \tag{1.47}$$

Consider the frequency limits of the real part (Z') of (1.29):

$$Z' = \frac{R_1}{1 + (\omega R_1 C_1)^2} + \frac{R_2}{1 + (\omega R_2 C_2)^2}$$

Low frequency: $\omega \to 0$

$$Z' = \frac{R_1}{1 + (0)^2} + \frac{R_2}{1 + (0)^2}$$

$$Z' \to R_1 + R_2 \tag{1.48}$$

High frequency: $\omega \to \infty$

$$Z' = \frac{R_1}{1 + (\infty)^2} + \frac{R_2}{1 + (\infty)^2}$$

$$Z' \to 0 \tag{1.49}$$

Since $R_2 >> R_1$ and $C_2 >> C_1$, from equation (1.17), the Debye frequency of R_2C_2 (f_{max2}) will occur at a lower frequency then the Debye frequency of R_1C_1 (f_{max1}). If we consider the contribution of R_2C_2 and R_1C_1 to Z' in the intermediate frequency range between f_{max2} and f_{max1}:

For R_2C_2:

$$Z' = \frac{R_2}{1 + (\omega R_2 C_2)^2}$$

At f_{max2}: $\omega R_2 C_2 = 1$

$$Z' \to \frac{R_2}{1 + (1)^2}$$

$$Z' \to \frac{R_2}{2} \tag{1.50}$$

As frequency increases beyond f_{max2}: $\omega \to \infty$

$$Z' \to \frac{R_2}{1 + (\infty)^2}$$

$$Z' \to 0 \tag{1.51}$$

Now considering R_1C_1, at f_{max2} ωR_1C_1 will tend to zero as we are far from f_{max1} hence:

For R_1C_1:

$$Z' = \frac{R_1}{1 + (\omega R_1 C_1)^2}$$

At f_{max2}: $\omega R_2C_2 = 1$

$$Z' = \frac{R_1}{1 + (0)^2}$$

$$Z' = R_1 \tag{1.52}$$

At higher frequencies increasing towards f_{max1}:

$\omega R_1C_1 \to 1$

$$Z' \to + \frac{R_1}{1 + (1)^2}$$

$$Z' \to + \frac{R_1}{2} \tag{1.53}$$

Consider equations (1.48) to (1.53) over the entire frequency range. From equation (1.48), at low frequency Z' will plateau at $Z'=R_1+R_2$. At intermediate frequencies past f_{max2} the contribution of R_2C_2 to Z' will drop to zero from (1.50) and (1.51). The contribution of R_1C_1 to Z' will decay from a value of R_1 and then to $R_1/2$ from (1.52) and (1.53), respectively. The decay of R_2C_2 will be quicker than R_1C_1 as the frequency is > f_{max2} but < f_{max1} leading to a plateau of $Z'=R_1$. Finally as frequency increases beyond f_{max1} Z' will drop off to zero from (1.49). This gives two plateaus of $Z'=R_1+R_2$ and $Z'=R_1$ at low and high frequencies, respectively (see fig. 24).

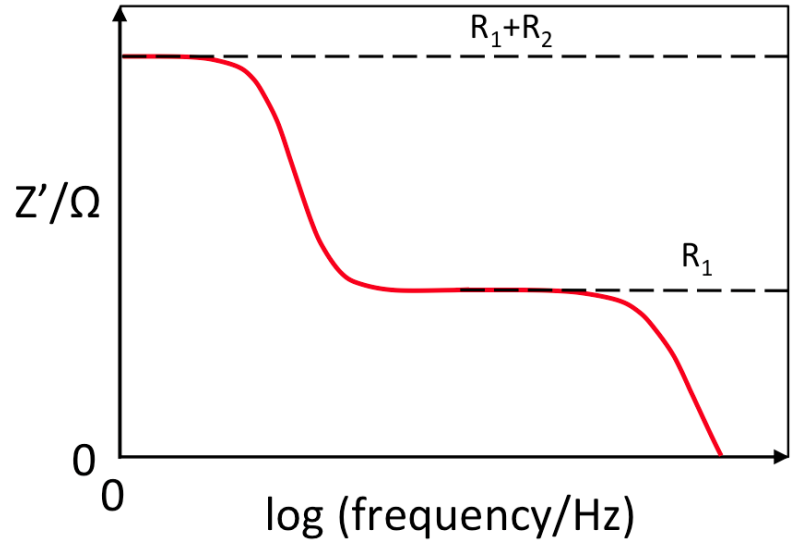

Fig. 24. *Schematic of the relation for Z' versus frequency for two parallel resistors and capacitors connected in series with intercepts.*

Considering the imaginary parts of equation (1.47):

$$-Z'' = R_1.\frac{\omega R_1 C_1}{1+(\omega R_1 C_1)^2} + R_2.\frac{\omega R_2 C_2}{1+(\omega R_2 C_2)^2} \qquad (1.54)$$

We see that there are two Debye functions, which will have peaks of values $R_1/2$ and $R_2/2$ when frequency equals f_{max1} and f_{max2}, respectively. If the time constants of the two parallel RC circuits are sufficiently different there will be two distinct Debye peaks in the Z'' spectroscopic plot (see fig. 25).

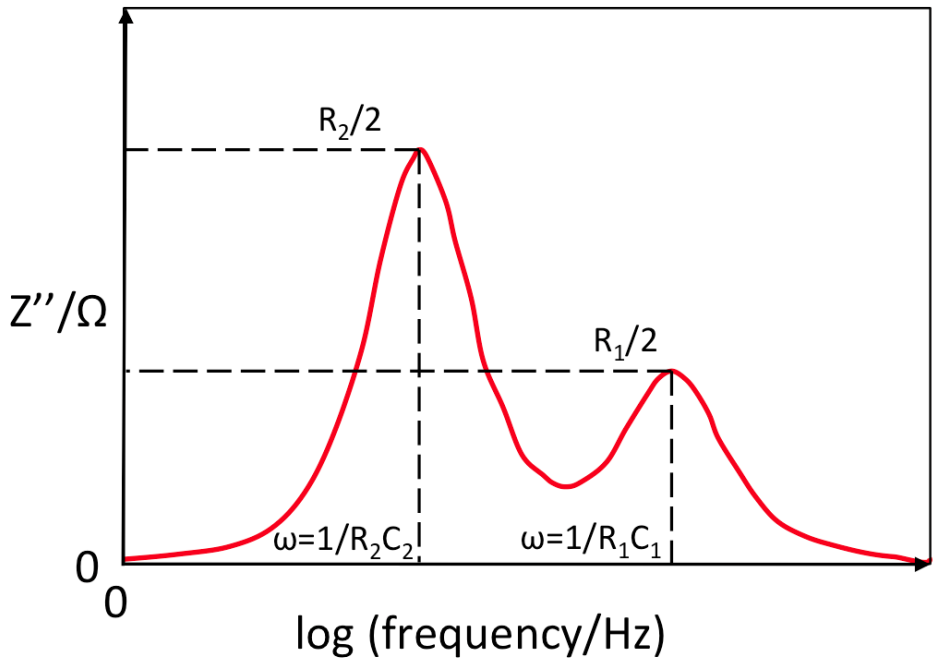

Fig. 25. *Schematic of Z'' versus frequency for two resistors and capacitors in parallel connected in series with intercepts.*

Combining the Z' and Z'' as a Nyquist plot gives two arcs of diameters R_1 and R_2 and heights $R_1/2$ and $R_2/2$, respectively. The peaks of the arcs coincide with f_{max1} and f_{max2} (see fig. 26).

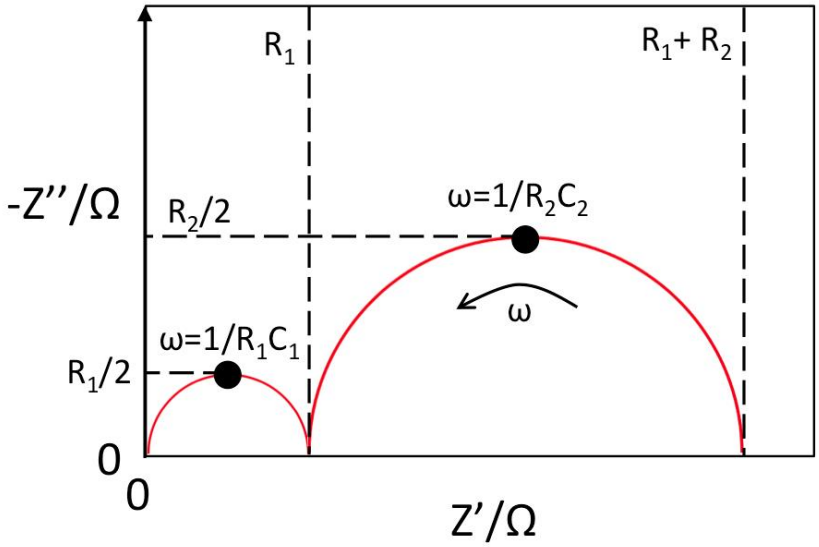

Fig. 26. *Schematic of a Nyquist plot for Z* (Z'' versus Z') with intercepts for two parallel resistors and capacitors connected in series with intercepts.*

Consider M^*:

$$M^* = \frac{1}{C_1}.\frac{\omega^2 R_1^2 C_1^2 + j\omega R_1 C_1}{1 + (\omega R_1 C_1)^2} + \frac{1}{C_2}.\frac{\omega^2 R_2^2 C_2^2 + j\omega R_2 C_2}{1 + (\omega R_2 C_2)^2} \tag{1.55}$$

First consider the frequency limits of the real part (M') of (1.55):

$$M' = \frac{1}{C_1}.\frac{\omega^2 R_1^2 C_1^2}{1 + (\omega R_1 C_1)^2} + \frac{1}{C_2}.\frac{\omega^2 R_2^2 C_2^2}{1 + (\omega R_2 C_2)^2} \tag{1.56}$$

Low frequency: $\omega \to 0$

$$M' \to \frac{1}{C_1}.\frac{(0)^2}{1 + (0)^2} + \frac{1}{C_2}.\frac{(0)^2}{1 + (0)^2}$$

$$M' \to 0 \tag{1.57}$$

High frequency: $\omega \to \infty$

$$M' \to \frac{1}{C_1}.\frac{(\infty)^2}{1 + (\infty)^2} + \frac{1}{C_2}.\frac{(\infty)^2}{1 + (\infty)^2}$$

$$M' \to \frac{1}{C_1} + \frac{1}{C_2} \tag{1.58}$$

Since $R_2 >> R_1$ and $C_2 >> C_1$, from equation (17), the Debye frequency of R_2C_2 (f_{max2}) will occur at a lower frequency than the Debye frequency of R_1C_1 (f_{max1}). If we

consider the contribution of R_2C_2 and R_1C_1 to M' in the intermediate frequency range between f_{max2} and f_{max1}:

For R_2C_2:

$$M' = \frac{1}{C_2} \cdot \frac{\omega^2 R_2^2 C_2^2}{1 + (\omega R_2 C_2)^2}$$

At f_{max2}: $\omega R_2 C_2 = 1$

$$M' = \frac{1}{C_2} \cdot \frac{(1)^2}{1 + (1)^2}$$

$$M' = \frac{1}{2C_2} \tag{1.59}$$

As frequency increases beyond f_{max2}: $\omega \to \infty$

$$M' \to \frac{1}{C_2} \cdot \frac{(\infty)^2}{1 + (\infty)^2}$$

$$M' \to \frac{1}{C_2} \tag{1.60}$$

Now considering R_1C_1, at f_{max2} $\omega R_1 C_1$ will tend to zero as we are far from f_{max1} hence:

For R_1C_1:

$$M' = \frac{1}{C_1} \cdot \frac{\omega^2 R_1^2 C_1^2}{1 + (\omega R_1 C_1)^2}$$

At f_{max2}: $\omega R_2 C_2 = 1$

$$M' \to \frac{1}{C_1} \cdot \frac{(0)^2}{1 + (0)^2}$$

$$M' \to 0 \tag{1.61}$$

At higher frequencies increasing towards f_{max1}:

At f_{max1}: $\omega R_1 C_1 \to 1$

$$M' \to \frac{1}{C_1} \cdot \frac{(1)^2}{1 + (1)^2}$$

$$M' \to \frac{1}{2C_1} \tag{1.62}$$

Consider equations (1.57) to (1.62) over the entire frequency range. At high frequency it can be seen that M' tends to $1/C_1 + 1/C_2$ from equation (1.48). As frequency decreases M' then decays. The contribution of R_1C_1 decays from $1/C_1$ to $1/2C_1$ between frequencies of ∞ and f_{max1}, from equations (1.58) and (1.62). However the contribution of R_2C_2 to M' decays from $1/C_2$ to $1/2C_2$ over a larger frequency range (∞ to f_{max2}) from equations (1.60) and (1.59). This means over the intermediate frequency range (f_{max1} to f_{max2}) the $1/C_2$ term will dominate causing a plateau of value $1/C_2$. As frequency decreases from f_{max2} to zero, M' will decay to zero from equation (57). This leads to two plateaus of $1/C_2$ and $1/C_1 + 1/C_2$ if M' is

plotted as a function of frequency for two resistors and capacitors in parallel connected in series (see fig. 27).

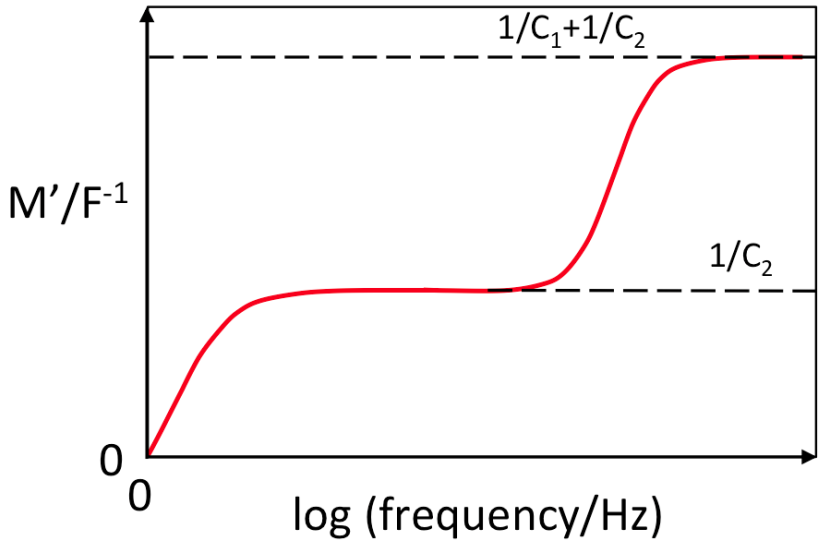

Fig. 27. *Schematic of the relation for M' versus frequency for a two resistors and capacitors in parallel connected in series with intercepts.*

Considering the imaginary parts of equation (1.55):

$$M'' = \frac{1}{C_1}.\frac{\omega R_1 C_1}{1+(\omega R_1 C_1)^2} + \frac{1}{C_2}.\frac{\omega R_2 C_2}{1+(\omega R_2 C_2)^2}$$

We see that there are two Debye functions, which will have peaks of values $1/2C_1$ and $1/2C_2$ when the frequency equals f_{max1} and f_{max2}, respectively. If the time constants of the two parallel RC circuits are sufficiently different there will be two distinct Debye peaks in the *M*'' spectroscopic plot (see fig. 28).

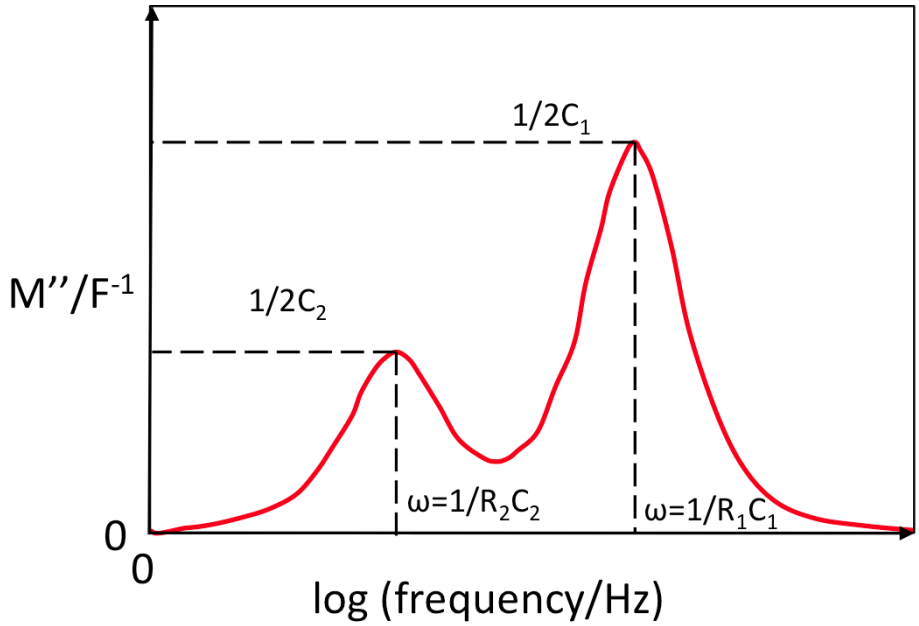

Fig. 28. *Schematic of the relation for M'' versus frequency for two parallel resistors and capacitors connected in series with intercepts.*

Combining the *M*' and *M*'' as a Nyquist plot gives two arcs of diameters $1/C_1$ and $1/C_2$ and heights $1/2C_1$ and $1/2C_2$, respectively. The peaks of the arcs coincide with f_{max1} and f_{max2} (see fig. 29).

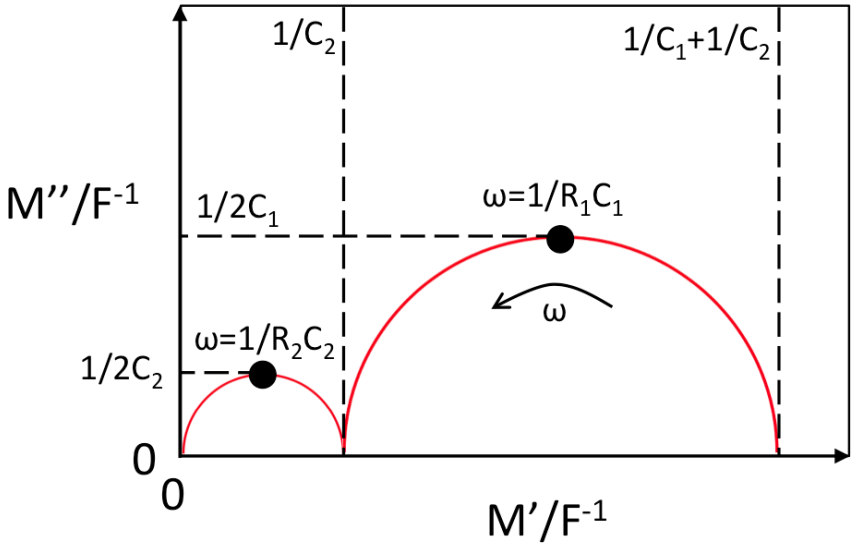

Fig. 29. *Schematic of a Nyquist plot for M* (M'' versus M') with intercepts for two parallel resistors and capacitors connected in series with intercepts.*

Consider *Y**:

$$Y^* = \frac{\left(\left(\frac{1}{R_1R_2}\right) + j\omega\left(\frac{C_1}{R_2} + \frac{C_2}{R_1}\right) - \omega^2 C_1C_2\right)\left(\left(\frac{1}{R_1} + \frac{1}{R_2}\right) - j\omega(C_1 + C_2)\right)}{\left(\frac{1}{R_1} + \frac{1}{R_2}\right)^2 + \omega^2(C_1 + C_2)^2} \qquad (1.63)$$

Expand equation (1.63) and collect the real components, an extra term is revealed from multiplying the two $j\omega$ terms:

$$Y' = \frac{\frac{1}{R_1R_2}\left(\frac{1}{R_1} + \frac{1}{R_2}\right) + \omega^2(C_1 + C_2)\left(\frac{C_1}{R_2} + \frac{C_2}{R_1}\right) - \omega^2 C_1C_2\left(\frac{1}{R_1} + \frac{1}{R_2}\right)}{\left(\frac{1}{R_1} + \frac{1}{R_2}\right)^2 + \omega^2(C_1 + C_2)^2} \qquad (1.64)$$

Consider the frequency limits of equation (1.64):

Low frequency:
$\omega \to 0$

$$Y' \to \frac{\frac{1}{R_1R_2}\left(\frac{1}{R_1} + \frac{1}{R_2}\right) + (0)^2 - (0)^2}{\left(\frac{1}{R_1} + \frac{1}{R_2}\right)^2 + (0)^2}$$

$$Y' \to \frac{\frac{1}{R_1R_2}\left(\frac{1}{R_1} + \frac{1}{R_2}\right)}{\left(\frac{1}{R_1} + \frac{1}{R_2}\right)^2} \qquad (1.65)$$

Cancel like terms and rearrange equation (1.65) to give:

$$Y' \to \frac{\frac{1}{R_1 R_2}\left(\frac{\cancel{1}}{\cancel{R_1}} + \frac{\cancel{1}}{\cancel{R_2}}\right)}{\left(\frac{1}{R_1} + \frac{1}{R_2}\right)^{\cancel{2}}}$$

$$Y' \to \frac{1}{\left(\frac{\cancel{R_1} R_2}{\cancel{R_1}} + \frac{R_1 \cancel{R_2}}{\cancel{R_2}}\right)}$$

$$Y' \to \frac{1}{R_1 + R_2} \tag{1.66}$$

At high frequency the ω^2 terms dominate:

High frequency: $\omega \to \infty$

$$Y' \to \frac{(C_1 + C_2)\left(\frac{C_1}{R_2} + \frac{C_2}{R_1}\right) - C_1 C_2\left(\frac{1}{R_1} + \frac{1}{R_2}\right)}{(C_1 + C_2)^2} \tag{1.67}$$

Expand the numerator of (1.67):

$$Y' \to \frac{\frac{C_1^2}{R_2} + \frac{C_1 C_2}{R_1} + \frac{C_1 C_2}{R_2} + \frac{C_2^2}{R_1} - \frac{C_1 C_2}{R_1} - \frac{C_1 C_2}{R_2}}{(C_1 + C_2)^2}$$

$$Y' \to \frac{\frac{C_1^2}{R_2} + \frac{\cancel{C_1 C_2}}{\cancel{R_1}} + \frac{\cancel{C_1 C_2}}{\cancel{R_2}} + \frac{C_2^2}{R_1} - \frac{\cancel{C_1 C_2}}{\cancel{R_1}} - \frac{\cancel{C_1 C_2}}{\cancel{R_2}}}{(C_1 + C_2)^2}$$

$$Y' \to \frac{\frac{C_1^2}{R_2} + \frac{C_2^2}{R_1}}{(C_1 + C_2)^2} \tag{1.68}$$

Hence the high frequency intercept of Y' is a composite term. Applying the assumptions made about the relative magnitude of R_1, R_2, C_1 and C_2:

$R_2 >> R_1$

$$\therefore \frac{C_1^2}{R_2} + \frac{C_2^2}{R_1} \sim \frac{C_2^2}{R_1}$$

$C_2 >> C_1$

$$\therefore (C_1 + C_2)^2 \sim C_2^2$$

$$\therefore Y' \sim \frac{\frac{C_2^2}{R_1}}{C_2^2}$$

$$\therefore Y' \sim \frac{1}{R_1} \tag{1.69}$$

Hence Y' plateaus at a value of $1/R_1 + 1/R_2$ at low frequency and increases to a composite value at high frequency that can be approximated as $1/R_1$ if $R_2 >> R_1$ and $C_2 >> C_1$ (see fig. 30).

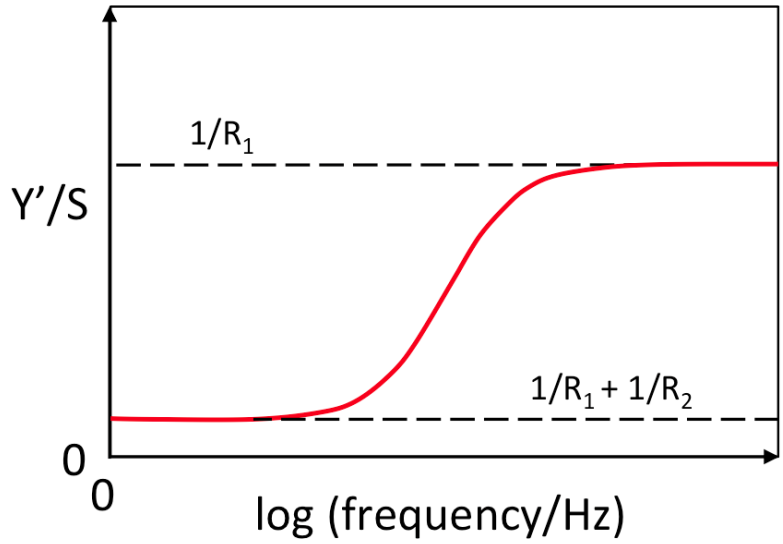

Fig. 30. *Schematic of the relation for Y' versus frequency for two parallel resistors and capacitors connected in series with intercepts.*

Now expand equation (1.63) and consider the imaginary components:

$$Y'' = \frac{-\omega\left(\frac{C_1 + C_2}{R_1 R_2}\right) + \omega\left(\frac{C_1}{R_2} + \frac{C_2}{R_1}\right)\left(\frac{1}{R_1} + \frac{1}{R_2}\right) + \omega^3 (C_1 + C_2) C_1 C_2}{\left(\frac{1}{R_1} + \frac{1}{R_2}\right)^2 + \omega^2 (C_1 + C_2)^2} \qquad (1.70)$$

Consider the frequency limits of (1.70):

Low frequency: $\omega \to 0$

$$Y'' \to \frac{(0) + (0) + (0)}{\left(\frac{1}{R_1} + \frac{1}{R_2}\right)^2 + (0)^2}$$

$$Y'' \to 0 \qquad (1.71)$$

At high frequency the terms that do not contain powers of ω can be neglected:

High frequency: $\omega \to \infty$

$$Y'' \to \frac{\omega^3 (C_1 + C_2) C_1 C_2}{\omega^2 (C_1 + C_2)^2}$$

$$Y'' \to \frac{\omega (C_1 + C_2) C_1 C_2}{(C_1 + C_2)^2}$$

$$Y'' \rightarrow \frac{\infty}{(C_1 + C_2)^2}$$

$$Y'' \rightarrow \infty \tag{1.72}$$

From equations (1.71) and (1.72) *Y*'' must rise from near zero at low frequency and tends to infinity as frequency tends to infinity. Further expansion of equation (1.70) results in a large amount of coefficients. A more direct route to understanding its relationship with frequency is obtained through consideration of how the paths of least resistance would alter with frequency through circuit three. From equation (1.20) the impedance of a capacitor is inversely proportional to frequency, hence at a higher frequency more current will pass through a capacitor. At low frequency the impedance of the capacitors in circuit three (C_1 and C_2) will be high, blocking current and forcing it to flow through the two resistors (R_1 and R_2, see fig. 31A).

From equation (1.19) the impedance of a resistor is independent of frequency and has no imaginary component. Hence *Y*'' tends to zero in agreement with (1.71). As the frequency increases to f_{max2} the impedance of C_2 will decreases until it is equal to the impedance of R_2. When the frequency increases beyond f_{max2} the impedance of C_2 will be less than R_2, shorting R_2 out (see fig. 31B). As $C_1 < C_2$, there will be a frequency range where C_2 can bypass R_2 but C_1 cannot bypass R_1. Here circuit three resembles a resistor and a capacitor connected in series and is referred to as a parasitic capacitance. From equation (29), the form of *Y*'' for a resistor and a capacitor connected in series as a function of frequency has a Debye peak. Here the Debye peak will be proportional to $1/2R_1$ and occur at $f_{max}=1/R_1C_2$. As the frequency increases past the Debye frequency of the parasitic capacitance the contribution of R_1 will decrease.

When the frequency exceeds f_{max1} the impedance of C_1 will be less than R_1 hence all current will flow through the two capacitors (see fig. 31C). This leads to an equivalent circuit of two capacitors connected in series. As the impedance of a capacitor decreases with frequency, from table 1, impedance is the inverse of admittance hence *Y*" will increase with frequency past f_{max1} in agreement with equation (1.72).

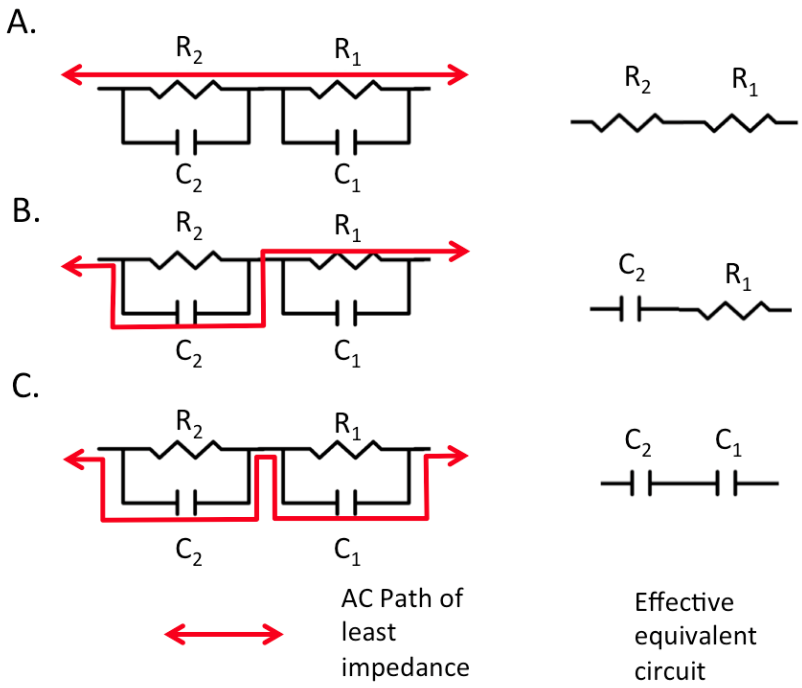

Fig. 31. *Variable AC pathways through two parallel resistors and capacitors connected in series, where $R_2 >> R_1$ and $C_2 >> C_1$ and the effective equivalent circuit as the pathway changes with frequency. At frequencies (A) from DC to less than f_{max2}, (B) from over f_{max2} to less than f_{max1} and (C) greater than f_{max1}.*

The trend of Y'' with frequency is the addition of a growth term with a Debye function of height $1/2R_1$ at the relaxation frequency of the parasitic capacitance (see fig. 32). Combining the real and imaginary components of Y^* as a Nyquist plot gives a semi circle offset from the origin by $1/(R_1 + R_2)$. The height of the semicircle is equal to $1/2R_1$ and their maximum coincides with the relaxation frequency of the parasitic capacitance. The high frequency intercept of the semicircle equals $1/R_1$. A further increase in frequency results in a spike of $Y'=1/R_1$ (see fig. 33).

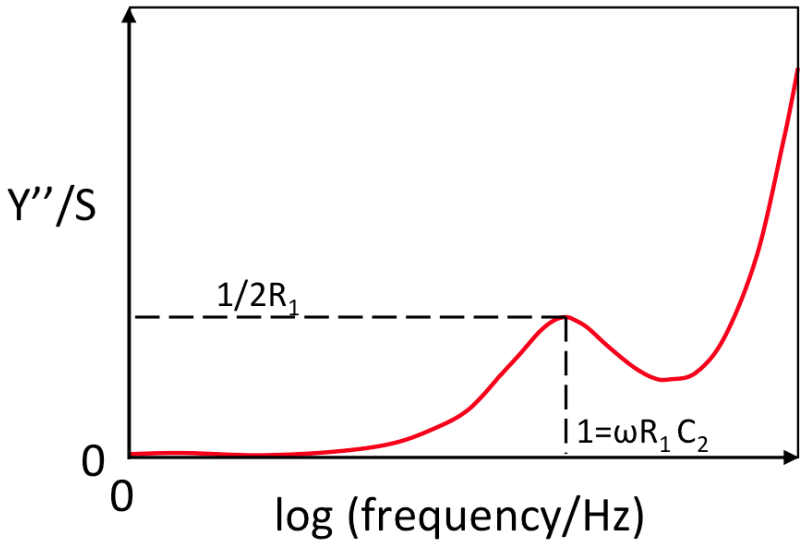

Fig. 32. *Schematic of the relation for Y'' versus frequency for two parallel resistors and capacitors connected in series with intercepts.*

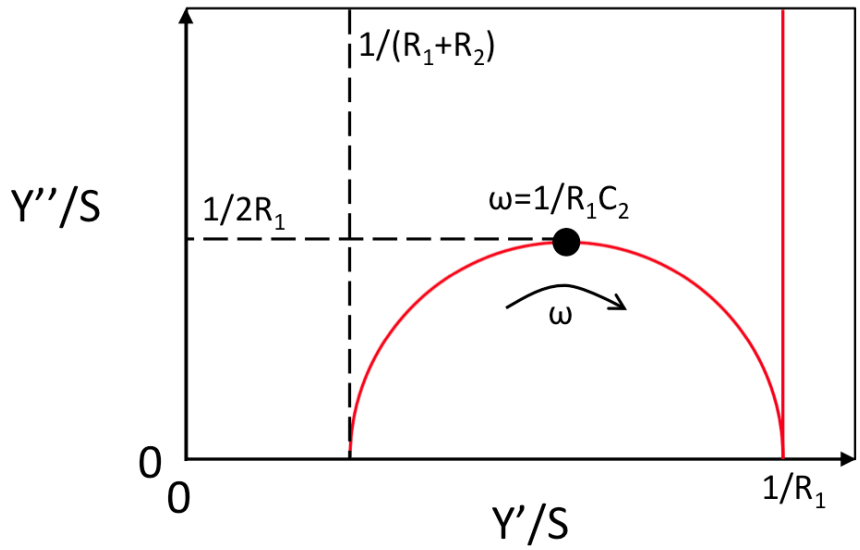

Fig. 33. *Schematic of a Nyquist plot for Y* (Y'' versus Y') with intercepts for two parallel resistors and capacitors connected in series with intercepts.*

Consider E^*:

From table (1):

$$E^* = \frac{1}{j\omega Z^*} = \frac{Y^*}{j\omega} \tag{1.73}$$

Substituting (1.73) into (1.63):

$$E^* = \frac{\left(\left(\frac{1}{R_1R_2}\right) + j\omega\left(\frac{C_1}{R_2} + \frac{C_2}{R_1}\right) - \omega^2 C_1C_2\right)\left(\left(\frac{1}{R_1} + \frac{1}{R_2}\right) - j\omega(C_1 + C_2)\right)}{j\omega\left(\frac{1}{R_1} + \frac{1}{R_2}\right)^2 + j\omega^3(C_1 + C_2)^2} \tag{1.74}$$

Multiply by j over j to make the denominator real:

$$E^* = \frac{j\left(\left(\frac{1}{R_1R_2}\right) + j\omega\left(\frac{C_1}{R_2} + \frac{C_2}{R_1}\right) - \omega^2 C_1C_2\right)\left(\left(\frac{1}{R_1} + \frac{1}{R_2}\right) - j\omega(C_1 + C_2)\right)}{-\omega\left(\frac{1}{R_1} + \frac{1}{R_2}\right)^2 - \omega^3(C_1 + C_2)^2}$$

$$E^* = \frac{\left(j\left(\frac{1}{R_1R_2}\right) - \omega\left(\frac{C_1}{R_2} + \frac{C_2}{R_1}\right) - j\omega^2 C_1C_2\right)\left(\left(\frac{1}{R_1} + \frac{1}{R_2}\right) - j\omega(C_1 + C_2)\right)}{-\omega\left(\frac{1}{R_1} + \frac{1}{R_2}\right)^2 - \omega^3(C_1 + C_2)^2} \tag{1.75}$$

Expand (1.75) and isolate the real component (E'):

$$E' = \frac{\omega(C_1 + C_2)\left(\frac{1}{R_1R_2}\right) - \omega\left(\frac{C_1}{R_2} + \frac{C_2}{R_1}\right)\left(\frac{1}{R_1} + \frac{1}{R_2}\right) - \omega^3 C_1C_2(C_1 + C_2)}{-\omega\left(\frac{1}{R_1} + \frac{1}{R_2}\right)^2 - \omega^3(C_1 + C_2)^2}$$

$$E' = \frac{\left(\frac{C_1}{R_2} + \frac{C_2}{R_1}\right)\left(\frac{1}{R_1} + \frac{1}{R_2}\right) + \omega^2 C_1C_2(C_1 + C_2) - (C_1 + C_2)\left(\frac{1}{R_1R_2}\right)}{\left(\frac{1}{R_1} + \frac{1}{R_2}\right)^2 + \omega^2(C_1 + C_2)^2} \tag{1.76}$$

Now consider the frequency limits of equation (1.76):

Low frequency: $\omega \to 0$

$$E' \to \frac{\left(\frac{C_1}{R_2} + \frac{C_2}{R_1}\right)\left(\frac{1}{R_1} + \frac{1}{R_2}\right) + (0)^2 - (C_1 + C_2)\left(\frac{1}{R_1R_2}\right)}{\left(\frac{1}{R_1} + \frac{1}{R_2}\right)^2 + (0)^2} \tag{1.77}$$

Multiply and cancel the numerator of (1.77):

$$E' \to \frac{\frac{C_1}{R_2R_1} + \frac{C_2}{R_2R_1} + \frac{C_1}{R_2^2} + \frac{C_2}{R_1^2} - \frac{C_1}{R_2R_1} - \frac{C_2}{R_2R_1}}{\left(\frac{1}{R_1} + \frac{1}{R_2}\right)^2}$$

$$E' \to \frac{\frac{C_1}{R_2^2} + \frac{C_2}{R_1^2}}{\left(\frac{1}{R_1} + \frac{1}{R_2}\right)^2} \tag{1.78}$$

Rearrange the denominator of (1.78) and multiply top and bottom by $R_1^2R_2^2$:

$$E' \to \frac{\frac{C_1}{R_2^2} + \frac{C_2}{R_1^2}}{\left(\frac{R_1 + R_2}{R_1R_2}\right)^2} \cdot \frac{R_1^2R_2^2}{R_1^2R_2^2}$$

$$E' \to \frac{C_1R_1^2 + C_2R_2^2}{(R_1 + R_2)^2} \tag{1.79}$$

Applying the assumptions that $R_2 >> R_1$ and $C_2 >> C_1$:

$$E' \to \frac{C_1R_1^2 + C_2R_2^2}{(R_1 + R_2)^2} \sim \frac{C_1R_1^2 + C_2R_2^2}{R_2^2}$$

$$E' \to \frac{C_1R_1^2 + C_2R_2^2}{(R_1 + R_2)^2} \sim \frac{C_1R_1^2}{R_2^2} + C_2$$

$$E' \to \frac{C_1R_1^2 + C_2R_2^2}{(R_1 + R_2)^2} \sim (0) + C_2 \tag{1.80}$$

Now consider E' at high frequency, neglecting the terms in (1.76) without ω:

High frequency: $\omega \to \infty$

$$E' \to \frac{\infty^2 C_1 C_2 (C_1 + C_2)}{\infty^2 (C_1 + C_2)^2}$$

$$E' \to \frac{C_1 C_2}{(C_1 + C_2)} \tag{1.81}$$

Again, applying the assumption that $C_2 >> C_1$:

$$E' \to \frac{C_1 C_2}{(C_1 + C_2)} \sim \frac{C_1 C_2}{C_2}$$

$$E' \to \frac{C_1 C_2}{(C_1 + C_2)} \sim C_1 \tag{1.82}$$

Equations (1.80) and (1.82) indicate that if $R_2 >> R_1$ and $C_2 >> C_1$, at low frequency E' will plateau at a value of C_2 and will decrease to another plateau of value C_1 at high frequency (see fig. 34). If the assumption is not true the low and high frequency plateaus will be the composite values given in equations (1.79) and (1.81), respectively.

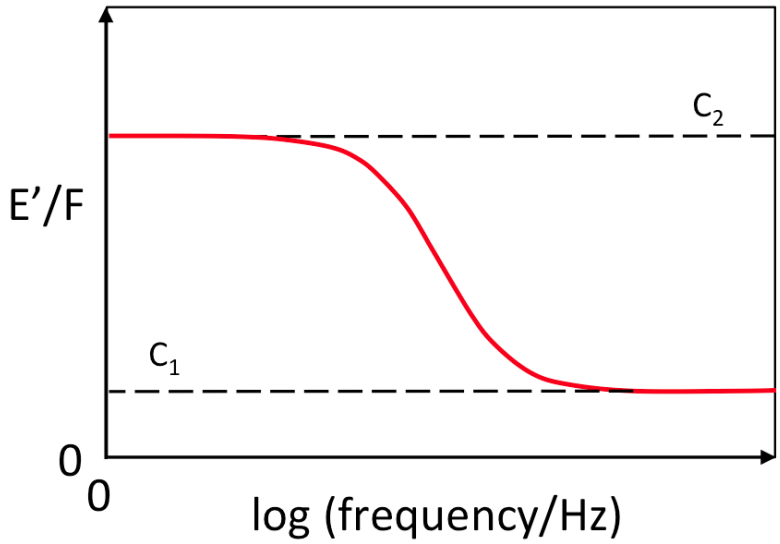

Fig. 34. *Schematic of the relation for E' versus frequency for two parallel resistors and capacitors connected in series with intercepts.*

Now expand (1.68) and isolate the imaginary component (E''):

$$E'' = \frac{\left(\frac{1}{R_1 R_2}\right)\left(\frac{1}{R_1} + \frac{1}{R_2}\right) + \omega^2 \left(\frac{C_1}{R_2} + \frac{C_2}{R_1}\right)(C_1 + C_2) - j\omega^2 C_1 C_2 \left(\frac{1}{R_1} + \frac{1}{R_2}\right)}{-\omega \left(\frac{1}{R_1} + \frac{1}{R_2}\right)^2 - \omega^3 (C_1 + C_2)^2} \tag{1.83}$$

Expand and rearrange the numerator of (1.83):

$$E'' = \frac{\left(\frac{1}{R_1R_2}\right)\left(\frac{1}{R_1}+\frac{1}{R_2}\right)+\omega^2\left(\frac{C_1C_2}{R_2}+\frac{C_1C_2}{R_1}+\frac{C_1^2}{R_2}+\frac{C_2^2}{R_1}\right)-j\omega^2\left(\frac{C_1C_2}{R_1}+\frac{C_1C_2}{R_2}\right)}{-\omega\left(\frac{1}{R_1}+\frac{1}{R_2}\right)^2-\omega^3(C_1+C_2)^2}$$

$$E'' = \frac{\left(\frac{1}{R_1R_2}\right)\left(\frac{1}{R_1}+\frac{1}{R_2}\right)+\omega^2\left(\frac{C_1^2}{R_2}+\frac{C_2^2}{R_1}\right)}{-\omega\left(\frac{1}{R_1}+\frac{1}{R_2}\right)^2-\omega^3(C_1+C_2)^2}$$

$$E'' = \frac{-\left(\frac{1}{R_1R_2}\right)\left(\frac{1}{R_1}+\frac{1}{R_2}\right)-\omega^2\left(\frac{C_1^2}{R_2}+\frac{C_2^2}{R_1}\right)}{\omega\left(\frac{1}{R_1}+\frac{1}{R_2}\right)^2+\omega^3(C_1+C_2)^2} \quad (1.84)$$

Consider the frequency limits of equation (1.84):

Low frequency: $\omega \to 0$

$$E'' \to \frac{-\left(\frac{1}{R_1R_2}\right)\left(\frac{1}{R_1}+\frac{1}{R_2}\right)-(0)^2}{(0)+(0)^3}$$

$$E'' \to \infty \quad (1.85)$$

High frequency: $\omega \to \infty$

$$E'' \to \frac{-\left(\frac{1}{R_1R_2}\right)\left(\frac{1}{R_1}+\frac{1}{R_2}\right)-(\infty)^2\left(\frac{C_1^2}{R_2}+\frac{C_2^2}{R_1}\right)}{(\infty)\left(\frac{1}{R_1}+\frac{1}{R_2}\right)^2+(\infty)^3(C_1+C_2)^2}$$

$$E'' \to \frac{-(\infty)^2}{(\infty)^3} \to 0 \quad (1.86)$$

From equations (1.85) and (1.86) we can see that *E*'' must decay from infinity at low frequency and tend to zero at high frequency. Similarly to *Y*'' a parasitic capacitance will form at frequencies between f_{max1} and f_{max2} where the equivalent circuit will reduce to a series connection of R_1 and C_2 (see fig. 31). From equation (1.35) it can be seen that *E*'' for a resistor and capacitor connected in series results in a Debye peak. In this case the peak will occur at a frequency of $f_{max} = 1/R_1C_2$ and the height will be proportional to $C_2/2$. The relationship between *E*'' and frequency will be a combination of the Debye peak and the decay term (see fig. 35). Plotting *E*'' and *E*' together as a Nyquist plot will give a semicircle displaced from the origin by the value of C_1 along the *E*' axis. The other real intercept of the semicircle will have a value of C_2. The semicircle will have a height of $C_2/2$ where the maximum point will coincide with the Debye frequency of the parasitic capacitance. After the C_2 intercept, as frequency decreases there will be a spike as the imaginary term tends to infinity (see fig. 36).

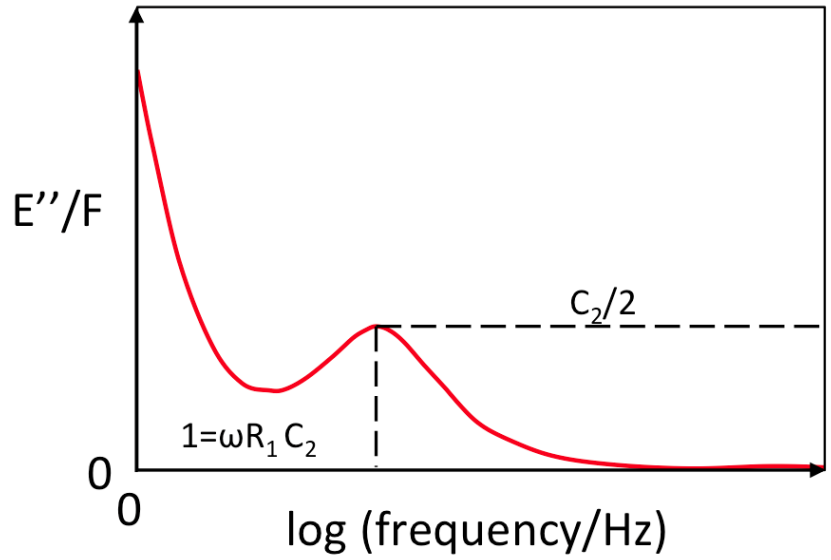

Fig. 35. *Schematic of the relation for E'' versus frequency for two parallel resistors and capacitors connected in series with intercepts.*

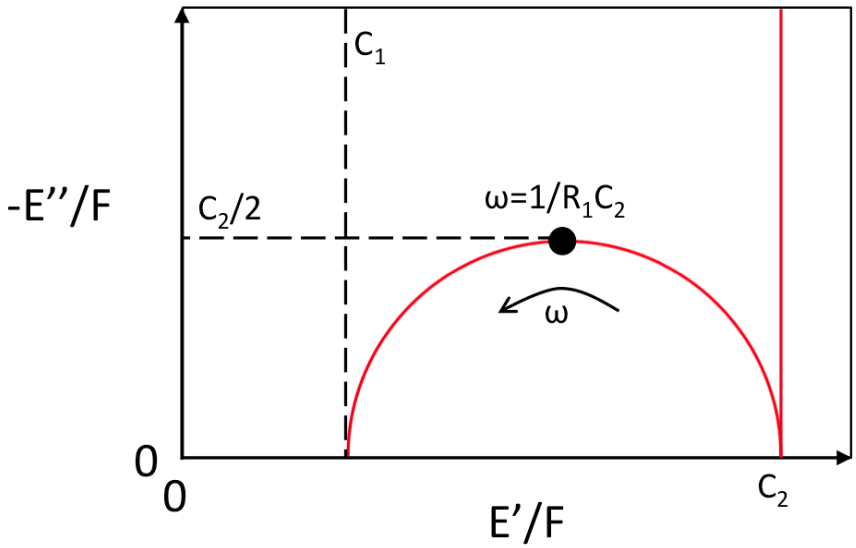

Fig. 36. *Schematic of a Nyquist plot for E* (E'' versus E') with intercepts for two parallel resistors and capacitors connected in series with intercepts.*

Comparing the derivations of the impedance response of circuits one to three explains the weightings of the four formalisms. For circuit one (a resistor and capacitor in series) the intercepts were straightforward for *Z** and *M** but more complex for *Y** and *E**. Conversely, for circuit two (a resistor and capacitor connected in parallel) the intercepts of *Y** and *E** were simple while *Z** and *M** were more complicated. This shows that *Y** and *E** are better for displaying the impedance data of parallel processes whilst *Z** and *M** are better for serial connectivity.

For all three circuits the main intercepts are common within each formalism. For *Z** the intercepts are resistances whilst for *Y** they are inverse resistances. Hence when examining the impedance response of a transport process *Z** would be used for more resistive processes whilst *Y** would be better suited to

more conductive processes. The same logic can be applied to capacitive processes. As *M** has intercepts that are inverse capacitances it would be a better formalism for probing processes with capacitances of small magnitude whilst *E** would be better for large capacitances.

When using impedance spectroscopy to characterise a material it may not be known what the connectivity or magnitudes of resistance and capacitance are present in a material. Hence it is important to study the impedance data in all four formalisms to fully probe all behaviour within a material. The strengths of each formalism are summarised in table 2. Circuit three is often used in the field of electroceramics and is typically analysed using *Z**. *M** should not be neglected as it can provide additional information about the capacitances present in the system. The intercepts of *Y** and *E** are more convoluted for circuit three due to the series connection of the two RC elements but can reduce to simpler expression if certain assumptions are valid. In this work spectroscopic plots of *E*' and *Y*' are used when the time constant separation allows for it or to probe how well time constants are separated.

Formalism	Preferential connectivity	Good for	Example material
Z*	Serial	Large resistances	Insulator
Y*	Parallel	Small resistances	Conductor
M*	Serial	Small capacitances	Secondary phases with comparable thickness to bulk
E*	Parallel	Large capacitances	High permittivity dielectric

Table. 2. *Summary of the strengths of all four impedance formalisms.*

1.2.3. Experimental Setup

To measure the impedance of a ceramic, a pellet is produced and then the top and bottom surfaces are electroded. Leads are held in contact with the electrode surface using a spring-loaded clamp, allowing the sample to be connected to an impedance analyser (see fig. 37). Two common methods of calculating the impedance use bridge balancing and Fourier transformation[11]. For the balancing method, the sample is used as one of four resistors in a bridge circuit (see fig. 38). The resistance of a variable resistor is changed until its resistance ratio with the sample matches the other two fixed resistors. When the ratios match, a null detector will detect no potential difference, implying no current flow. The sample's

resistance and hence impedance may be calculated as it is the only unknown. Originally, the bridge balancing was done by hand but now this is automated. Impedance measurements must still be taken sequentially for each frequency. Alternatively, all frequencies can be applied to the sample at once and then deconvoluted using Fourier transformations.

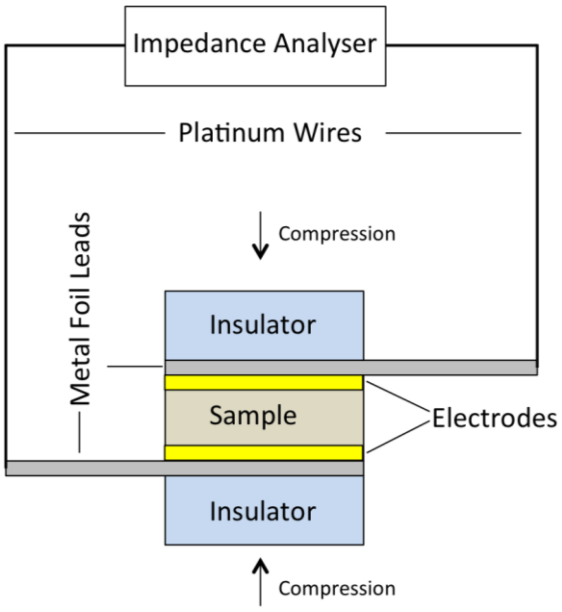

Fig. 37. *Schematic of a typical setup of an impedance spectroscopy experiment measuring a ceramic sample.*

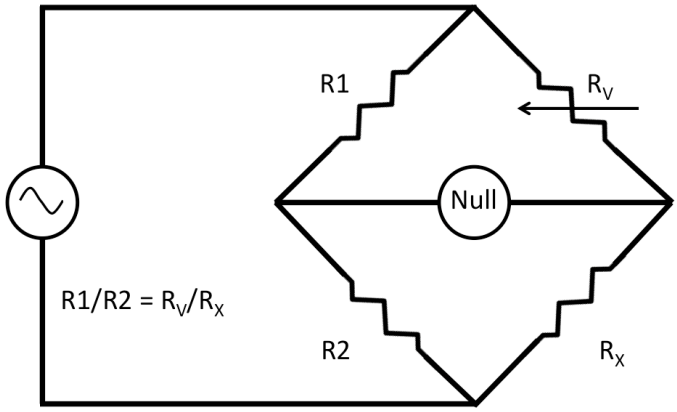

Fig. 38. *Schematic of an AC bridge balance circuit. Where R1 and R2 are resistors of known resistance, R_v is a variable resistor and R_x is the sample which the impedance is to be calculated.*

1.2.4. Strengths and Weaknesses of Impedance Spectroscopy.

Impedance spectroscopy has advantages over traditional direct current (DC) and fixed frequency measurements as it has the potential to uncover more information from the subject of investigation. DC electrical measurements will be dominated by the most resistive components and fixed frequency measurements will be dominated by the component that is most electrically active at a given frequency[12].

Measuring over a spectrum of frequencies mitigates this issue but it is still possible for a process to be out of the frequency window measured. Very resistive processes may have such a low f_{max} that measuring them would take an unfeasibly long time. Experimentalists can counter this by taking measurements at higher temperatures, reducing the energy barrier for such a process to occur. Likewise, phenomena that occur at frequencies too high to be measured can be brought down into the frequency window by cooling the sample down. The sample must also be less resistive than electronics of the impedance measuring instrument.

The strength of impedance spectroscopy can also be its weakness. Measuring the impedance over a range of frequencies can retrieve information regarding many of the electrical processes within a material. Simply put, the more data acquired the more involved the fitting will be. In addition, often many equivalent circuits can fit the same data[13]. Basing the equivalent circuit used for fitting the impedance spectra on processes known to occur within the material can counter this ambiguity and increases the confidence in the fit. Comparing the equivalent circuit fit with the data in all four formalisms offers a robust method to refine the fit. A good equivalent circuit will be able to mimic the measured data in all the weightings the four formalisms provide. However, this is a time- consuming process.

When assigning capacitances obtained from spectra to microstructural components the magnitudes of the capacitances should be considered as a rough guide. Thicker components will typically have a lower capacitance. A summary of typical magnitudes of the capacitance for common microstructural features is given in table 3.

Microstructural feature	Capacitance/Fcm^{-1}
Bulk ceramic	10^{-12}
Secondary phase	10^{-11}
Grain boundary	10^{-11} to 10^{-8}
Electrode/ceramic interface	10^{-7} to 10^{-5}

Table. 3. *List of typical capacitances normalised to sample geometry for microstructural features[14]. Note the units favoured in the literature are Farads per centimetre; conversion to Farads per metre would be achieved by multiplying the present values by 100.*

It is possible to make assumptions for equivalent circuits based upon microscopy data, however an important concept for impedance is physical microstructure versus electrical microstructure. The physical microstructure is essentially what is traditionally thought of as microstructure - how the different phases, defects and dopants are distributed throughout a material (see fig. 39A). The electrical microstructure is how space charge is distributed throughout a material (see fig. 39B). When an impedance measurement is taken, it is the electrical not the physical microstructure that will define the spectra. Previously we have discussed how the relative thickness of bulk and grain boundary will affect their capacitances. Space charge is known to extend past grain boundaries[15].

If this space charge was responsible for a grain boundary capacitance its effective thickness would be larger than the physical dimensions of the grain boundary. The conditions under which the electrical microstructure is representative of the physical microstructure of dielectric ceramics will be a significant topic for this thesis.

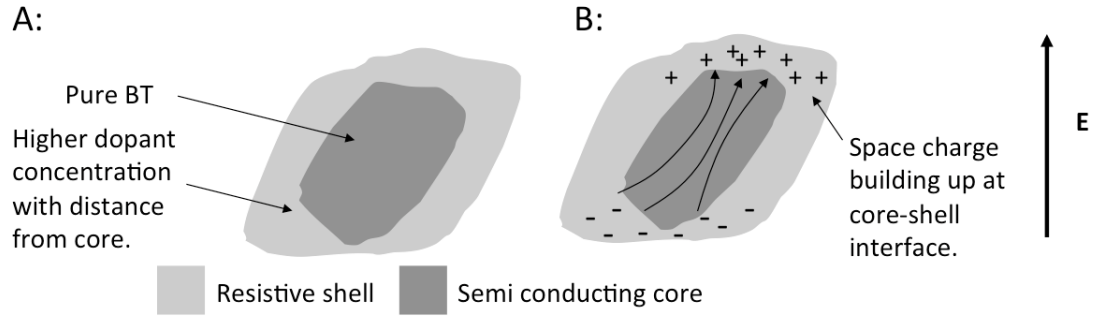

Fig. 39. *(A) The physical microstructure of a core-shell grain of barium titanate. (B) The electrical microstructure of the same grain as an electric field (**E**) is applied to it.*

Another issue for impedance spectroscopy is that although we can attempt to fit impedance spectra with ideal circuit elements or even parallel or series combinations of circuit elements, real spectra display non-ideal impedance responses. Non-ideal responses take the form of depressed semicircles in Nyquist plots or broadening of Debye peaks in spectroscopic plots, leading to a full width half max (FWHM) greater than 1.14 decades in frequency (see figs 40 and 41). There are many theories on the exact cause of these departures from ideality. Large deviations have been observed in samples with microscopic defects (e.g. pores), but also in what appear to be well-defined microstructures with high density samples or single crystals[16]. This has led to theories that try to explain non-ideality as either a mesoscopic or a nanoscopic phenomenon.

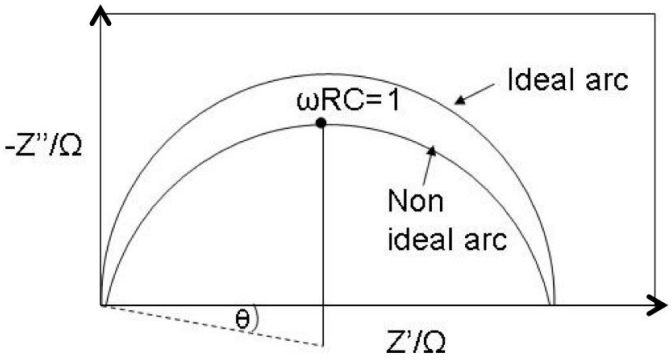

Fig. 40. *Comparison of ideal Debye response and depressed non-ideal response in Z* arcs.*

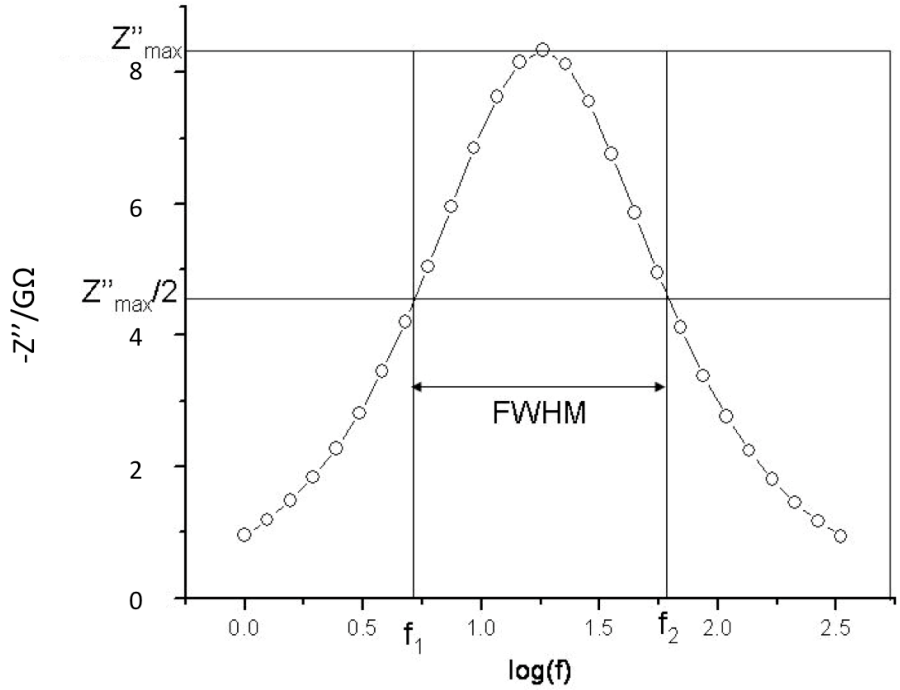

Fig. 41. *A Debye peak for a Z" spectroscopic plot. For an ideal response the FWHM will measure 1.14 decades on a log(f) scale. Typically this is broader in real samples.*

Work by Jonscher has fitted this non-ideality as a universal frequency dispersion (see fig 42) using a power law[17]. A general form of this is given in equation (1.87)[18]. This equation is often referred to as the universal power law, as it can be used to fit many different systems[19, 20, 21].

$$\sigma_\omega = \sigma_0 A\omega^n \qquad (1.87)$$

where σ_ω is the AC conductivity, σ_0 is the DC conductivity, A is a temperature dependent parameter and n has a value between 0 and 1. This has led to the belief that a there is a universal mechanism responsible for high frequency dispersion. At the time of writing, this mechanism has not been found, and so the universal power law is still an empirical fit. However, as the power law can fit such a variety of systems (it has been applied to ceramics, glasses and polymers), its significance should not be discounted.

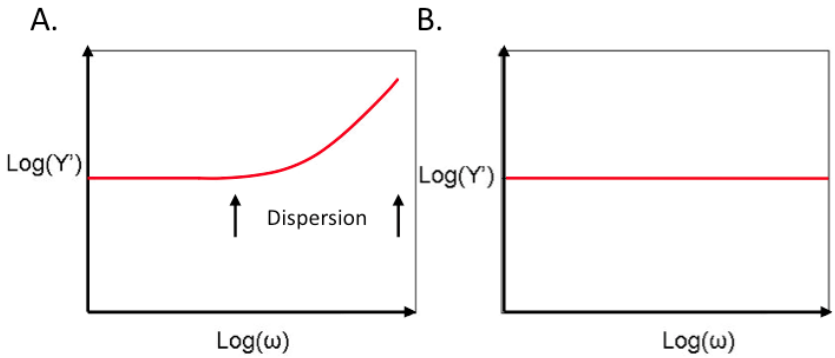

Fig 42. *(A) High frequency dispersion in admittance spectroscopic plot for a system with a single time constant, (B) ideal behaviour for the same graph.*

Another school of thought is that discrete mechanisms must be present in different materials. Popular mechanisms include distributions of relaxation times (DRT)[22] and distributions of hopping probabilities (DHP)[23]. Whereas traditional theory would assign a single time constant (with a degree of non ideality) to an extracted resistance and capacitance. DRT, as its name implies, assumes that there is a distribution of relaxation times (or time constants) with their values distributed so that their mean value is centred on what would be the traditional time constant. The spread of time constants would cause a broadening of the Debye peak, as their responses would merge (time constants do not have enough separation). It is thought that the cause of DRT could be due to electrical heterogeneity in materials (differing lengths of conduction pathways, caused by defects etc.). DHP is similar to DRT, but instead of relaxation times it is theorised that a distribution of hopping probabilities causes non-Debye responses. It has been suggested that for DRTs to exist in a material there must be a DHP causing it[17].

A major argument against the DRT and DHP theories is that while they are mathematically sound, it is very difficult to prove the existence of such distributions experimentally[24]. With more computational power available, simulations may be able to probe the cause of non-ideality, particularly with regards to phenomena occurring within materials during relaxation processes. There is also the difficulty of applying these distribution-based theories to all materials that show non-ideality that can be described by Jonscher's 'universal power law' in their admittance response. Bowen and Almond managed to model power law behaviour with a random resistor-capacitor network based on an idealised microstructure made from porous lead zirconate titanate (PZT) impregnated with water[25] . The PZT was 78% of the theoretical density, leaving porous regions for the impregnated water to reside. This gave a microstructure with pockets of water (a relatively conductive phase, modelled as a resistor) and PZT (resistive phase, modelled as a capacitor). The different geometries of the water and PZT regions lead to a distribution of values of the resistance and capacitance which depend on the material. Both computer simulations and physical modelling (using the PZT-water system) exhibited a high frequency dispersion.

A common method of modelling non-ideality in equivalent circuits is the use of constant phase elements (CPEs). A CPE is a mathematical construct with an admittance (Y^*_{CPE}) definied as:

$$Y^*_{CPE} = A(j\omega)^n \tag{1.88}$$

that, depending on assigned values of the n parameter, can behave as an ideal capacitor (n = 1) or as an ideal resistor (n = 0). Values of n between 0 and 1, give a non-ideal capacitor with a resistive component (e.g. current leakage in a capacitor). It is common for a CPE to be used in parallel to a resistor and capacitor to model a non ideal RC element[13] (CPE-RC). The impedance for a CPE-RC element is defined by a frequency dependent relationship (see 1. 89), leading to a greater dispersion at higher frequencies. A method developed to fit CPEs involves obtaining values of n and A from a log-log plot of Y' verses ω. The n parameter is

taken from the gradient of the high frequency dispersion (HFD) and A from the Y' intercept of the dispersion (see fig 43A) [13].

$$Y' = R^{-1} + A\omega^{n}\cos(n\pi/2) \qquad (1.89)$$

These intercept impedance measurements must be taken in a temperature range containing the HFD and the low frequency DC conductivity plateau (without the plateau it is difficult to say where the HFD begins). CPEs can be used in conjunction with resistors, capacitors and inductors to fit data using software that can simulate equivalent circuits (Zview is a commonly used package[26]). An RC element can be modified to account for non-ideality by adding a CPE in parallel (see fig 43B).

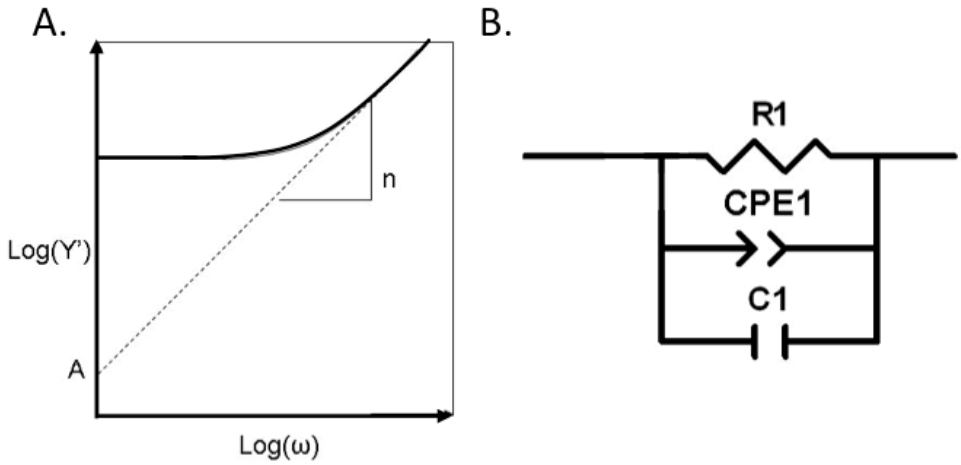

Fig. 43. *(A) Intercepts required to estimate A and n parameters for equations (1.88) and (1.89), (B) equivalent circuit modified with a CPE to fit non-ideality.*

1.3. Conclusions

Impedance spectroscopy is a powerful technique that can be used to probe the frequency-dependent electrical microstructure of functional oxides. However, it is important to understand the limitations of impedance spectroscopy and use additional techniques to confirm observations. In-depth understanding of the limitations of impedance spectroscopy can be provided by computer modelling. By simulating the electrical response of a material where the simulator has defined the microstructure and intrinsic properties of a material it is possible to use an experimental methodology to extract intrinsic properties. Then the value of extracted properties can be compared to the original inputs allowing the accuracy of the experimental methodology to be evaluated.

1.4. Refernces

1. G. H. Haertling, "Ferroelectric ceramics: History and technology," *Journal of the American Ceramic Society,* 82[4] 797-818 (1999).

2. L. Q. Chen, "Phase-field models for microstructure evolution," *Annual Review of Materials Research,* 32 113-40 (2002).

3. H. Kishi, Y. Mizuno, and H. Chazono, "Base-metal electrode-multilayer ceramic capacitors: Past, present and future perspectives," *Japanese Journal of Applied Physics Part 1-Regular Papers Short Notes & Review Papers,* 42[1] 1-15 (2003).

4. T. B. Adams, D. C. Sinclair, and A. R. West, "Characterization of grain boundary impedances in fine- and coarse-grained CaCu3Ti4O12 ceramics," *Physical Review B,* 73[9] 9 (2006).

5. P. K. Panda, "Review: environmental friendly lead-free piezoelectric materials," *Journal of Materials Science,* 44[19] 5049-62 (2009).

6. A. Jordens, Y. P. Cheng, and K. E. Waters, "A review of the beneficiation of rare earth element bearing minerals," *Minerals Engineering,* 41 97-114 (2013).

7. S.-C. Jeon, B.-K. Yoon, K.-H. Kim, and S.-J. L. Kang, "Effects of core/shell volumetric ratio on the dielectric-temperature behavior of BaTiO3," *Journal of Advanced Ceramics,* 3[1] 76-82 (2014).

8. S.-C. Jeon, C.-S. Lee, and S.-J. L. Kang, "The Mechanism of Core/Shell Structure Formation During Sintering of BaTiO3-Based Ceramics," *Journal of the American Ceramic Society,* 95[8] 2435-38 (2012).

9. J. E. Bauerle, "Study of Solid Electrolyte Polarization by a Complex Admittance Method," *Journal of Physics and Chemistry of Solids,* 30[12] 2657-2670 (1969).

10. D. C. Sinclair and A. R. West, "Impedance and Modulus Spectroscopy of Semiconducting $BaTiO_3$ Showing Positive Temperature-Coefficient of Resistance," *Journal of Applied Physics,* 66[8] 3850-56 (1989).

11. J. R. Macdonald, "Impedance spectroscopy : emphasizing solid materials and systems," (1987).

12. A. R. West, D. C. Sinclair, and N. Hirose, "Characterization of electrical materials, especially ferroelectrics, by impedance spectroscopy," *Journal of Electroceramics,* 1[1] 65-71 (1997).

13. E. J. Abram, D. C. Sinclair, and A. R. West, "A strategy for analysis and modelling of impedance spectroscopy data of electroceramics: Doped lanthanum gallate," *Journal of Electroceramics,* 10[3] 165-77 (2003).

14. D. C. Sinclair, "Characterization of Electro-materials using ac Impedance Spectroscopy," *Bol. Soc, Esp. Cerám. Vidrio,* 34[2] 55-65 (1995).

15. M. Vollman and R. Waser, "Grain-Boundary Defect Chemistry of Acceptor-Doped Titanates - Space-Charge Layer Width," *Journal of the American Ceramic Society,* 77[1] 235-43 (1994).

16. P. Abelard and J. F. Baumard, "Study of The DC and AC Electrical-Properties of An Yttria-Stabilized Zirconia Single-Crystal (ZrO_2)0.88-(Y_2O_3)0.12," *Physical Review B,* 26[2] 1005-17 (1982).

17. A. K. Jonscher, "A New Understanding of the Dielectric-Relaxation of Solids," *Journal of Materials Science,* 16[8] 2037-60 (1981).

18. D. P. Almond, G. K. Duncan, and A. R. West, "The Determination of Hopping Rates and Carrier Concentrations in Ionic Conductors by a New Analysis of AC Conductivity," *Solid State Ionics,* 8[2] 159-64 (1983).

19. M. M. Jastrzebska, S. Jussila, and H. Isotalo, "Dielectric response and ac conductivity of synthetic dopa-melanin polymer," *Journal of Materials Science,* 33[16] 4023-28 (1998).

20. B. Roling, "Scaling properties of the conductivity spectra of glasses and supercooled melts," *Solid State Ionics,* 105[1-4] 185-93 (1998).

21. M. Suzuki, "AC Hopping Conduction in Mn-Co-Ni-Cu Complex Oxide Semiconductors with Spinel Structure," *Journal of Physics and Chemistry of Solids,* 41[11] 1253-60 (1980).

22. J. R. Macdonald, "Some Statistical Aspects of Relaxation Time Distributions," *Physica,* 28[5] 485-492 (1962).

23. P. N. Butcher and P. L. Morys, "Exact Solution of AC Hopping Conductivity Problem at Low Site Densities," *Journal of Physics C-Solid State Physics,* 6[13] 2147-57 (1973).

24. A. K. Jonscher and Ieee, "The Universal Dielectric Response and its Physical Significance," *Proceedings of the 3rd International Conference on Properties and Applications of Dielectric Materials, Vols 1 and 2* 1-11 (1991).

25. C. R. Bowen and D. P. Almond, "Modelling the 'universal' dielectric response in heterogeneous materials using microstructural electrical networks," *Materials Science and Technology,* 22[6] 719-24 (2006).

26. S. Associates, "http://www.scribner.com/software/general-electrochemistry/68-general-electrochemistr/376-zview-for-windows." in, Vol. 2016.

Chapter 2: Literature Review

Here an overview of existing simulation and modelling work on the impedance response of electrical composites that exists in the literature is given for areas that are relevant to all sections of this thesis. A summary of more specific literature results is given as required in the results chapters. Key findings are summarised and knowledge gaps identified.

2.1. Modelling of Electroceramics

Modelling the electrical properties of a ceramic at scales greater than micrometres and towards engineering length scales can be divided into two broad categories, analytical and numerical approaches. Earlier attempts typically use analytical methods as, for simple cases, electrical composites can be modelled using simple mixing laws and simplified microstructures. Using equivalent circuits to model the electrical microstructure of a ceramic is common practice. In this chapter the development of equivalent circuits used for electro- ceramics is detailed in addition to analytical approaches. For the theory under pinning equivalent circuits, the reader is directed to chapter one. More recently, the increased availability of computational resources has made numerical methods increasingly viable. This allows the simulation of more complex microstructures possible where convenient analytical solutions do not exist.

2.1.1. Development of the Brick Work Layer Model

A measured impedance spectrum is usually fitted using an equivalent circuit, where the electrical response of a ceramic is modelled using a collection of circuit elements representing polarisation and transport processes within the material. To extract data using equivalent circuits, intercepts and inflection points of the experimental data and the equivalent circuit are matched up and the behaviour of the components of the circuit matched to the frequency-dependent impedance responses of the ceramic[1]. For example, take a typical dual arc impedance (Z*) spectrum from a polycrystalline ceramic with resistive grain boundaries (see fig. 1A). This is usually modelled with two parallel resistor–capacitor circuits (RC element) connected in series (see fig. 1B). The bulk has a RC element with a low resistance and capacitance, whilst the grain boundary is modelled by an RC element with a higher capacitance and resistance (see fig. 1C). The difference in resistances accounts for the more resistive grain boundary and the higher capacitance is due to the grain boundary being thinner than the bulk. Using simple AC circuit theory it can be shown that the Z* arc diameters give the resistances and the capacitances can then be found as a function of the resistances and angular frequency (see fig. 1A). This approach can be extended to other impedance formalisms, which is covered at length in chapter one.

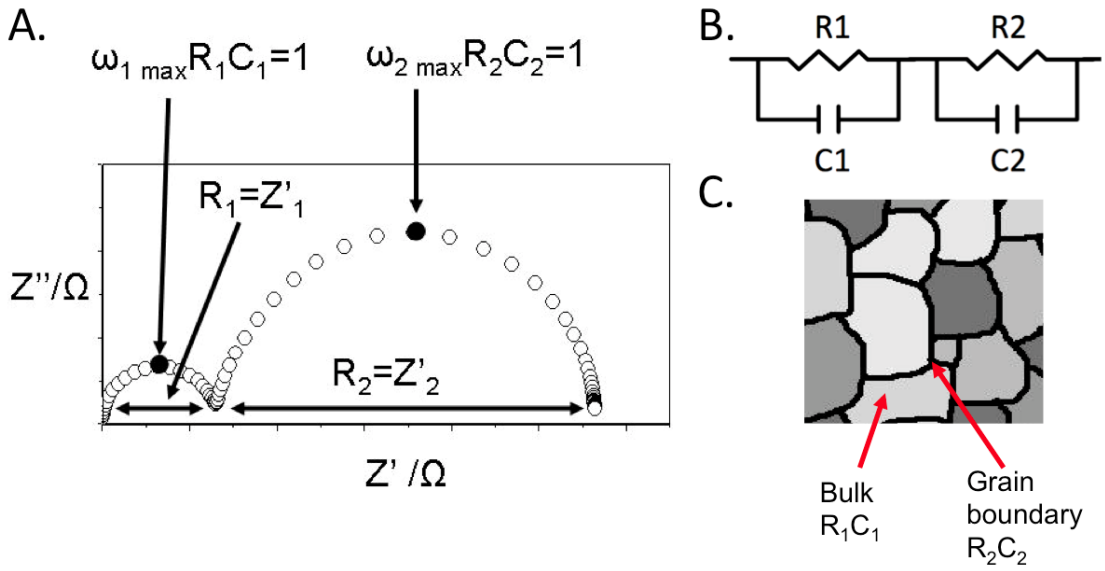

Fig. 1. *(A) Schematic of intercepts for the dual impedance arc response of a polycrystalline ceramic with resistive grain boundaries. (B) An equivalent circuit consisting of two parallel resistor–capacitor circuits connected in series, used to model polycrystalline ceramics. (C) Schematic of a ceramic microstructure with circuit element assignment annotated.*

The dual parallel RC element equivalent circuit was first used by Bauerle to model electrolyte polarisation in yttria-stabilised zirconia[2]. Beekmans used RC circuits to model bulk and grain boundaries of calcia-stabilised zirconia[3]. By assuming that all grain boundary and bulk material had the same respective time constants and applying a uniform electric field, a large network of equivalent circuits reduces to a single R-RC circuit (capacitance of the bulk was not considered). Beekmans converted this equivalent circuit into a boundary layer model (see fig. 2A), which was later referred to by Verkerk as the Brick Layer Model (BLM). The BLM can be described as nested cubes, the inner cube representing the bulk (grain) and the area between the outer and inner cube representing the grain boundary (see fig. 2B). If these nested cubes are stacked together, the bulk cubes can be thought of as 'bricks' and the interconnected boundary regions as 'mortar', hence the name of the model.

Making the same assumptions as Beekmans (homogenous applied field and fixed time constants) allows the parallel pathways (through the resistive boundary 'mortar') to be neglected. The rationale for this is that the current will take the path of least resistance through the BLM, flowing through the less resistant bulk cubes in preference to the parallel boundary mortar (see fig. 2C). A contribution to conductivity by the parallel mortar was considered by Naffe[4]. This parallel version of the BLM was applied to nano-grained ceramics by Hwang[5]. His reasoning was that, in the nano regime, the thickness of grain boundaries is similar size to the diameter of the bulk grain resulting in higher boundary conductivity than typically found in micro-grained ceramics. Hence, it is only reasonable to neglect the parallel boundary if the resistance of the core is less than the parallel mortar. Another system where use of the BLM becomes problematic is the case of conductive grain boundaries; here the current percolates through the boundaries and completely avoids the bulk.

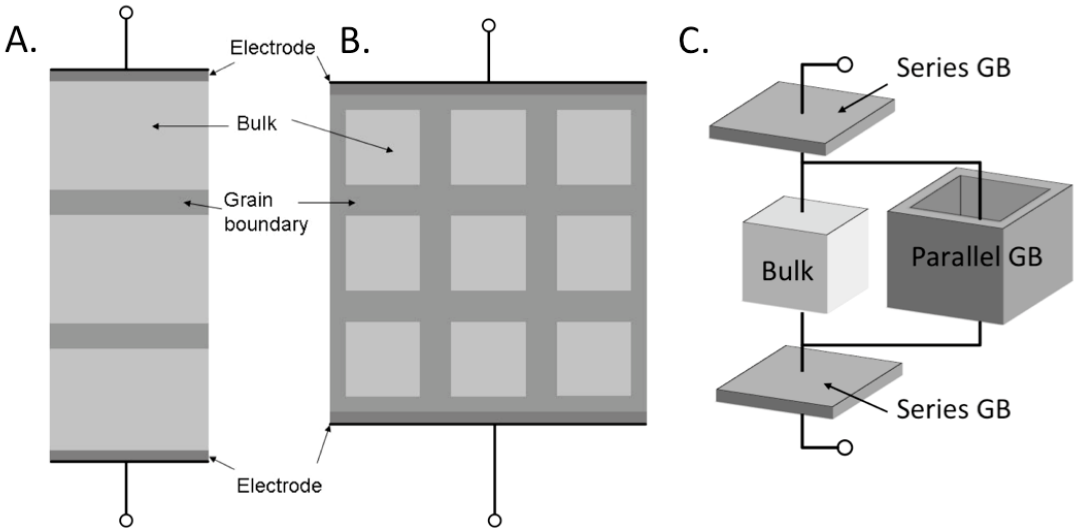

Fig. 2. *(A) Schematics of Beekmans' boundary layer model and (B) 'bricks and mortar' nested cubes of the BLM. (C) Schematic of the BLM showing the parallel and series conduction paths through the grain boundary (GB).*

2.1.2. Effective Medium theory and Maxwell's Layer Models

Perhaps one of the most simple models for describing an electrical composite is Maxwell's layered condenser model[6]. It considers two layers either connected in series (see fig. 3A) or in parallel (see fig. 3B) with a fixed electrode area (A in m). The series configuration is referred to as the Series Layer Model (SLM) and the parallel configuration as the Parallel Layer Model (PLM). Each layer has a volume fraction (ϕ) defined by a thickness (d) in addition to a permittivity (ε_r) and conductivity (σ). The SLM and PLM are analytically solvable. A resistance (R in Ω) and capacitance (C in F) for each layer can be calculated for each layer using equations (2.1) and (2.2) respectively:

$$R = \frac{d}{\sigma A} \tag{2.1}$$

$$C = \frac{\varepsilon_r \varepsilon_0 A}{d} \tag{2.2}$$

where ε_0 is the permittivity of free space in Fm^{-1} and A is the area in m. Values for the total resistances and capacitances of both layer models can be calculated by adding resistances in series and capacitances reciprocally for the SLM. Likewise, total values are calculated for the PLM by adding capacitances and adding resistances reciprocally. The SLM impedance response is equivalent to two parallel RC elements connected in series (see fig. 3A), whilst the PLM is equivalent to a two parallel RC elements connected in parallel (see fig. 3B). This makes the layer models useful for comparison purposes.

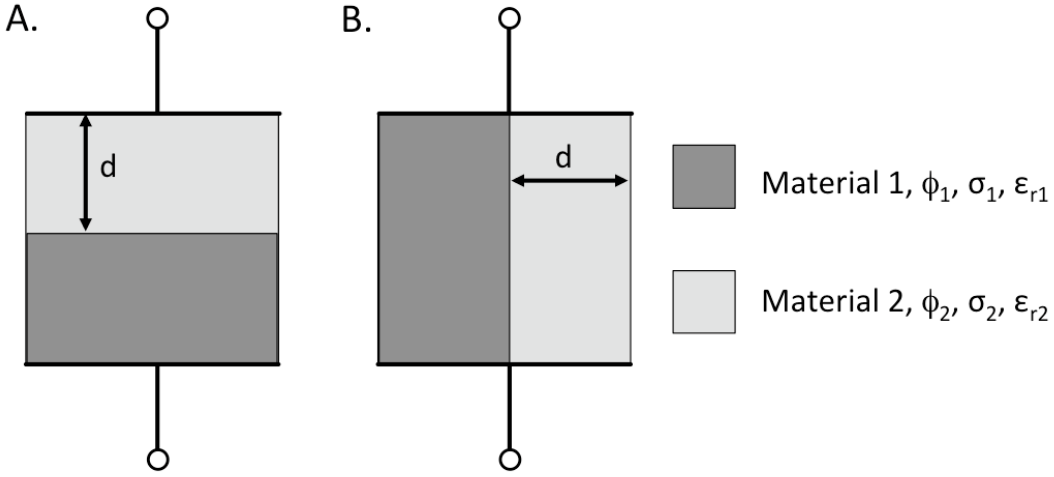

Fig. 3. *(A) Physical microstructure of the Series Layer Model. (B) Physical microstructure of the Parallel Layer Model.*

An alternative method for modelling electrical composites is effective medium theory (EMT). The various EMTs have a common origin, being developed from Maxwell's equations[6]. Originally Maxwell's EMT was only designed to work for DC conductivity but Wagner showed that it could also be used for AC complex conductivity[7]. It is important to note that Maxwell's EMT is only valid in the dilute limit where the inclusion phase is a sufficiently small volume fraction that individual inclusions do not interfere with each other electrically. EMTs are based upon a hypothetical microstructure made up of spherical inclusions imbedded into a matrix (see fig. 4). Here the conductivity of the inclusions is different to that of the matrix. An effective composite conductivity (σ_t) can be calculated for the resultant composite or effective medium. EMT can also be used to describe composite materials with different permittivities present in the inclusions and matrix.

There are variations of EMT that use different shape factors to represent other shapes, such as ellipsoids instead of just spheres and additional functions to represent particle orientation[8]. When the inner sphere is set to the lower conductivity and the outer region set to the higher conductivity, the EMT is at its lower bound of allowed conductivity. Conversely, if these conductivity assignments are reversed the upper bound of conductivity is revealed. Maxwell's EMT was extended to work beyond the dilute limit by Maxwell Garnett[9, 10], resulting in the Maxwell Garnett equation (a modern review is given by Markel[11])*. The Maxwell Garnett equation allows the modelling of the entire range of possible volume fractions of matrix and inclusions. The lower and upper bounds of Maxwell Garnett equations are mathematically equivalent to the bounds of the Hashin-Shtrikman equations; first used to model magnetic permeability[12]. If a composite conductivity falls within the upper and lower bounds of an EMT, it is said to be a physically reasonable value of composite conductivity (see fig. 5). This approach

* It should be noted that James Clerk Maxwell and James Clerk Maxwell Garnett are separate people. The Maxwell Garnett relation is the work of Garnett as detailed in references 9 and 10.

has been used before to evaluate conductivity measurements predicted by models[13].

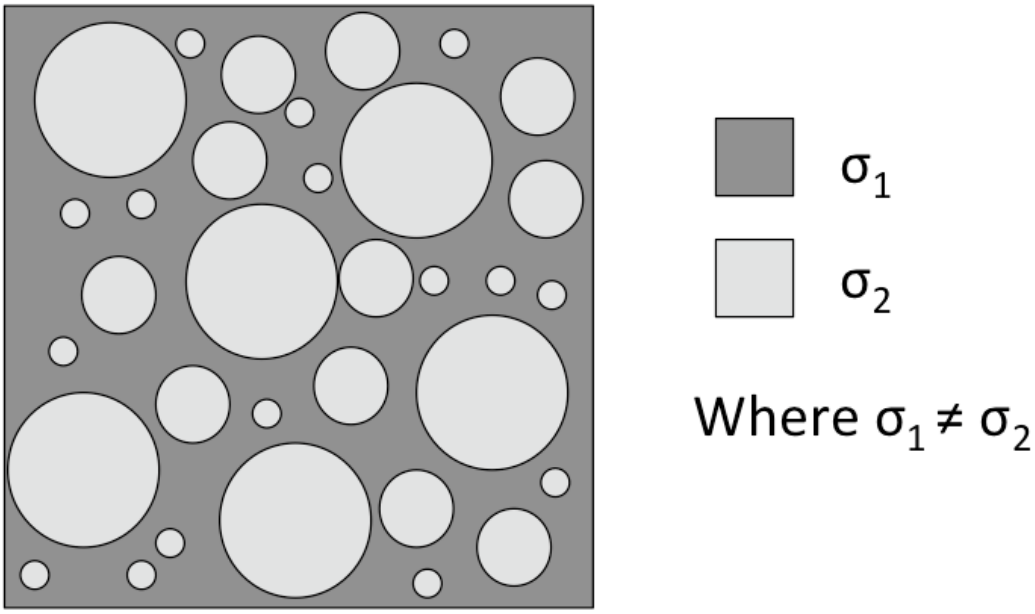

Fig. 4. *Schematic of the physical microstructure considered by effective medium theory.*

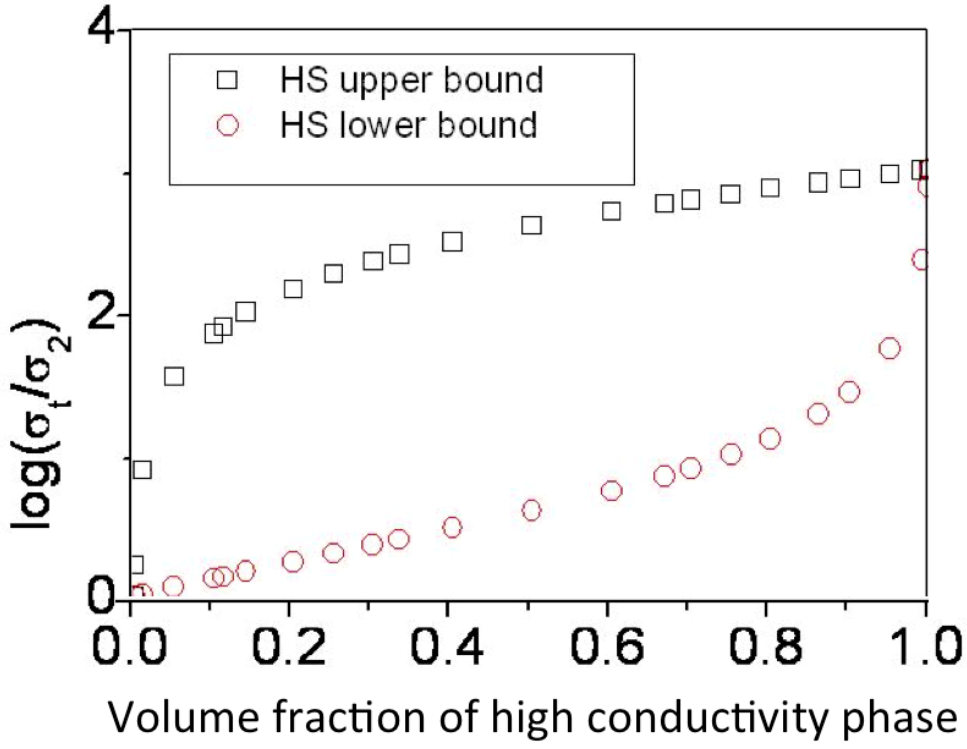

Fig. 5. *Conductivity bounds predicted by the Hashin-Shtrikman equations for a two-phase composite, with σ_1 = 100 μSm^{-1} (core phase) and σ_2 = 0.1 μSm^{-1}.*

Bonanos and Lilley combined EMT with Bauerle's dual RC circuit to derive a set of equations to predict values of resistance and capacitance from phase volume fractions, conductivities and permittivities[14]. The equations were derived by equating the response from Maxwell's EMT for insulators for a unit cube of material to a dual RC circuit. An important consideration of this approach is that the equations for both the high and low frequency resistances and capacitances contain permittivity and conductivity terms from both phases implying an interaction between the two. The set of equations was successfully used to model the complex electric modulus diameters for Suzuki phase precipitates ($Cd_{\square}Na_6Cl_8$) in sodium chloride for low volume fractions of the Suzuki phase. If the permittivities of the Suzuki phase and sodium chloride were the same, it can be assumed that the capacitance of each phase is proportional to the geometry and hence to the volume fraction. Using an impedance formalism that is weighted in favour of small capacitances (the electric modulus, with arc diameters equal to the inverse capacitance) can probe capacitance ratios and hence estimate volume fractions.

The assumptions made in this approach are that all phases present have an equal relative permittivity (whether this is applicable is material dependent) and that the entire microstructure contributes to the impedance response. If percolation is present in a microstructure, regions of low conductivity may experience less current flow, reducing the contribution to electrical behaviour by the resistive phase. Costa used this approach to study volume fractions associated with core-shell microstructures in calcium copper titanate (CCTO). While increasing sintering temperature, it was found that the modulus predicted that he volume fractions of a semi-conductive phase increased[15]. Costa made the observation that, without intricate knowledge of the CCTO 3D microstructure (electron microscopy can only provide information for a 2D plane), the comparison of electric modulus diameters can only give qualitative information about volume fractions. The exact geometry of the microstructure would have to be known in 3D to extract quantitative volume fractions.

An EMT developed by Zuzovsky and Brenner to model conduction problems (thermal, electric and diffusion processes) offers a better approximation to ceramic microstructures than most EMTs, as it consists of conductive spheres situated cubically in a less conductive matrix phase (see fig. 6A)[16]. A flaw in this approach is that if the conductive phase's volume fraction exceeds ~0.52 the diameters of the spheres will be the same length as the unit cell (see fig. 6B). This causes percolation through the conductive phase reducing the conductivity contribution of the matrix to nothing. Therefore Zuzovsky's model cannot be used to describe systems with thin grain boundaries. Kidner compared Zuzovsky's model with the series BLM and his own 3D BLM, finding that Zuzovsky's EMT was applicable to small bulk volume fractions. If unwanted, percolation effects can be avoided by having both phases adopt the same shape, scaling down the filler phase (see fig. 6C). Perhaps unintentionally, the BLM's resistance to percolation has resulted in the success of attempts based on computer modelling to simulate electroceramics. This has allowed for visualisation of the electrical microstructure of the BLM, as both Kidner and Flieg have shown[17, 18]. Sometimes it is difficult to acquire reliable measurements of the microstructure-related parameters (grain boundary thickness may not be constant and hard to measure reliably) so EMT

should not be neglected, particularly when only conductivity extraction is required.

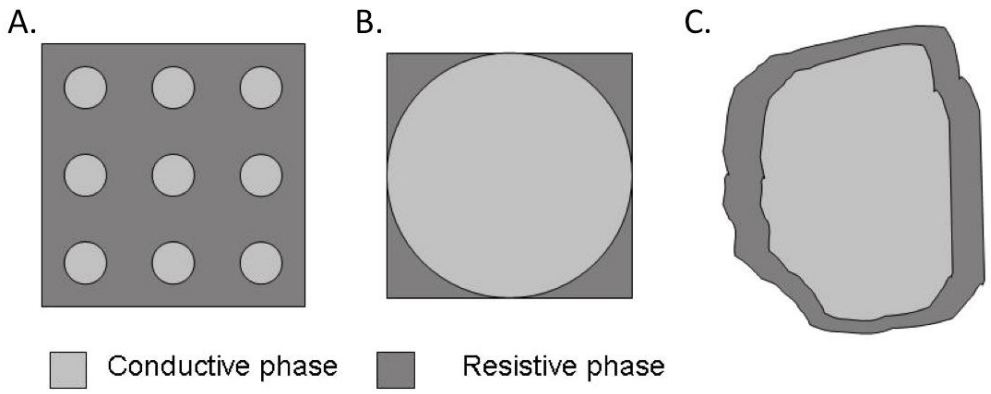

Fig. 6. (A) *Microstructure of Zuzovsky's EMT. (B) Unit cell of Zuzovsky's EMT with conductive phase volume fraction at the percolation limit. (C) Two phase composite with both materials adopting the same shape to allow a range of volume fractions without percolation for regular and irregular geometries.*

2.1.3. Finite Difference Methods

A recent development of the BLM is a 3D finite difference model developed by Kidner et al[17]. The BLM was represented by a nested cube structure built up by voxels. Each voxel consisted (electrically) of six orthogonal RC elements that were connected to its six nearest neighbours to produce a 3D equivalent circuit (see fig 7). Due to complexity of the system, Kidner's model had no analytical solution and had to be solved numerically. Whether a voxel was in a bulk or grain boundary (GB) region determined what properties were assigned to its RC elements. For example, to simulate resistive grain boundaries a GB voxel would have a higher resistance assigned to its RC element. This model was deemed to be more suitable for the simulation of nano-grain ceramics where the GB has similar thickness to the grain bulk or systems where the space charge extends outwards from GBs producing an electrical microstructure where the GBs are more significant[19].

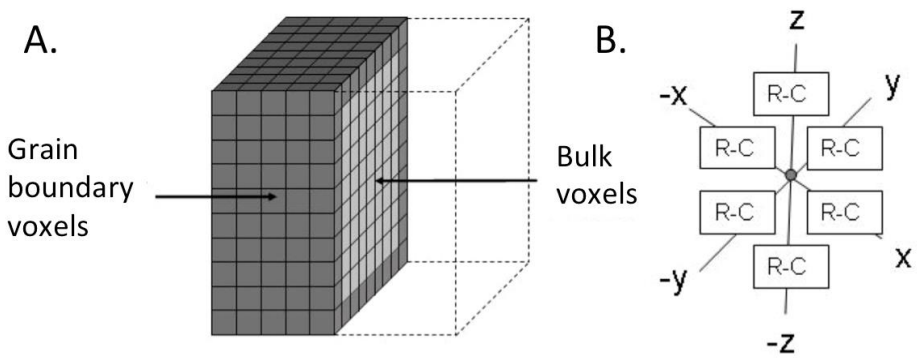

Fig 7. *(A) A single ceramic grain made up from voxels, darker voxels indicate grain boundary, lighter voxels indicate bulk. (B) Schematic of orthogonal RC connectivity for a single voxel.*

Kidner's model produced impedance spectra for a range of bulk volume fractions that were deemed to fall within bounds that were physically reasonable composite conductivity for a two-phase electrical composite (calculated using the Maxwell-Garnett effective medium theory). The 3D BLM was compared to other models including the analytical BLM variants (with and without parallel grain boundary paths) and Zuzovsky's EMT. Out of all these methods, only the 3D BLM and Maxwell's EMT could model an entire range of volume fractions. The series BLMs could only model thin grain boundaries. This was theorised to be because the serial BLM (see fig. 8A) neglects the contribution of the parallel GB, which become significant when the GB is of similar thickness to the bulk ceramic. The parallel BLM (see fig. 8B) becomes physically unreasonable, as it cannot model current leakage between the parallel GB and bulk material. Kidner was successful in extracting inputted material properties (conductivity and permittivity) using the Bonanos-Lilley equations[14, 19].

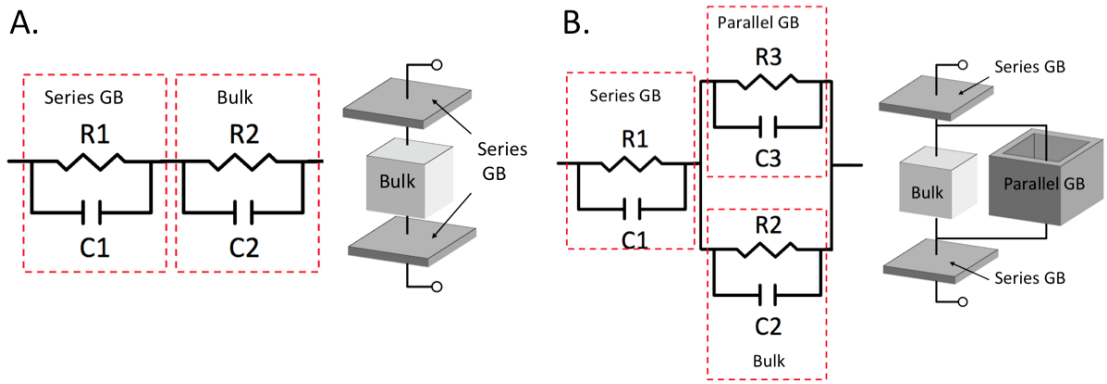

Fig. 8. *(A) Serial BLM equivalent circuit and representative microstructure. (B) Parallel BLM equivalent circuit and representative microstructure.*

It was noted that the calculated DC conductivity bounds for the 3D BLM were above the lower bound of the Hashin-Shtrikman equations. This can be explained by considering the shape of the high conductivity material used in both approaches. For the 3D BLM the high conductivity inclusions are cubes, whilst the Hashin-Shtrikman equations are based on EMT and therefore the conductive inclusions are spheres. If we consider the surface area provided by a sphere and a cube of the same volume, the surface area of the cube is larger. In the context of conduction this means that the cube presents more area for current to flow through. This was studied quantitatively by Mansfield et al, who calculated intrinsic conductivity factors for different shapes of unit volume[20]. Cubes had the largest conductivity factor whereas spheres had the lowest. The 3D BLM (being cube-based) had a higher conductivity than the (sphere-based) EMT, leading to higher conductivity bounds for the 3D BLM.

A final development to the 3D BLM was the addition of variations in the properties of the grain boundary region[21] . This was achieved with a cubic 'onion' structure (see fig. 9). The grain boundary region was divided into three zones, each making up another layer of the 'onion'. The zone closest to the bulk had a conductivity and permittivity of 50% of the normal assigned properties, the middle zone 100% and the outer zone 150%. This approximated a gradual variation of the grain boundary properties that theoretically could be caused by space charge

layers extending past structural boundaries or a gradient in composition. This produced an increase in the model's resistance (taken from a Z* Nyquist plot) and also an increase in the low frequency Z* arc depression. The change in resistance was not of much concern, as the change in layer properties had been chosen arbitrarily - not obeying any laws of mixture. However, the increase in Z* arc depression could prove to be a cause of deviation from the Debye type responses in impedance spectroscopy.

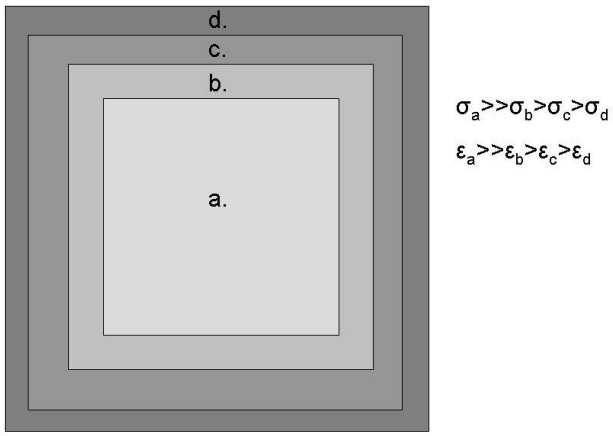

Fig. 9. *Cross section of Kidner's 3D BLM nested cube 'onion', where (a) is the bulk and (b) to (d) represent the grain boundary with decreasing conductivity and permittivity of each layer away from the bulk.*

A potential issue with Kidner's approach is that conduction is limited to the orthogonal connections of the pixels. Obviously this would be a problem when modelling a material where conduction is not limited to just the XYZ axes. The effect of this can be minimised with increased pixel resolution. For simple cases, the 3D BLM shows how the series BLM is good for thin grain boundaries (micron grain-sized regime). The parallel BLM can become useful when faced with grain boundaries of similar thickness to the bulk (nano grain-sized regime) and neither of the traditional models work well for intermediate bulk volume fractions.

2.1.4. Finite Element Modelling

More recent work has forgone the use of equivalent circuits (for the actual simulation of impedance spectra, equivalent circuits are still used for analysing spectra). By using finite element modelling (FEM), regions of a model can be assigned intrinsic material properties (e.g. conductivity) instead of extrinsic properties as used for circuit elements (e.g. resistance). The basic principle of FEM is to break a complicated problem (often too difficult to solve analytically) into smaller problems that can be solved locally; local equations can then be used to solve the global equation numerically[22]. A more in depth overview of the FEM code used in this project is given in chapter three. First applied to solve 2D plane stress on the wings of early military jets[23], FEM was improved upon and, with increasing availability of computers in the late 20th century, became an industry standard for solving mechanical problems. The technique has been expanded into other areas of physics, allowing for the simulation of heat flow, electromagnetism and other dynamical systems [24, 25, 26].

In the context of solving AC impedance by FEM, initial work was pioneered by Fleig and Maier first in 2D[27] and later in 3D[28] . Both approaches gave reasonable results, producing a dual arc response for simulated ceramic microstructures with resistive grain boundaries and single-sized cubic grains (analogous to the BLM). Fleig made the argument that the BLM would not be able to analyse the impedance data of all microstructures due to the limits of equivalent circuits. For an equivalent circuit to be an exact representation of a microstructure, several conditions must be met[28]. Assuming a cube of material with a single permittivity and conductivity, if the sides that are perpendicular to the applied voltage have a uniform potential difference between them and if no current can leak out of the free sides parallel to the applied voltage, all the current can be assumed to flow from the surface with the higher potential to the surface with the lower potential (see fig. 10A). Here the cube's electrical response is mathematically equivalent to a single RC element.

Taking the same cube and dividing its volume into two layers with a perfectly flat interface stacked perpendicular to the applied voltage, we arrive at the SLM. If each layer has its own value of permittivity and conductivity, the same conditions hold, as the interface between the two layers will also be equipotential (see fig. 10B). Here the cube can be represented exactly as a two RC elements connected in series. If the configuration of the two materials of the cube is altered so that not all interfaces are perpendicular to the applied voltage, the remaining perpendicular interfaces will not be equipotential (see fig. 10C, surface 2) and so current will be able to flow between any parallel interfaces (see fig. 10C, surface 3). Here an equivalent circuit will not be an exact representation even if extra parallel branches are added. It should be noted that just because an equivalent circuit is not a mathematically exact representation of an electrical microstructure does not mean that it is necessarily a bad approximation. It is important to test under what conditions such an approximation is appropriate.

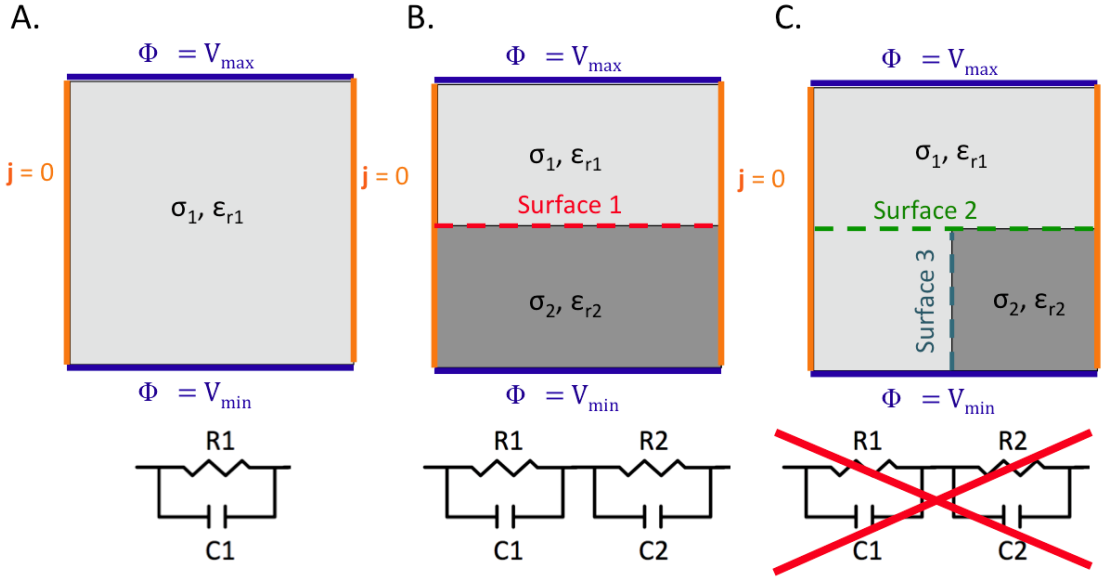

Fig. 10. *Several cross sections of a cube of material that has a uniform potential difference (ΔΦ) applied between the top and bottom surfaces (blue) and the condition that no current may flow through any of the other free sides (orange). (A) Situation where the cube has only one material of conductivity σ_1 and permittivity ε_{r1} and can be represented by a single RC element. (B) Situation where the cube is a layered composite material with one region having a conductivity σ_1 and permittivity*

ε_{r1} and the other having a conductivity σ_2 and permittivity ε_{r2}, and can be represented by two RC elements connected in series as surface 1 (red) is equipotential. (C) Situation where the cube is a composite material with one region having a conductivity σ_1 and permittivity ε_{r1} and the other having a conductivity σ_2 and permittivity ε_{r2}, and cannot be represented exactly by two RC elements connected in series as surface 2 (green) will not be equipotential and surface 3 (turquoise) will have current flowing through it[28].

Fleig has shown that even small deviations from homogenous layers can lead to a frequency dependent potential distribution[18, 27, 28, 29]. At low frequency, the potential is distorted around microstructural features that offer paths of least resistance and at higher frequencies the potential becomes less distorted as capacitive pathways short out the conduction pathways. An example of this was a 2D simulation of an imperfect electrode, consisting of a layer of ceramic with an air gap between the ceramic and the electrode[27]. The air gap was significantly more resistive than the ceramic and a small part of the electrode infiltrated the air gap to make contact with the ceramic layer. This configuration can approximate poorly wetting electrode paste or poorly contacted foil electrodes. At low frequency the potential drop was greater around the electrode contact point (see fig. 11A). Potential contours were highly distorted around the contact point also. As frequency increased, the potential drop was spread more evenly across the model and the potential contours were less distorted at the contact point (see fig. 11B).

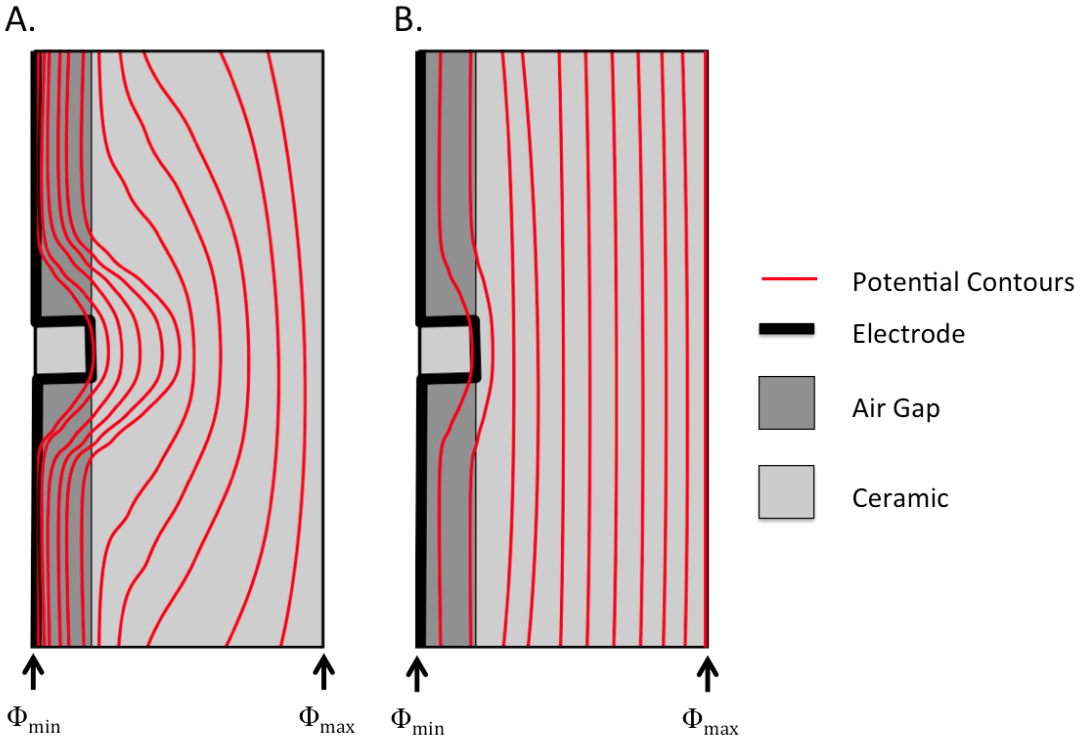

Fig. 11. *Schematic of the potential distribution through a ceramic with a poorly contacted electrode at (A) low frequency and (B) high frequency.*

Two arcs were found in an impedance Nyquist plot. The high frequency arc had the same resistance and capacitance to a ceramic layer with a perfect electrode. The low frequency arc was deemed to be a composite containing the

effect of the air gap capacitance and the bulk ceramic resistance. This effect was also present in a 3D equivalent of the same study[28], showing that heterogeneity in the electrical microstructure can lead to a distinct impedance response.

A 2D investigation of grain boundary morphology[30] showed that, when grain boundaries are thin and more resistive than the bulk ceramic, small deviations from the ideal microstructure of the BLM (see fig. 12A) also altered the impedance response. Constructing single-sized grains from a variety of shapes (see figs 12B to F) altered the potential distribution throughout the grains, particularly at low frequency. This altered the low frequency arc diameter in impedance Nyquist plots by up to a factor of two. The reason for this deviation was a change in the area of grain boundary presented to the incoming current. If a greater area of grain boundary was presented, the effective resistance of the grain boundary was reduced. At high frequency, the potential distribution was homogenous and the bulk arc was not affected. A model using randomised grain shapes deviated less from the BLM-predicted grain boundary resistance. Fleig suggested that, for a randomised grain shape, some areas of the microstructure will present more grain boundary area to the incoming current, others less and hence will average out to some extent. This implies that for experimental analysis of polycrystalline ceramics with thin and resistive grain boundaries, the BLM is a good approximation for the electrical response.

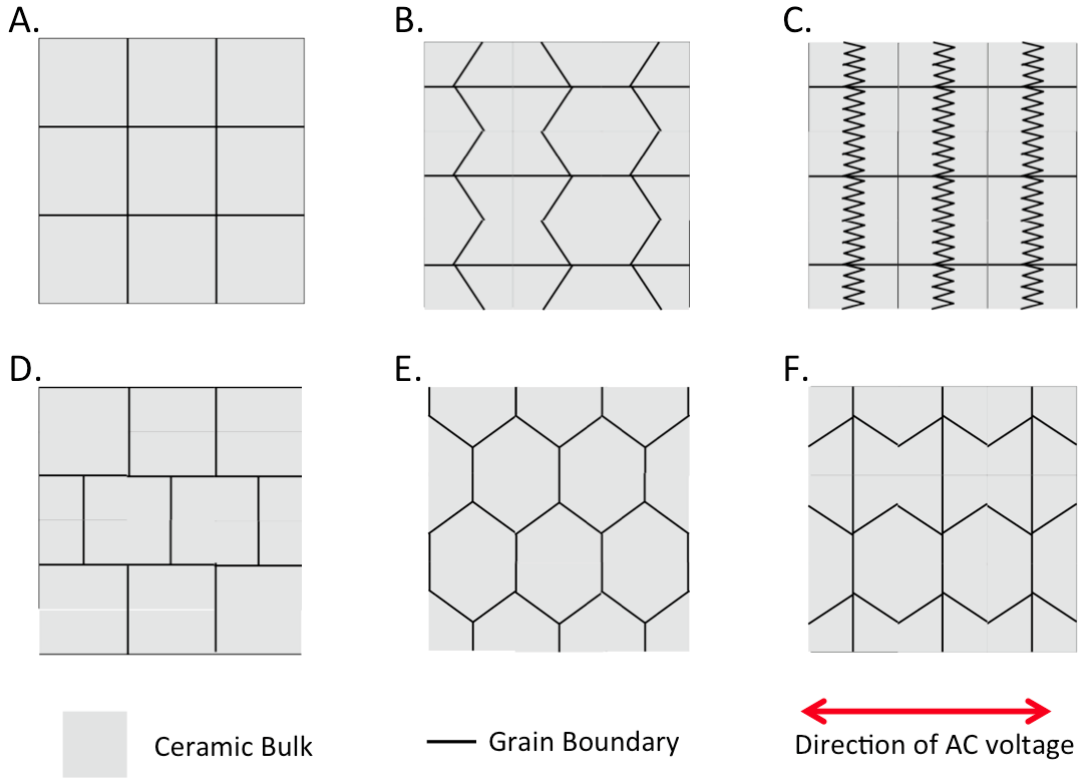

Fig. 12. *Schematic of a Brick Layer Model and several 2D microstructures that deviate from the Brick Layer Model by alteration of their grain boundaries. (A) Brick Layer Model; (B) parallel sloping grain boundaries; (C) zigzag grain boundaries; (D) displaced brick layer grain boundaries; (E) hexagonal grain boundaries; and (F) perpendicular sloping grain boundaries.*

Larger deviations from the BLM occurred when attempting to simulate more complex microstructures such as inhomogeneous distributions of grain size

and grain boundary properties. Heterogeneity in microstructure was shown to cause inhomogeneous potential distributions, implying current flowing through the path of least resistance (see fig. 13), missing out more resistive regions (such as clusters of smaller grains, giving a higher density of grain boundaries and hence a greater resistance for the current to overcome)[30].

Similarly if a microstructure forces current to pass through a more resistive region it was found that the current will disperse throughout the ceramic boundary; maximising the area to reduce the effective resistance[31]. Simulations of micro contacts placed on individual grains demonstrated this. If the grains were mono-sized cubes and all grain boundaries had the same properties (more resistive than the grains), current only passed through the minimum amount of grain boundaries required to flow from one micro-contact to the other (see fig. 14A). A simulation of the same model, but where the resistance of the grain boundaries that the current had flowed through was increased and the remaining grain boundaries had the original value of resistance, showed the current detouring past the altered grain boundaries and flowing through the less resistive grain boundaries (see fig. 14B). Using a 2D simulation of a randomised ceramic microstructure (with a distribution of grain sizes and shapes to mimic a real microstructure), Fleig used current density distribution plots to show that on average a larger current density passed through the larger grains, providing visual evidence of current taking the path of least resistance through the model [32].

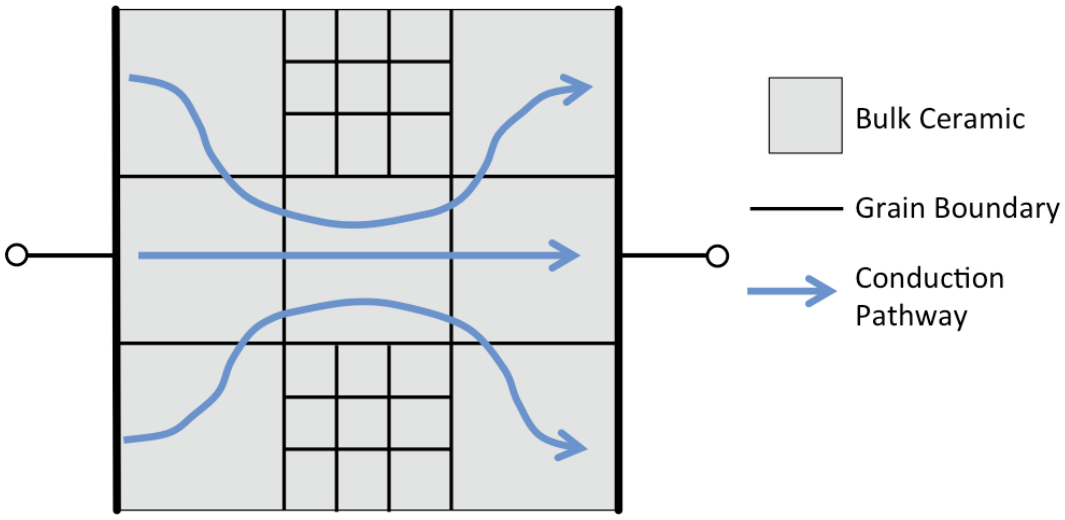

Fig. 13. *Schematic of current avoiding regions of the microstructure that have a higher density of grain boundaries. Given the grain boundaries are more resitive than the bulk, the regions with a higher density of grain boundaries will be more resistive over all presenting an obstruction to current flow. Hence the current will detour through the region that has lower grain boundary density.*

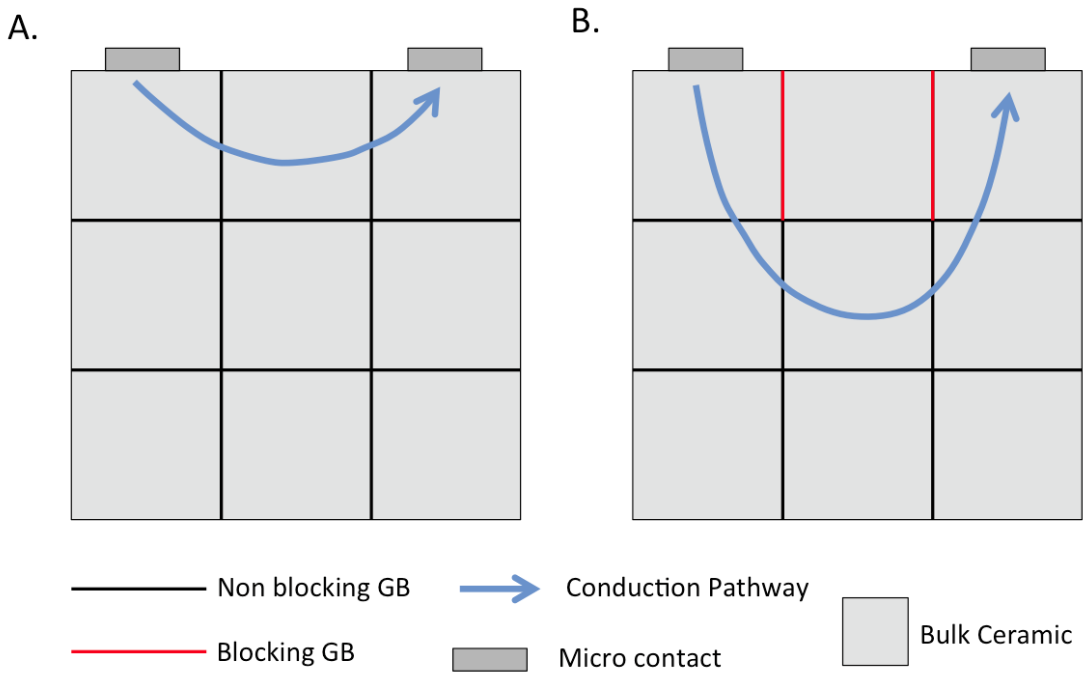

Fig. 14. *Schematic of micro contact impedance analysis simulations. (A) Current curvature to pass through two non-blocking grain boundaries. (B) Current taking a longer path of least resistance to avoid blocking grain boundaries.*

One of the main limitations of Fleig's approach was due to the limited availability of computer processing power at the time of his studies. The models he produced could only be meshed with fewer elements than comapared with more recent studies (producing a smaller system of equations to solve) and, for more complex problems, 2D simulations had to be used. A finer mesh allows for a more accurate simulation and gives a better resolution when using visualisation techniques. This was utilised by Dean et al[33] to show current density distributions and how their inhomogeneity leads to departures from ideal Debye behaviour.

Several microstructures were simulated. The first was a layered structure analogous to Maxwell's SLM[6] (see fig. 15A and B) and the second was a nested cube model (referred to as the encased model, see fig. 15C and D). Both models were composed of two regions, representing core and shell materials. The core was three orders of magnitude more conductive than the shell and both materials had the same permittivity. First, a comparison of both models was made where the volume of core and shell was the same. Giving the same amount of material a different configuration in space was found to alter the resistances and capacitances of the core and shell material. The SLM agreed with analytical predictions; the encased model deviated from predictions. Another finding was that the Full Width at Half Maximum (FWHM) of the high frequency imaginary electric modulus component measured 1.15 decades on a log frequency scale for the SLM and a larger 1.23 decades for the encased model (see fig. 15E). As discussed in the theory section of chapter one, a FWHM of 1.14 decades would be expected for an ideal Debye response. Examining the current density of each model revealed homogenous current density in each layer of the SLM whereas the current density in the encased model was more heterogeneous

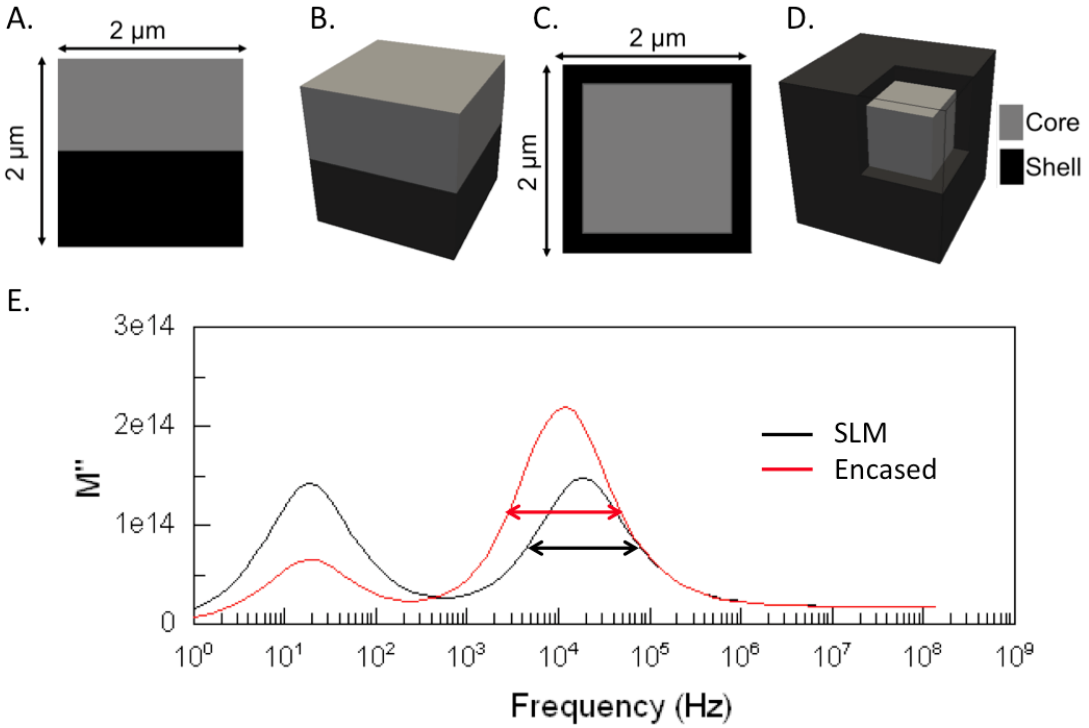

Fig. 15. *(A) Cross-section of the series layer model with (B) three dimensional representation. (C) Cross-section of the encased model with (D) three-dimensional representation with part of the shell removed to show the core. (E) Spectroscopic plot of the imaginary component of the electric modulus formalism. Note the increase in the Full Width at Half Maximum of the encased model's high frequency peak. These simulations have been reproduced using the same FEM code as Dean et al[30]; more detailed discussion is presented in chapter four.*

These results imply that although each component of an electrical composite may have relatively homogenous electrical properties, the configuration of the physical microstructure can produce a heterogeneous electrical microstructure. This heterogeneity will be reflected by increased deviations from an ideal Debye response in impedance spectra. It was shown that the deviations from ideality were increased as the volume fraction of the shell material in the encased model increased. This correlated to increased heterogeneity in current density as the shell volume fraction increased. Dean *et al* also repeated these simulations with a randomised 3D microstructure using Voronoi tessellation[30]. The average grain size was comparable to the previous models allowing for comparison. It was found the FWHM of the high frequency imaginary electric modulus peak further increased to a maximum 1.32 decades when the volume fraction of the shell material was highest (with a value of 0.5). More current density plots showed increased heterogeneity in the random Voronoi microstructures. It was also shown that current flowed through preferred paths of least resistance in good agreement with theory and previous simulation work[13, 32].

2.2. Summary of findings

It is possible to model the AC characteristics of electrical composites with several approaches. The variants of the BLM provide approximations of an electro-ceramic microstructure allowing for its use in data extraction from spectra, but can be unreliable if the correct version is not used for the grain boundary volume fraction presented. Simple layer models such as the SLM and PLM are useful for modelling electrical composites that have only serial and parallel connectivity respectively, but cannot model more complex scenarios where significant parallel and serial conduction pathways exist within the same microstructure. EMT can model a whole range of volume fractions but has a microstructure that is very different to a real ceramic, making it unsuitable for visualisation.

FEM and finite difference modelling can be used to simulate impedance numerically, allowing any bulk volume fraction to be studied with microstructures at least as realistic as the BLM. Using advanced model generation it is possible to surpass the BLM in terms of microstructure realism[33]. Where simulated microstructures are relatively simple, FD can be more computationally efficient than FEM but FD is less flexible when simulating complex geometries compared to FEM. This is due to FEM's ability to discretise space with an unstructured mesh (or a non-regular sized numerical grid). An additional advantage of an unstructured mesh is the ability to vary the resolution of the mesh depending on the accuracy of the calculation required locally within a model. An example of this could be having a finer mesh around an important microstructural feature and a coarser mesh where accuracy is not so important. Perhaps the greatest strength of computer modelling is the ability to study the internal behaviour of a model and how it governs output spectra. Already studied qualitatively[21, 33], it is possible to see what parameters can lead to departures from simple Debye-like behaviour. The development of new analysis techniques will allow quantitative analysis of such deviations, potentially providing insight into the origins of non-ideal behaviour.

2.3. Gaps in our knowledge

As computational power becomes more readily available the versatility of FEM will prove attractive over the more performance- friendly (simpler to implement and less computationally intensive to run) finite difference based approaches. The ability of FEM to handle complex geometries has already been utilised for simulations of impedance spectroscopy of ceramics at the device scale. Recent work has used serial sectioning technology to produce 3D models of portions of multi-layer capacitors for conversion into meshed models[34, 35, 36]. These models were then used to simulate electric field distributions and hence investigate reliability issues. The models had averaged properties for the ceramic layers (grain boundaries and secondary phases were consolidated into the bulk properties) in order to capture detail at a larger scale, such as the interface roughness. This approach can be applied on a smaller scale to simulate more local detail in ceramic microstructures and therefore allow the influence of grain boundaries, pores and secondary phases to be considered in full 3D. Shape effects considered by Kidner[13] *et al* were calculated from analytical solutions[20]. Such effects can easily be

simulated by FEM allowing shape effects to be studied in less ideal, randomised microstructures where no exact analytical solutions exist.

Kinder[21], Dean[33] and Flieg[29] observed non-ideality in simulated impedance spectra. For Kidner this was due to many time constants of similar magnitude being present, in good agreement with some of the theory present in the literature that considers distributions of relaxation times (see chapter one for a detailed discussion). For Fleig and Dean, such behaviour occurred in systems with only two well-separated time constants. The apparent non-ideality was due to heterogeneity in the electrical microstructure. This would imply that there is a contribution to non-ideality from microstructural effects in addition to the well-discussed intrinsic effects. Whilst FEM and other continuum approaches are unsuitable for studying the intrinsic contribution to non-ideality in impedance spectra, due to the most likely atomistic nature of the intrinsic contribution. However, FEM is ideal for the study of microstructural contribution to non-ideality. Techniques for the quantitative analysis of current density or potential distributions throughout a simulated microstructure should be developed to study how the electrical microstructure correlates with non-ideal impedance spectra.

Another consequence of heterogeneity in electrical microstructures is the reduced applicability of fitting with equivalent circuits[28] (see fig. 10). The simulations of Dean *et al* [33] showed that, as the shell of an encased model became thicker, the current density in the core becomes more heterogeneous. An encased model with a thick shell can approximate a core-shell microstructure. Previously a BLM analysis has been used to extract volume fractions from core-shell microstructures[15, 37]. A FEM study could test this analysis by performing an exact calculation where core-shell volume fractions are known and then extract volume fractions using the BLM. This would show under what conditions such analysis is accurate and what magnitude of error(s) could be present (see fig. 16). This approach can also be applied to equivalent circuit fitting. Hwang *et al* attempted to fit nano-grained ceria with the parallel BLM equivalent circuit[5]. Again, FEM could be used to simulate a nano-grained ceramic (grain boundary similar thickness to the bulk) and, by extracting known values of permittivity and conductivity using the parallel BLM, could evaluate the methodology.

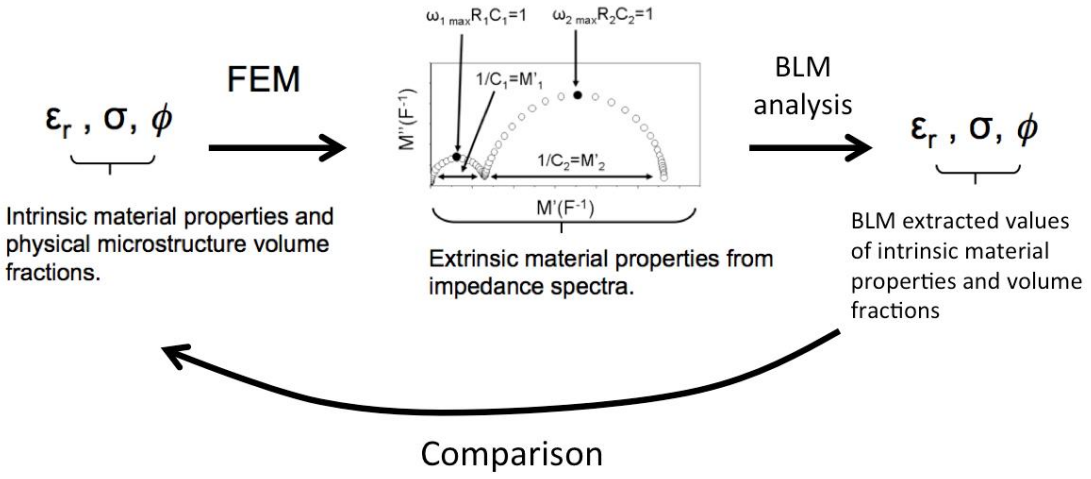

Fig. 16. *Methodology for evaluation of the BLM by comparison of input and output data from a computer model.*

Generally, previous studies simulating impedance spectroscopy have used the complex impedance formalism (Z*) to analyse data. While a few previous works have used an alternative formalism, such as the work of Dean *et al* which used a combination of Z* and the electric modulus (M*). As stated in chapter one, impedance data can be analysed using several formalisms, each with its own weighting to different magnitudes of resistance and capacitance. It would be beneficial for a computational study to analyse data using all four formalisms and compare extracted values of conductivity and permittivity with pre-defined values. This could show practitioners what formalism (or combination of formalisms) is best for a given scenario (microstructure and/or material properties).

Finally, not much attention has been given to the impedance response of materials with more than one permittivity present. Several of the studies discussed above have assigned different permittivities to the bulk and grain boundary regions, typically to ensure that the time constants of bulk and grain boundary are sufficiently different. There have been no studies of the impedance spectroscopy of a material where the conductivity is fixed throughout the entire microstructure and only the permittivity is varied. The closest work to this in the literature is in the field of microwave dielectrics but is limited to DC[38] or fixed frequency[39] measurements. Once the effect of a difference in permittivity is understood in isolation, a more complex analysis of materials with mixed conductivity and mixed permittivity can be attempted.

In summary this gives five research questions that are the subjects of the work presented in this thesis:

- How do shape effects affect the impedance response of physical microstructures that have no analytical solution?
- What is the cause of non-ideality observed in previous modelling studies on impedance spectroscopy that did not contain the intrinsic contribution to non-ideality present in real materials?
- Can the brick layer model be applied to the analysis of core-shell microstructures or nano-grained ceramics where the current density distribution is more heterogeneous than in ceramics with thin grain boundaries and could a parallel version of the brick layer model be applied to these systems?
- For a given microstructure and material properties, what is the best impedance formalism for the extraction of material properties by comparison of extracted values to the original input values?
- How does the impedance response of a material with homogenous conductivity and heterogeneous permittivity vary with the microstructural configuration of the low and permittivity material?

2.4. References

1. A. R. West, D. C. Sinclair, and N. Hirose, "Characterization of electrical materials, especially ferroelectrics, by impedance spectroscopy," *Journal of Electroceramics,* 1[1] 65-71 (1997).

2. J. E. Bauerle, "Study of Solid Electrolyte Polarization by a Complex Admittance Method," *Journal of Physics and Chemistry of Solids,* 30[12] 2657-2670 (1969).

3. N. M. Beekmans and L. Heyne, "Correlation Between Impedance, Microstructure and Composition of Calcia-Stabilized Zirconia," *Electrochimica Acta,* 21[4] 303-310 (1976).

4. H. Nafe, "Ionic-Conductivity of ThO_2-Based and ZrO_2-Based Electrolytes Between 300-K and 2000-K," *Solid State Ionics,* 13[3] 255-63 (1984).

5. J. H. Hwang, D. S. McLachlan, and T. O. Mason, "Brick layer model analysis of nanoscale-to-microscale cerium dioxide," *Journal of Electroceramics,* 3[1] 7-16 (1999).

6. J. C. Maxwell, "A Treatise on Electricity and Magnetism." Cambridge University Press, (2010).
7. K. W. Wagner, "Erklärung der dielektrischen Nachwirkungsvorgänge auf Grund Maxwellscher Vorstellungen," *Archiv für Elektrotechnik,* 2[9] 371-87 (1914).

8. D. S. McLachlan, M. Blaszkiewicz, and R. E. Newnham, "Electrical-Resistivity of Composites," *Journal of the American Ceramic Society,* 73[8] 2187-203 (1990).

9. J. C. M. Garnett, "Colours in metal glasses and in metallic films," *Philosophical Transactions of the Royal Society of London Series a-Containing Papers of a Mathematical or Physical Character,* 203 385-420 (1904).

10. J. C. M. Garnett, "Colours in metal glasses, in metallic films, and in metallic solutions - II," *Philosophical Transactions of the Royal Society of London Series a-Containing Papers of a Mathematical or Physical Character,* 205 237-88 (1906).

11. V. A. Markel, "Introduction to the Maxwell Garnett approximation: tutorial," *Journal of the Optical Society of America a-Optics Image Science and Vision,* 33[7] 1244-56 (2016).

12. Z. Hashin and S. Shtrikman, "A Variational Approach to Theory of Effective Magnetic Permeability of Multiphase Materials," *Journal of Applied Physics,* 33[10] 3125-3131 (1962).

13. N. J. Kidner, N. H. Perry, T. O. Mason, and E. J. Garboczi, "The brick layer model revisited: introducing the nano-grain composite model," *Journal of the American Ceramic Society,* 91[6] 1733-46 (2008).

14. N. Bonanos and E. Lilley, "Conductivity Relaxations in Single-Crystals of Sodium-Chloride Containing Suzuki Phase Precipitates," *Journal of Physics and Chemistry of Solids,* 42[10] 943-52 (1981).

15. S. I. R. Costa, M. Li, J. R. Frade, and D. C. Sinclair, "Modulus spectroscopy of CaCu3Ti4O12 ceramics: clues to the internal barrier layer capacitance mechanism," *Rsc Advances,* 3[19] 7030-36 (2013).

16. M. Zuzovsky and H. Brenner, "Effective Conductivities of Composite-Materials Composed of Cubic Arrangements of Spherical-Particles Embedded in an Isotropic Matrix," *Zeitschrift Fur Angewandte Mathematik Und Physik,* 28[6] 979-92 (1977).

17. N. J. Kidner, Z. J. Homrighaus, B. J. Ingram, T. O. Mason, and E. J. Garboczi, "Impedance/dielectric spectroscopy of electroceramics - Part 1: Evaluation of composite models for polycrystalline ceramics," *Journal of Electroceramics,* 14[3] 283-91 (2005).

18. J. Fleig and J. Maier, "Finite-element calculations on the impedance of electroceramics with highly resistive grain boundaries: I, laterally inhomogeneous grain boundaries," *Journal of the American Ceramic Society,* 82[12] 3485-93 (1999).

19. N. J. Kidner, Z. J. Homrighaus, B. J. Ingram, T. O. Mason, and E. J. Garboczi, "Impedance/dielectric spectroscopy of electroceramics - Part 2: Grain shape effects and local properties of polycrystalline ceramics," *Journal of Electroceramics,* 14[3] 293-301 (2005).

20. M. L. Mansfield, J. F. Douglas, and E. J. Garboczi, "Intrinsic viscosity and the electrical polarizability of arbitrarily shaped objects," *Physical Review E,* 64[6] (2001).

21. N. J. Kidner, B. J. Ingram, Z. J. Homrighaus, T. O. Mason, and E. J. Garboczi, "Impedance/dielectric spectroscopy of electroceramics in the nanograin regime," pp. 39-50 in Symposium on Solid State Ionics held at the 2002 MRS Fall Meeting. Vol. 756, *Materials Research Society Symposium Proceedings*. S. Mat Res, (2003).

22. J. E. Akin, "Finite Element Analysis with Error Estimators : An Introduction to the FEM and Adaptive Error Analysis for Engineering Students," (2005).

23. M. J. Turner, R. W. Clough, H. C. Martin, and L. J. Topp, "Stiffness and Deflection Analysis of Complex Structures," *Journal of the Aeronautical Sciences,* 23[9] 805-823 (1956).

24. E. L. Wilson and R. E. Nickell, "Application of Finite Element Method to Heat Conduction Analysis," *Nuclear Engineering and Design,* 4[3] 276-286 (1966).

25. O. Biro and K. Preis, "On the Use of the Magnetic Vector Potential in the Finite-Element Analysis of 3-Dimensional Eddy Currents," *Ieee Transactions on Magnetics,* 25[4] 3145-3159 (1989).

26. G. A. Greenbau and M. F. Rubinste, "Creep Analysis of Axisymmetric Bodies Using Finite Elements," *Nuclear Engineering and Design,* 7[4] 379-397 (1968).

27. J. Fleig and J. Maier, "Finite element calculations of impedance effects at point contacts," *Electrochimica Acta,* 41[7-8] 1003-09 (1996).

28. J. Fleig and J. Maier, "The influence of laterally inhomogeneous contacts on the impedance of solid materials: A three-dimensional finite-element study," *Journal of Electroceramics,* 1[1] 73-89 (1997).

29. J. Fleig, "Impedance spectroscopy on solids: The limits of serial equivalent circuit models," *Journal of Electroceramics,* 13[1-3] 637-44 (2004).

30. J. Fleig and J. Maier, "A finite element study on the grain boundary impedance of different microstructures," *Journal of the Electrochemical Society,* 145[6] 2081-89 (1998).

31. J. Fleig, S. Rodewald, and J. Maier, "Microcontact impedance measurements of individual highly resistive grain boundaries: General aspects and application to acceptor-doped SrTiO3," *Journal of Applied Physics,* 87[5] 2372-81 (2000).

32. J. Fleig, "The grain boundary impedance of random microstructures: numerical simulations and implications for the analysis of experimental data," *Solid State Ionics,* 150[1-2] 181-93 (2002).

33. J. S. Dean, J. H. Harding, and D. C. Sinclair, "Simulation of Impedance Spectra for a Full Three- Dimensional Ceramic Microstructure Using a Finite Element Model," *Journal of the American Ceramic Society,* 97[3] 885-91 (2014).

34. M. M. Samantaray, K. Kaneda, W. Qu, E. C. Dickey, and C. A. Randall, "Effect of Firing Rates on Electrode Morphology and Electrical Properties of Multilayer Ceramic Capacitors," *Journal of the American Ceramic Society,* 95[3] 992-98 (2012).

35. M. M. Samantaray, A. Gurav, E. C. Dickey, and C. A. Randall, "Electrode Defects in Multilayer Capacitors Part I: Modeling the Effect of Electrode Roughness and Porosity on Electric Field Enhancement and Leakage Current," *Journal of the American Ceramic Society,* 95[1] 257-63 (2012).

36. M. M. Samantaray, A. Gurav, E. C. Dickey, and C. A. Randall, "Electrode Defects in Multilayer Capacitors Part II: Finite Element Analysis of Local Field Enhancement and Leakage Current in Three-Dimensional Microstructures," *Journal of the American Ceramic Society,* 95[1] 264-68 (2012).

37. D. C. Sinclair and A. R. West, "Impedance and Modulus Spectroscopy of Semiconducting $BaTiO_3$ Showing Positive Temperature-Coefficient Of Resistance," *Journal of Applied Physics,* 66[8] 3850-56 (1989).

38. Y. G. Wu, X. H. Zhao, F. Li, and Z. G. Fan, "Evaluation of mixing rules for dielectric constants of composite dielectrics by MC-FEM calculation on 3D cubic lattice," *Journal of Electroceramics,* 11[3] 227-39 (2003).

39. L. Padurariu, L. P. Curecheriu, and L. Mitoseriu, "Nonlinear dielectric properties of paraelectric-dielectric composites described by a 3D Finite Element Method based on Landau-Devonshire theory," *Acta Materialia,* 103 724-34 (2016).

Chapter 3: Methodology

In this chapter the methodologies used in this work are detailed. The mathematics specific to our finite element code is described. For a more general overview of the finite element method, the reader is directed to the FEM section in the literature review (chapter 2). Model generation is also covered here. Finally algorithms written to analyse the physical and electrical microstructure are explained.

3.1. Finite Element Modelling

3.1.1. Applying the finite element method to impedance spectroscopy

In this study a finite element code, developed in-house, called ElCer (**El**ectro **Cer**amics) is employed[1]. This software uses Maxwell's equations[2] to calculate the impedance response of a ceramic microstructure with electrode contacts over a given frequency range. The mathematics behind ElCer is described in greater detail in a recent publication[1]. Here we highlight the key steps to show the general methodology, the assumptions made and the implications for this work.

We first consider Maxwell's continuity equation[2].

$$\frac{\partial \rho}{\partial t} + \nabla . \mathbf{j} = 0 \tag{3.1}$$

where ρ is the charge density, t is time and **j** is the current density. To find the current flowing through the microstructure we must evaluate $\nabla . \mathbf{j}$. The current density has two components: a conductive term ($\mathbf{j_c}$) and a displacement current term ($\mathbf{j_d}$). These terms are:

$$\mathbf{j_c} = \sigma \mathbf{E} \tag{3.2}$$

$$\mathbf{j_d} = \frac{\partial \mathbf{D}}{\partial t} \tag{3.3}$$

$$\nabla . \mathbf{j} = \nabla . (\mathbf{j_c} + \mathbf{j_d}) \tag{3.4}$$

where **D** is the electric displacement, σ is the conductivity and **E** is the electric field. The material simulated obeys Ohm's Law, is isotropic and has no time dispersion. We can therefore approximate the permittivity of the material, $\varepsilon(\mathbf{r})$, as simply a function of position. We can therefore write **D** as:

$$\mathbf{D}(\mathbf{r}, t) = \varepsilon(\mathbf{r})\mathbf{E}(\mathbf{r}, t) \tag{3.5}$$

Substituting (3.3) into (3.5) gives:

$$\mathbf{j_d} = \varepsilon(\mathbf{r}) \frac{\partial \mathbf{E}(\mathbf{r}, t)}{\partial t} \tag{3.6}$$

Substituting (3.6) and (3.2) into (3.4), $\nabla . \mathbf{j}$ becomes:

$$\nabla.\mathbf{j} = \nabla.\left(\sigma\mathbf{E} + \varepsilon(\mathbf{r})\frac{\partial}{\partial t}\mathbf{E}(\mathbf{r},t)\right) \tag{3.7}$$

As the frequency range for measuring impedance spectroscopy experimentally is within the millihertz to megahertz range, inductive effects are ignored as generally they are dominated by capacitive effects in resistive ceramics up to the terahertz frequencies. This allows **E** to be written as a function of the electric potential ($\Phi(\mathbf{r},t)$).

$$\mathbf{E} = -\nabla\Phi(\mathbf{r},t) \tag{3.8}$$

where $\Phi(\mathbf{r},t)$ can be approximated using shape functions for a given mesh element. Substituting (3.8) into (3.7) gives a partial differential equation for $\nabla.\mathbf{j}$ where, given values of permittivity and conductivity, the electric potential can be obtained:

$$\nabla.\mathbf{j} = -\nabla.\left(\sigma\nabla\Phi(\mathbf{r},t) + \varepsilon(\mathbf{r})\frac{\partial}{\partial t}\nabla\Phi(\mathbf{r},t)\right) \tag{3.9}$$

Using the Galerkin scheme[3] for time discretisation allows the local values of electric potential to be obtained given three boundary conditions. A Dirichlet boundary condition sets the electric potential to known values at the electrode surfaces of the model. This is analogous to applying a potential difference in a real impedance measurement (see fig. 1). A Neumann condition is applied to the free surfaces of the model, setting the current density to zero at the ceramic-air boundary. This confines the current density inside the model. Finally there is the internal boundary condition (considering the boundary of an individual element) that allows current to flow from one element to its neighbours. This allows current to flow freely through the model.

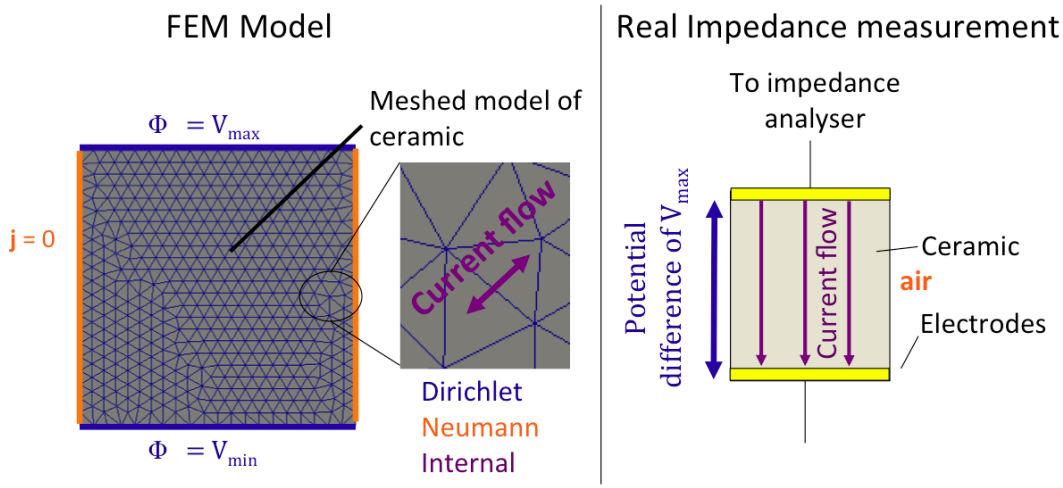

Fig. 1. *How the three boundary conditions used in the FEM model relate to an experimental impedance measurement.*

Once the local values for Φ have been found, local values of **j** and **E** can be back- calculated using equations (3.7) and (3.8) respectively. These can be plotted as a function of position in order to visualise the electrical microstructure. The global values of **j** and **E** can then be calculated by the integration of the local values over the whole microstructure. Current (I) flowing through the electrode surface at any time step is calculated by integrating the global current density over the electrode surface (S_{El}):

$$I(t) = \iint_{S_{El}} \mathbf{J}(\mathbf{r}, t).\mathbf{n}dA \tag{3.10}$$

where **J**(**r**,t) is the global current density, **n** is the unit vector normal to the electrode surface and A is the area of a given element present on the electrode surface.

At the top of the model there is always a layer of elements with only a conductivity assigned to it (permittivity is set to zero) called the reference layer. A zero value for permittivity means, mathematically, that the layer is a pure resistor with no capacitance. This is, strictly speaking, unphysical but is computationally convenient since it makes the current flowing through the reference layer frequency independent, simplifying the calculation. The known current in the reference layer gives the code a point of reference with which to compare the current in the rest of the model. This current will be frequency dependent since the materials in the microstructure have permittivity and conductivity values assigned to them. As both the current flowing through the electrode and the potential applied across it are known at any time step, a current-voltage characteristic can be obtained for a given frequency. The difference in phase between the current and voltage sinusoids can then be calculated. The impedance can then be found by combining the phase difference with the ratio of the amplitudes of the current and voltage. This process is repeated over the frequency range defined by the user, producing an impedance spectrum (see chapter 1).

The benefit of this approach is that it allows the study of how a *three* dimensional physical microstructure affects the electrical microstructure. This is unlike previous studies which considered only two dimensions[4] allowing the electrical microstructure to be studied in full 3D at any time step – which is particularly difficult (and expensive) to do experimentally. The geometry of the modelled microstructure is limited only by what can be drawn (with a computer aided design package) and whether that geometry can be sub-divided into a mesh. Then, by assigning intrinsic physical properties (conductivity and permittivity) to distinct microstructural regions (individual grains and boundaries), a rigorous representation of 3D microstructures is produced.

3.1.2. Work flow for the finite element simulation

Our approach for setting up a simulation is first to draw a representative 3D model of the desired microstructure. Voronoi tessellation is used to automate the generation of polycrystalline ceramic microstructures (detailed in the next section). An overview of the approach used to generate models in this project is

shown in fig. 2. Firstly a wire frame of the desired microstructure is drawn creating distinct volume regions and meshed using the open source software Gmsh[5]. A meshed volume is then attached to the top of the model to form the reference layer. Next, material properties are assigned to individual regions depending on what parts of the microstructure the elements are describing. Finally boundary conditions are assigned to nodes on the outer surface of the model.

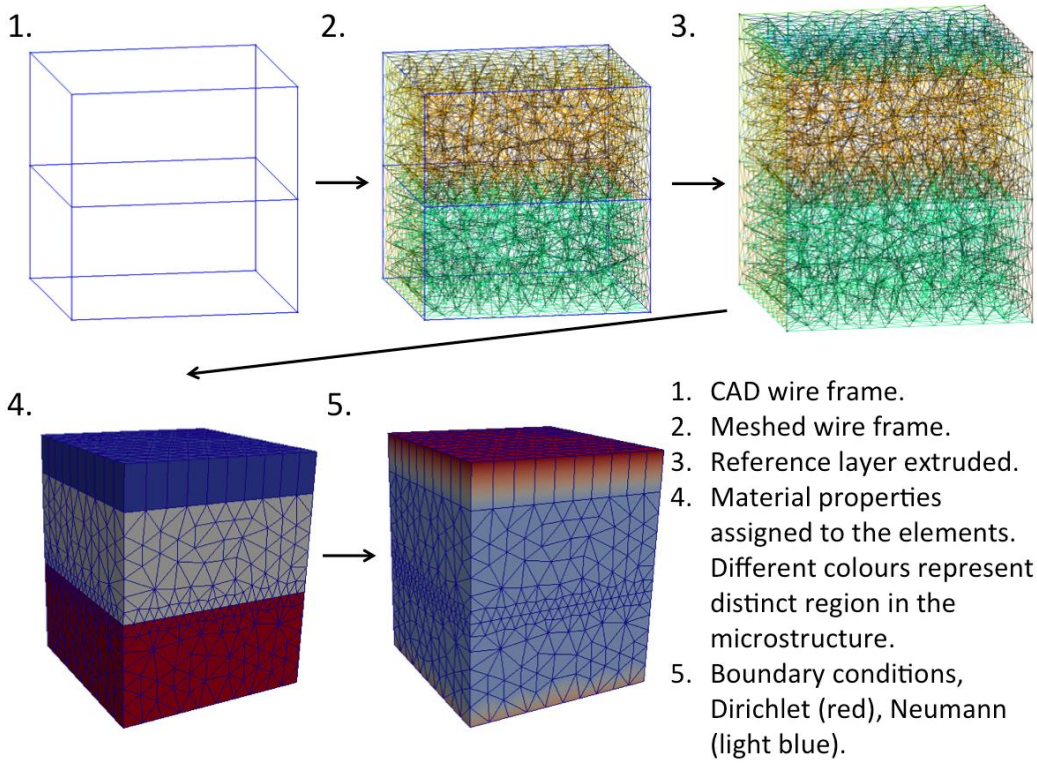

Fig. 2. *The process for making a finite element model of a bi-layer from wire frame to meshed volume with boundary conditions.*

Once the model is set up, the finite element code can be used to solve for the impedance response of the model over a frequency range defined by the user. In this study models have been constructed typically with over one million elements. It is possible to run these simulations on a desktop computer. To acquire a large volume of results, however, access to high power-computing resources is advisable. Calculating the real and imaginary components of the impedance at each frequency produces the complex impedance spectrum. Typically, these spectra are plotted using specialist software such as Zview[6] that allows data to be plotted in any representation of the impedance and offers equivalent circuit fitting tools. Should it be desired, the electrical microstructure (current density, electric field or electric potential) can also be visualised at a chosen frequency and time step. Typically, this involves re-running the simulation at specific frequencies that coincide with points of interest on the impedance spectra. For a model with a high-resolution mesh, the corresponding electrical microstructure plots can require over 1GB of storage each so data storage limits must be taken into consideration.

3.2. Microstructure Model Generation

3.2.1. Voronoi tessellation

To produce complex granular models that represent polycrystalline ceramics efficiently and automatically, this project has made extensive use of Voronoi Tessellation[7]. This can be used to produce a cellular geometry by bisecting space around points (sometimes referred to as a Voronoi diagram). For ease of visualisation a 2D example is given in fig. 3. Firstly, several points are defined (fig. 3A). A Delaunay triangulation is performed on the points connecting all the nearest neighbours without crossing any lines[8] (see fig. 3B). The mid point on each Delaunay triangulation line is found (in green, see fig. 3C). Finally, the midpoints of the Delaunay lines are bisected perpendicularly (see fig. 3D). The bisecting lines terminate when they meet each other or the boundary of the Voronoi diagram. This can be extended to 3D systems (see fig. 4).

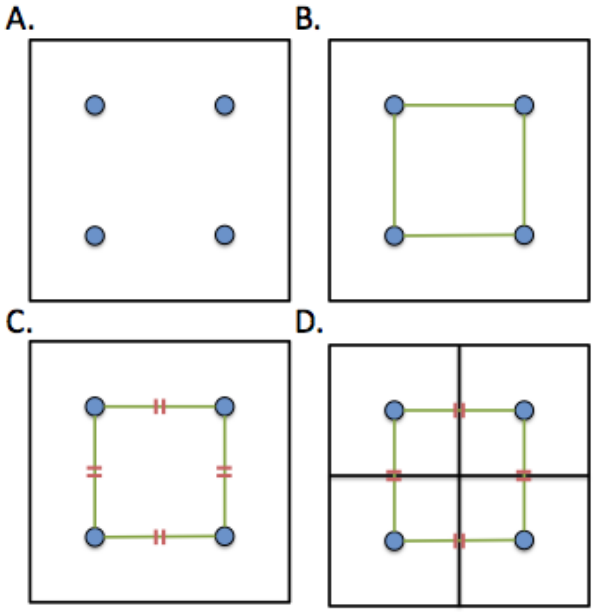

Fig. 3. (A) *How Voronoi tessellation creates a cellular structure from a set of points in a Voronoi diagram. (B) Delaunay triangulation of points. (C) Finding midpoints and (D) bisecting midpoints.*

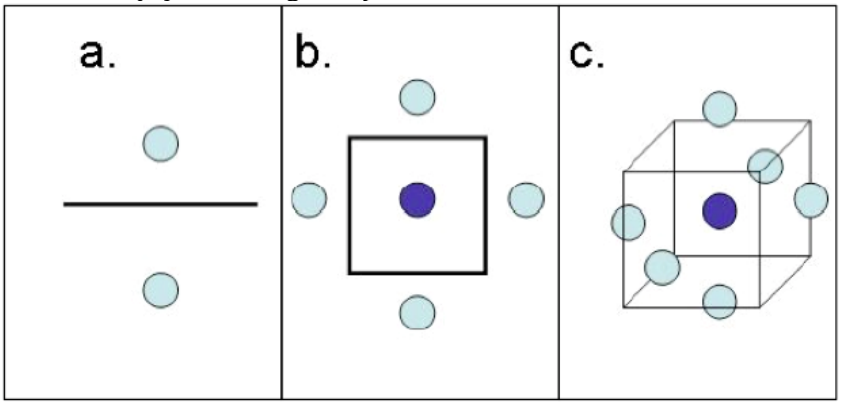

Fig. 4. *Progressively higher dimensional objects produced using Voronoi tessellation: (a) line, (b) square and (c) cube.*

There are many methods for constructing Voronoi diagrams with different algorithms for the Delaunay triangulation and additional features. In this work the open source implementation Voro++[9] has been used. Voro++ allows weighting factors to be included for individual cells. A larger weight assigned to a given point will generate a larger cell around it. This allows greater control over size distribution. It can also provide statistics such as the volume and areas of individual faces for each cell. Voro++ also provides accurate grain size distributions and connectivity information.

3.2.2. Using voronoi tessellation to build granular models

Many groups have used Voronoi tessellation to produce cellular or granular systems in 2 and 3D for a wide range of applications[10]. Changing how the points used for Voronoi tessellation are distributed greatly alters the shapes that can be produced. Regular lattices of points produce regular tessellating shapes (see fig. 5A and B). Dispersing the points randomly will produce a collection of random space-filling volumes (see fig. 5C).

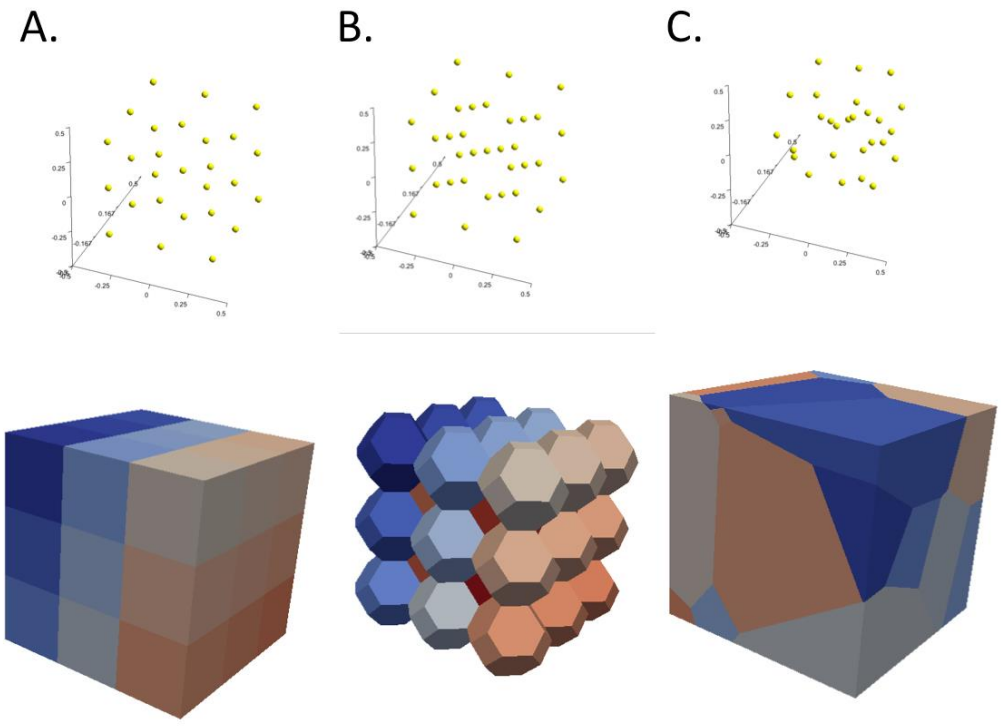

Fig. 5. *How different distributions of Voronoi points affect the shape of the cells produced. (A) A cubic lattice produces tessellating cubes. (B) A body centred cubic lattice produces tessellating truncated octahedra and (C) randomly placed points produce random space filling cells. The colours highlight each individual grain.*

A microstructural package has been developed in-house to produce granular microstructures based upon all three of the morphologies shown above. This package also allows the user to add a random disturbance to the Voronoi point location allowing randomised shapes based on the cubic or tessellating truncated

octahedra seen in figure 5 to be modified to more realistic structures as shown in fig. 6.

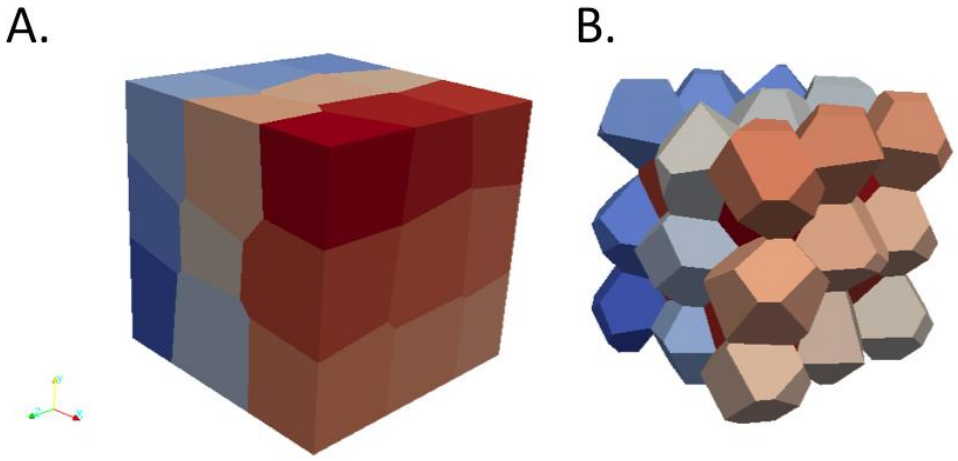

Fig. 6. (A) *Cubic volumes created with disturbed Voronoi points. (B) The same approach applied to truncated octahedra. The colours highlight each individual grain.*

Each Voronoi cell is considered to be an individual ceramic grain. Additional microstructural features can be generated from the initial model. For example, three distinct microstructural regions can represent core-shell microstructures: a core, a surrounding shell and a thin grain boundary encapsulating the whole structure. To generate this, first the overall grain shape is produced (see fig. 7A). Using the Voronoi point that generated the volume as the centroid of the grain, a grain boundary can be formed by shrinking the surface of the Voronoi cell towards its centre by a pre-determined value (see fig. 7B). The volume between the initial geometry and the shrunken one can then be defined as the grain boundary. This process can then repeated, shrinking the newest geometry closer to its centroid leaving a thicker volume between the grain boundary and itself (see fig. 7C). This region can then be attributed as a shell (doped) material. The remaining innermost volume is the grain core. This process can be used to construct layered particles of regular and irregular shape (see Fig. 7E).

Each microstructural region can have its own mesh size, allowing for variable levels of detail. This can be useful when dealing with large grain sizes. There are large regions of bulk ceramic that can be adequately represented by a coarse mesh. Microstructural features that can greatly distort the electrical microstructure (such as pore and interface roughness) require a finer mesh. Representing very thin features can also be an issue. Typically the models are meshed with tetrahedra. However, in thin regions, a large number of (very small) tetrahedra are required to fill space. This leads to a finer mesh than would be required for the calculations to converge, resulting in a longer simulation time with diminishing returns on accuracy. To address this issue, the thin regions are meshed with prism elements (see fig. 7F). These elements can fill thin spaces much more efficiently.

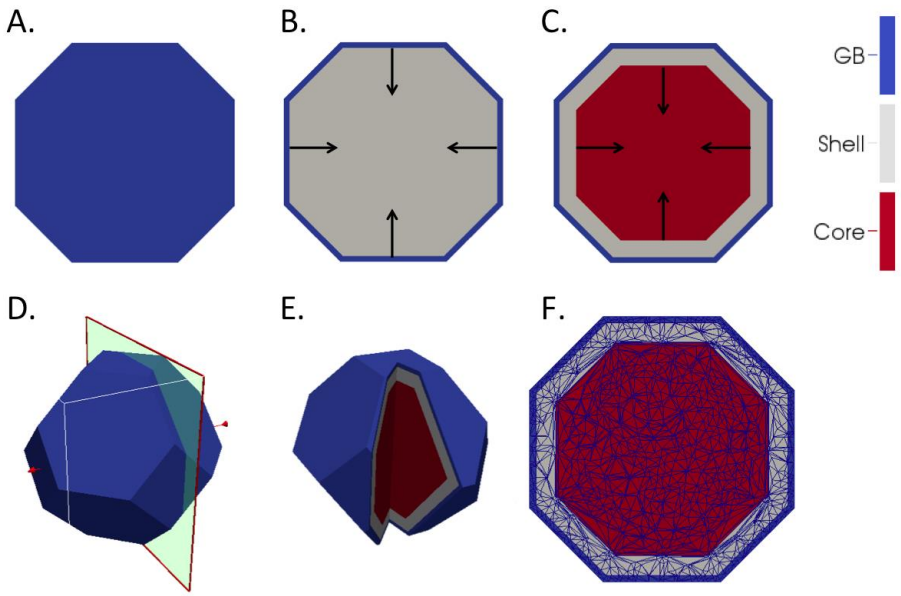

Fig. 7. *Overview of the microstructure generation of layered structures.* (*A*) *The initial grain shape.* (*B*) *The grain boundary is formed by shrinking a copy of the initial structure.* (*C*) *Another shrinking forms the shell and core volumes. (D) The plane marks the cross sections of a 3D model corresponding to (A-C).* (*E) The resulting 3D layered structure with a segment removed.* (*F*) *A cross section of the mesh where the outer (blue) layer has been meshed with prism elements, the grey and red regions are meshed with tetrahedra.*

3.3. Stream Tracing

3.3.1. Visualising vector fields with stream tracing

One of the key advantages of using FEM to simulate impedance spectroscopy is the ability to study the electrical microstructure in full 3D. This requires the analysis of a 3D data set. Although this is possible, it is quite complex to extract information, to reduce the complexity we can visualise a 2D slice of the electrical microstructure. This allows slices of the microstructure to be compared qualitatively with one another. Fig. 14A and B shows an example of an electrical microstructure of a nested cube system at low and high frequency. A quantitative analysis can be performed for a line scan of a 2D slice (see fig 14C and 14D) giving a direct comparison between the two electrical microstructures.

As this is a 2D slice it may miss important details above and below the plane visualised. One possible improvement is to take many slices through the electrical microstructure, with a fixed separation. This can then show how the data varies with depth (see fig. 15A). An additional approach is to section the data orthogonally (see fig. 15B). This approach depends on the data being symmetrical.

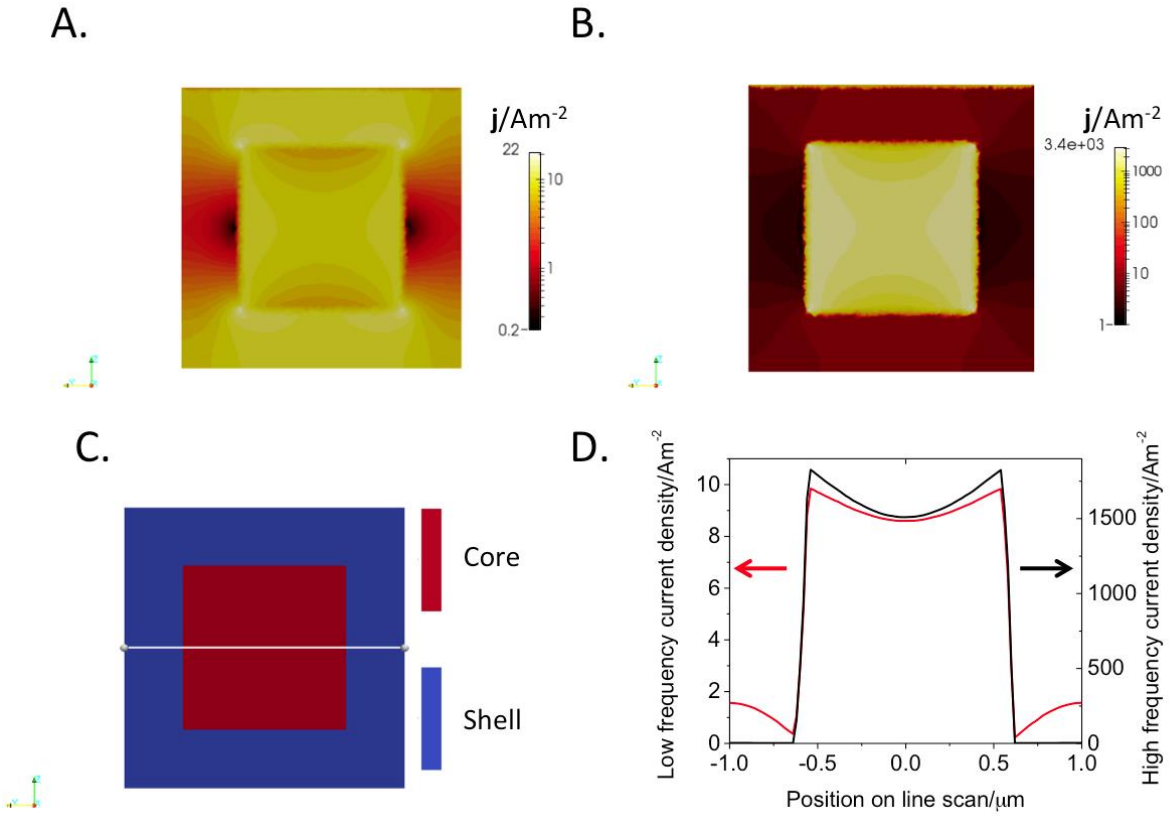

Fig. 14. *Analysis of a 2D slice of a nested cube microstructure.* (A) *Current density plot at low frequency.* (B) *Current density plot at high frequency.* (C) *Position of line scan.* (D) *Current density* ***(j)*** *plotted against position on the line scan for both frequencies*

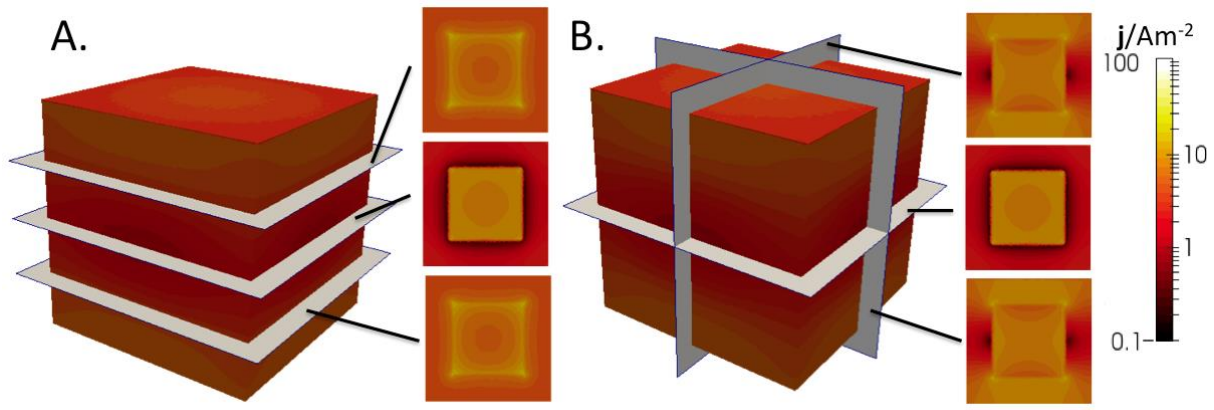

Fig. 15. *Different approaches for analysing sectioned 3D data. A current density plot of a nested cube microstructure is used for demonstration. (A) Serial sectioning with indicated cross sections. (B) Orthogonal sectioning with indicated sections for the x, y and z planes.*

In this work the 3D data are either the current density or the electric field as a function of position in a microstructure. There are strong analogies with computational fluid dynamics (CFD) simulations, particularly for the current density. The current density is a vector field describing how current flows through

a microstructure. For CFD, the corresponding vector field is the flow velocity. A popular way of visualising a velocity field is to use stream traces, also referred to as streamlines[12]. The general principle for streamlines is to place a massless particle in a velocity vector field and track its position as it moves through the field (see fig. 16). The trajectory is calculated by finding the resultant vector on the particle and integrating the product of the resultant vector and the change in time[13]. Plotting the trajectories of the streamlines enables interesting features such as stagnation points to be seen.

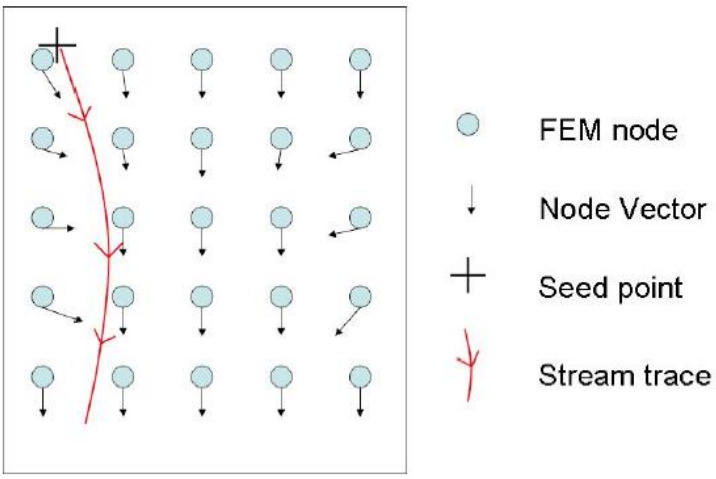

Fig. 16. *2D schematic of how a stream trace is produced for a vector field calculated for a FEM mesh.*

3.3.2. Distributions of conduction pathway lengths

In this work stream traces have been employed for data analysis as well as just for visualisation. Visualisation is useful as *three-dimensional* animations of the current pathways can be made by rotating the model. However, it is important to be able to represent data in a manner that retains meaning when presented in 2D media (e.g. a journal page). A method for gaining quantitative data from vector fields has therefore been developed. Consider a basic FEM simulation of a cube of material of length *d* with homogenous conductivity and permittivity. Applying the usual boundary conditions (see fig. 17A), current will flow linearly from the maximum potential (top surface) to the minimum potential (bottom surface), see fig. 17B. All the pathways through the cube have a length equal to *d*. Obviously this leads to the mean path length being *d* and a zero standard deviation.

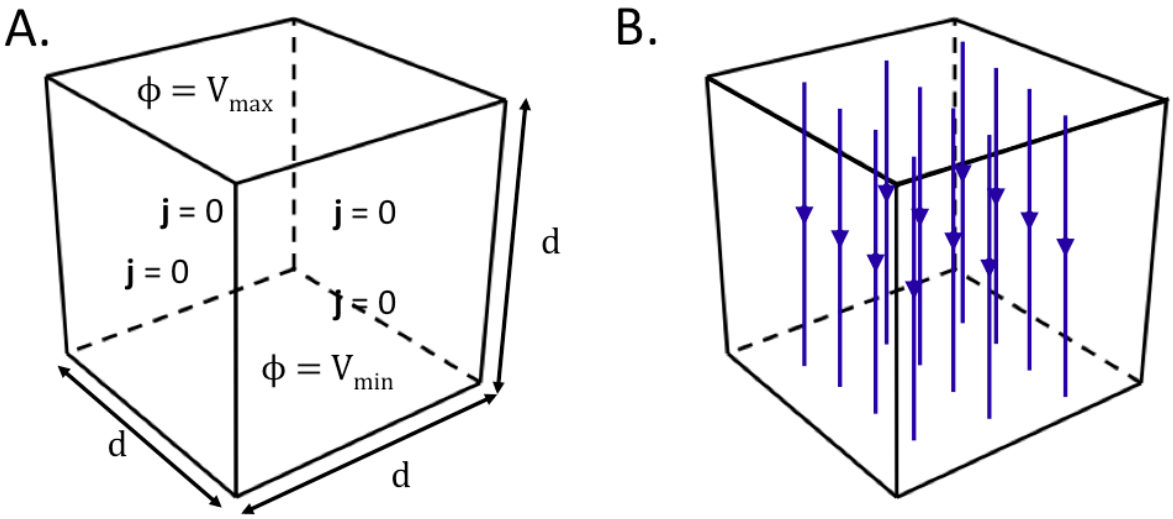

Fig. 17. *Schematic of stream trace of current density of a homogenous cube.* (*A*) *The potential is applied to the top and bottom. (B) Current flows linearly through from the top to the bottom surface.*

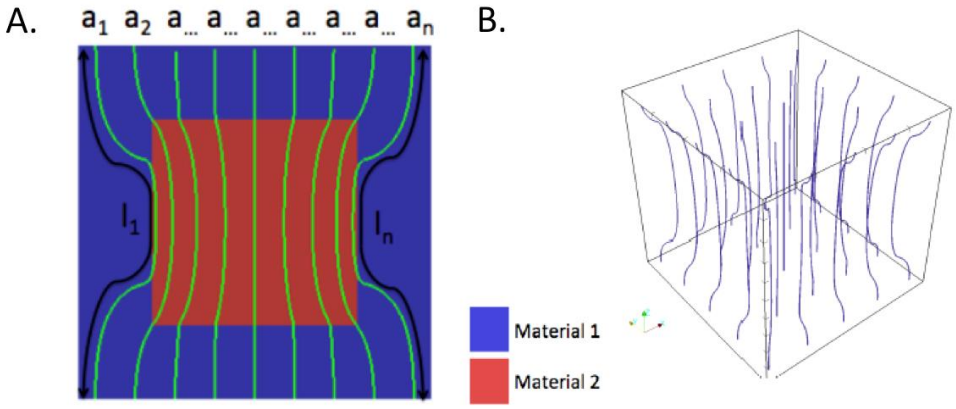

Fig. 18. (*A*) *Cross section of a nested cube model with overlaid conduction pathways. (*B*) A 3D schematic of how conduction pathways curve through the model.*

Let us now consider the case where there are two material regions in the cube and that these regions possess different material properties. In fig. 18A, two materials are present in nested cubes. The material of the inner cube (red) is more conductive than the outer region (blue). This difference in conductivity will lead to preferential pathways through the microstructure, resulting in curvature of the conduction pathways (see fig. 18B). This increases the conduction path lengths through the microstructure. Statistical analysis of the distribution of conduction path lengths will give a quantitative measure of the degree of curvature in the current flow.

In this work, Paraview software[11] has been used to generate and visualise stream traces. To perform a stream trace of vector data in Paraview the user must first define a source. This is a single point or a collection of points that act as the initial positions for the massless tracer particles. Our source is defined as a plane

divided into a regularly spaced grid. For consistency, the grid is always placed 20 nm below the top surface of the model (i.e. the one at maximum potential). The slight displacement is necessary because if the starting position of the stream trace is exactly on the surface, the stream trace algorithm defines the initial positions to be out of the bounds of the vector field and fails to start. Once Paraview has calculated the stream trace of the vector field, the positions of the tracer particles can be extracted for all time steps. We then process this data to find the length of each stream and perform statistical analysis upon the many tracer particle trajectories. A practical problem in Paraview is that the stream traces may end prematurely due to errors in the integration step. This can lead to conduction path lengths that are lower than the distance between the known potential surfaces, analogous to electrode separation. These path lengths are considered unphysical. To prevent the short lengths from skewing the statistics, the measurement program ignores any path lengths that are smaller than the minimum electrode separation.

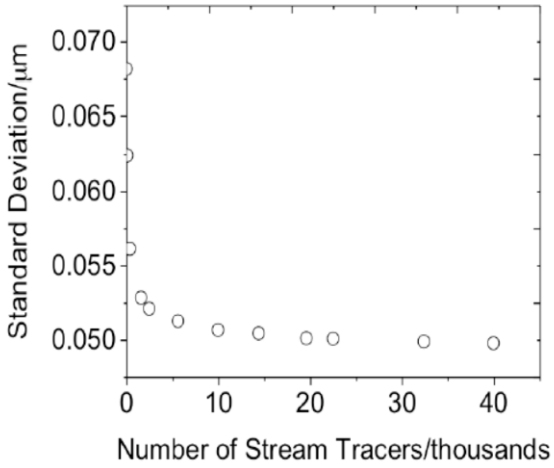

Fig. 19. *Convergence of the distribution of conduction pathway lengths for an arbitrary microstructure with non-linear current flow.*

To determine how many stream traces are required and hence the source plane resolution needed, a convergence study was performed. As fig. 19 shows, as the number of stream traces increases, the statistics of the distribution of conduction paths lengths converge. For more complex microstructure models, the number of stream traces required is likely to increase, however our results show there is a characteristic distribution for each microstructure. For the case shown in fig. 19, 20,000 stream traces provided a good compromise between convergence and simulation time.

3.4. References

1. J. S. Dean, J. H. Harding, and D. C. Sinclair, "Simulation of Impedance Spectra for a Full Three- Dimensional Ceramic Microstructure Using a Finite Element Model," *Journal of the American Ceramic Society,* 97[3] 885-91 (2014).

2. J. C. Maxwell, "A Treatise on Electricity and Magnetism." Cambridge University Press, (2010).

3. C. P. Anastasis, "Introduction to the Finite Element Method in Electromagnetics," *Synthesis Lectures on Computational Electromagnetics,* 1[1] 1-126 (2006).

4. J. Fleig, "The grain boundary impedance of random microstructures: numerical simulations and implications for the analysis of experimental data," *Solid State Ionics,* 150[1-2] 181-93 (2002).

5. C. Geuzaine and J. F. Remacle, "Gmsh: A 3-D finite element mesh generator with built-in pre- and post-processing facilities," *International Journal for Numerical Methods in Engineering,* 79[11] 1309-31 (2009).

6. S. Associates, "http://www.scribner.com/software/general electrochemistry/68-general-electrochemistr/376-zview-for-windows." in, Vol. 2016.

7. M. Tanemura, T. Ogawa, and N. Ogita, "A New Algorithm for 3-Dimensional Voronoi Tessellation," *Journal of Computational Physics,* 51[2] 191-207 (1983).

8. D. T. Lee and B. J. Schachter, "Two algorithms for constructing a Delaunay triangulation," *International Journal of Computer & Information Sciences,* 9[3] 219-42 (1980).

9. C. H. Rycroft, "VORO plus plus : A three-dimensional Voronoi cell library in C plus," *Chaos,* 19[4] (2009).

10. F. Aurenhammer, "Voronoi diagrams—a survey of a fundamental geometric data structure," *ACM Comput. Surv.,* 23[3] 345-405 (1991).

11. "36 - ParaView: An End-User Tool for Large-Data Visualization," 717 - 31 (2005).

12. R. S. Laramee, D. Weiskopf, A. Schneider, and H. Hauser, "Investigating swirl and tumble flow with a comparison of visualization techniques," *Ieee Visualization 2004, Proceeedings* 51-58 (2004).

13. D. N. Kenwright and G. D. Mallinson, "A 3-D streamline tracking algorithm using dual stream functions," pp. 62-68. in Proceedings of the 3rd conference on Visualization '92. IEEE Computer Society Press, Boston, Massachusetts, 1992.

Chapter 4: Core-Shell Microstructures

Core-shell microstructures are used in many applications. Tailoring the properties of the core and shell materials produces composites that make use of the best aspects of both components. In the context of this work, we are interested in the application of core-shell microstructures for use in multi-layer ceramic capacitors (MLCCs). Such microstructures provide temperature stability of capacitance in MLCCs, which is discussed in more detail in the literature review (chapter 2). Here we will focus on characterisation of core-shell microstructures and present simulations demonstrating how such structures affect the electrical microstructure and raise issues for characterisation using impedance spectroscopy.

4.1. Core-shell Characterisation Literature

An industry standard figure of merit for MLCCs is the temperature coefficient of capacitance (TCC). This is a profile of capacitance, normalised to the room temperature capacitance, as a function of temperature (see fig 1). The deviation from the room temperature capacitance value and the temperature range over which this is achieved defines the industrially-recognised specification for a capacitor[1]. A recent study found that the volume fraction of the core (or shell) regions in rare-earth-doped barium titanate MLCCs is important in controlling this behaviour. Jeon *et al*[2] used electron microscopy to characterise the volume fractions of core and shell regions. This was related to fixed frequency capacitance measurements to gauge the effects of physical microstructure on the dielectric properties. Although there are problems with extrapolating volume fractions from *two-dimensional* sections from microstructures[3], there is clearly a trend. Given that these microstructural effects are probably present in other electrically composite materials, a robust *three-dimensional* characterisation is desirable.

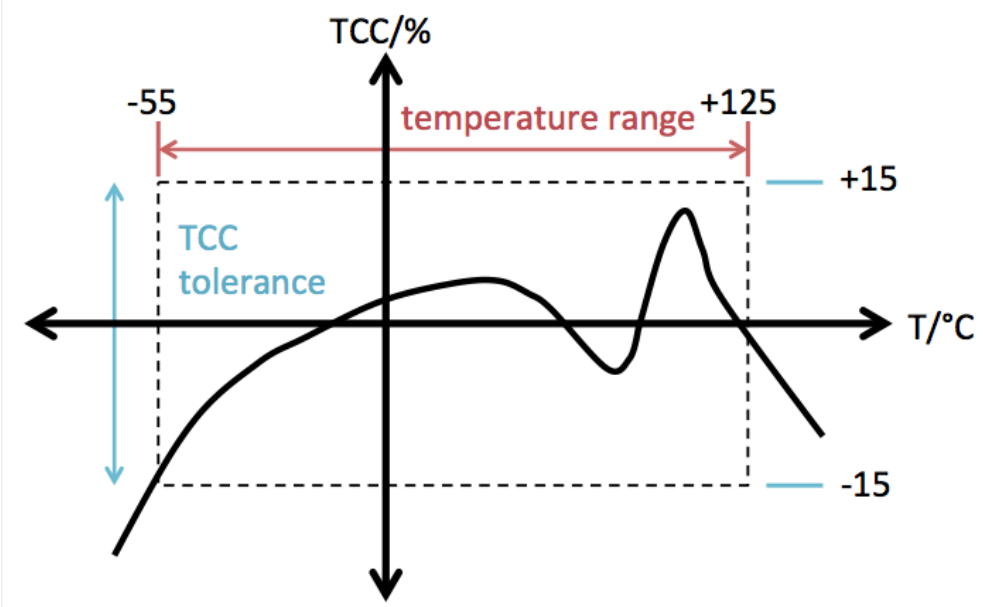

Fig. 1. *Schematic for a TCC profile that would fit the XR7 specification (±15% deviation from room temperature capacitance from -55 to 125 °C).*

Recent advances in tomography allow ceramic microstructures to be imaged in three dimensions[4]; however, these techniques are time-consuming and expensive. If only volume fractions are desired, a more accessible approach is to use capacitance ratios. The microstructural regions probed in this manner must have well-resolved impedance responses. If impedance arcs overlap it will be impossible to resolve volume ratios with any confidence. The magnitude of an impedance response can indicate what microstructural feature causes it. As capacitance is inversely proportional to thickness, a thinner feature such as a grain boundary often has a larger capacitance than the bulk. This assumes that the permittivity of the two features is similar. If a brick layer model[5] (approximation of a ceramic microstructure, see chapter 1) is assumed for the ceramic microstructure, the inverse capacitance ratio of the micro-structural components will be equal to the volume ratio (see fig. 2).

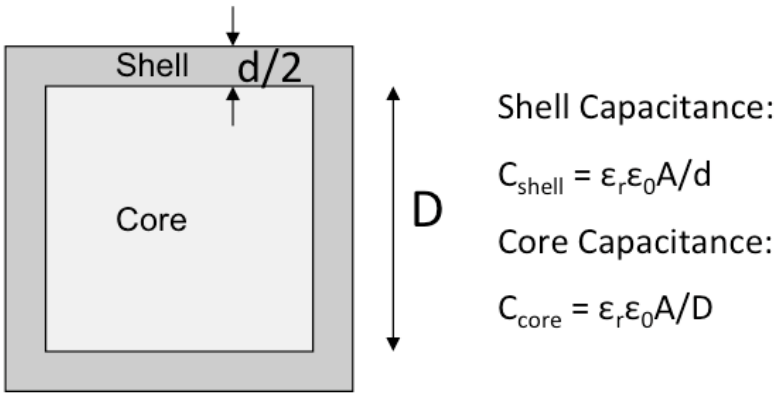

Fig. 2. *Brick layer model approximation of a core shell microstructure allowing the core-shell volume ratio to be inferred from the capacitance ratio assuming a fixed area (A).* ε_r *is the relative permittivity and* ε_0 *is the permittivity of free space.*

Bonanos and Lilley first used this method to characterise volume fractions of Suzuki phases in cadmium-doped sodium chloride[6]. They also found that the electrical response of the composite could be modelled using Maxwell's dispersed phase model[7], particularly at lower volume fractions of a Suzuki phase. To model the capacitance ratio measured, equations were derived by expressing Maxwell's dispersed phase model as the electrical response of a dual resistor- capacitor equivalent circuit. This gave an analytical solution for the high and low frequency resistances and capacitances for given values of conductivity and permittivity assigned to each phase. These equations are commonly referred to as the Bonanos-Lilley equations[6] in the literature.

Sinclair and West extended the technique of probing volume ratios using capacitance ratios to study the positive temperature coefficient of resistance (PTCR) of barium titanate ceramics that had a core-shell microstructure[8]. They estimated that the core made up 80% of the ceramic's volume. Using conductive atomic force microscopy to image the electrical microstructure of PTCR barium titanate ceramics provided good agreement with the estimate from capacitance data[9]. This method was also used by Costa *et al* to demonstrate the existence of a

core-shell micro-structure in calcium copper titanate and how processing conditions affected the volume ratio[10].

All three groups used the electric modulus (M*) impedance formalism to resolve their capacitance data. A useful feature of the electric modulus analysis is its sensitivity to small capacitances[11]. This method weights impedance data towards microstructural components that are thicker, such as bulk ceramic and secondary phases. Often these features can be missed when analysing impedance data as other formalisms are dominated by regions with higher capacitances and resistances[12]. Assuming well-separated time constants, a capacitance ratio can be obtained from an M* Nyquist plot (see fig. 3.), where the M* arc diameters are equal to inverse capacitances.

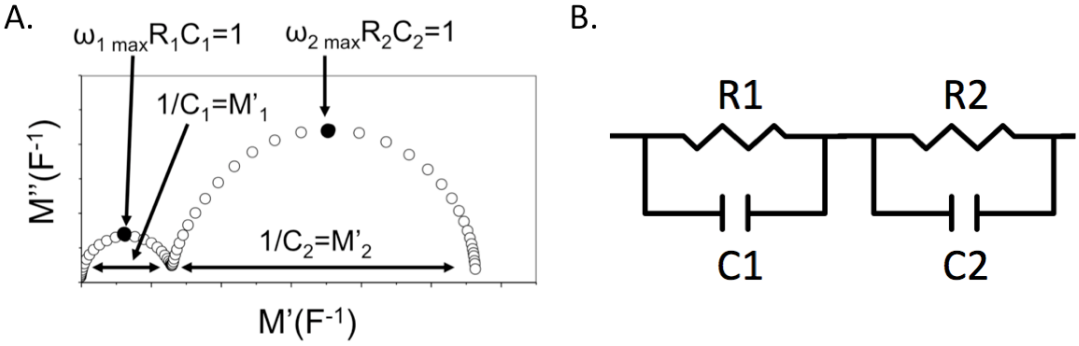

Fig. 3. *(A) Schematic of the M* Nyquist plot for a dual RC circuit (B) where R1 > R2 and C1 > C2. Adapted from[13].*

Previous finite element simulations by Dean *et al*[14] showed that a change in physical microstructure could alter the electrical microstructure. Changing the configuration of two material types from a layered to a nested cube structure (whilst keeping the volume fractions of the materials constant) gave different impedance spectra. This implies that there is an electrical contribution from the physical microstructure independent of material properties. The change in capacitance and resistance measured from the spectra meant that values for the permittivity and conductivity extracted using geometric factors deviated from the expected known values. Current density plots showed a heterogeneous current density for the regular nested cubes and randomised shapes using Voronoi tessellation compared to the layered model. This gave values of the full width at half maximum of the Debye peak for the imaginary electric modulus (M'') that exceeded the theoretical value of 1.14 decades on a logarithmic frequency scale. If practitioners want to gain information about microstructures from electrical measurements, they must check how electrical microstructures match or differ from physical microstructures for a given scenario.

Cubic grains have been used in numerous simulation studies[14, 15, 16] as they are simple geometries to produce and analyse. Although real grains are not regular cubes, the wide applicability of the brick layer model[5] to ceramics indicates that it is a good approximation for grains with thin, resistive grain boundaries. Here we investigate whether this approach can be transferred to other systems. Recent advances in ceramics processing have allowed cubic grains to be produced. Kato *et al* have used aqueous processing routes to produce nano-sized cubes of $BaTiO_3$[17, 18]. So far only permittivity data has been published, but advances in this field may

allow for direct comparison of experimental and simulated results for complete impedance data.

4.2. Core-Shell Volume Fractions from Capacitance Ratios

In this section we investigate when core-shell volume fractions can be extracted reliably from capacitance ratios†. This has often been attempted[8]. However, using finite element simulations allows us to test the assumptions behind the methods used. In our simulations, the true volume fraction is known, as we have generated artificial microstructures. Initially we compared two basic microstructures. Each had two distinct material regions. One region modelled a semi-conducting *core* material and the other a resistive *shell* material. Both had equal permittivity. The material properties are listed in Table 1. These material properties were chosen for ease of simulation and data analysis. This allows us to examine the effects of the physical microstructure in isolation without a mismatch in permittivity values affecting results. Both microstructures were contained in a 2 μm long cube.

Material	Conductivity/(μS cm^{-1})	Relative Permittivity
Core	100	100
Shell	0.1	100

Table 1. *Material properties used for core and shell regions in the simulations*.

The first microstructure is called the series layer model (SLM) and was first derived by Maxwell[7]. As its name implies, the SLM consists of homogenous layers of material stacked perpendicularly to the applied voltage (see fig. 4A and B). Series equivalent circuits can represent the SLM when each layer has a single value for permittivity and conductivity and the potential (Φ) is homogenous across the top and bottom surfaces so the current flows perpendicularly between these surfaces[19] (see fig. 5). This allows the SLM to be solved analytically using the basic equations for capacitance and resistance. In this study we have chosen to simulate the electrical response of the SLM with finite element modelling (FEM) as well as solve it analytically. Comparison of the analytical and FEM results for the SLM was used to validate the FEM code.

† Some work reported in this section has been published in the *Journal of the American Ceramics Society* by the author. All figures reproduced have been referenced in accordance to the creative commons attribution license.

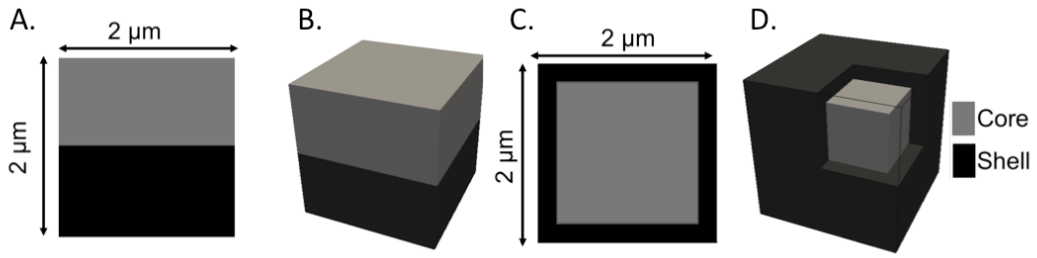

Fig. 4. *(A) Cross-section of the series layer model with (B) three dimensional representation. (C) Cross-section of the encased model with (D) three-dimensional representation with part of the shell removed to show the core.*

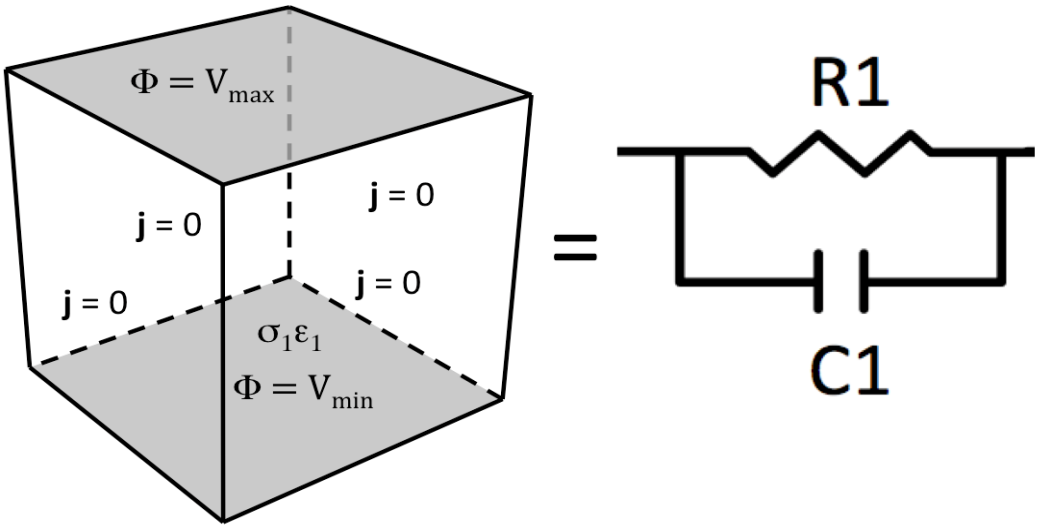

Fig. 5. *The conditions where a region in a microstructure can reduce exactly into an RC equivalent circuit assuming only one conductivity (σ_1) and permittivity (ε_1) is present. The potential (Φ) must be homogenous at the top and bottom surface and the current must flow only between the potential surfaces (current density (**j**) is zero at the free surfaces).*

Our second microstructure is a nested cube that approximates the core-shell microstructure and is referred to as the encased model. This consists of an inner cube of core material encased in an outer volume of shell material (see fig. 4C and D). Since there are now parallel pathways as well as the series pathway through the core (see fig. 6), the electrical response of the encased model must be solved numerically using FEM. The electrical response of the encased model can then be compared to the SLM.

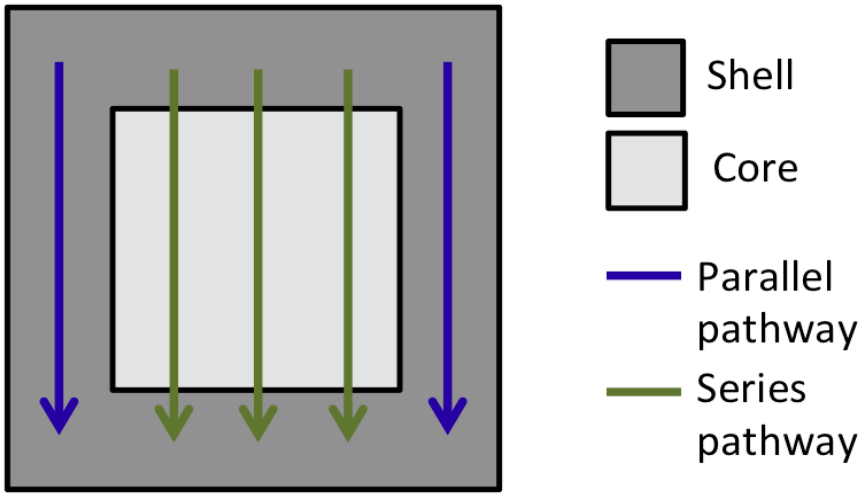

Fig. 6. *Schematic of parallel and series pathways available in the encased model.*

In order to find a suitable mesh size for both the SLM and encased model a convergence study was performed (for a definition of mesh size, see chapter 1). Ideally a convergence study would be performed for every change in model microstructure. This would take a very long time given the number of volume fractions simulated. To get a good estimate for convergence, we tested a model with equal core and shell volumes. For the SLM the mesh size was decreased and the capacitance ratio of core and shell material measured. This was compared with the analytical solution for the SLM. The magnitude of the difference between the analytical solution and the FEM results was expressed as a percentage of the analytical solution (see fig. 7). The error appears to be independent of the mesh size and is very small (less than ±0.12%). The random spread is a combination of rounding errors within the FEM code and that FEM method is an approximation to the true solution.

A different method was used to find a suitable mesh size for the encased model, as there is no analytical solution. Here an encased model with equal volumes of core and shell was simulated with decreasing mesh division. The arc diameters for both the high and low frequency M* arcs were extracted (see fig. 8) and convergence found. It was established that the high frequency arc diameters, associated with the core, converged faster than the lower frequency arc diameters, associated with the shell. Sufficient convergence was achieved for a 0.08 μm mesh.

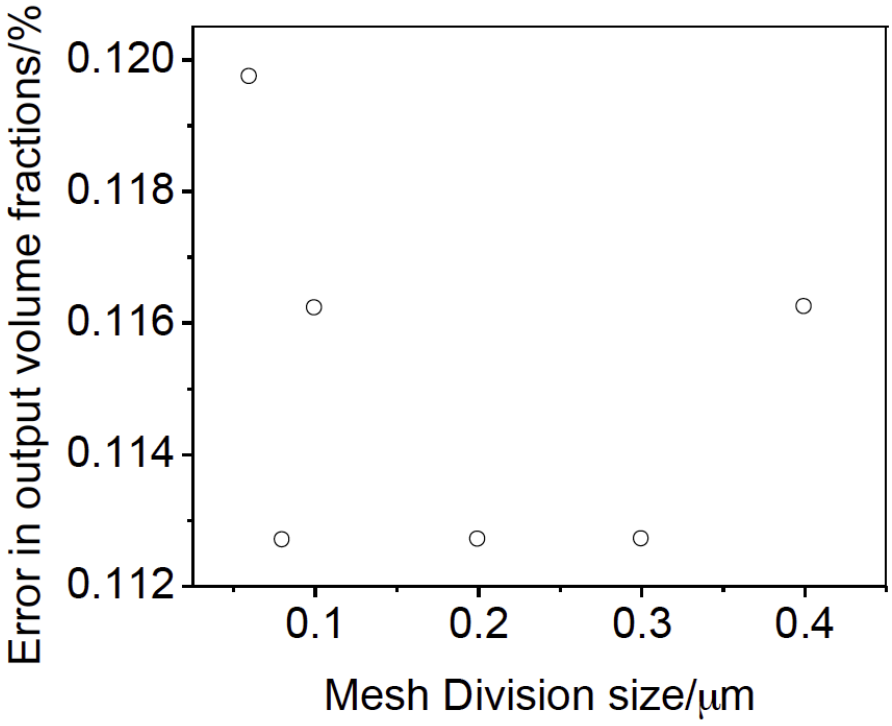

Fig. 7. *Graph of mesh division size against the error in the FEM simulation compared to the analytical solution for a SLM with equal volumes of core and shell regions.*

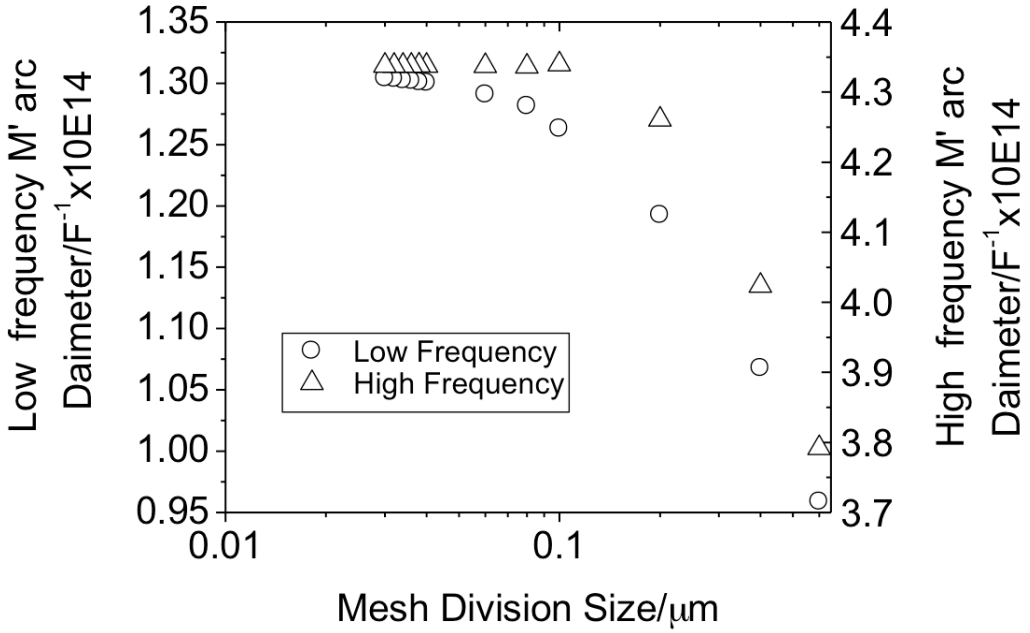

Fig. 8. *Convergence of high and low frequency electric modulus (M*) arc diameters for an encased model with equal volumes of core and shell as the mesh division size is decreased.*

As acceptable convergence for the SLM and encased model was achieved, the modulus spectra could now be compared. First, we consider the case where both microstructures have equal volumes of core and shell material. For the SLM we have two arcs of equal diameter (see fig. 9A). This implies an equal capacitance

for each layer and hence a core volume fraction (ϕ_{core}) of 0.5 is obtained. For the equivalent encased model the arc diameters are different (see fig. 9B). The high frequency arc is larger than the low frequency arc. Given that the time constant (τ)for the shell should be around 3 orders greater than that of the core and that τ is the inverse of the Debye frequency, it is reasonable to assign the low frequency arc to the shell and the high frequency arc to the core. This implies that the value of ϕ_{core} measured from the capacitance ratio is greater than 0.5, as the M* arc diameter is greater for the core than the shell.

To understand the discrepancy in volume fractions obtained from capacitance ratios between the SLM and encased model, the electrical microstructure must be examined. Current density plots were obtained at the highest applied voltage for a given frequency. This showed the largest current density in the region of the microstructure that should be associated with a given frequency. Current density plots at the indicated frequencies for the SLM (see fig. 9C) and the encased model (see fig. 9D) show how the electrical microstructure is dependent on the physical microstructure and frequency. The most important frequencies are the Debye points, the maxima of the imaginary M* component. For the SLM at the low frequency Debye point (fig. 9C i) the current density is greatest in the shell layer. Increasing frequency to the high frequency Debye point (fig. 9C iii), current density is concentrated in the core layer. For the SLM at all frequencies the current density is homogenous in each layer.

For the encased model, at the low frequency Debye point (fig. 9D iv) there is higher current density in the shell but only for the series component. At the high frequency Debye point (fig. 9D vi) the current density is concentrated relatively homogenously in the core. For the encased model this implies that there is only a partial response from the shell material but a full response from the core. Hence the volume fraction of the core material is over-estimated.

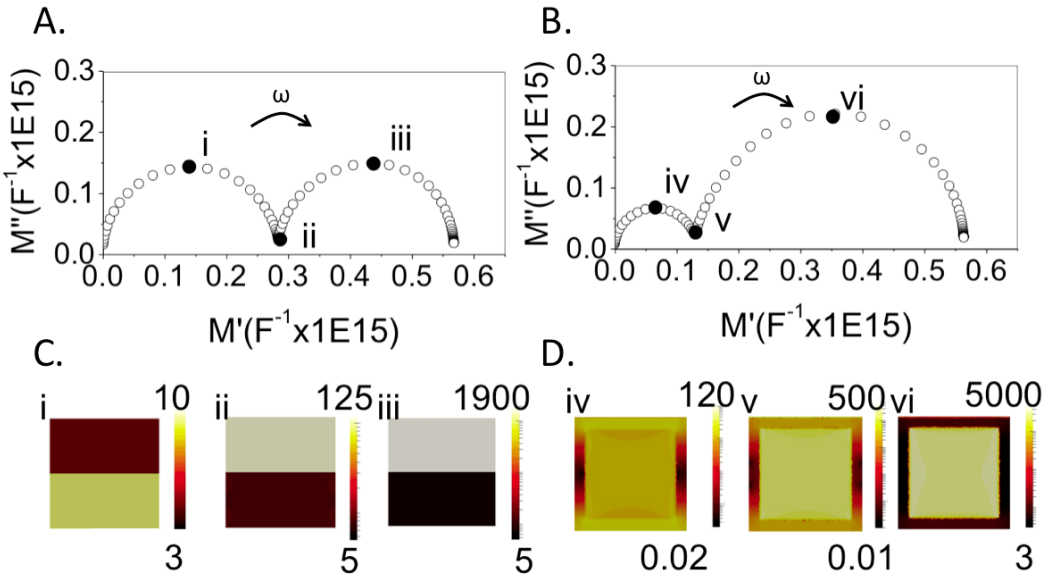

Fig. 9. *(A) Electric modulus Nyquist plot for the SLM, (B) electric modulus Nyquist plot for the encased model, (C) current density plots taken at the indicated points on the SLM M* plot, (D) current density plots taken at the indicated points on the encased M* plot. All current density plots have units Am^{-2}. Note for the electric modulus formalism, frequency increases away from the origin (opposite to impedance). Figure adapted from[13].*

The comparison of the SLM and encased model was repeated over a range of known core volume fractions. Extracting ϕ_{core} from capacitance ratios showed that the magnitude of the discrepancy between the SLM and encased model varied with the inputted ϕ_{core} (see fig. 10A). A reasonable fit of this behaviour is provided by the Bonanos-Lilley equations[6] using the same volume fraction, permittivity and conductivity values. Given the wide applicability of the effective medium theory that they are based on, this gives us confidence that these results are physically meaningful. If we consider the extracted value of ϕ_{core} as a percentage of the known value, it is found that the extracted value deviates the most at lower values of ϕ_{core} (see fig. 10B).

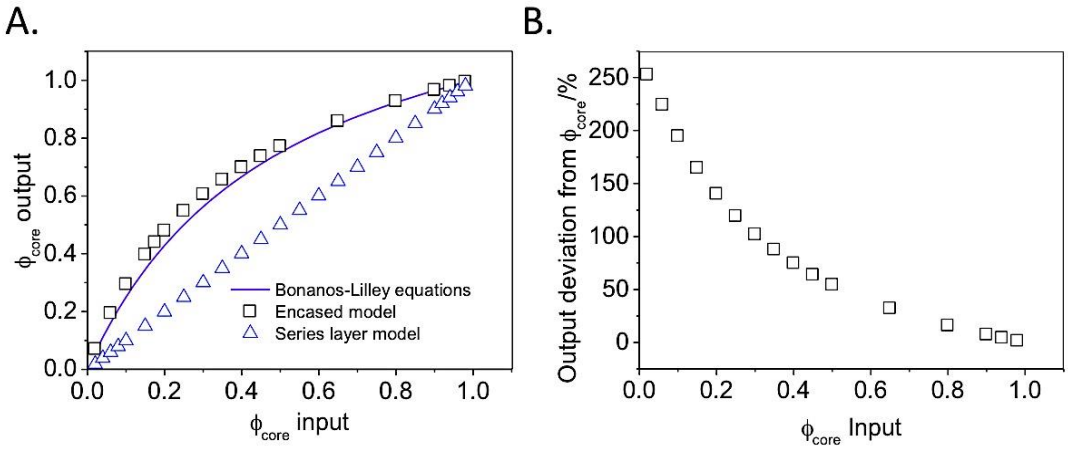

Fig. 10. *(A) ϕ_{core} values extracted from capacitance ratios of the simulated modulus spectra for the SLM and encased model against the known values of ϕ_{core}. A line for the Bonanos-Lilley equations is also plotted. (B) Extracted ϕ_{core} values as a percentage of the known ϕ_{core} values against the known ϕ_{core} values for the encased model. Figure adapted from[13].*

Another fit for the encased model's deviation from the behaviour of the SLM used an equivalent circuit derived from the electrical microstructure. We will refer to it as the series brick layer model (SBLM). From the evidence of the frequency-dependent current density distribution in the electrical microstructure of the encased model (see fig. 9), it can be seen that the low frequency impedance response is dominated by the series component of the shell material, whereas at high frequency the core region dominates. Taking the geometries of the core and series shell components and their respective conductivity and permittivity values, allows the resistance and capacitance for each microstructural component to be calculated (see fig. 11). Using the capacitance ratios predicted by this model, the volume ratios can be calculated, neglecting the capacitance contribution from the parallel components of the shell. The SBLM provided a better fit to the encased models capacitance ratio than the SLM but not as good as the Bonanos-Lilley equations (see fig. 12).

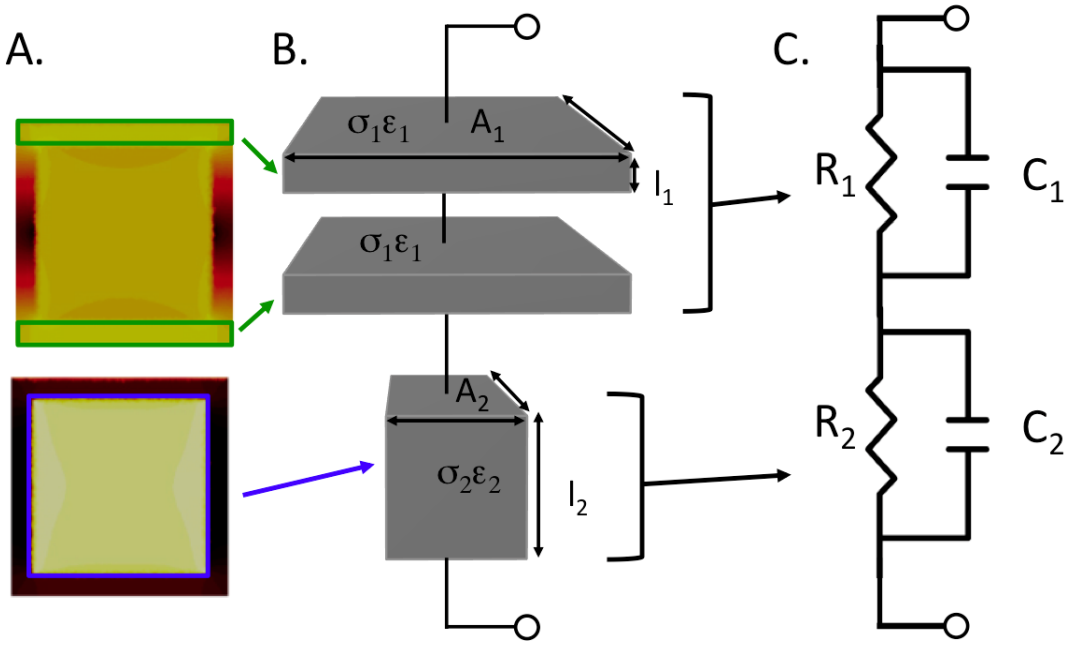

Fig. 11. *(A) Electrical microstructure of the encased model at low and high frequency (top and bottom, respectively). Plots are current density where lighter colour indicates a higher value. (B) Geometries of the series shell and core components (subscript 1 and 2, respectively) with their intrinsic properties. (C) Equivalent circuit derived from intrinsic properties of the microstructural components and their geometries.*

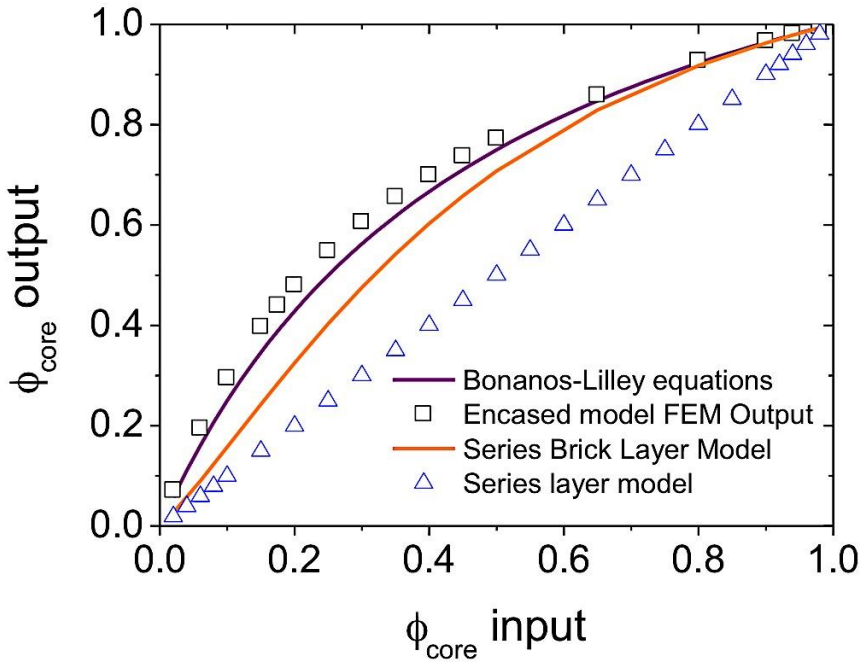

Fig. 12. ϕ_{core} *values extracted from capacitance ratios of the simulated modulus spectra for the SLM and encased model against the known values of* ϕ_{core}*. Lines for the Bonanos-Lilley equations and the SBLM are also plotted.*

A study of the difference in the ϕ_{core} values obtained from the encased model simulations and the SBLM revealed an interesting trend with the known values of ϕ_{core} (see fig. 13). The difference varied with ϕ_{core} with a peak at

ϕ_{core}~0.2. This trend proves to be significant in a more rigorous analysis of the electrical microstructure and is discussed at the end of this section.

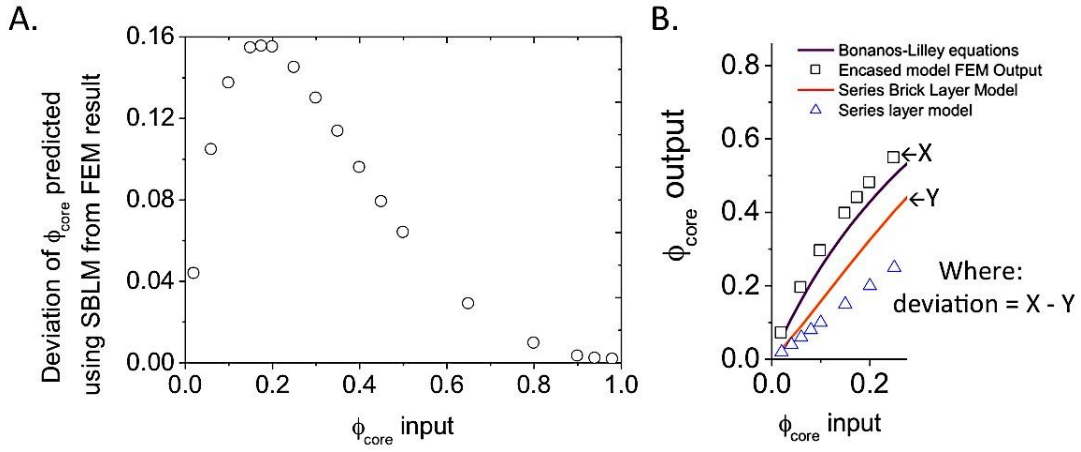

Fig 13. *(A) Encased model deviation from SBLM predicted* ϕ_{core} *against input* ϕ_{core} *(B) How this deviation is calculated.*

Further understanding was provided by extracting the resistance and capacitance values from the M* arc intercepts (as explained in fig. 3). Analysis of the SLM M* arcs gave time constants for the core and shell layers of 8.65 μs and 8.75 ms, respectively for all core volume fractions. This agreed well with the inputted values of permittivity and conductivity. For the encased model the shell response was also 8.75 ms for all values of ϕ_{core} but the core response increased as ϕ_{core} decreased (see fig. 14). This does not agree with the principle that time constants are geometry independent. The resistance and capacitance geometric factors should cancel[20]. The M* Nyquist plots in fig. 14 show that, as ϕ_{core} decreases, the core response merges with the shell response. The greatest uncertainty, obtained by measuring arc overlap, for the core arc was ±30%. This alone could not explain why the core time constant is nearly five times greater for the encased model than for the SLM.

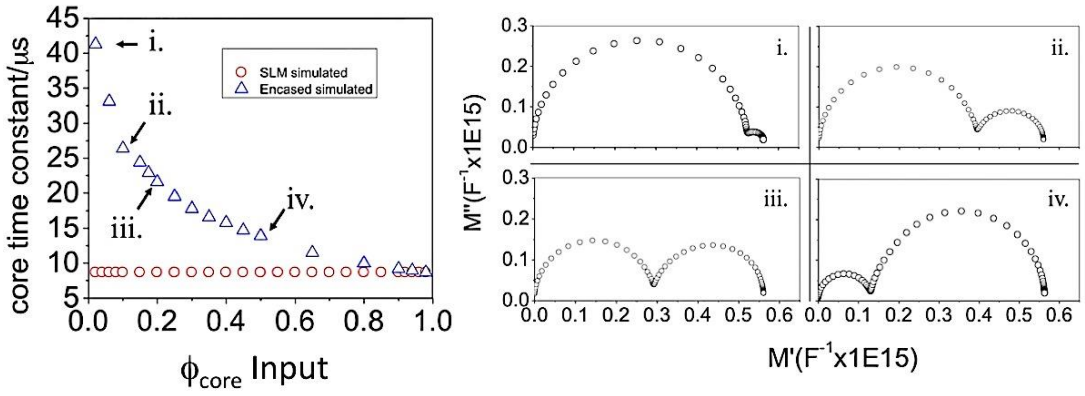

Fig. 14. *Plot of core material time constants extracted from simulated modulus plots for the SLM and encased model with M* Nyquist plots at indicated volume fractions. Figure adapted from ref. 13.*

In order to understand why the core time constant did not behave as expected, the extracted resistance and capacitance values were examined individually. Fig. 15 shows how these vary over all simulated volume fractions. The

core and shell resistances of the SLM (fig. 15 A and B, respectively) vary linearly with core volume fraction. All core and shell capacitances for both microstructures are inversely proportional to the core and shell volume fractions, respectively (see fig. 15 C and D). The behaviour of the encased model's shell and core resistances (fig. 15 A and B) is non-linear. There are also transitions in the encased core resistance as ϕ_{core} varies. The core resistance increases linearly as values of ϕ_{core} fall from near unity to 0.4, then gradually tapers off for ϕ_{core} values from 0.4 to 0.2, finally reducing rapidly as ϕ_{core} goes to zero. Clearly the conductive behaviour is likely to be responsible for the unusual encased core time constant values.

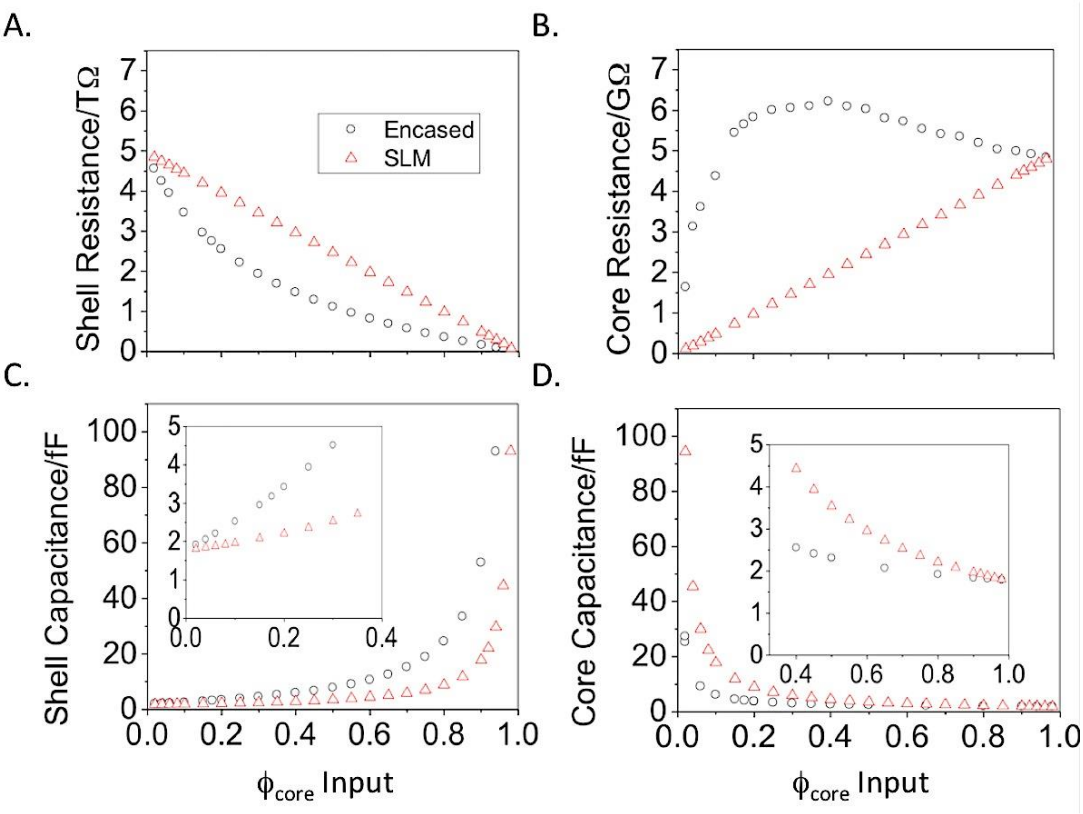

Fig. 15. *Values for (A) shell resistance, (B) core resistance, (C) shell capacitance and (D) core capacitance for the SLM and encased models extracted from M* Nyquist plots for a range of volume fractions. Figure adapted from ref 13.*

To probe the conductive behaviour of the encased model further, current density plots taken at high frequency to obtain the Debye response of the core region were calculated for a range of ϕ_{core} values (a selection is presented in fig. 16A). A stream trace analysis was used to display conduction pathways; this is overlaid in green. The conduction pathways become more curved as ϕ_{core} decreases resulting in increased heterogeneity in the current density. The full width at half maximum (FWHM) of the imaginary modulus (M'') Debye peaks also broadened as ϕ_{core} decreased (see fig. 16B). A 19 by 19 grid of stream tracers was used for quantitative analysis of the distribution of conduction path lengths (DCPL). The methodology used to extract the DCPL is described in greater detail in chapter 3. Later an improved version of this technique was developed, that allowed a much greater resolution of stream tracers within a practical calculation time. The DCPL gives a quantitative measure of the curvature of current flowing

through a model - the broader the distribution, the more non-linear the current flow. The DCPL increases as ϕ_{core} is reduced, roughly correlating with broadening of the M'' FWHM (see fig. 16C).

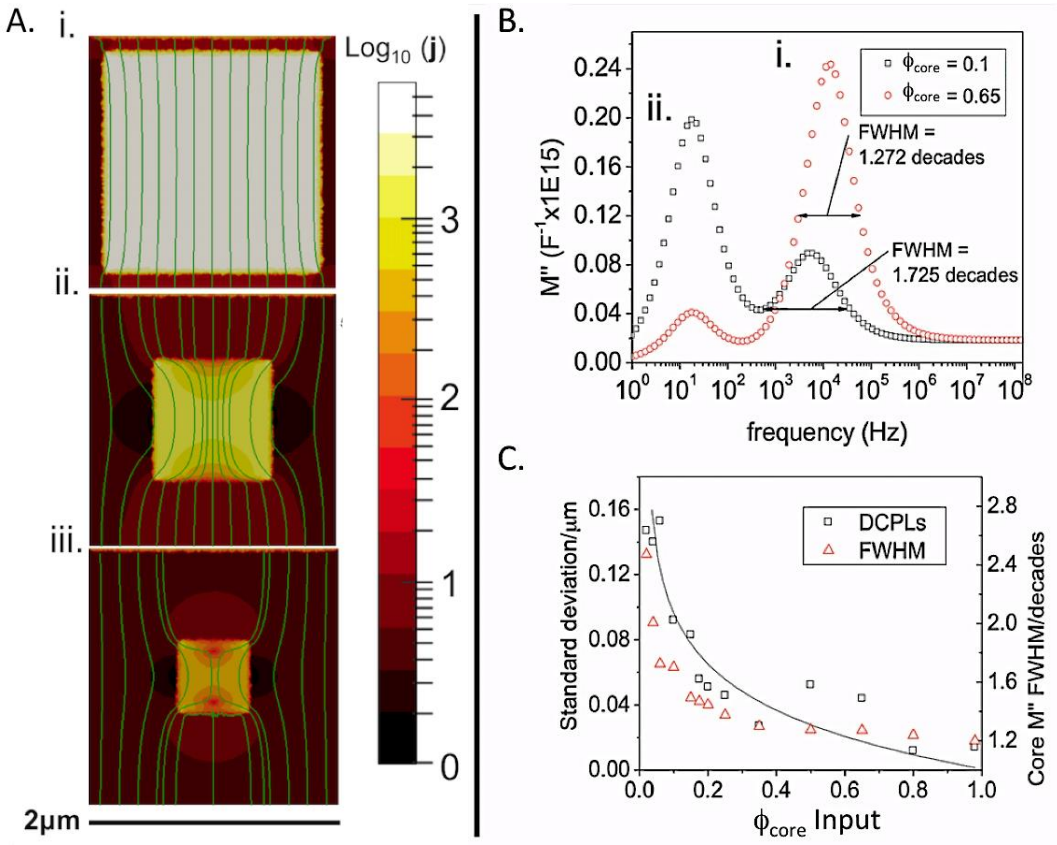

Fig. 16. *(A) Current density plots (**j** in Am^{-2}) for encased models of ϕ_{core} = 0.65, 0.10 and 0.02 (i, ii and iii, respectively) with overlaid stream traces highlighting conduction pathways. The initial positions for the stream tracers are evenly spaced for (i) and (ii). For (iii) the initial points are chosen to show the largest conduction pathways. (B) M'' spectroscopic plots for encased models with ϕ_{core} = 0.65 (i) and 0.10 (ii). (C) The standard deviation of the DCPL and FWHM of the M'' Debye peak as a function of ϕ_{core}. The solid black line is a guide to the eye for the DCPL. Figure adapted from ref 13.*

To understand the effect of decreasing core size on current flow linearity, the electric field present in the microstructures was examined. For the SLM, the electric field was homogenous in each layer just like the current density (see fig. 17 A). For the encased model, the electric field was relatively homogenous in the core region for larger values of ϕ_{core} (see fig. 17 B), however as ϕ_{core} decreased the electric field became more heterogeneous in the core region.

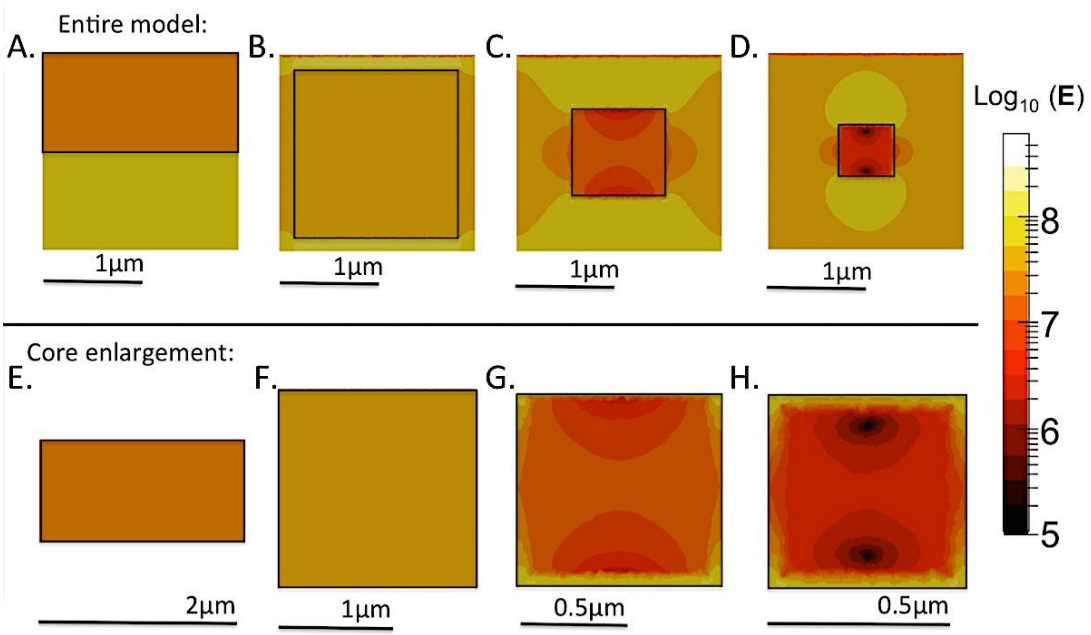

Fig. 17. *Electric field (**E** in Vm^{-1}) plots taken at the core materials high frequency Debye response for (A) the SLM with ϕ_{core} = 0.50 and (B-D) encased models with ϕ_{core} = 0.65, 0.10 and 0.02, respectively. (E-H) Core regions of A to D, surrounded by a black line but enlarged. Figure adapted from ref 13.*

The stream trace analysis of conduction pathways between electrode surfaces was also repeated for current density plots taken at the low frequency M'' Debye peak associated with the shell material. Statistical analysis found a peak in the low frequency DCPL at a ϕ_{core} value just below ~0.20 (see fig. 18). This peak coincided with the difference between ϕ_{core} values extracted from the encased models and those predicted by the series brick layer models (see fig. 13). Plotting the difference between the encased model and SBLM against the low frequency DCPL revealed a positive correlation (see fig. 19). There were outliers at the extremes of volume fraction and at ϕ_{core} = 0.10. The deviation at extreme volume fractions may be due to poor meshing solutions. For a high value of ϕ_{core} the shell region will be meshed with flattened tetrahedrons reducing the quality of the mesh, whereas for low values of ϕ_{core} the mesh elements are becoming comparable in volume to the core also reducing the mesh quality. Further investigation did not reveal the cause of the anomaly at
ϕ_{core} = 0.10.

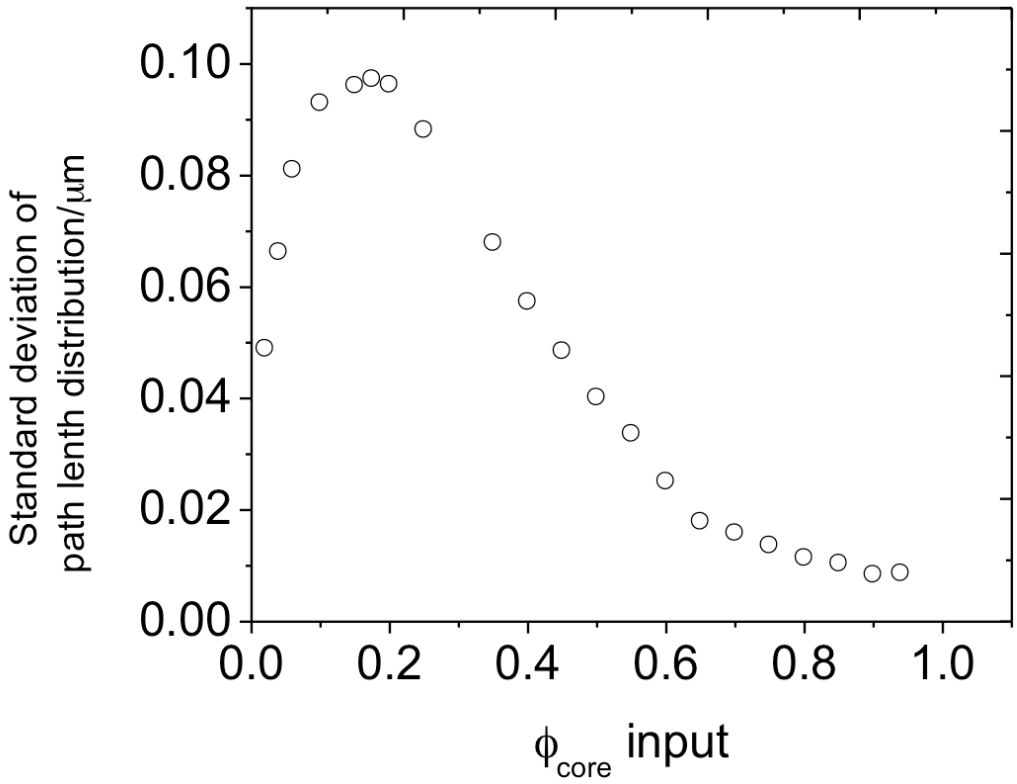

Fig. 18. *Standard deviation of conduction pathway length distribution for the low frequency current density plot of the encased model against* ϕ_{core}

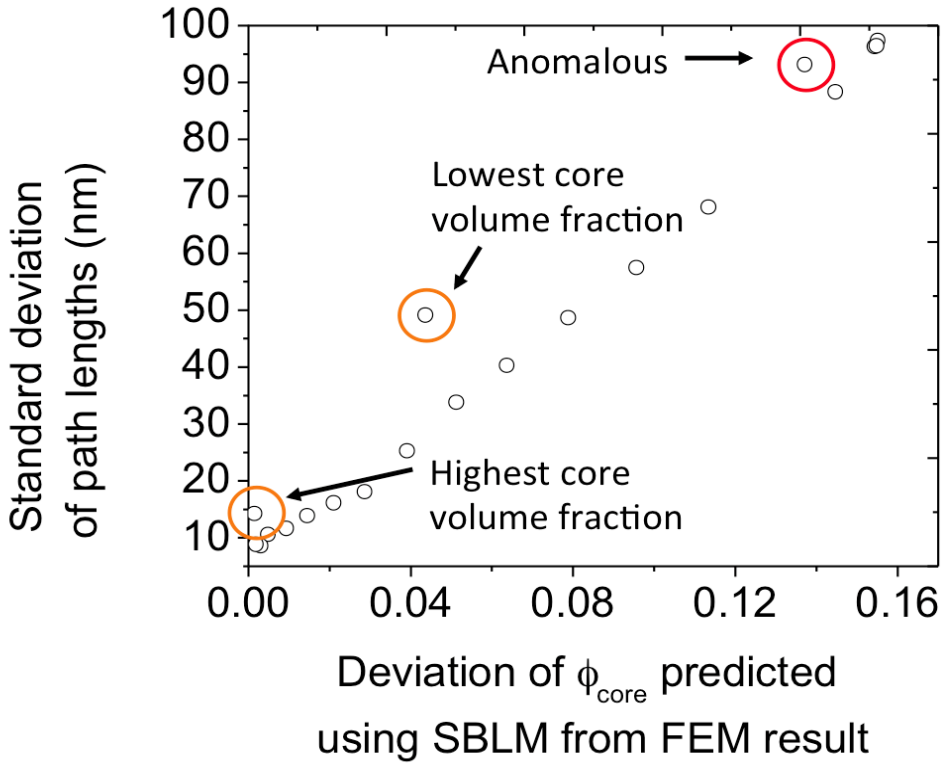

Fig. 19. *Standard deviation of path lengths plotted against the encased model's deviation from the SBLM. Note the circled outliers.*

4.3. Grain Shape

4.3.1. Truncated Octahedral Grains

Real ceramic grains are rarely cubic and have more complex and irregular shapes. In order to use a more faceted shape for the grains without introducing a grain size distribution, regular truncated octahedral grains were used. These were produced using Voronoi tessellation as described in chapter 3. In order to fit a truncated octahedra into the same two micron cube as the previous microstructures, nine grains were used. One is in the centre of the model and the other surrounds this at the corners of the cube (see fig. 20) producing a tessellated structure. The surface of the grains could be shrunk inwards to produce core and shell volumes using the same method as the encased model. This allowed us to repeat the previous study on estimating volume fractions from capacitance ratios for a different grain shape.

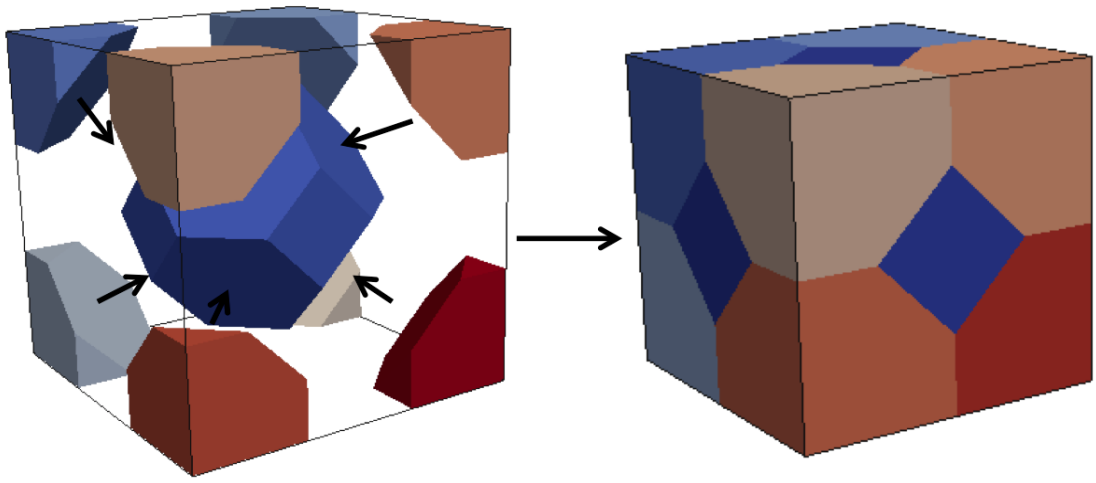

Fig. 20. *Arranging two truncated octahedral grains to tessellate in a cube.*

As before, a mesh convergence study was performed. The value of the high and low frequency M* arc diameters was measured as a function of mesh size (see fig. 21). It was found that a truncated octahedral model with equal volumes of core and shell required a finer mesh to reach convergence. Adequate convergence was achieved with a mesh consisting of ~770,000 nodes giving a mesh division size of 0.038 μm. The high frequency arc converges somewhat faster than the low frequency arc but this was not as obvious as for the encased model.

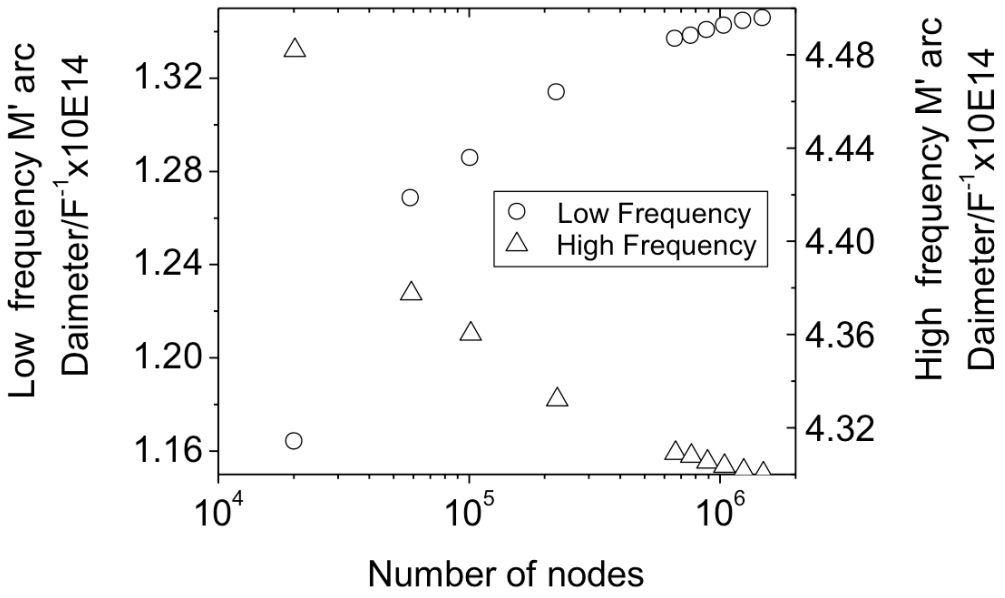

Fig. 21. *Convergence of high and low frequency modulus (M*) arc diameters for an encased model with equal core and shell volumes as mesh division size decreases.*

The impedance response of the truncated octahedral model was simulated over a range of ϕ_{core} values. Using M* Nyquist plots, the ratio of core to shell capacitances was found and ϕ_{core} estimated (see fig. 22). A similar trend to that of the encased model was observed; ϕ_{core} was over estimated compared to the known values. This over-estimate of ϕ_{core} fell between the values given by the Bonanos-Lilley equations and the values extracted for the encased model.

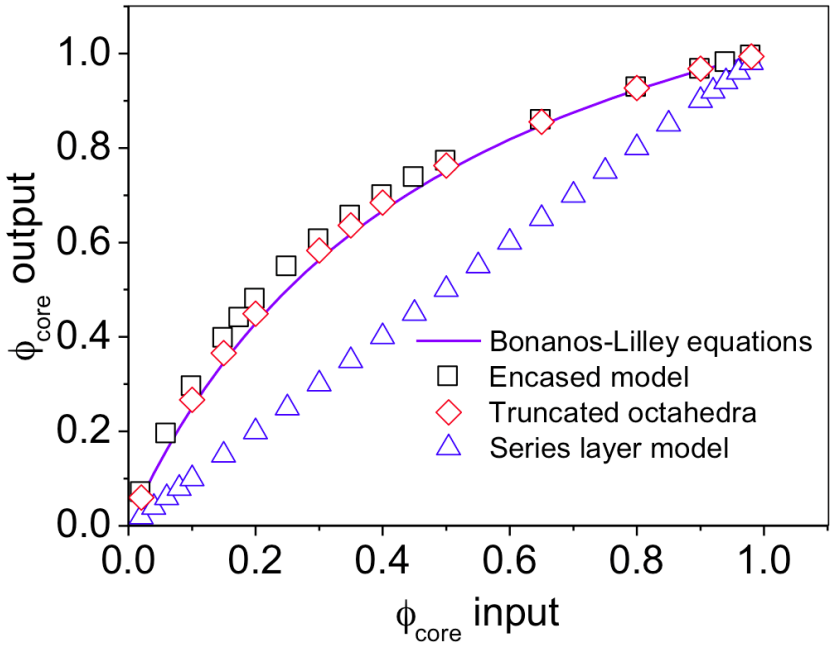

Fig. 22. *Comparison of ϕ_{core} extracted from capacitance values with the true value for the SLM, encased model and truncated octahedral model. The solid line is the Bonanos-Lilley equations for the same volume fractions, conductivity and permittivity values.*

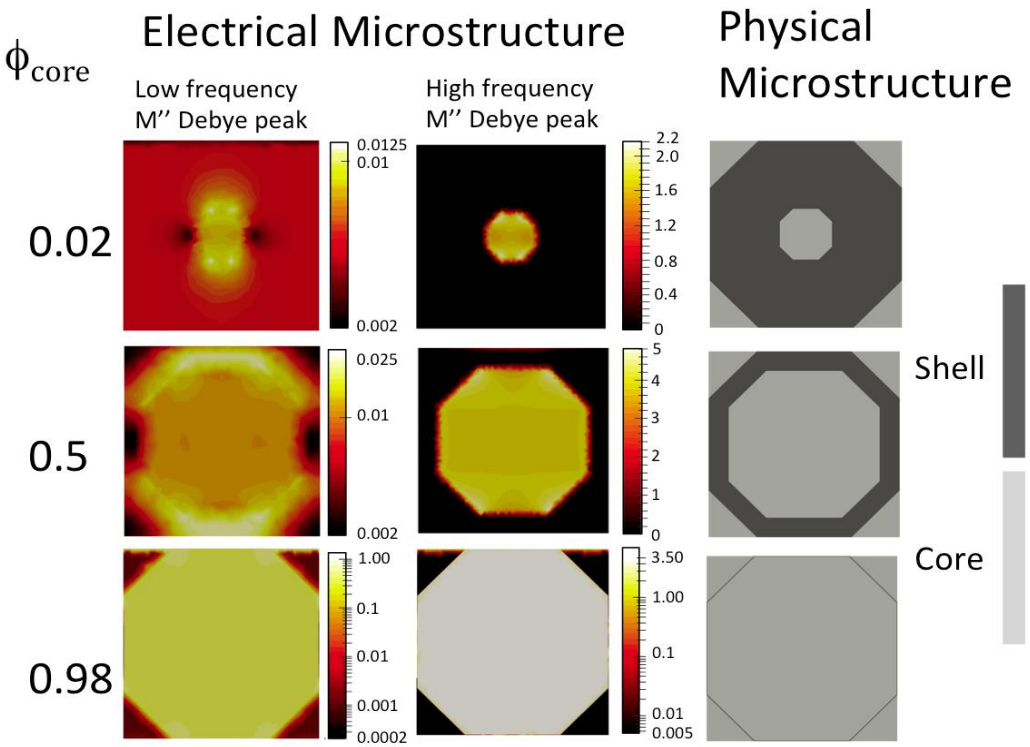

Fig. 23. *A comparison of the frequency-dependent electrical microstructure (current density in Am^{-2}) and physical microstructure for truncated octahedral core-shell microstructures of the indicated* ϕ_{core} *values.*

The electrical microstructure of the truncated octahedral model showed similar features to the encased model (fig. 23). At low frequency the current density was heterogeneous in the shell region with large concentrations in the series component of the shell. As the core volume fraction reduced, more current density was seen in the parallel component of the shell. At high frequency, the current density concentrates in the core and becomes more heterogeneous as ϕ_{core} falls. The full width at half maximum (FWHM) of the high frequency M'' peak associated with the core region broadens at lower values of ϕ_{core} (fig. 24).

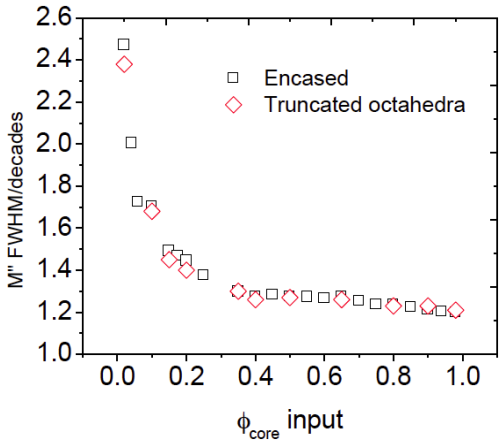

Fig. 24. *FWHM of the high frequency core M'' peak for the encased and truncated octahedral models for a range of* ϕ_{core} *values.*

Examination of resistance and capacitance values for the truncated octahedral models show that the core time-constants depend on geometry

whereas shell time-constants do not (see fig. 25). Like the encased model, the unexpected core time-constant values were caused by transitional behaviour in the core resistance as a function of ϕ_{core} compared to less dramatic but still non-linear behaviour in the shell resistance (see fig. 26). Values of the core and shell capacitances are inversely proportional to the core and shell volume fractions, respectively (see fig. 27). The general trends in all measured properties of the truncated octahedral simulations are very similar to the encased models.

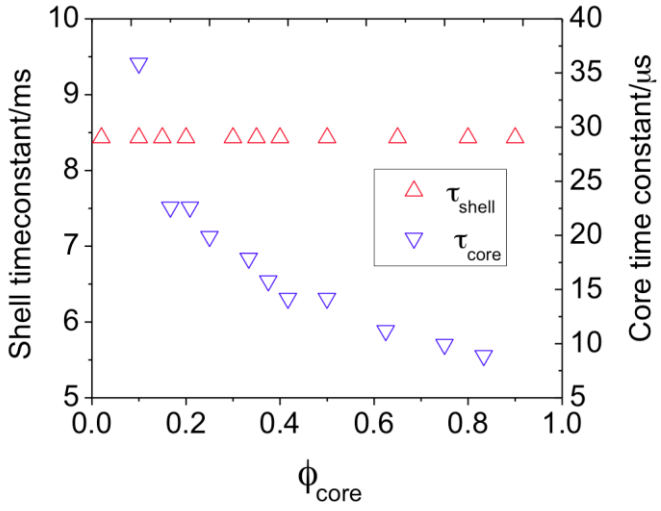

Fig. 25. *Plot of the core and shell material time constants extracted from simulated modulus plots for the truncated octahedral models.*

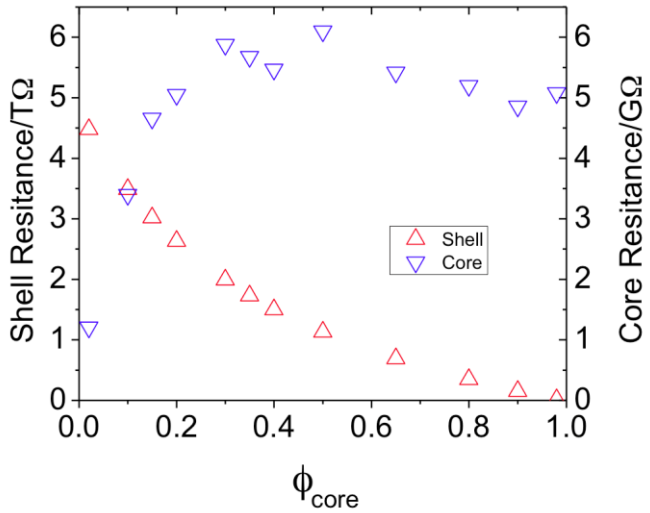

Fig. 26. *Values for shell resistances and core resistances for the truncated octahedral models extracted from M* Nyquist plots for a range of volume fractions.*

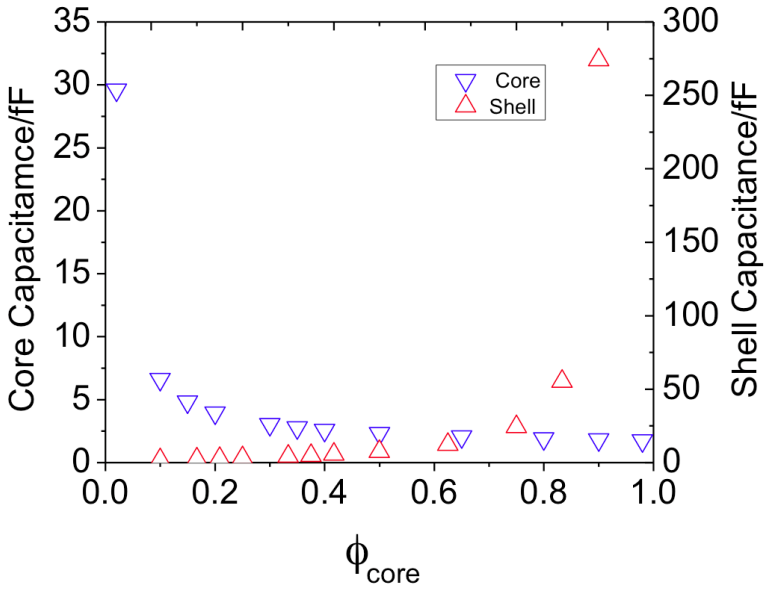

Fig. 27. *Values for shell capacitances and core capacitances for the truncated octahedral models extracted from M* Nyquist plots for a range of volume fractions.*

4.4. Polycrystalline Simulations

In previous studies, simulations of regular and mono-sized grains with the same shape and size were carried out on the smallest fraction of the grain volume that allowed generation of the full grain by symmetry operations. This reduction was justified by the symmetry of these idealised systems[19] (see fig. 28). Here, we have opted to simulate the whole grain. This allows us to simulate a single grain in great detail, achieving a convergence of calculated values and high resolution plots of the electrical microstructure. It is possible to simulate polycrystals with many grains. In this section, results for poly-crystals made from 6x6x6 nested cube grains are presented to demonstrate the equivalence to single grain simulations. For larger systems it is impractical to attempt a convergence study to optimise the mesh size. Instead the nested cube models were meshed with 1.1 million elements. Using more elements than this can have issues with lack of computer memory and long simulation times (months). As there is uncertainty in the convergence of these simulations, the results obtained should be treated as illustrative.

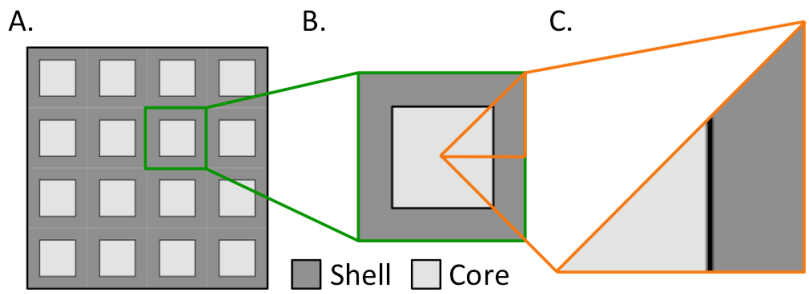

Fig. 28. *(A) Nested cube polycrystal, (B) reduction of the polycrystal to a single grain as used in this study and (C) reduction of a single nested cube grain to minimise computation cost, as used in ref. 19.*

In order to show that a single nested cube grain is representative of a polycrystal with all grains the same, the impedance response of several 6x6x6 nested cube microstructures was simulated for a range of $\phi_{core.}$ The resulting spectra were analysed with the M* formulism to obtain the core and shell capacitances, from which volume fractions could be extracted as for the previous studies. It was found that the polycrystalline models had similar ϕ_{core} values to the single grain simulations (see fig. 29).

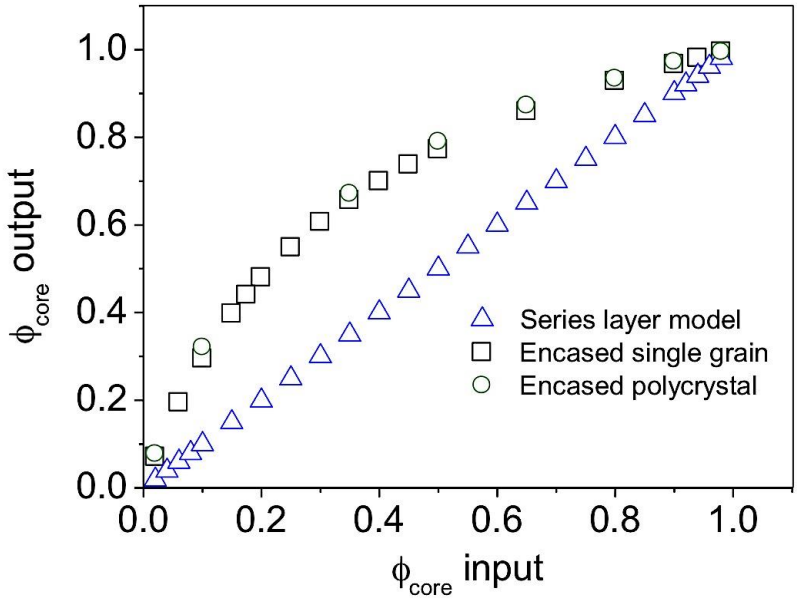

Fig. 29. *Comparison of ϕ_{core} extracted from M* arc diameters against the true value of ϕ_{core} for the SLM, encased model and polycrystalline encased model.*

As with the single grain encased model, a stream trace analysis of current density at high and low frequency was performed. Since they have a larger area than the single grain models, the convergence of the conduction pathway for polycrystals as more stream tracers were added was slower (see fig. 30). Similar trends were found for the distribution of conduction pathway lengths (DCPL) at low frequency and high frequency for polycrystals to the single grain encased model but there was more scatter in the data points (see fig. 31).

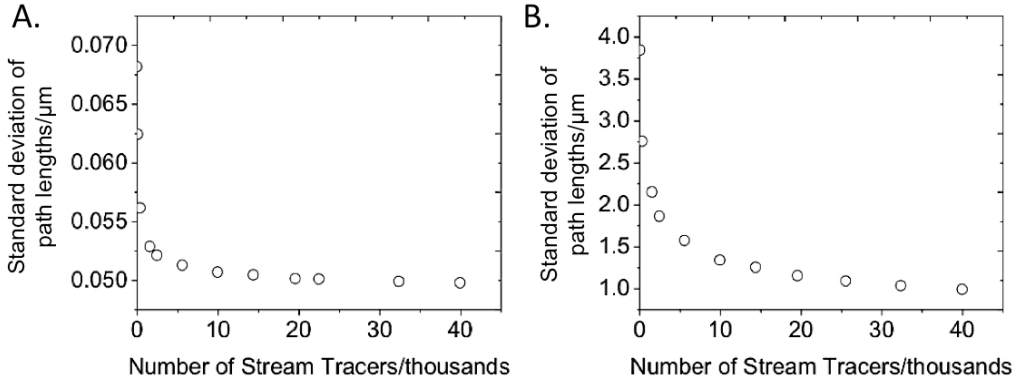

Fig. 30. *Convergence of the DCPL for an increasing number of stream tracers for (A) single grain encased models, (B) polycrystalline encased models.*

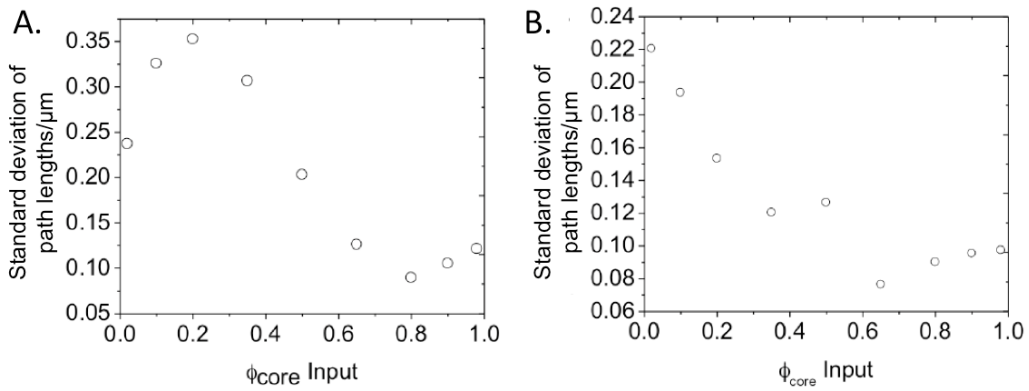

Fig. 31. *Standard deviation of the DCPL for polycrystalline models at (A) the shell material's Debye frequency and (B) the core material's Debye frequency.*

4.5. Discussion

It is clear, even from our early results comparing the impedance response of the SLM and the encased model, that the physical microstructure can affect the electrical microstructure. The results of the SLM show that a system with purely series connections in the microstructure allows values of resistance and capacitance of all material regions to be extracted with exact agreement with a dual RC circuit (provided that all materials present have sufficiently different time constants). The surfaces and interfaces of the SLM that are parallel to the 'electrode' boundary conditions are equipotential at all frequencies and hence the current density is homogenous in each layer (see fig. 9). Hence the time constants of the core and shell regions are geometry-independent. In the case of the SLM the electrical microstructure is representative of the physical microstructure (see fig. 32 A and B), allowing volume fractions to be extracted accurately from capacitance ratios (see fig. 10). The good agreement of our FEM simulations of the SLM with the analytical results provides a validation for our FEM method.

When we change the distribution of core and shell material to an encased model we do not have purely series connections. The addition of parallel pathways has a profound effect on the electrical microstructure (see fig. 9). At low frequency, the current will flow relatively homogenously through the series component of the shell, as the current has nowhere else to go. When presented with parallel pathways through the core and shell, the current takes the path of least resistance through the microstructure, flowing through the conductive core region to avoid the more resistive shell region. This reduces the shell contribution to the impedance response at low frequency (see fig. 32C).

At high frequency the current density is concentrated in the core region (see fig. 32 D). Although the current density can be heterogeneous in the core, the average magnitude of core current density is relative high compared to the parallel shell regions, giving the core a strong contribution to the impedance response at high frequency. This mismatch in the core and shell impedance contributions leads to an over-estimation of ϕ_{core} when extracting ϕ_{core} from capacitance ratios. This over-estimation is present, with variation in its magnitude, at all values of ϕ_{core} input into the model (see fig. 10A).

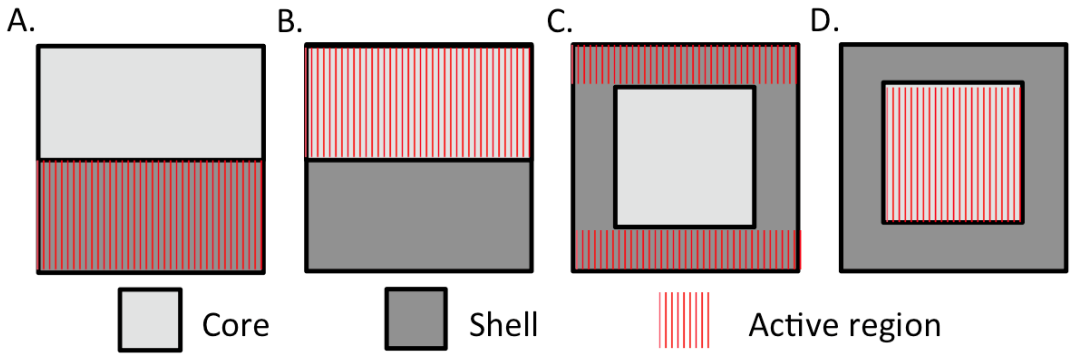

Fig. 32. *Schematic showing which regions in the SLM and encased microstructure are active at high and low frequency. (A) SLM low frequency shell layer response, (B) SLM high frequency core layer response, (C) encased low frequency series shell response and (D) encased high frequency core response.*

We attempted to predict the overestimation of ϕ_{core} made by conventional equivalent circuits by deriving a dual RC circuit whose constituent elements were based upon the electrical microstructure (as shown in fig. 9D). The values for the low and high frequency RC elements were functions of the shell and core geometries when in series and their respective intrinsic material properties (see fig. 11). This fit was not successful, as it does not account for curvature of current flow through the microstructure as revealed by a stream trace of the low frequency current density (fig. 18). The differences between the ϕ_{core} values extracted from the encased model and those predicted by the series brick layer model (SBLM) were proportional to the curvature of the current flow as measured by a stream trace analysis (see fig. 19). The Bonanos-Lilley equations provided a better fit (see fig. 10) in good agreement with the work of Kidner *et al*[15, 21] but these equations are further removed from a real ceramic micro-structure than a nested cube model and still underestimate ϕ_{core}.

Examination of the core and shell resistances and capacitances (see fig. 15) revealed that there was a transition in conduction behaviour in the core region. Current density plots (see fig. 16) and electric field plots (see fig. 17), taken for the high frequency response of the core, showed that as ϕ_{core} became smaller, the electrical microstructure of the core became more heterogeneous and did not represent the physical microstructure. When the electrical microstructure was no longer homogenous in the core and that heterogeneity varied with ϕ_{core} the core time constant was not independent of geometry. This contrasted with the encased model's shell time constant. This was geometry independent because the current density spreads relatively homogenously through the series component of the shell in order to minimise resistance, in good agreement with a previous modelling study[22]. In the more traditional view of the brick layer model, all time constants are independent of geometry as the geometric terms in the basic equations for resistance and capacitance cancel[20]. For the encased model, these equations cannot describe capacitances and resistances derived from the more complex electrical microstructures.

Examination of the high frequency imaginary modulus (M'') Debye peaks showed that they became broader as ϕ_{core} decreased. A mathematically 'perfect' Debye peak has a full width at half maximum (FWHM) of 1.14 decades on a logarithmic scale of frequency; however, this is rarely observed experimentally[23].

There are many theories for this departure from Debye-like behaviour. These are discussed in the literature review in this thesis. However none of these are incorporated into the finite element simulation. Another possibility is that a distribution of time constants is present. In this study there are only two time constants present and these have three orders separation in magnitude. Therefore this is unlikely to be the cause. This implies that there is a contribution to the FEM response that causes a non-Debye like response and that this is independent of the material properties.

A simple explanation for the non-Debye like response could be that there is an extra time constant present at intermediate frequencies when the current flows through the capacitive part of the shell and the resistive component of the core (see chapter one, fig. 31B) resulting in a time constant that is the product of the shells resistance and the cores capacitance. If this extra time constant were significant it would be present regardless of microstructure and hence would exist in the FEM and equivalent circuit simulations of the SLM. The SLM simulations had core and shell time constants of 8.65 μs and 8.75 ms respectively. These values were in good agreement with the theoretical core and shell time constants of 8.85 μs and 8.85 ms respectively, implying there was no significant contribution of the effective equivalent circuit at intermediate frequency. Hence there must be some other effect causing the non-ideality in the encased model.

A stream trace analysis of the high frequency current density that is associated with the core's Debye response explains the deviations from predicted behaviour (see fig. 16A). It was observed that, as ϕ_{core} decreases, the conduction pathways increasingly curve towards the core (see fig 33A), increasing the distribution of conduction pathway lengths (DCPL). For particularly small ϕ_{core} values the conduction pathways that pass through the core have extremely large curvatures due the heterogeneous electric field experienced by the core. Small values of ϕ_{core} mean much thicker shells. Due to the increase in shell thickness, the effective resistance of the parallel component of the shell is reduced. This allows parallel conduction pathways through the shell to form (see fig. 33B). A combination of short parallel pathways and highly curved series pathways through the core gives a very broad DCPL. There is some correlation between the FWHM of the high frequency M'' Debye peak and the DCPL (see fig. 16C). The parallel pathways have a low current density and hence do not contribute to the magnitude of the impedance response but can broaden the high frequency M'' Debye peak.

As the current flowing through the encased model is non-linear at the characteristic frequencies of the core and the shell, it is no surprise that a BLM analysis that depends on ϕ_{core} is of limited use. Using the values selected in this study for conductivity and permittivity we found that, if ϕ_{core} was reduced below 0.7, the error in extracting ϕ_{core} from core-shell capacitance ratios exceeded 25% of the true value and up to 250% for a ϕ_{core} value of 0.02. Clearly care should be taken when attempting to use capacitance ratios to extract volume ratios from core-shell microstructures for encased models or any other system where the physical microstructure does not resemble the electrical microstructure.

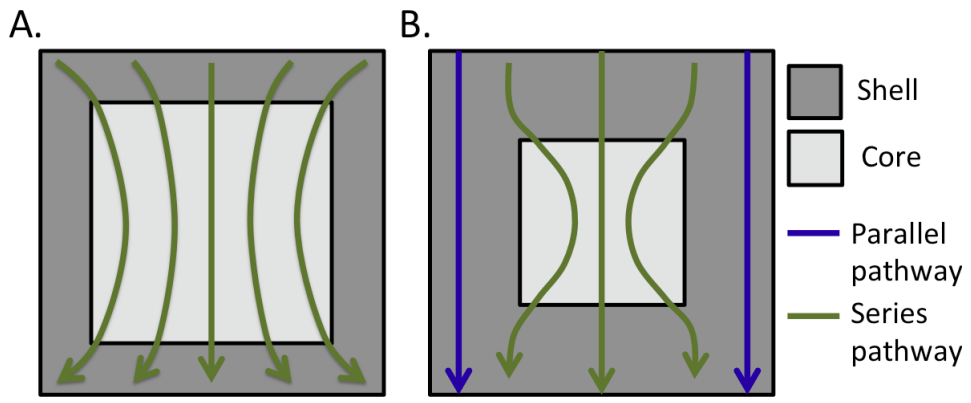

Fig. 33. *Schematic showing encased model with a (A) medium and (B) small core volume fraction and how parallel conduction pathways form in the latter.*

Results for nested cube poly-crystals agreed with single grain simulations (see fig. 29 and 31). This demonstrates that using symmetry is a valid strategy to reduce the simulation cost for polycrystals with single-size, regular grains as used in previous studies[13, 14, 15, 19]. However, the difficulties in reaching convergence of extrinsic properties extracted from impedance spectra (see fig. 30) shows that either more computational power or more efficient numerical techniques are required to simulate poly-crystals with realistic microstructures at the same level of detail and accuracy.

Finally, contrasting the results of the encased model, truncated octahedral model and the Bonanos-Lilley equations reveals shape effects in regular grains. All three approaches model a two-material electrical composite consisting of a high conductivity inclusion material surrounded by a low conductivity matrix material. The main difference between the three models is the shape of the conducting inclusion. For the encased model the inclusion is a cube; for the truncated octahedral model it is a truncated octahedron; and a sphere for the Bonanos-Lilley equations. Going from the encased model to the Bonanos-Lilley equations, these inclusions become more faceted (a sphere can be thought of as infinitely faceted, see fig. 34). Whilst all three approaches are in good agreement for the ϕ_{core} values extracted for a given volume ratio of conductive and resistive material and fixed intrinsic properties, there are small deviations that follow a trend at all input values of $\phi_{core.}$ The encased model gave the largest overestimate of ϕ_{core} from capacitance ratios whilst the Bonanos-Lilley equations overestimated ϕ_{core} the least (see fig. 22). In other words: the less faceted the conductive inclusion the more ϕ_{core} will be overestimated.

The reason for this small shape effect is probably the intrinsic conductivity of shapes. Mansfield *et al* showed by a simulation study that, for a fixed conductivity and volume, shapes that are less faceted are more conductive[24]. In terms of percentage difference from the actual ϕ_{core}, this effect only becomes significant for very small values of ϕ_{core}. At a ϕ_{core} value of 0.25 the difference between percentage errors of ϕ_{core} extracted from capacitance ratios of the encased and Bonanos-Lilley equations is ~20%, increasing to ~64% for a ϕ_{core} value of 0.02. Conversely at a ϕ_{core} value of 0.80 this difference is only ~0.5%. From this result, it is clear that the existence of a mixture of active parallel and series pathways through the microstructure rather than the shape of a conductive inclusion dominates a materials electrical response for grains with larger values of ϕ_{core}

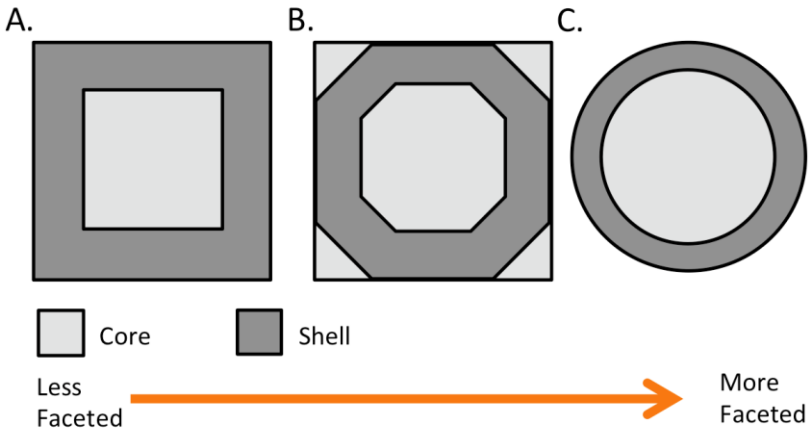

Fig. 34. *Schematic showing cross-sections of the encased, truncated octahedral and Bonanos-Lilley microstructures with an arrow indicating the level of faceting. (A) Nested cube, (B) truncated octahedral and (C) nested sphere (Bonanos-Lilley).*

4.6. Conclusion

Here the extraction of volume fractions from capacitance ratios obtained from impedance data has been investigated using FEM. The effect of variables including the volume of core and shell, grain shape effects and the distribution of materials in a microstructure were examined. Key results are:

- For an electrical composite material where phases of different conductivities are present, the electrical microstructure depends on the path of least resistance that the electric current will flow through.
- Application of the BLM to core-shell microstructures becomes increasingly unreliable as ϕ_{core} decreases. The error in estimating volume fractions from capacitance ratios exceeds 25% when ϕ_{core} is lower than 0.70 for the parameters used in this study. This is because, as ϕ_{core} decreases, the electrical microstructure becomes increasing different from the physical microstructure.
- Non-ideality in impedance spectra can be influenced by heterogeneous current flow that is a result of microstructure and is independent of a distribution of relaxation times and atomistic mechanisms.
- Regions of low current density in a microstructure have a lower contribution to the magnitude of an impedance response but, if their resistance is low enough, can give rise to parallel conduction pathways that can broaden high frequency Debye peaks.
- Grain shape effects can affect extracted capacitance values, particularly at low values of ϕ_{core}, but not to the same extent as the presence of series and parallel pathways.
- Heterogeneous current flow can cause extracted time constants of a material to have geometry dependence.

4.7. References

1. J. S. Dean, P. Y. Foeller, I. M. Reaney, and D. C. Sinclair, "A resource efficient design strategy to optimise the temperature coefficient of capacitance of BaTiO3 based ceramics using finite element modelling," *Journal of Materials Chemistry A,* 4[18] 6896-901 (2016).

2. S.-C. Jeon, B.-K. Yoon, K.-H. Kim, and S.-J. L. Kang, "Effects of core/shell volumetric ratio on the dielectric-temperature behavior of $BaTiO_3$," *Journal of Advanced Ceramics,* 3[1] 76-82 (2014).

3. S. Srinivasan, J. C. Russ, and R. O. Scattergood, "Grain-Size Measurements Using the Point-Sampled Intercept Technique," *Scripta Metallurgica Et Materialia,* 25[4] 931-34 (1991).

4. K. Thornton and H. F. Poulsen, "Three-diemensional materials science: an intersection of three-dimensional reconstructions and simulations," *Mrs Bulletin,* 33[6] 587-95 (2008).

5. J. E. Bauerle, "Study of Solid Electrolyte Polarization by a Complex Admittance Method," *Journal of Physics and Chemistry of Solids,* 30[12] 2657-2670 (1969).

6. N. Bonanos and E. Lilley, "Conductivity Relaxations in Single-Crystals of Sodium Chloride Containing Suzuki Phase Precipitates," *Journal of Physics and Chemistry of Solids,* 42[10] 943-52 (1981).

7. J. C. Maxwell, "A Treatise on Electricity and Magnetism." Cambridge University Press, (2010).

8. D. C. Sinclair and A. R. West, "Impedance and Modulus Spectroscopy of Semiconducting $BaTiO_3$ Showing Positive Temperature-Coefficient of Resistance," *Journal of Applied Physics,* 66[8] 3850-56 (1989).

9. P. Fiorenza, R. Lo Nigro, P. Delugas, V. Raineri, A. G. Mould, and D. C. Sinclair, "Direct imaging of the core-shell effect in positive temperature coefficient of resistance-$BaTiO_3$ ceramics," *Applied Physics Letters,* 95[14] (2009).

10. S. I. R. Costa, M. Li, J. R. Frade, and D. C. Sinclair, "Modulus spectroscopy of CaCu3Ti4O12 ceramics: clues to the internal barrier layer capacitance mechanism," *Rsc Advances,* 3[19] 7030-36 (2013).

11. I. M. Hodge, M. D. Ingram, and A. R. West, "Impedance and modulus spectroscopy of polycrystalline solid electrolytes," *Journal of Electroanalytical Chemistry and Interfacial Electrochemistry,* 74[2] 125 - 43 (1976).

12. E. J. Abram, D. C. Sinclair, and A. R. West, "A strategy for analysis and modelling of impedance spectroscopy data of electroceramics: Doped lanthanum gallate," *Journal of Electroceramics,* 10[3] 165-77 (2003).

13. J. P. Heath, J. S. Dean, J. H. Harding, and D. C. Sinclair, "Simulation of Impedance Spectra for Core-Shell Grain Structures Using FiniteElement Modeling," *Journal of the American Ceramic Society,* 98[6] 1925-31 (2015).

14. J. S. Dean, J. H. Harding, and D. C. Sinclair, "Simulation of Impedance Spectra for a Full Three- Dimensional Ceramic Microstructure Using a Finite Element Model,"

Journal of the American Ceramic Society, 97[3] 885-91 (2014).

15. N. J. Kidner, N. H. Perry, T. O. Mason, and E. J. Garboczi, "The brick layer model revisited: introducing the nano-grain composite model," *Journal of the American Ceramic Society,* 91[6] 1733-46 (2008).

16. J. Fleig and J. Maier, "Finite-element calculations on the impedance of electroceramics with highly resistive grain boundaries: I, laterally inhomogeneous grain boundaries," *Journal of the American Ceramic Society,* 82[12] 3485-93 (1999).

17. K. Kato, K.-i. Mimura, F. Dang, H. Imai, S. Wada, M. Osada, H. Haneda, and M. Kuwabara, "BaTiO3 nanocube and assembly to ferroelectric supracrystals," *Journal of Materials Research,* 28[21] 2932-45 (2013).

18. F. Dang, K. Mimura, K. Kato, H. Imai, S. Wada, H. Haneda, and M. Kuwabara, "In situ growth BaTiO3 nanocubes and their superlattice from an aqueous process," *Nanoscale,* 4[4] 1344-49 (2012).

19. J. Fleig and J. Maier, "The influence of laterally inhomogeneous contacts on the impedance of solid materials: A three-dimensional finite-element study," *Journal of Electroceramics,* 1[1] 73-89 (1997).

20. D. C. Sinclair, "Characterization of Electro-materials using ac Impedance Spectroscopy," *Bol. Soc, Esp. Cerám. Vidrio,* 34[2] 55-65 (1995).

21. N. J. Kidner, Z. J. Homrighaus, B. J. Ingram, T. O. Mason, and E. J. Garboczi, "Impedance/dielectric spectroscopy of electroceramics - Part 2: Grain shape effects and local properties of polycrystalline ceramics," *Journal of Electroceramics,* 14[3] 293-301 (2005).

22. J. Fleig, S. Rodewald, and J. Maier, "Microcontact impedance measurements of individual highly resistive grain boundaries: General aspects and application to acceptor-doped SrTiO3," *Journal of Applied Physics,* 87[5] 2372-81 (2000).

23. A. K. Jonscher, "A New Understanding of the Dielectric-Relaxation of Solids," *Journal of Materials Science,* 16[8] 2037-60 (1981).

24. M. L. Mansfield, J. F. Douglas, and E. J. Garboczi, "Intrinsic viscosity and the electrical polarizability of arbitrarily shaped objects," *Physical Review E,* 64[6], 061401 (2001).

Chapter 5: The influence of permittivity on capacitive pathways in selected physical microstructures

In chapter 4 the effect of a core-shell microstructure on the electrical response of ceramics was considered for the case when the core and shell permittivity were fixed at the same value and the shell conductivity was three orders lower than that of the core. Here the core and shell conductivity are fixed and the effect of a difference in permittivity between the two material regions is tested. Simulations of parallel and series layer models as well as the encased model used previously are analysed when the volume fractions of the low and high permittivity material are equal. Finally, an encased model, where the volume fractions are varied to study the effect of physical microstructure on electrical microstructure, is investigated for the case where a two phase electrical composite has uniform conductivity and different values of permittivity.

5.1. Literature

The impedance response of electrically heterogeneous materials can be deconvoluted if the time constants present in the material are sufficiently different[1]. For example, impurities segregating to the grain boundaries may greatly alter the transport properties of the grain boundary regions giving them different (or a distribution of) time constants. The grain boundary and bulk components may have the same (or similar) permittivity but the grain boundary is usually much thinner than the bulk ceramic[2]. From the basic equation for a capacitor, see equation (2.2), we see that for the same permittivity and area the thinner grain boundary would have a higher capacitance. This allows for separation of the bulk and grain boundary impedance responses by the magnitudes of their capacitance. For other materials, the presence of dopants can also affect the permittivity of a material region. In the case of rare earth-doped barium titanate, the core of undoped-barium titanate (BT) is ferroelectric giving a high measured permittivity whereas the shell is paraelectric, due to the presence of dopants, and thus has a lower permittivity[3, 4]. To further complicate matters, depending on the processing conditions the core can be semi-conducting whilst the shell is more resistive. Core-shell BT can have different conductivities and permittivities present[5]. To understand the consequences for analysing the impedance spectra of electrically heterogeneous materials, it is important first to test the case where the conductivity of the two regions is the same but the permittivity of the two regions start to differ.

There have been several studies on electrical composites with mixed permittivities, typically attempting to calculate an effective permittivity for the whole composite. Wu *et al* considered direct current permittivity bounds for a cube of material subdivided into 30 x 30 x 30 sub-cubes[6]. A randomly selected portion of the sub-cubes had a higher permittivity than the rest. The number of sub-cubes selected was varied, creating a range of volume fractions of low and high permittivity material. The effective permittivity of the whole cube was then

calculated; this was then compared to values obtained using different mixing rules. There has also been interest in modelling materials with mixed permittivities for microwave applications. Padurariu *et al* performed fixed frequency simulations of how different configurations of physical microstructure affected the total capacitance and other figures of merit relevant to their field[7]. Neither approach considers conductivity explicitly.

Previously it has been shown that a difference in conductivity can result in preferential conduction pathways forming throughout a microstructure[8]. When core and shell conductivity have the same value there can be no alternative conduction pathways present. The impedance of a pure capacitor has only an imaginary component with a dependence on frequency given by[9] :

$$Z'' = -\frac{1}{\omega C} \tag{5.1}$$

where Z'' is the imaginary component of impedance in Ω, ω is the angular frequency in rad/s (where $\omega = 2\pi f$ and f is the applied frequency in Hz) and C is capacitance in F. The impedance of a pure resistor is frequency independent.

Consider an equivalent circuit consisting of two parallel resistor-capacitor (RC) elements connected in series. For simplicity we will assume that the resistors have the same resistance, R, and that one capacitor has a higher capacitance of 70 fF (C1). The other has a lower capacitance of 0.35 fF (C2). As the capacitances of C1 and C2 differ, the impedance of the capacitors will reduce at different rates as the frequency increases (see fig. 1A) as per equation (5.1). At zero frequency (DC), the impedance of both capacitors will be infinite and the current must flow through the two resistors (see fig. 1B i). As the frequency increases the impedance of C1 will eventually become lower than the resistance before C2. Thus the current will preferentially flow through C1 instead of R for the first RC element but will continue to be blocked by C2, flowing through R in the second RC element (see fig. 1B ii). Finally, at still higher frequencies the impedance of C2 will become less than R and the current will preferentially flow through C1 followed by C2 and therefore bypass the resistors (see fig. 1B iii). Different capacitive pathways will be available for an alternating current (AC) to flow through the circuit as frequency varies. As impedance spectroscopy uses variable frequency, capacitive pathways must be considered. This chapter investigates whether capacitive pathways can have similar effects to conduction pathways and therefore influence the electrical microstructure of three-dimensional physical microstructures.

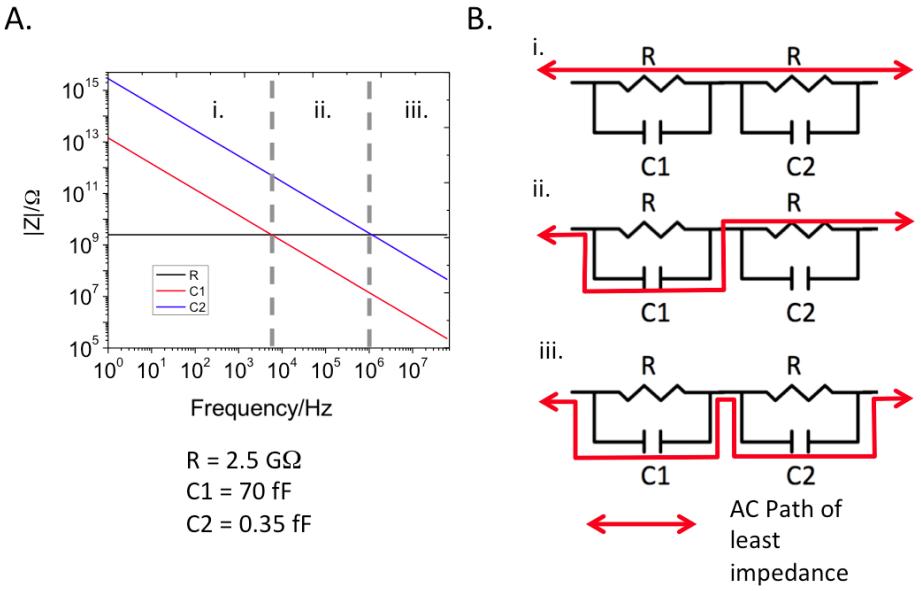

Fig. 1. (A) *Relationship between the magnitude of impedance and frequency for two resistors with equal values of resistance and two capacitors where the capacitance of C1 = 200 C2 assuming a configuration of two parallel RC elements connected in series.* (B) *How the path of least impedance changes at the indicated frequency ranges for the equivalent circuit.*

5.2. Methodology

The methodology here was similar to that used in chapter 4. All models consisted of two materials; both with a fixed conductivity of 0.1mSm^{-1} and permittivities of 10 and 2000 giving a difference in time constants that can be resolved. The impedance response of all microstructures was simulated using finite element modelling (FEM) over a frequency range of 1 Hz to 10 MHz and an applied alternating voltage of 100 mV. The first simple models simulated were equivalent to Maxwell's series layer (SLM, fig. 2A) and parallel layer models (PLM, fig 2B)[10]. The SLM and PLM consist of layers of low and high permittivity material stacked parallel and perpendicular to the electrode surface (expressed using the appropriate boundary conditions), respectively. Due to their simplicity both these models can be solved analytically and hence can validate the finite element model for the fixed conductivity, varied permittivity case.

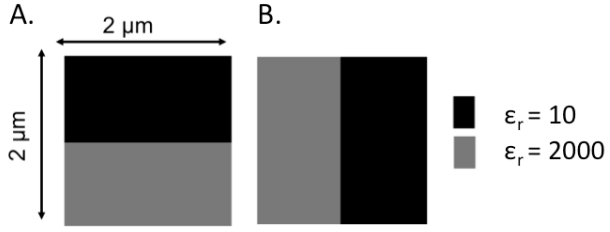

Fig. 2. *Schematic of the* (A) *series layer model and* (B) *parallel layer model composed of two material regions of equal volume fraction and the permittivities indicated. Note the conductivity of each region is fixed at 0.1 mSm^{-1} and the field is across the samples, from top to bottom.*

The next model was the same nested cube structure as used previously[8, 11] that we refer to as the encased model (see fig. 3A), consisting of a cube of high permittivity material encased in a shell of low permittivity material (see fig. 3B). The electrical response of this configuration is more complex and does not have an analytical solution. Hence we must use the finite element code to solve the encased model's material response.

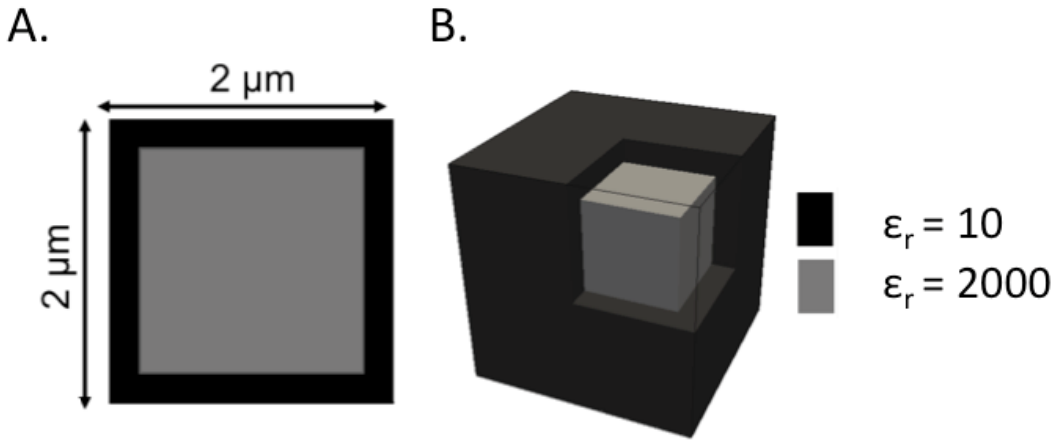

Fig. 3. *Schematic of the* (A) *encased model composed of two material regions of equal volume fraction and the permittivities indicated. Note the conductivity of each region is fixed at 0.1 mSm*$^{-1}$*.* (B) *Three dimensional image of the encased model with some of the shell material removed to show the nested cube structure.*

For the PLM and SLM a mesh division of 0.1 µm was used as in the previous study[8]. For the encased models, a mesh size of 0.08 µm was used as in the convergence study used in chapter four. Stream tracing was employed to visualise curvature in plots of electrical microstructure. Unless stated otherwise, all stream traces are started from the bottom free surface of the model where a Dirichlet boundary condition applies the AC voltage (see fig. 4).

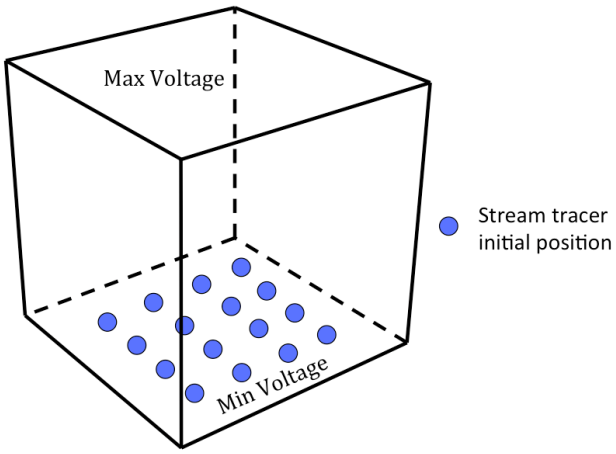

Fig. 4. *Schematic of initial positions of stream tracers.*

In chapter 4 when considering the core-shell microstructure, core volume fractions (ϕ_{core}) were estimated from capacitance ratios. The electric modulus

formalism was used to extract core and shell capacitances as this formalism had resolved arcs better than the impedance for most values of ϕ_{core}. The reason for this can be demonstrated using an equivalent circuit simulation in Zview[12]. Here we have two parallel resistor-capacitor circuits connected in series. Circuit 5A(i) consists of two capacitors both with a capacitance of 10 fF and two resistors with resistances of 2.5 and 250 GΩ respectively. Likewise, circuit 5A(ii) consists of two resistors fixed at 2.5 GΩ and capacitors with capacitances of 10 fF and 0.1 fF (see fig. 5A).

When examining the impedance response of circuit 5A(i) as an impedance Nyquist plot (see fig. 5B), the response of R2 dominates the smaller resistance of R1. A partial arc is observed in the high frequency region near the origin (see inset graph, fig. 5B). Displaying the data as a modulus Nyquist plot reveals two arcs of equal diameter due to C1 equalling C2 (see fig. 5C). There are two arcs since the difference in R1 and R2 gives a different time constant for each parallel RC element.

If we examine circuit 5A(ii) in the same manner, we observe two arcs fully resolved in an impedance Nyquist plot (fig. 5D), whereas it is difficult to resolve both RC elements from the modulus Nyquist plot (see fig. 5E, the higher capacitance arc is just visible in the inset graph). Again, the arcs have equal diameter but this time it is due to the equal resistors. This indicates that, when analysing microstructures that have fixed conductivity and differing permittivity, better arc resolution can be achieved with the impedance formalism. It is also possible to estimate volume fractions using resistance ratios instead of capacitance ratios for the fixed conductivity case as the resistance ratio will be related to the thickness ratio of the materials present. This may become less accurate if microstructural effects are significant in non-ideal microstructures as has been demonstrated previously[8]. To probe microstructural effects, current density plots are examined. It will be shown that, when the conductivity is homogenous and the permittivity varies, the electrical microstructure is more complex than the results shown in chapter four.

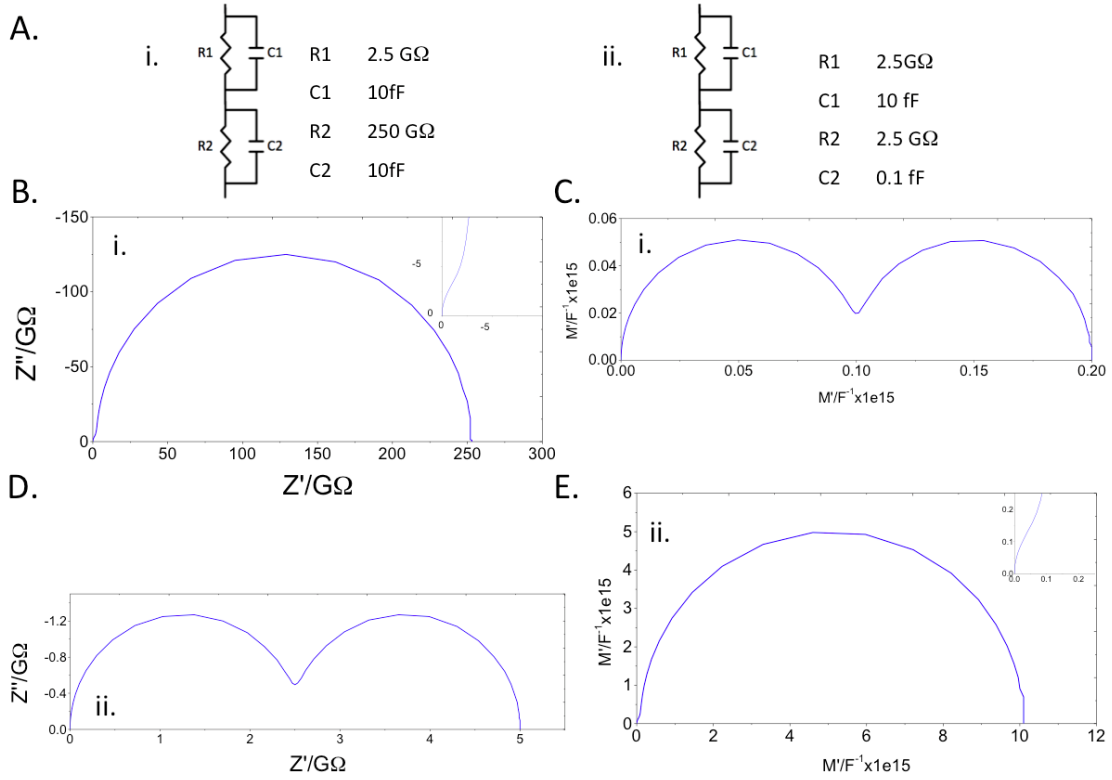

Fig. 5. (A) *The two equivalent circuits simulated. Relevant element values given.* (B) *Impedance Nyquist plot with enhancement of the high frequency region (inset) and* (C) *electric modulus Nyquist plot of equivalent circuit* (*i*)*.* (D) *Impedance Nyquist plot and* (E) *electric modulus Nyquist plot with enhancement of the high frequency region (inset) of equivalent circuit* (*ii*)*.*

5.3. Results

5.3.1. Series Layer Model

The first microstructure simulated was the Series Layer Model (SLM) with equal volumes of high and low permittivity material (see fig. 6A). Due to the simplicity of the SLM, values for the resistance and capacitance of both layers can be calculated analytically using the intrinsic conductivity and permittivity of each layer and their geometries. These values were used in a dual parallel RC element equivalent circuit to fit the SLM's impedance response (see fig. 6B). The impedance response from 0.1 Hz to 10 MHz was calculated using FEM. Examining the simulations revealed two responses in all four formalisms, these values are summarised in table 1. All FEM simulated values were in good agreement with those obtained using the equivalent circuit.

Table 1. *Comparison of analytical values for both RC elements used to model the SLM with values extracted from simulation by FEM and equivalent circuits. Note* C_t *denotes the total capacitance of the model.*

Circuit element	Element value	Formalism	FEM extracted values	Equivalent circuit extracted value
R1	2.500 GΩ	Z*	2.490 GΩ	2.503 GΩ
		M*	2.467 GΩ	2.503 GΩ
		Y'	2.504 GΩ	2.525 GΩ
		E'	-	-
C1	0.354 fF	Z*	0.346 fF	0.337 fF
		M* (C_t)	0.352 fF	0.352 fF
		Y'	-	-
		E'	0.352 fF	0.352 fF
R2	2.500 GΩ	Z*	2.510 GΩ	2.497 GΩ
		M*	-	-
		Y'	2.490 GΩ	2.475 GΩ
		E'	-	-
C2	70.80 fF	Z*	73.49 fF	69.66 fF
		M*	-	-
		Y'	-	-
		E'	17.80 fF	17.79 fF

A Nyquist plot of the electric modulus had difficulty resolving both responses as the plot was dominated by C1 (see fig. 6C). The beginnings of C2's response can be seen at low frequency close to the origin (see fig. 6C inset). This arc is not resolved well enough to extract RC values. Taking the total diameters of both arcs as the inverse of the total capacitance agrees exactly with the analytical solution.

Two plateaus were observed (see fig. 6D) in a spectroscopic plot of the real admittance (Y'). The apparent dispersion at high frequency for Y' is present in all FEM Y' spectroscopic plots due to the reference layer which is required for the finite element calculation (see chapter three) and is considered to be an artefact. The low frequency plateau was 0.2 nS or the value of the direct current (DC) conductance. The high frequency plateau was at 0.396 nS. This was interpreted as R1 because R1C1 has a lower time constant and hence relaxes at higher frequency. An impedance Nyquist plot gave two well-defined arcs of equal diameter each measuring ~2.5GΩ (see fig. 6E). The high and low frequency arcs are interpreted as R1 and R2 respectively, in good agreement with the analytical solution. Equating the volume ratio of the two layers to the resistance ratios extracts the exact volume fraction of 0.5.

The real component of the capacitance (E') plotted against frequency also gives two plateaus (see fig. 6F). The high frequency plateau gives a capacitance of 0.352 fF, which is close to the analytical solution and the equivalent circuit. The low frequency plateau gives a capacitance of 17.8 fF, lower than the 70.8 fF predicted by equation (2.2) for C2. E' is more suited to resolving capacitances in parallel systems. The values obtained from the plateaus do agree with the solution

for the low and high frequency E' plateaus for a series dual RC circuit. These solutions contain composite terms including the values of resistance and capacitance (see chapter one) and only tend to the high and low frequency capacitances where the magnitudes of both the capacitances and resistances are very different. Here the resistances are the same and so this approximation fails.

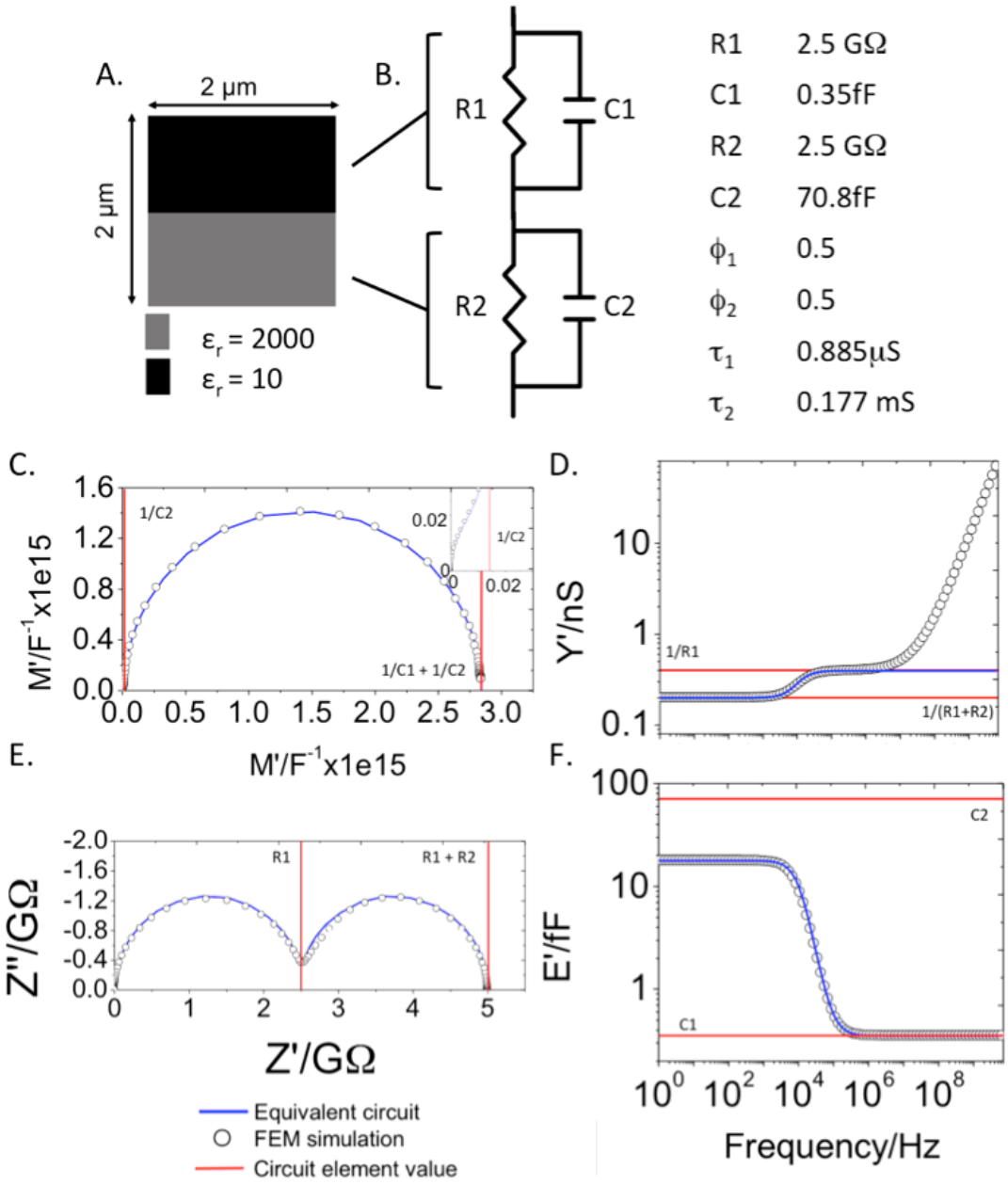

Fig. 6. (A) *Physical microstructure of the series layer model (SLM).* (B) *Equivalent circuit used to model the SLM with resistance and capacitance values of individual circuit elements, the volume fractions and time constants of the low and high permittivity layer (ϕ_1, ϕ_2, τ_1 and τ_2, respectively). FEM simulated impedance spectra for the SLM with equivalent circuit fit (blue line) and intercepts for equivalent circuit element values (red lines) plotted as:* (C) *a modulus Nyquist plot,* (D) *real component of the admittance spectroscopic plot,* (E) *impedance Nyquist plot and* (F) *the real component of capacitance spectroscopic plot.*

Two arcs were observed in the impedance Nyquist plot (see fig. 7). Previously it has been found that the electrical microstructure at the Debye frequencies defines the impedance spectra[8]. To probe the electrical microstructure of the SLM, current density plots were taken in a plane perpendicular to the interface at the indicated frequencies (see fig. 8). The apparent jaggedness at the interface is an artefact of interpolation by the visualisation software across the elements at that surface. The interface is perfectly flat as indicated in fig. 2. At both frequencies the current density was concentrated in the low permittivity layer but there was a much greater difference between the magnitudes of the current density in both layers at higher frequency.

A stream trace of the current density vector field was performed using a grid of initial positions of the tracer particles placed at the bottom of the model (as outlined in the methodology chapter, chapter 3). This showed the conduction pathways to be straight for the low frequency Debye response (see fig. 8A). This was also the case for the high frequency Debye response (see fig. 8B) but the stream trace terminated at the interface. Repeating the stream trace with starting positions defined at the reference layer interface for the low and high frequency Debye responses (see fig. 9A and B, respectively) showed the low frequency stream trace to be unaffected. However, the stream trace for the high frequency response travels through the low permittivity layer and stops at the interface. This would imply the termination of the stream trace is an effect of the interface between regions of different permittivity rather than one of the individual layers. A model where the order of the layers was reversed was also simulated producing identical impedance spectra. All trends in the electrical microstructure were reversed as expected.

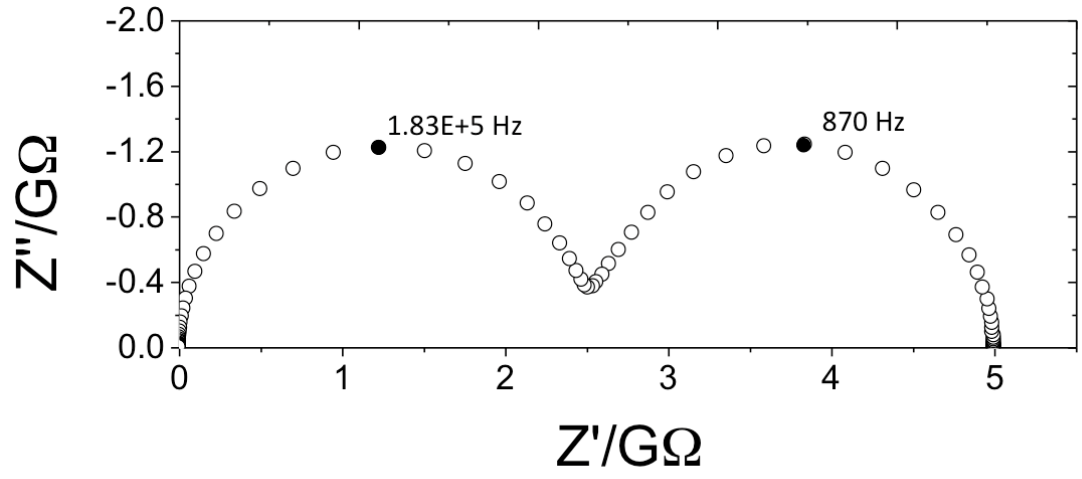

Fig. 7. *Impedance Nyquist plot of the series layer model with Debye frequencies indicated.*

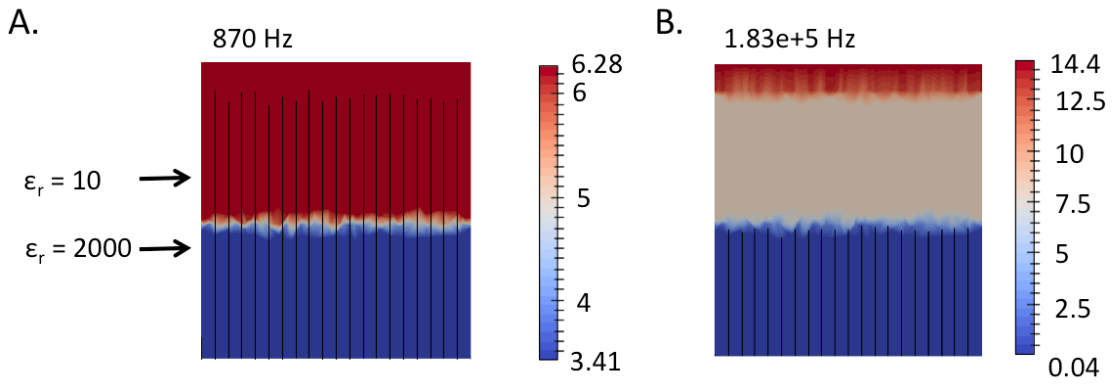

Fig. 8. *Current density plots of a series layer model with equal volume fractions of high and low permittivity material taken at the indicated frequencies. A stream trace of the current density vector field is plotted as black lines. These plots were taken at the instance of maximum current on the current sinusoids. Units are* Am^{-2}

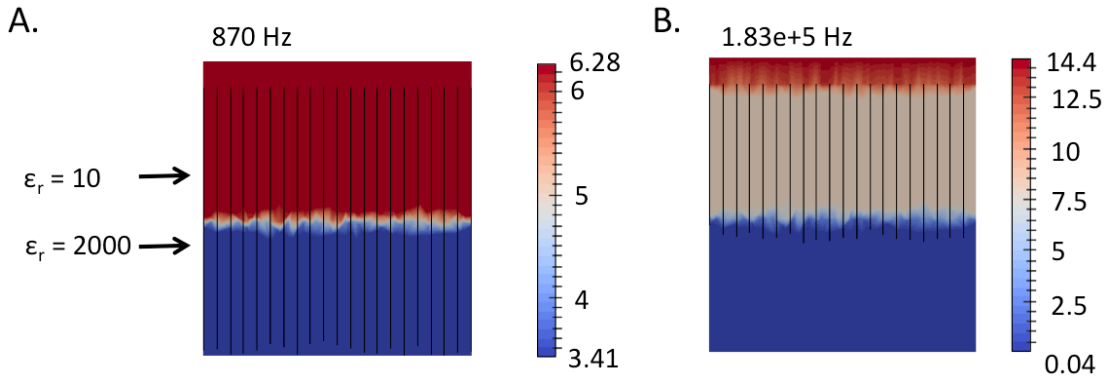

Fig. 9. *Repeat of figure 8 with stream trace seed points placed underneath the reference layer.*

Additional current density plots were taken at very low frequency (1 Hz, see fig. 10A) and very high frequency (10 MHz, see fig. 10B). At very low frequency there was a slight concentration of current density in the high permittivity layer although this heterogeneity was only observable at the third decimal place. As the FEM code is accurate to at least six decimal places (assuming scientific notation) and the change in current density correlates with a change in physical microstructure, this indicates a physically meaningful response. At 10 MHz it was observed that the current density was still concentrated in the low permittivity layer but the stream trace could now travel through the interface.

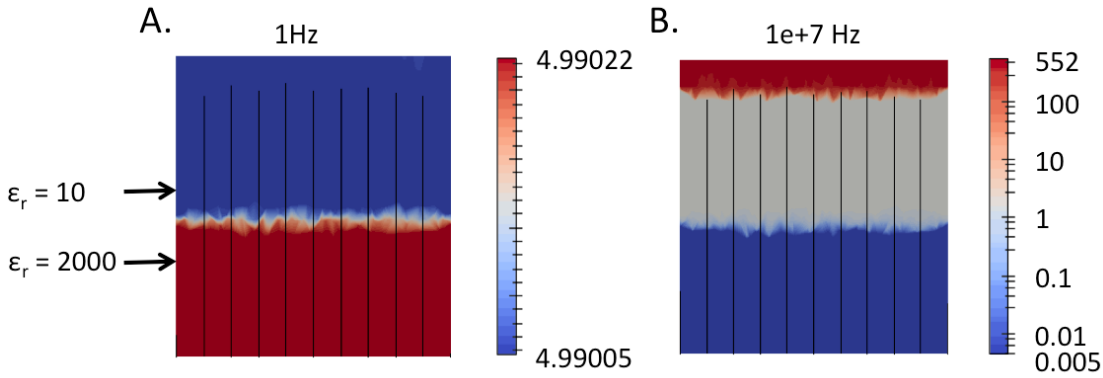

Fig. 10. *Current density plots of a series layer model with equal volume fractions of high and low permittivity material taken at the indicated frequencies. A stream trace of the current density vector field is plotted as black lines. These plots were taken at the instance of maximum current on the current sinusoids. Units are* Am^{-2}*. Note the scale of* (B) *is logarithmic and covers a larger range of values than* (A).

5.3.2. Parallel Layer Model

A parallel layer model (see fig. 11A) was also simulated as this would show if current prefers to flow down the low or high permittivity layer. Only one impedance response was observed in the impedance spectrum, which was modelled with two parallel RC elements connected in parallel (see fig. 11B). Single arcs were present in impedance (see fig. 11C) and modulus (see fig. 11E) Nyquist plots. Single plateaus were found in spectroscopic plots of the real components of the admittance (see fig. 11D) and real capacitance (see fig. 11F). The resistances and capacitances extracted from these arcs and plateaus corresponded to the total resistance and capacitance of two RC elements connected in parallel. All values extracted from the FEM and equivalent circuits agreed with the analytical solutions (see table 2). The PLM collapses into a single response with a composite value of both RC elements added in parallel.

Table 2. *Comparison of analytical values for both RC elements used to model the PLM with values extracted from simulation by FEM and equivalent circuits.*

Circuit element (composite)	Element value	Formalism	FEM extracted values	Equivalent circuit extracted value
$\left(\frac{1}{R1}+\frac{1}{R2}\right)^{-1}$	5.000 GΩ	Z*	5.000 GΩ	5.000 GΩ
		M*	5.120 GΩ	5.148 GΩ
		Y'	5.000 GΩ	5.000 GΩ
		E'	-	-
$(C1+C2)$	17.79 fF	Z*	18.22 fF	18.32 fF
		M*	17.79 fF	17.80 fF
		Y'	-	-
		E'	17.78 fF	17.80 fF

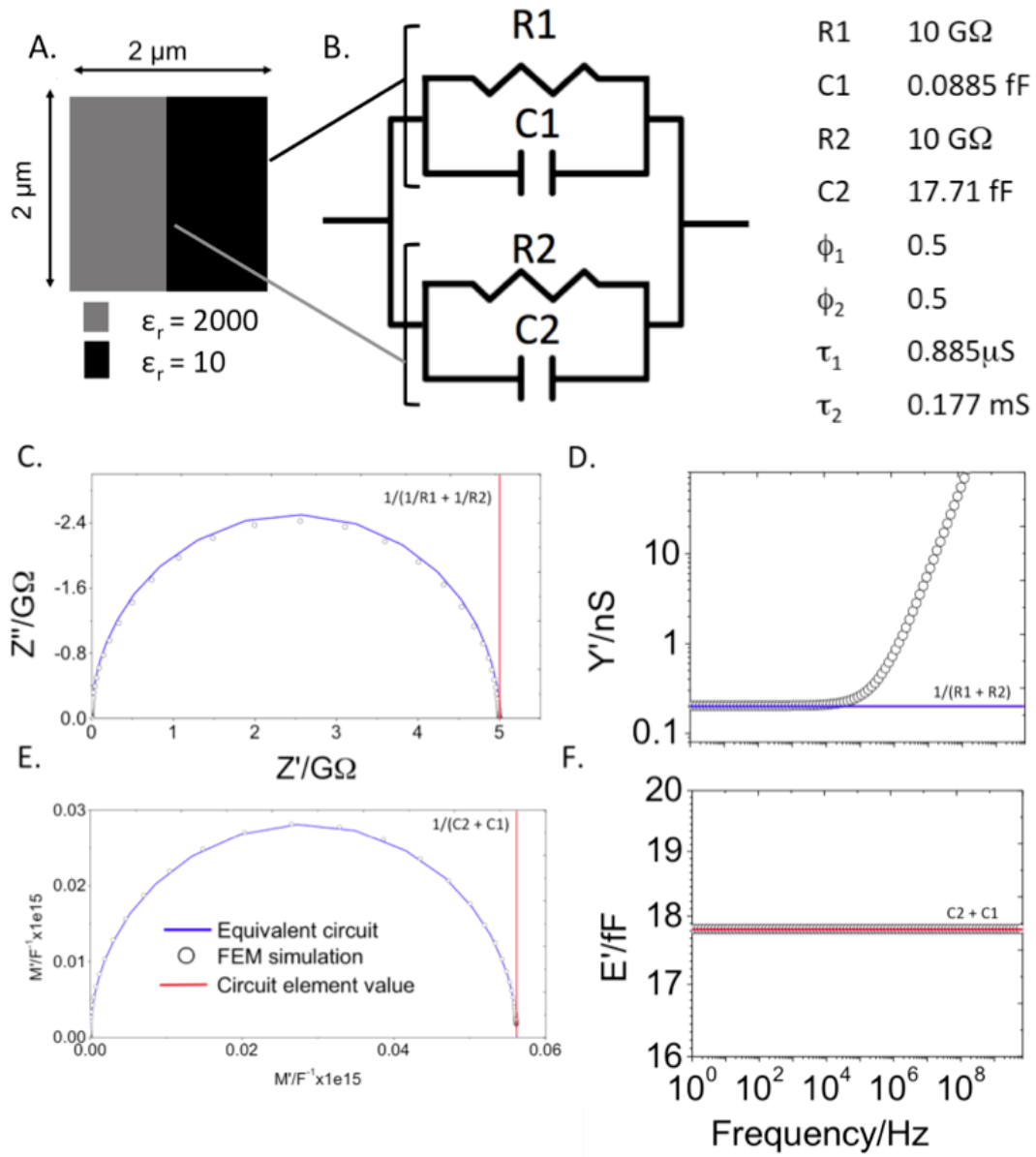

Fig. 11. (A) *Physical microstructure of the parallel layer model (PLM).* (B) *Equivalent circuit used to model the PLM with resistance and capacitance values of individual circuit elements, the volume fractions and time constants of the low and high permittivity layer (ϕ_1, ϕ_2, τ_1 and τ_2, respectively). FEM simulated impedance spectra for the PLM with equivalent circuit fit (blue line) and intercepts for equivalent circuit element values (red lines) plotted as:* (C) *an impedance Nyquist plot,* (D) *real component of admittance spectroscopic plot,* (E) *modulus Nyquist plot and* (F) *real component of capacitance spectroscopic plot. For* (D) *and* (F) *the circuit element values and equivalent circuit fits overlap.*

Plots of current density for several frequencies were obtained to visualise the electrical microstructure. The frequencies examined coincided with: the Debye frequencies (f_{max}) of the impedance (Z*) and electric modulus (M*) arcs; the two frequencies at the full width at half maximum of the peaks of the imaginary components of Z* and M*; and the end members of the frequency range (see fig. 12). While heterogeneity in the current density was observed in the reference layer (see fig. 13 for the location) generally the current density appeared to be homogenous in both layers of the PLM (see figs. 14 A to F). Inside the reference layer at 1Hz the current density was concentrated over the low permittivity layer of the PLM (see fig. 14A). For all higher frequencies the current density was concentrated over the high permittivity layer. A stream trace of the current density vector field was straight for 1 Hz to 7055 Hz. For frequencies of 10 MHz and 1 GHz the stream trace bent towards the high permittivity layer. The curvature of the stream trace increased with frequency.

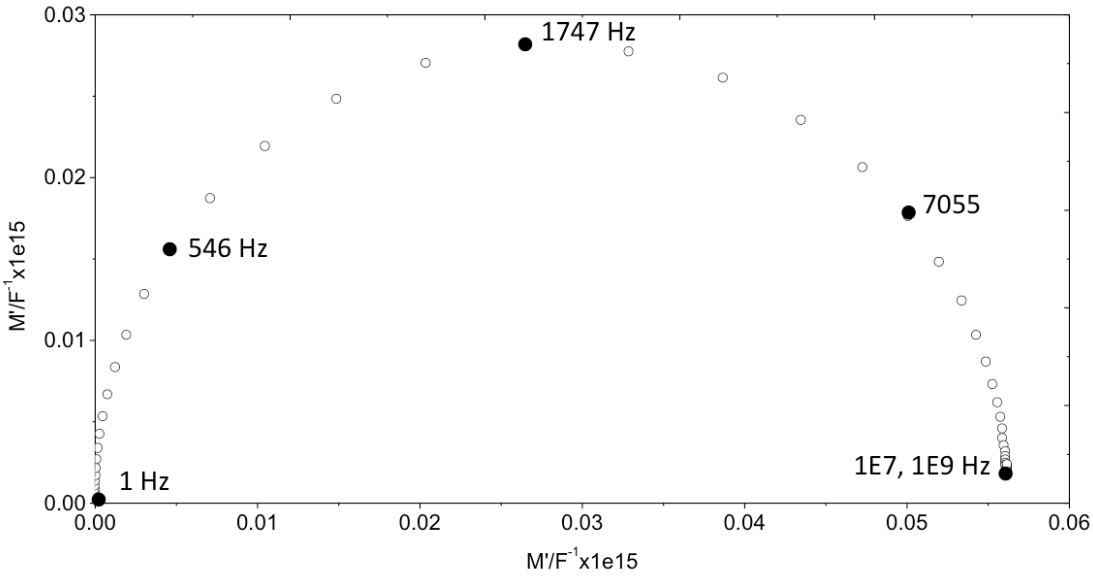

Fig. 12. *Modulus Nyquist plot of the parallel layer model with frequencies of interest indicated.*

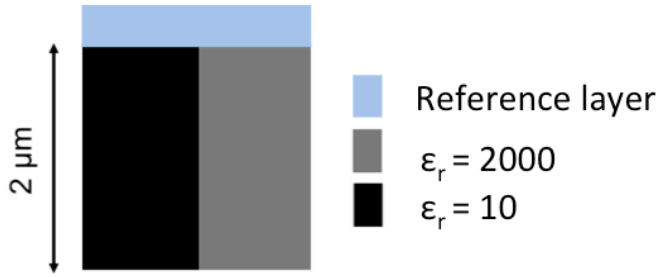

Fig. 13. *Schematic of the PLM with the location of the reference layer.*

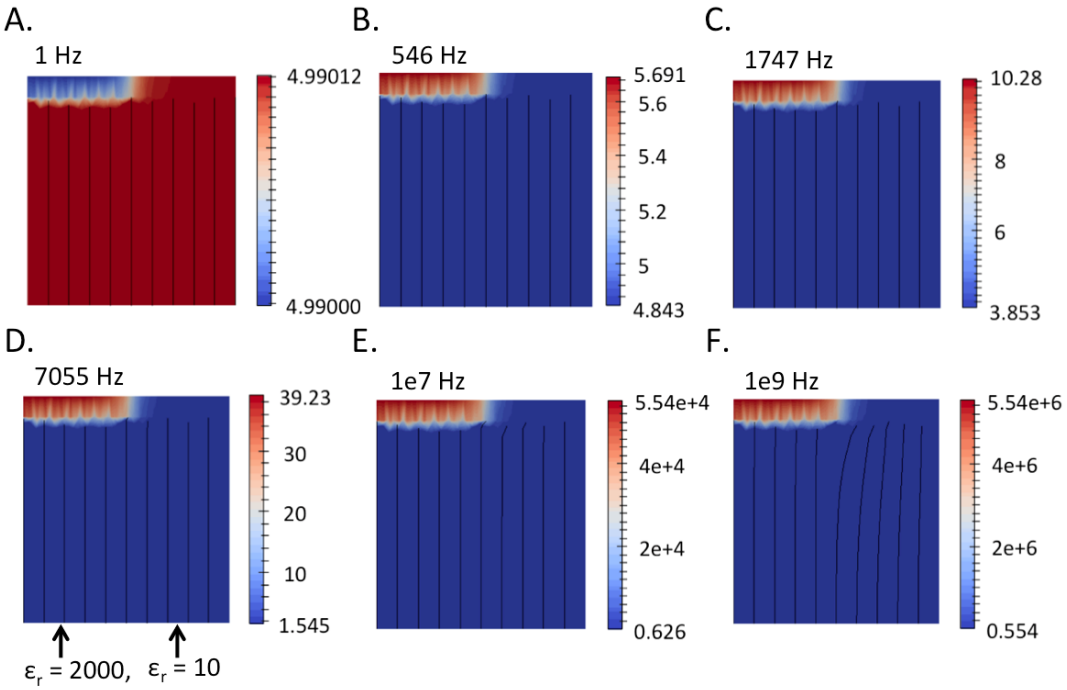

Fig. 14. *Current density plots of a parallel layer model with equal volume fractions of high and low permittivity material taken at the indicated frequencies. A stream trace of the current density vector field is plotted as black lines. These plots were taken at the instance of maximum current on the current sinusoids. Units are Am^{-2}. Note that the range of current density is frequency dependent and is much greater as frequency increases.*

The stream trace of current density deviated from uniformity at high frequencies. This implies that there was some heterogeneous current density in the parallel layers, not just within the reference layer. Altering the visualisation software's scale so that it was not dominated by the high current density in the reference layer revealed a higher concentration of current density at the interface between the parallel layers (see fig. 15A). This effect is more pronounced at higher frequency (see fig. 15B). Here the contours of current density show preferential current flow from the interface to the high permittivity layer.

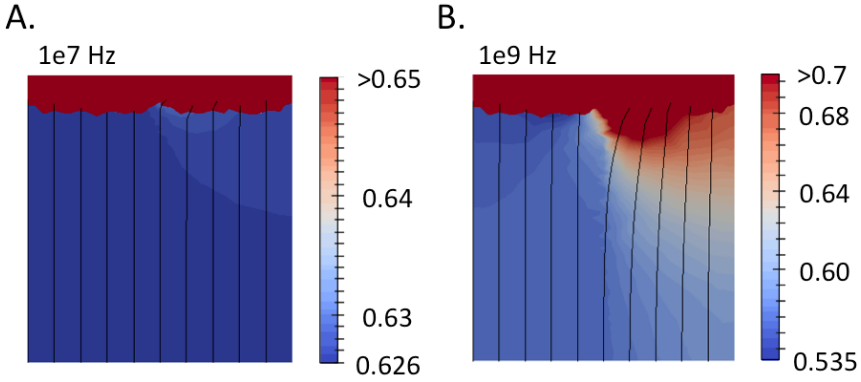

Fig. 15. *Current density plots of a parallel layer model with equal volume fractions of high and low permittivity material taken at the frequencies indicated. A stream trace of the current density vector field is plotted as black lines. These plots were taken at the point of maximum current on the current sinusoids. Units are Am^{-2}. Note: the scales have been manipulated from figure 13 to show detail at low current density.*

5.3.3. Encased Model

After comparing the purely series and purely parallel connectivity for materials with heterogeneous permittivity, the same methodology was employed for the encased model (see fig. 16A) with equal volumes of low and high permittivity material. Unlike the PLM and SLM, the encased model has no analytical solution. However, similarly to the SLM, two responses were observed in all impedance formalisms (see table 3 for summary) so a comparison was made with the analytical solution and equivalent circuit of the SLM (see fig. 16B).

Two well-defined arcs were visible in an impedance Nyquist plot (see fig. 16C). The low and high frequency arc diameters measured 3.885 and 1.090 GΩ, respectively. This did not agree with the prediction of equal arc diameters since the volume fraction of the core and shell are the same. Time constants calculated from R and C values extracted from impedance Nyquist plots gave 0.87 μs and 0.15 ms for the low and high frequency arcs, respectively. This is in good agreement with the values calculated for the SLM indicating that the high frequency response was due to the shell and the low frequency response was due to the core. This allowed the core to shell resistance ratio to be calculated. Using the resistance ratio to estimate the volume ratio gave a ϕ_{core} value of 0.78.

An electric modulus Nyquist plot was poorly resolved (see fig. 16D). While individual capacitances could not be extracted, the total capacitance was 0.743 fF, just over twice the value of the SLM's total capacitance (0.352 fF). Conductances extracted from the low and high frequency plateaus of the real part of the admittance spectroscopic plot (see fig. 16E) were 0.201 and 0.850 nS, respectively. These corresponded to the total conductance (low frequency) and shell conductance, respectively. This gave a deviation of the core to shell resistance ratio from the SLM predicted value, as found with the value extracted from the impedance spectra.

Two plateaus from a real capacitance spectroscopic plot (see fig. 16F) were extracted. The low frequency plateau measuring 17.88 fF was in good agreement with the equivalent circuit, but lower than the analytical value for C2. This is consistent with the behaviour displayed by the SLM, where the E' plateaus are composites of all R and C terms for a dual RC circuit. The high frequency plateau had a value of 0.76 fF, which is more than double the 0.352 fF measured for the same plateau of the SLM.

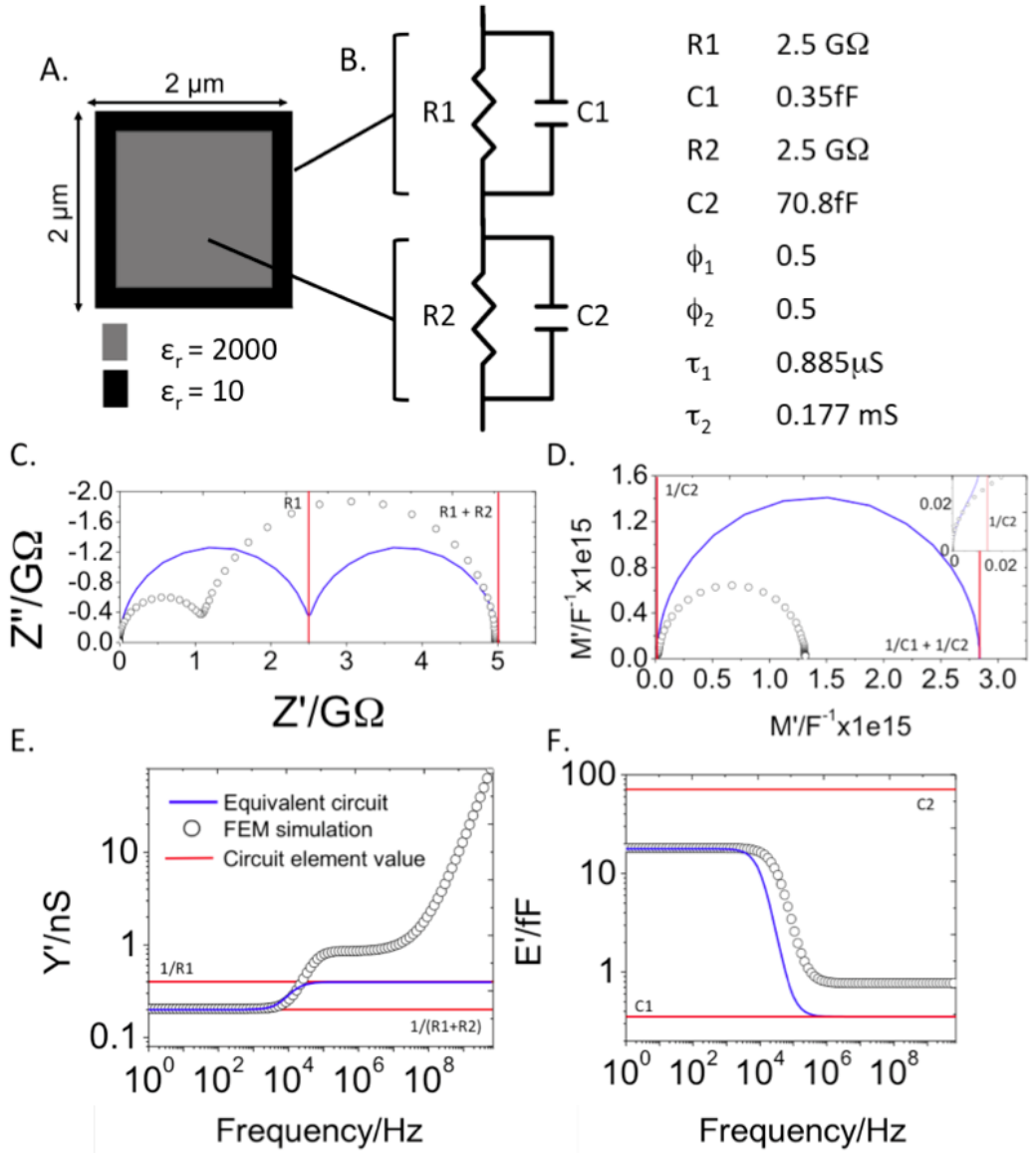

Fig. 16. (A) *Physical microstructure of the encased model.* (B) *Equivalent circuit used to model the SLM with resistance and capacitance values of individual circuit elements, the volume fractions and time constants of the low and high permittivity layer (ϕ_1, ϕ_2, τ_1 and τ_2, respectively). FEM simulated impedance spectra for the encased model with equivalent circuit fit (blue line) and intercepts for equivalent circuit element values (red lines) plotted as:* (C) *an impedance Nyquist plot,* (D) *modulus Nyquist plot,* (E) *real part of admittance spectroscopic plot and* (F) *real part of capacitance spectroscopic plot. Note: the equivalent circuit fit and intercept values are for the SLM with equal volumes of low and high permittivity material.*

Table 3. *Comparison of analytical values for both RC elements used to model the SLM with values extracted from simulation by equivalent circuits and a simulation of the encased model by FEM. Note* C_t *denotes the total capacitance of the model.*

Circuit element	Element value	Formalism	FEM extracted values	Equivalent circuit extracted value
R1	2.500 GΩ	Z*	1.090 GΩ	2.503 GΩ
		M*	1.170 GΩ	2.503 GΩ
		Y'	1.177 GΩ	2.525 GΩ
		E'	-	-
C1	0.354 fF	Z*	0.798 fF	0.337 fF
		M* (C_t)	0.743 fF	0.352 fF
		Y'	-	-
		E'	0.760 fF	0.352 fF
R2	2.500 GΩ	Z*	3.885 GΩ	2.497 GΩ
		M*	-	-
		Y'	3.798 GΩ	2.475 GΩ
		E'	-	-
C2	70.80 fF	Z*	29.58 fF	64.31 fF
		M*	-	-
		Y'	-	-
		E'	17.88 fF	17.79 fF

Viewing the electrical microstructure of the encased model as current density plots showed that the electrical microstructure did not resemble the physical microstructure. Current density plots were taken at 1 Hz and at the low and high frequency Debye frequencies on the encased model's impedance Nyquist plot (see fig. 17A). At 1 Hz the current density is slightly concentrated in the core region but current leakage into the parallel component of the shell can be observed (see fig. 17B). A stream trace at this frequency showed that there was no curvature in the current density vector field. At the frequency that corresponded to the low frequency Debye response the current density is concentrated in the series shell component directly above the core (see fig. 17C). There is a notable decrease in current density in the series shell that is adjacent to the parallel component of the shell. This is reinforced by the stream trace showing slight bending away from the parallel shell component. Finally at a frequency associated with the high frequency Debye response the current density is seen to be also concentrated in the series shell directly connected to the core (see fig. 17D). Here the stream trace shows a preferential pathway avoiding the parallel shell.

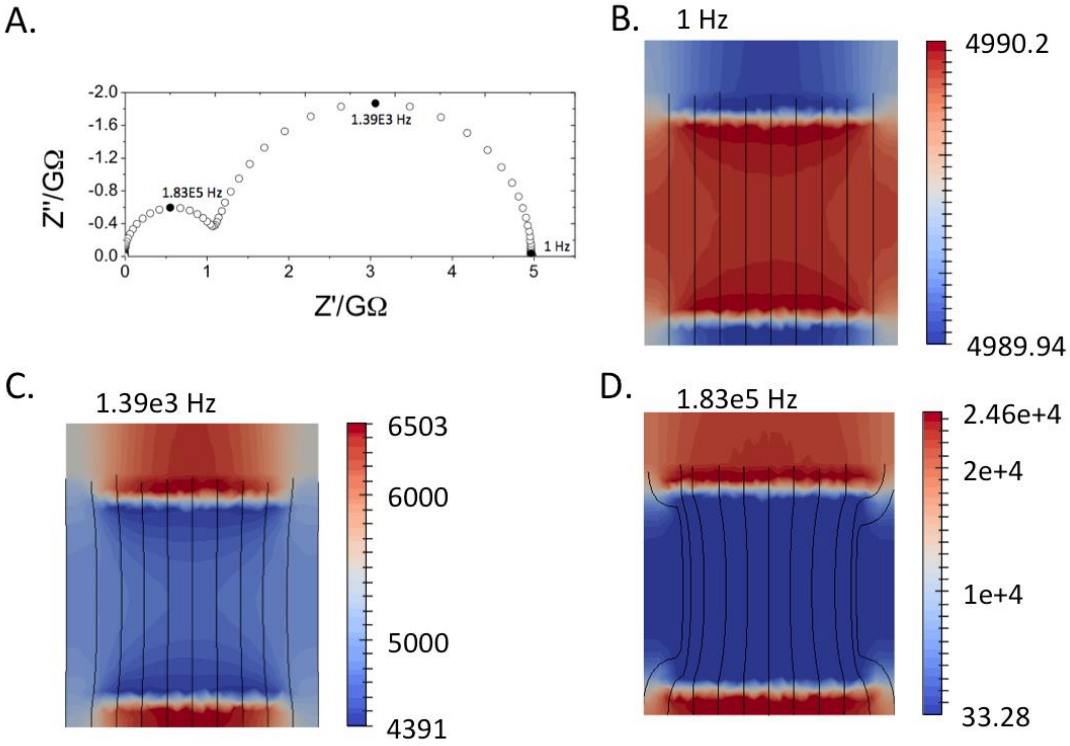

Fig. 17. *Current density plots of an encased model with equal volume fractions of high and low permittivity material taken at the indicated frequencies. A stream trace of the current density vector field is plotted as black lines. These plots were taken at the instance of maximum current on the current sinusoids. Units are* Am^{-2}*. Note: the range of current density is frequency dependent and is much greater as frequency increases.*

5.3.4. Encased Model Volume Fraction

In the previous chapter, volume fractions of the core and shell material of an encased model were estimated from the core to shell capacitance ratio, where the permittivity of both materials was fixed and the core was more conductive than the shell. It was established that, as the physical microstructure was altered by increasing ϕ_{core}, the error in extracting ϕ_{core} from the capacitance ratios was reduced. Here this methodology is extended to an encased model where the conductivity of the core and shell material is fixed and the core has a higher permittivity than the shell. From the methodology of this chapter it is demonstrated that calculating resistance ratios from impedance Nyquist plots is more appropriate for estimating volume fractions for physical microstructures where the conductivity is homogenous throughout and the permittivity varies depending on the material region. For clarity, the results obtained for this chapter will be referred to as the fixed conductivity case and those obtained in chapter four as the fixed permittivity case.

A fixed conductivity encased model with the same material properties as the SLM, PLM and encased models with equal volume fractions examined earlier in this chapter had its ϕ_{core} value varied from 0.02 to 0.98. At each volume fraction the impedance response was simulated by FEM and a resistance ratio was calculated from the impedance Nyquist plots. Applying the time constant analysis used for the

encased model discussed previous in this chapter, the low frequency resistance (R2) was assigned to the core and the high frequency (R1) resistance assigned to the shell. The Ratio of R1 to R2 was used to calculate ϕ_{core} using:

$$\phi_{core} = \frac{R2}{R1 + R2} \tag{5.2}$$

For the fixed permittivity case, all values of ϕ_{core} extracted from resistance ratios (ϕ_{core} output) were greater than the exact value (ϕ_{core} input). The trend of the output ϕ_{core} with input ϕ_{core} for the fixed conductivity case was identical to the trend observed for the fixed permittivity case (see fig. 18). Resistances predicted by an analytical model based on the electrical microstructure of the encased model, neglecting the parallel shell component (see figs. 17D and 19), called the series brick layer model (SBLM) could not fit the difference between the known volume fraction and that estimated from resistance ratios.

The agreement between the fixed permittivity and conductivity cases also extended to the conversion of the error in ϕ_{core} estimated by resistance or capacitance ratios into a percentage of ϕ_{core} input (see fig. 20). For the fixed conductivity case with ϕ_{core} input values of ≥ 0.8, the deviation of ϕ_{core} output was less than 20%. This deviation increased to 192% for ϕ_{core} input = 0.1 in good agreement with the fixed permittivity case. Plotting the difference between the output values of ϕ_{core} and values predicted by the SBLM for the fixed conductivity case also showed the same trend with the fixed permittivity case (see fig. 21).

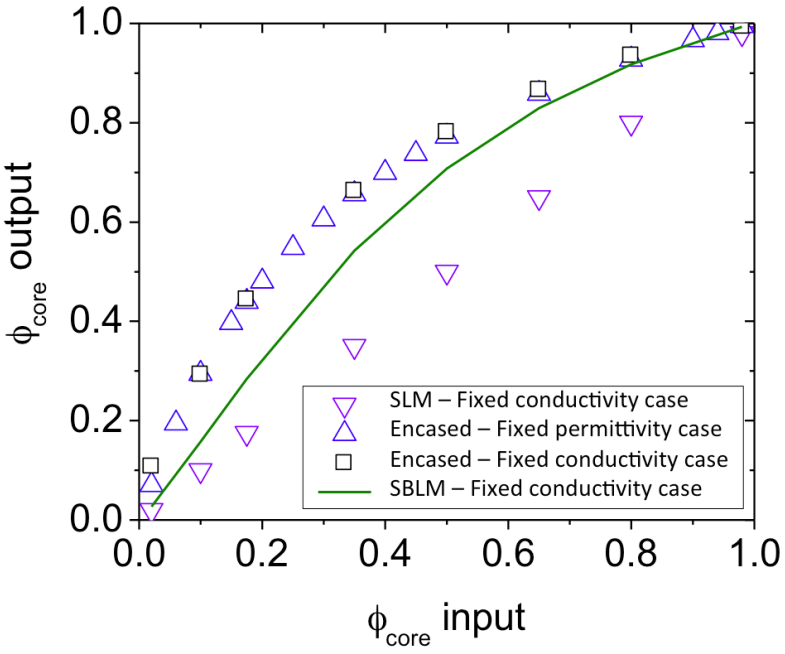

Fig. 18. *ϕ_{core} values extracted from resistance ratios of the simulated impedance spectra for the SLM and encased model against the known (input) values of ϕ_{core}. Note: the line for the ϕ_{core} values extracted from capacitance values for the encased model with a fixed permittivity in the core and shell regions studied in chapter 4 (blue triangles). A line for the SBLM predicted values is plotted in green.*

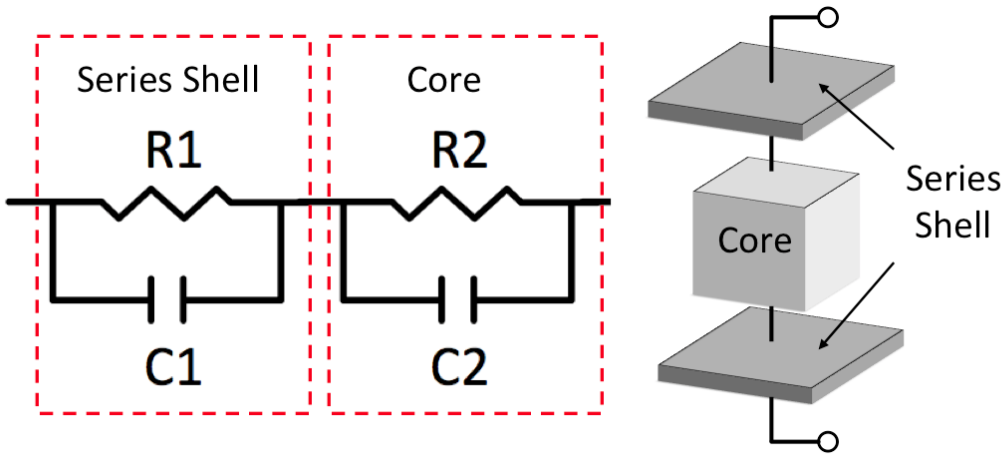

Fig. 19. *Schematic showing how the equivalent circuit for the series brick layer model is derived from the microstructure of the encased model.*

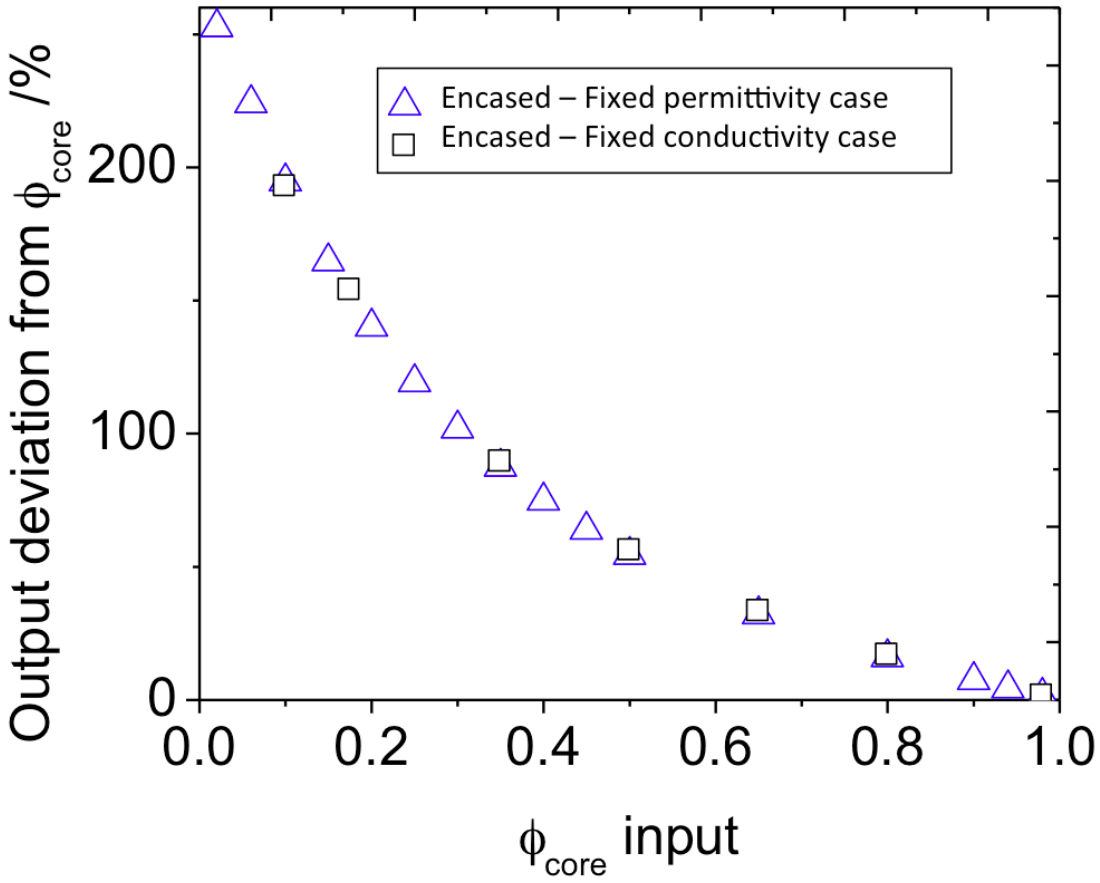

Fig. 20. *Extracted ϕ_{core} values as a percentage of the known (input) ϕ_{core} values against the known ϕ_{core} values for the encased model. Note: the line for the ϕ_{core} values extracted from capacitance values for the encased model with a fixed permittivity in the core and shell regions studied in chapter 4 (blue triangles).*

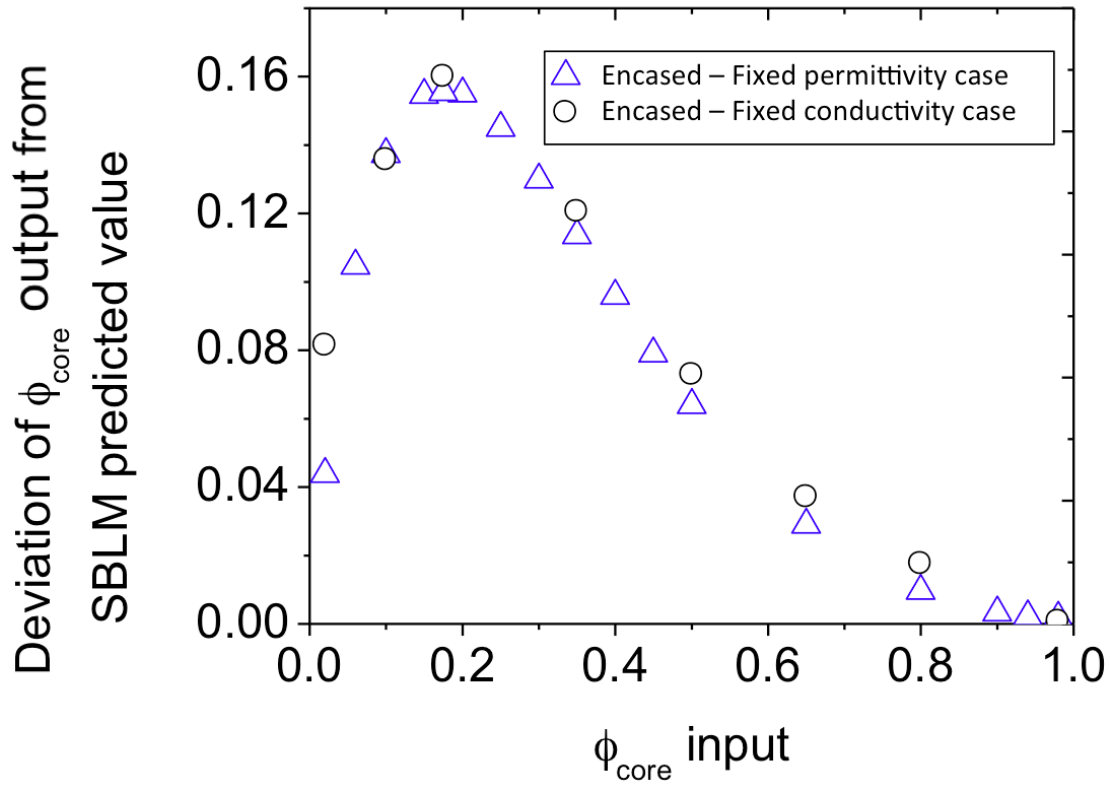

Fig. 21. *Deviation of the encased model from series brick layer model predicted values. Note: the line for the ϕ_{core} values extracted from capacitance values for the encased model with a fixed permittivity in the core and shell regions studied in chapter 4 (blue triangles).*

Current density plots for an encased model with a large core (ϕ_{core} = 0.8) and a small core (ϕ_{core} = 0.1) were obtained at low frequency (1 Hz) and at the Debye frequencies (see fig 22A and 23A). Previously it was found (in chapter four) that the electrical microstructure changed considerably with ϕ_{core}. For the encased model with ϕ_{core} = 0.8, at 1 Hz there was a slight concentration of current density in the core and parallel shell component (see fig. 22B). Although the change in current density concentration can be visualised, it is only of the order of 1 mAm^{-2}. A stream trace showed the current density vector field was straight.

At the low frequency Debye response, the highest concentration of current density is within the series component of the shell material (see fig. 22C). There was also a noticeable concentration in the parallel shell (although the magnitude was slightly less than in the series component). Here a stream trace showed a small amount of curvature towards the core material. The current density of the high frequency Debye response was concentrated in the series shell with significantly lower current density within the core and parallel shell (see fig. 22D).

Stream tracing revealed the vector field avoiding the parallel shell in favour of the higher permittivity core.

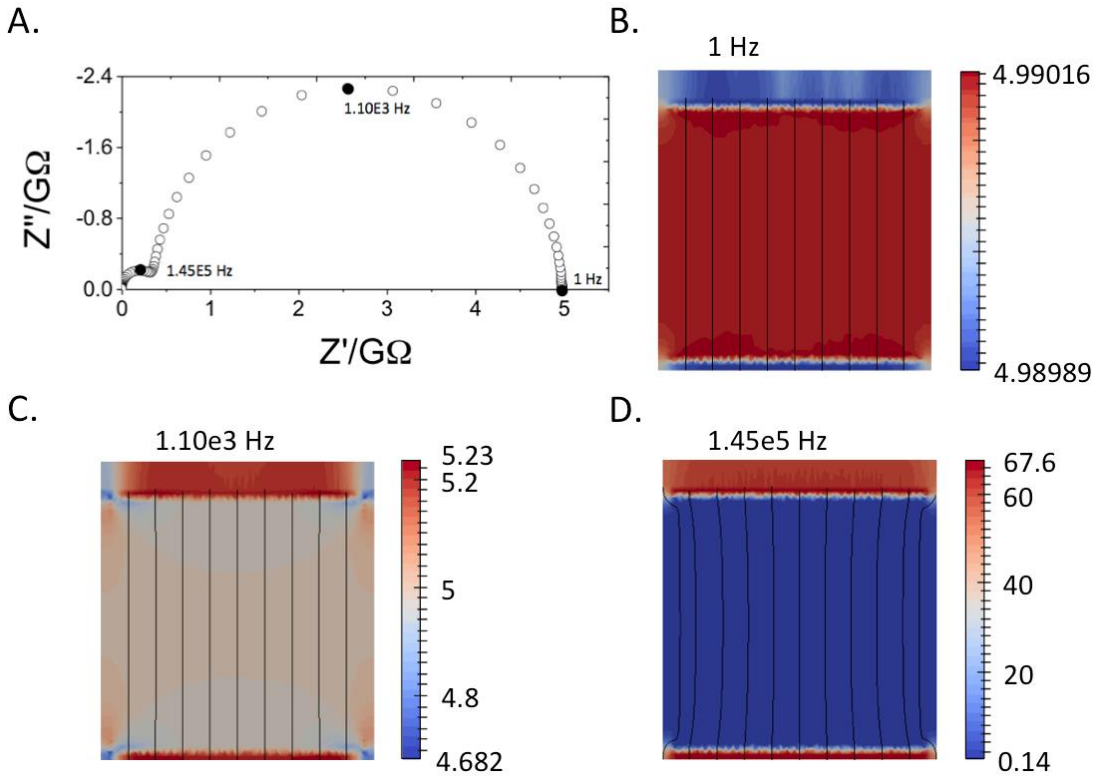

Fig. 22. *Current density plots of an encased model with a large core (ϕ_{core} = 0.8) taken at the indicated frequencies. A stream trace of the current density vector field is plotted as black lines. These plots were taken at the point of maximum current on the current sinusoids. Units are Am^{-2}. Note: the range of current density is frequency dependent and is much greater as frequency increases.*

The encased model with a smaller core (ϕ_{core} = 0.1) also had two arcs in an impedance Nyquist plot (see fig. 23A). The low frequency arc was now larger than the high frequency arc. The current density at 1Hz again had a slight increase in current density in the core region, however there was not as much in the parallel shell as in the larger core model (see fig. 23B). The stream trace was straight. The current density at the low frequency Debye response was concentrated in the series shell but was more heterogeneous than that for the larger core model (see fig. 23C). A stream trace of current density showed increased bending towards the core. Finally, the high frequency Debye response current density was also concentrated in the series shell component (see fig. 23D). The current density was both more heterogeneous and the stream trace showed more curvature than that for the low frequency Debye response.

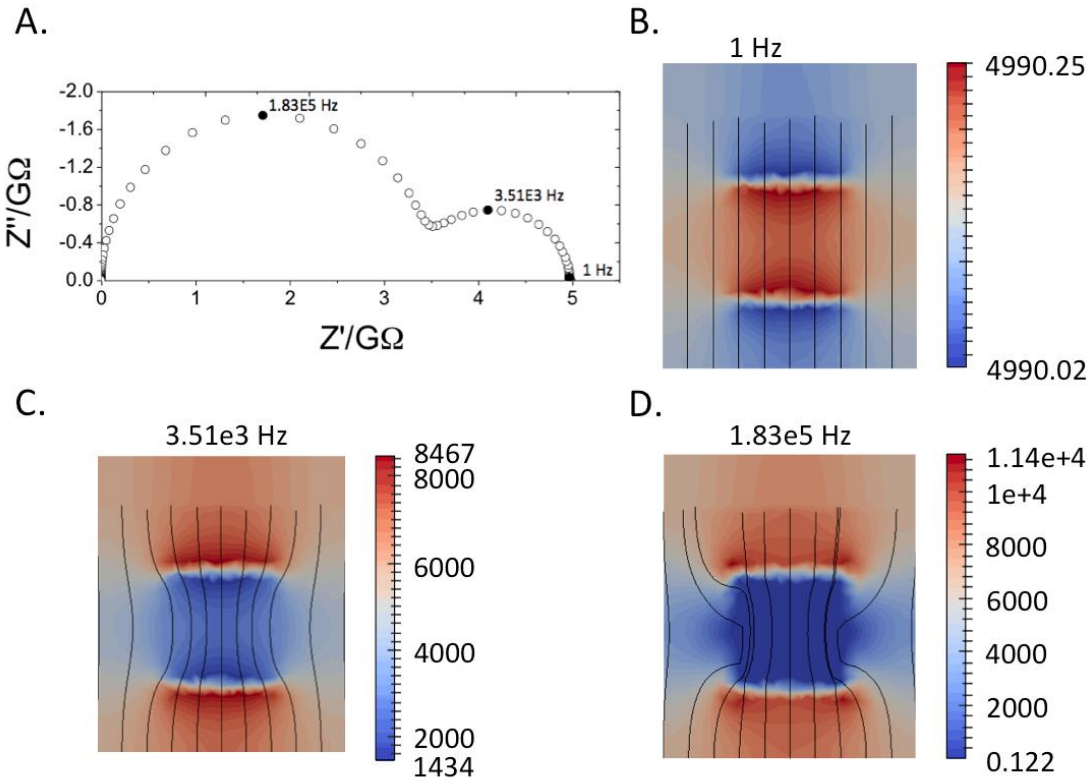

Fig. 23. *Current density plots of an encased model with a small core (ϕ_{core} = 0.1) taken at the indicated frequencies. A stream trace of the current density vector field is plotted as black lines. These plots were taken at the point of maximum current on the current sinusoids. Units are Am^{-2}. Note: the range of current density is frequency dependent and is much greater as frequency increases.*

5.4. Discussion

Comparing the impedance response of the SLM, PLM (see figs. 6 and 11) and encased models for the case where there are equal volumes of low and high permittivity material gives an insight into how heterogeneity in permittivity can affect series and parallel pathways in microstructures. All three physical microstructures were modelled using two parallel RC elements connected in series (SLM and encased model) or parallel (PLM) as appropriate. The low permittivity material was assigned the R1C1 element and the high permittivity material the R2C2 one. In the discussion section these material regions will be referred to as the low and high permittivity material, respectively. For the SLM, two responses were observed whereas for the PLM only one response was present. These responses agree with equivalent circuit calculations based on simple circuit theory (see tables 1 and 2). It is important to note that the PLM collapses into a single response with a composite value of both RC elements added in parallel.

The encased model is similar to the SLM in that it has two impedance responses (see fig. 16). Extracting capacitances from impedance Nyquist plots it was found that the magnitude of the high and low frequency responses of the encased model (0.798 and 29.85 fF, respectively) did not match the SLM values (0.346 and 73.49 fF, respectively) but are of the same order of magnitude. Individual capacitances could not be obtained for the PLM but a value for the total

capacitance could be obtained from the electric modulus formalism, measuring 17.79 fF. Obtaining the total capacitance for the SLM and the encased model by the same method gave values of 0.352 fF and 0.743 fF, respectively. For the SLM and encased model the lower capacitance values dominate the total capacitance, whereas for the PLM the higher capacitance dominates. As capacitors add in parallel and add reciprocally in series, the lower total capacitances of the SLM and encased models are consistent with series pathways dominating within the encased model. The encased total capacitance is larger than that of the SLM due to the reduction in thickness of the shell presented to the applied potential difference than the thicker layer of the SLM (see fig. 24).

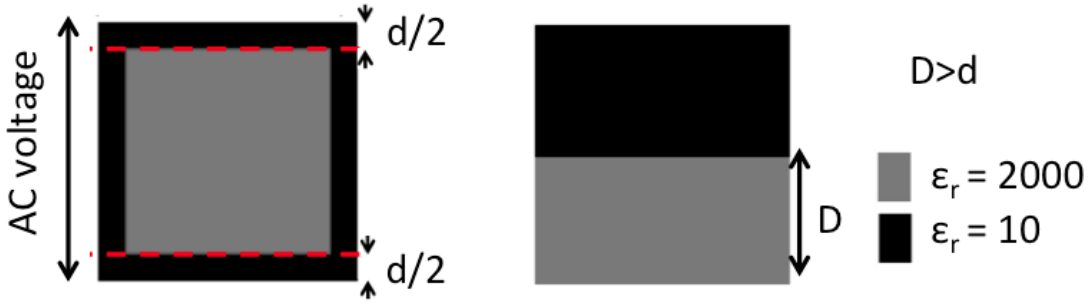

Fig. 24. *Schematic showing the difference in thickness of the low permittivity material presented to the applied potential difference between the encased and series layer model for a given core volume fraction.*

Since the magnitude of the two resistances of the encased model (3.885 GΩ and 1.090 GΩ for the low and high frequency response, respectively) do not agree with those of the SLM (2.510 GΩ and 2.490 GΩ) and the low frequency resistance of the core material is larger than the high frequency resistance of the shell, we conclude that the whole volume of the shell is not contributing fully to the impedance response. Combining this with the evidence of a series pathway through the encased model suggests a similar effect to that encountered in the previous chapter where a conductivity difference in the physical microstructure of the encased model led to an alteration of the electrical microstructure.

Examining the electrical microstructure of the three configurations (figs. 8, 14 and 17 for the SLM, PLM and encased model, respectively) allowed us to visualise the series and parallel pathways through the microstructure. For the SLM at very low frequency (1Hz) the current density was slightly concentrated in the high permittivity material (see fig. 25A). At both the low and high frequency (f_{max}) Debye response the current density was concentrated in the low permittivity layer (see figs. 25 B and C, respectively). The stream trace of the SLM current density was straight at all frequencies as would be expected from purely series connectivity with no alternative pathways available. The stream trace halted at the interface between layers at the high frequency f_{max} Debye response. Reversing the initial position of the tracer particles confirmed this to be an interface related effect.

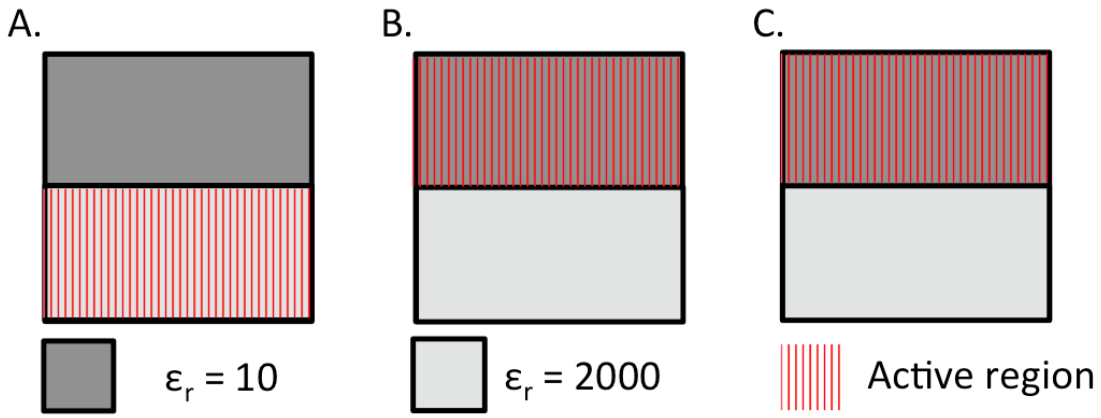

Fig. 25. *Schematic showing how the electrically active region in the SLM varies with frequency. (A) At 1Hz, (B) at f_{max} of the low frequency Debye response and (C) at f_{max} of the high frequency Debye response.*

For the PLM, the current density was generally homogeneous and its vector field straight at most frequencies. This is consistent with the parallel model simulated by Padurariu[7]. Some heterogeneity could be observed in the reference layer. To understand why this results in a single impedance arc we must examine the electrical microstructure of the PLM. Only at very high frequency can we see heterogeneity in the current density outside the reference layer (visible just to the right of the interface, see fig. 26A). If the scale is altered to stop the current density in the reference layer dominating the plot, current density can be seen building up at the interface between the reference layer and the low permittivity layer appearing to flow towards the high permittivity layer (see fig. 26B).

Changing the plot to show the locations of the two materials and then examining the stream trace shows this effect more clearly (see fig. 26C). If a stream trace is close enough to the interface it will cross it. Note the starting position of the stream trace has been changed to be just under the reference layer to show current flow from the reference layer better. Usually changing the starting position of the stream trace has no effect, however the current density is asymmetrical, resulting in an asymmetrical stream trace. Finally, a line scan of current density across the interface (see fig. 26D) shows the increase in current density in the high permittivity layer just left of the interface, confirming that current density leaks into the low permittivity layer at high frequency. It is possible that, if the frequency were increased further, the current would become more heterogeneous and an additional response would become visible in the impedance spectra. To obtain fig. 26 the frequency was in the region of GHz and therefore well outside the range used experimentally and the frequency range where the assumptions underpinning the FEM code hold. The heterogeneity observed was also very small. The difference between the maximum and minimum current density outside the reference layer was less than $0.4 Am^{-2}$. For the permittivities considered, the effect of parallel capacitive pathways is minimal over the frequency range of interest.

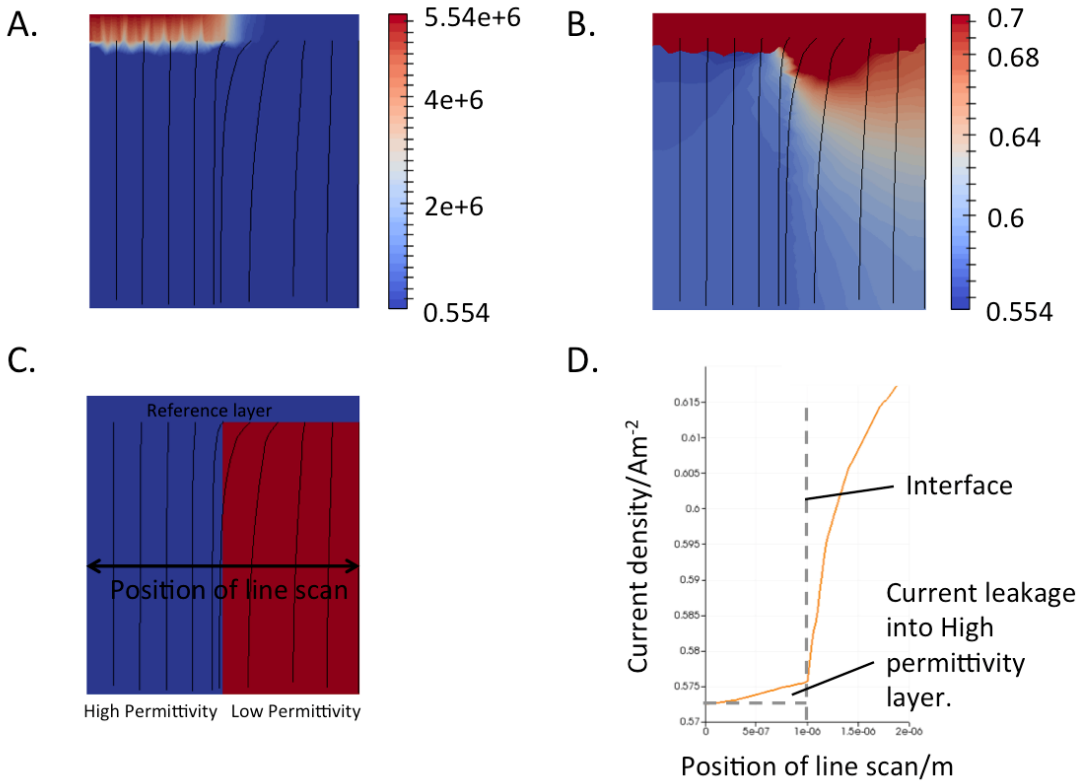

Fig. 26. (A) *Current density plot of PLM at 1 GHz where the scale is current density in* Am^{-2} *and is logarithmic and stream traces in black.* (B) *Same plot with high current density removed from the scale to better show current heterogeneity outside the reference layer; scale is current density in* Am^{-2} *and is linear.* (C) *Plot of material type with 1GHz stream trace and line scan position overlaid.* (D) *Current density versus position on line scan for PLM at 1 GHz.*

The current density of the encased model showed complex behaviour. At 1 Hz the current density was slightly concentrated in the high permittivity core region, similarly to the SLM, however the marginal increase of current density also extended into the parallel component of the shell (see fig. 27A). A current density plot of the frequency associated with the low frequency Debye response showed current density concentrating in the series shell component adjacent to the core but it did not spread to the series shell above and below the parallel component of the core (see fig. 27B). For the high frequency Debye response, the current density was still concentrated in the series shell but had spread across the whole of the series component (see fig. 27C). This can also be compared to the electrical microstructure visualised by Padurariu *et al*. One of their simulations considered a cube of low permittivity material with high permittivity spherical inclusions. A concentration of electric field was observed in the low permittivity matrix perpendicular to the applied potential between the inclusions[7]. This area is equivalent to the series shell component in this work.

The frequency-dependent configuration of heterogeneous current density in the encased model is explained by a stream trace analysis. At low frequency, the stream trace is straight implying a uniform current flow (see fig. 28A). Here the frequency is too low for capacitive pathways to form, from equation (5.1). Hence the conductive pathways dominate. As the core and shell conductivity is equal,

only straight conduction pathways are available and the current density builds up in the core due to its higher time constant. At the first Debye response, the capacitive pathways in the core region become favourable before those in the shell due to the higher permittivity of the cores. As the impedance of the core capacitive pathways is only marginally greater than the pathways available in the shell, some conductive pathways remain through the parallel component of the shell (see fig. 28B). This would explain why current density only builds up adjacent to the core. It can still flow through the parallel shell. For the high frequency Debye response, the impedance of the capacitive pathways through the core has become so low that the capacitive pathways curve into the core, by-passing the parallel shell (see fig. 28C). Current density now concentrates in the series shell. The contribution (and equivalent circuit fitting) of the parallel shell's impedance response in the encased model is evaluated in depth in the next chapter.

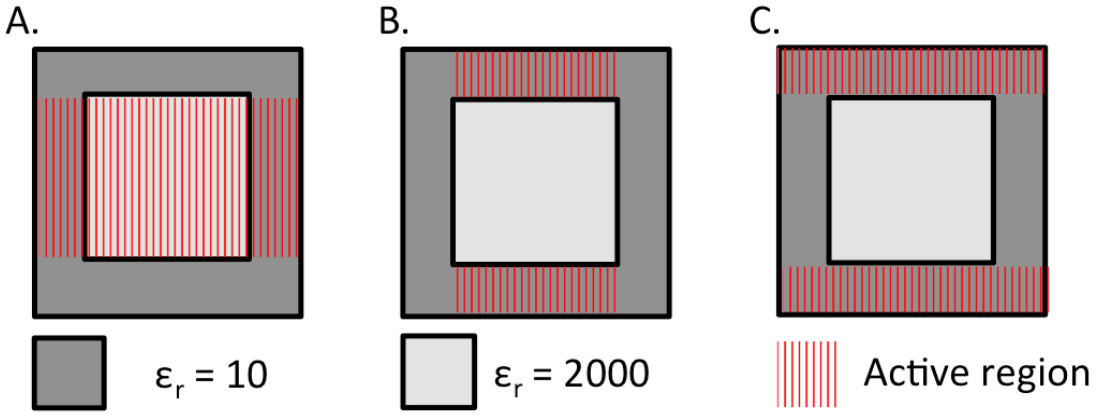

Fig. 27. *Schematic showing which components of the encased model are electrically active at key frequencies.* (A) *1 Hz,* (B) *the low frequency Debye Response and* (C) *the high frequency Debye response.*

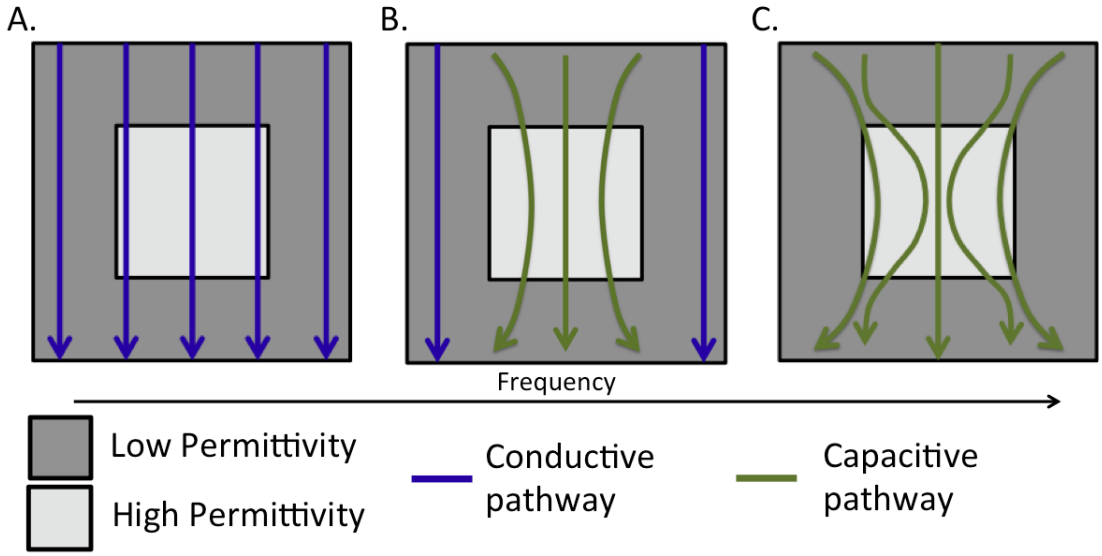

Fig. 28. *Schematic showing where conductive and capacitive pathways form in the encased model as frequency increases.* (A) *1 Hz,* (B) *the low frequency Debye Response and* (C) *the high frequency Debye response.*

Due to the current density heterogeneity, the electrical microstructure of the encased model did not resemble the physical microstructure. The features of

the electrical microstructures of models with a homogenous conductivity and varied permittivity were not as simple as those presented in chapter four. We recall that, for the fixed permittivity case, the low and high Debye f_{max} values of the models correspond with low and high conductivity regions being electrically active[8]. The fixed conductivity with varied permittivity models presented here appear to show a transition from the core to the series shell for the low frequency Debye response and a stronger signal from the series shell for the high frequency response.

Assuming that the low frequency response is mainly due to the core and that the high frequency response is due to the shell, which agrees well with the time constants for the two materials, there are similarities to the encased models in chapter four. Extracting a core volume fraction (ϕ_{core}) from core-shell resistance ratios of the fixed conductivity case simulations (as detailed in the methodology section) gave a ϕ_{core} value of 0.78 for the encased model with equal volume fractions of core and shell. Note that this is the same value as that extracted for an encased model from the fixed permittivity case using capacitance ratios (in chapter four), where the volume of core and shell are the same. The high frequency shell response discussed in this chapter shared the reduced impedance contribution of the parallel shell observed in the low frequency encased shell response in chapter four. Clearly the preferential pathway through the series shell and the evidence in capacitance magnitudes pointing to series connection dominated behaviour show that the two systems have much in common.

Repeating some of the encased models with variable core-shell volume fractions but with fixed conductivity and extracting ϕ_{core} values from resistance ratios showed near exact agreement with the trends observed for the fixed permittivity case (see figs 18, 20, 21). Current density plots also showed increased heterogeneity as ϕ_{core} decreased (see figs. 17, 22, 23). Thus, volume fractions can be accurately extracted from resistance ratios where ϕ_{core} is greater than 0.8. It is likely that the trends observed for the fixed conductivity case using a more qualitative analysis of distributions of conduction (or capacitive) path lengths would also agree well with those observed with the varied conductivity case. Before undertaking a more robust analysis of electrical microstructure vector data there are important issues that must be resolved.

When plots of the electrical microstructure are produced, they are taken at specific frequencies, either at the maximum value for current or voltage (I_{max} or V_{max}) from the I-V sinusoids simulated by the FEM code to calculate impedance spectra (see fig. 29A). This approach has worked well for the fixed permittivity - varied conductivity case, as the low conductivity material was more active at the low frequency Debye response and the high conductivity material was more active at the high frequency Debye response. This agreed with the time constants for the two materials. For models of the fixed conductivity case with series connectivity (SLM and encased), there were two Debye responses present but current density plots taken at these frequencies showed concentration of current density in the low permittivity material. Given that the low frequency Debye response of the fixed conductivity models had a time constant associated with the high permittivity material, we would expect that the high permittivity material would have the greatest concentration of current density at the low frequency Debye point. The high permittivity material has only a very small concentration of current

density at much lower frequency (~ 1Hz) than the low frequency Debye, $f_{max,}$ contradicting this prediction.

It is possible that the maximum of current or voltage is not the correct point on the sinusoid to consider when studying electrical microstructure. When there are different permittivities present in the microstructure there are capacitive pathways that have different frequency dependencies. This creates a more complex dependence on frequency and therefore on time. The present approach does not adequately probe the electrical microstructure through all time steps simulated and may miss important features on a given sinusoid. Another possibility is that the FEM code is not simulating the exact current where we wish to interrogate it. The code simulates a finite number of time steps or data points for the applied voltage using a sinusoid. The current, due the phase difference to the applied voltage, does not perfectly align with the voltage sinusoid (see fig. 29B). This means that finding and simulating the exact maximum current plot is very hard. This is more of an issue when simulating the extreme case of composites with homogenous conductivity and mixed permittivity. This may be a limitation of the FEM approach used in this work. Additional work could clarify whether specific points on a sinusoid or an average of electrical microstructure over a whole sinusoid would be a better option for vector data analysis.

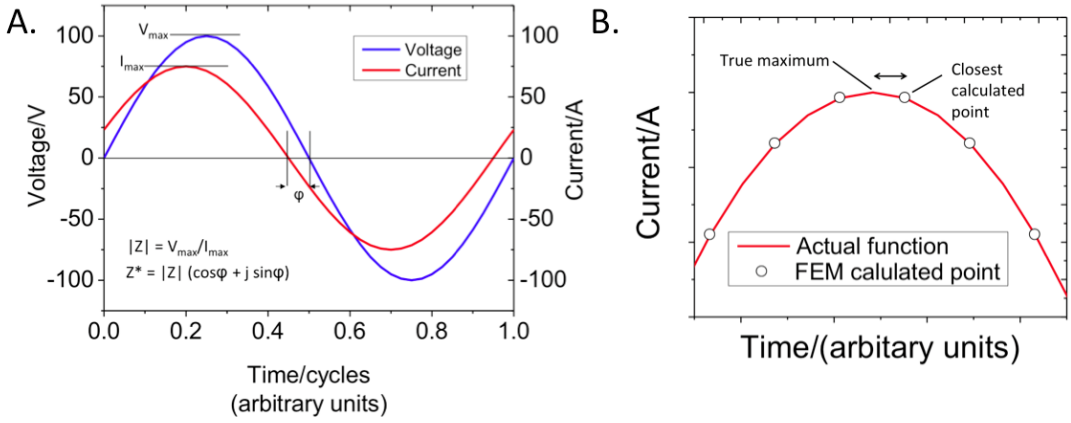

Fig. 29. (A) *Current and voltage sinusoids used to calculate the total impedance of a given model.* (B) *Schematic of an enlargement of the current maximum where points calculated by the FEM program will not be exactly at the maxima of the sinusoid.*

5.5. Conclusions

Electrical composites with homogenous conductivity and heterogeneous permittivity have been investigated. Several simple microstructural configurations have been simulated and their impedance spectra analysed. A method of extracting volume ratios from capacitance ratios has been extended to use resistance ratios. Key findings are:

- When a material has regions with different permittivities but the same conductivity the electrical microstructure can be affected by the configuration of the physical microstructure. This is caused by capacitive pathways forming between the regions that are electrically active at a given frequency due to their time constants.

- Capacitive pathways can alter the electrical microstructure so that it no longer resembles the physical microstructure, which can cause complications when applying a brick work layer model analysis to impedance data.
- Series capacitive pathways have a greater effect on electrical microstructure than parallel ones given that the magnitude of the total capacitance for both the SLM and encased simulation tended towards a lower value, implying reciprocal addition of capacitors in series.
- It is more effective to extract volume fractions from resistance ratios than from capacitance ratios when permittivity varies and conductivity is fixed.
- Similar trends emerge when the core volume fraction of an encased model is varied and its value extracted from resistance ratios as the case where conductivity is varied and permittivity is fixed for the same microstructure. The brick layer model therefore works well for modelling the impedance response of the varied permittivity encased model when the core volume fraction is > 0.7. Core volume fractions < 0.7 will have errors > 25% when extracted using resistance ratios.

5.6. References

1. E. J. Abram, D. C. Sinclair, and A. R. West, "A strategy for analysis and modelling of impedance spectroscopy data of electroceramics: Doped lanthanum gallate," *Journal of Electroceramics,* 10[3] 165-77 (2003).

2. A. R. West, D. C. Sinclair, and N. Hirose, "Characterization of electrical materials, especially ferroelectrics, by impedance spectroscopy," *Journal of Electroceramics,* 1[1] 65-71 (1997).

3. S.-C. Jeon, C.-S. Lee, and S.-J. L. Kang, "The Mechanism of Core/Shell Structure Formation During Sintering of $BaTiO_3$-Based Ceramics," *Journal of the American Ceramic Society,* 95[8] 2435-38 (2012).

4. D. Hennings and G. Rosenstein, "Temperature-Stable Dielectrics Based on Chemically Inhomogeneous $BaTiO_3$," *Journal of the American Ceramic Society,* 67[4] 249-54 (1984).

5. M. J. Pan and C. A. Randall, "A Brief Introduction to Ceramic Capacitors," *Ieee Electrical Insulation Magazine,* 26[3] 44-50 (2010).

6. Y. G. Wu, X. H. Zhao, F. Li, and Z. G. Fan, "Evaluation of mixing rules for dielectric constants of composite dielectrics by MC-FEM calculation on 3D cubic lattice," *Journal of Electroceramics,* 11[3] 227-39 (2003).

7. L. Padurariu, L. P. Curecheriu, and L. Mitoseriu, "Nonlinear dielectric properties of paraelectric-dielectric composites described by a 3D Finite Element Method based on Landau-Devonshire theory," *Acta Materialia,* 103 724-34 (2016).

8. J. P. Heath, J. S. Dean, J. H. Harding, and D. C. Sinclair, "Simulation of Impedance Spectra for Core-Shell Grain Structures Using FiniteElement Modeling," *Journal of the American Ceramic Society,* 98[6] 1925-31 (2015).

9. J. R. Macdonald, "Impedance spectroscopy : emphasizing solid materials and systems," (1987).

10. J. C. Maxwell, "A Treatise on Electricity and Magnetism." Cambridge University Press, (2010).

11. J. S. Dean, J. H. Harding, and D. C. Sinclair, "Simulation of Impedance Spectra for a Full Three- Dimensional Ceramic Microstructure Using a Finite Element Model," *Journal of the American Ceramic Society,* 97[3] 885-91 (2014).

12. S. Associates, "http://www.scribner.com/software/general-electrochemistry/68-general-electrochemistr/376-zview-for-windows." in, Vol. 2016.

Chapter 6: Resolving Material Properties

In the previous chapter the effect of the microstructure was studied with fixed material properties. Here the microstructure is fixed and the material properties are varied. Having the benefit of knowing the assigned intrinsic material properties (conductivity and permittivity) allows us to compare directly to the extracted material properties using the standard methodology employed experimentally. By comparing the extracted values with the known values, it is possible to map out where material properties can be reliably extracted and what is the best methodology to do so.

6.1. Literature

Theoreticians have the luxury of choosing idealised parameters to input into their models. This approach has its merits as it can be much easier to analyse data and spot trends but the idealised parameters can be far from what could occur in the real world. An example is barium titanate which, depending on processing conditions and dopant chemistry, can lead to a wide range of electrical properties[1]. This work aims to investigate how different combinations of material properties can alter the impedance spectra and the confidence in the extraction of accurate material properties.

Typically, impedance spectra are analysed using equivalent circuits. The different electrical processes that occur within a material can be modelled by a network of capacitors, resistors and other circuit elements. An issue with using equivalent circuits is that it is possible to produce the same spectra with different equivalent circuits[2]. To get the correct equivalent circuit one must consider whether all physical processes are represented in the circuit. By comparing the impedance response of a material to the spectra of an equivalent circuit in multiple impedance formalisms it is possible to examine the impedance data with different weights. An example of this is the commonly used impedance (Z*) formalism, which is weighted towards large resistances. In contrast, the electric modulus (M*) is more weighted towards small capacitances. This principle has been used to characterise the electrical microstructure of positive temperature coefficient of resistance barium titanate[3]. Work by Abram *et al* selected an equivalent circuit that fitted doped lanthanum gallate samples better by using multi-formalism analysis[4].

In the field of electroceramics a popular equivalent circuit is two parallel resistor and capacitor elements (RC element) connected in series. This was originally proposed by Bauerle[5], and has been since referred to as the brick layer model. One RC element represents a grain boundary response; the other represents the bulk (grain) ceramic response (see fig. 1). The brick layer model (BLM) has been very successful in modelling ceramics with thin resistive grain boundaries as it considers only grain boundaries that are parallel to either the electrodes or the series pathway through the microstructure and neglects the grain boundaries that run perpendicular to the electrode (as the bulk ceramic would be an easier conduction pathway).

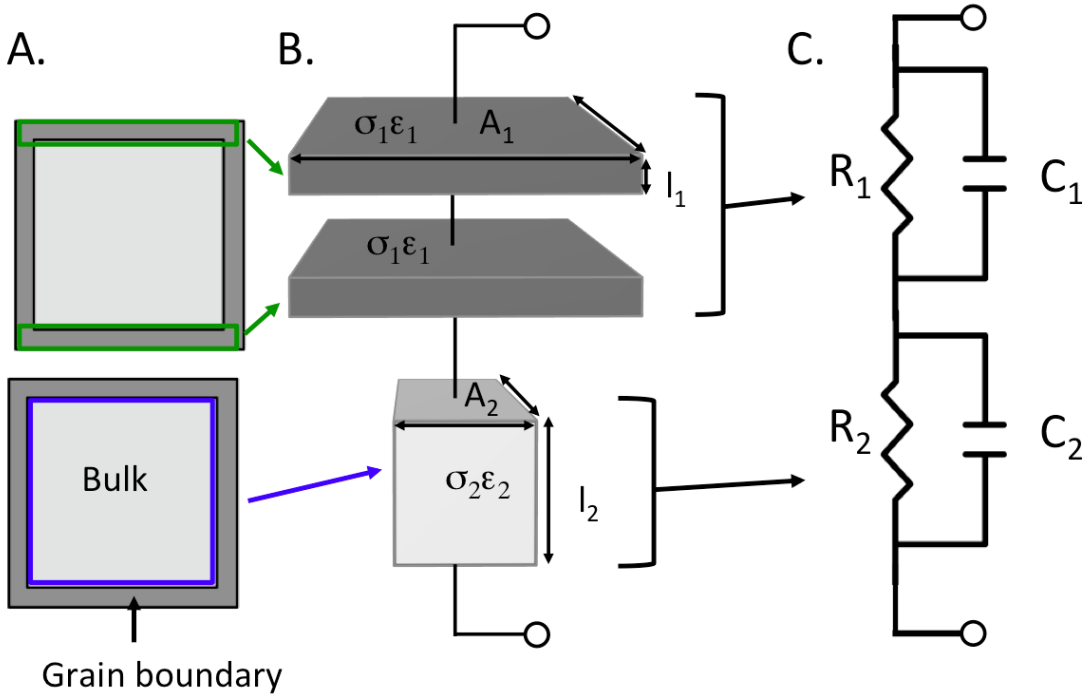

Fig. 1. *Schematic of the brick layer model where subscript 1 indicates grain boundary parameters and subscript 2 denotes bulk parameters.*

There have been attempts to modify the BLM to account for these parallel grain boundaries. For example, scenarios where the grain boundaries are thicker, reducing their effective resistance, and where the grain boundaries are a more conductive material than the ceramic bulk, parallel pathways may need to be accounted for. This parallel version of the BLM was first proposed by Näfe[6], who considered only conductivity, and was later extended by Hwang[7] to include dielectric properties. Hwang's work was concerned with nano-grain sized cerium dioxide. Here the grain boundary is of comparable thickness to the bulk grain. It is arguable that similar methods could be used to characterise core-shell microstructures, where the shell is thicker than a grain boundary and may have different electrical properties depending on the dopant chemistry and conditions of materials processing.

6.2. Methodology

6.2.1. Simulation of Material Properties

Previously, the effect of varying core-shell volume fractions on impedance spectroscopy was investigated[8]. It was found that, for a core volume fraction (ϕ_{core}) larger than 0.8, extracting volume fractions from capacitance ratios gave errors of less than ±25%. This study used idealised material properties for the core and shell region to aid simulation and analysis. The following work investigates the impact of varied material properties on impedance measurements for a core-shell like system. The physical microstructure was fixed as a nested cube configuration with a ϕ_{core} of 0.8. The core material properties were constant and based upon

semi-conducting barium titanate whilst the shell properties varied from being those of the core to a more resistive shell material (see fig. 2).

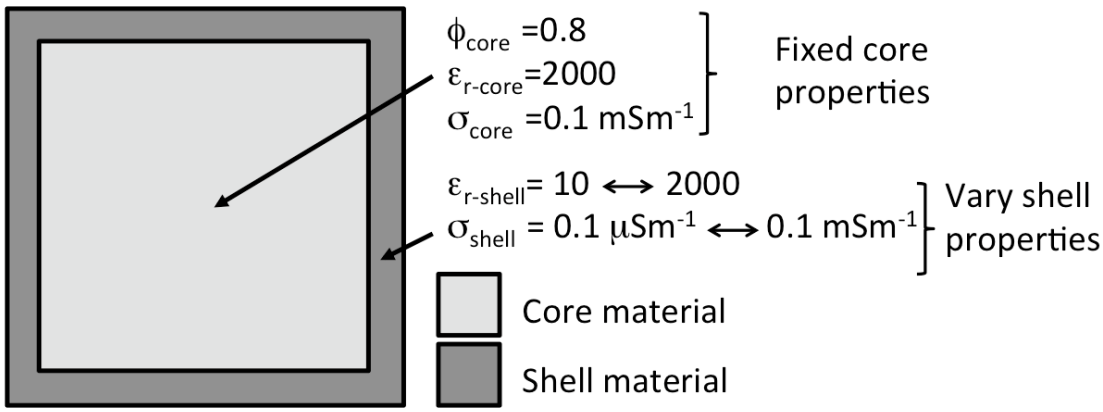

Fig. 2. *Schematic of the physical microstructure and the range of material properties simulated.*

It is important to note that the permittivity and the conductivity are varied simultaneously. A finite element simulation of the impedance response of the nested cube structure is conducted for each variation of conductivity and permittivity producing a two dimensional array of 100 points that will be referred to as a material property space. The frequency range simulated was 1 Hz to 10 MHz based upon experimental practice. More data points were gathered in the region where the core and shell time constants were similar, in an attempt to better resolve the behaviour (see fig. 3).

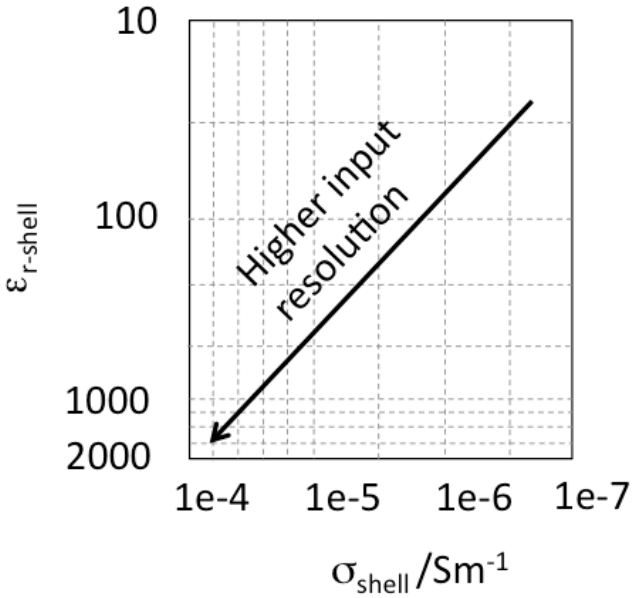

Fig. 3. *Schematic showing the placement of more simulations on the material property space where the core and shell properties become similar.*

6.2.2. IS analysis and Equivalent Circuits used

FEM-simulated impedance spectra were analysed using Nyquist plots of impedance (Z*) and electric modulus (M*). Spectroscopic plots of the real component of the complex admittance (Y') and the real component of complex capacitance (E') were also used. While this is not the full set of available impedance formalisms, this analysis is sensitive to capacitances and resistances of varying magnitude (see table. 1) whilst keeping the data analysis of a large system manageable.

Table. 1. *Table of the formalisms used, their relation to Z* and their sensitivities. ω is the angular frequency (ω=2πf), f is frequency (in Hz), Z' and Z'' are the real and imaginary components of Z*, respectively.*

Formalism	Relation to Z*	Sensitive to:
Z*	-	Large resistances
M*	jωZ*	Small capacitances
Y'	1/Z'	Small resistances
E'	1/ jωZ''	Large capacitances

Three equivalent circuits were used to analyse the FEM spectra. These were the series layer model (SLM), the series brick layer model (SBLM) and the parallel brick layer model (PBLM). Each of these equivalent circuits has a simplified microstructure associated with it (see fig. 4). The values of resistance (R) and capacitance (C) for the constituent elements are calculated using the basic equations for resistance and capacitance given in equations (2.1) and (2.2) respectively. The same intrinsic values of conductivity (σ) and permittivity (ε_r) as inputted into the FEM code and the geometry of the constituents of the simplified microstructures are used to evaluate equations (2.1) and (2.2) for a given combination of material properties.

The SLM is the simplest representation of a two phase electrical composite and was first described by Maxwell[9]. In this work, there are two layers of fixed area and thickness varying to make up the volume fractions of core and shell material (see fig. 4A). Previously it has been shown that microstructures that have more complex connectivity cannot be fitted using the SLM as it assumes there are no preferential conduction pathways through the microstructure and that all the volume of the core and the shell material contribute to the impedance response[8]. For completeness, we will test how well the SLM can model systems with varied material properties.

Previously[8] an equivalent circuit based upon the electrical microstructure of a core-shell system was derived called the SBLM. By assuming a nested cube approximation of the core-shell structure, the parallel component of the shell material is neglected (see fig. 4B). This approach is valid for the case where the shell is thin and resistive, as the current will preferentially flow through the core instead of the parallel shell.

Finally, a third configuration was used for when the parallel component of the shell cannot be neglected, the PBLM (see fig. 4C). Whilst the shell region is

relatively thin in this material properties study, σ and ε_r are variable. This could cause preferential pathways to form through the parallel shell regions. This equivalent circuit is interpreted in a similar manner to the dual RC circuits in that its impedance spectra only have two responses. One might expect that there would be three responses as there are three RC elements. This is not the case as the series and the parallel shell components have the same time constant since they are derived from the same values of σ and ε_r and the geometric factor cancels[10].

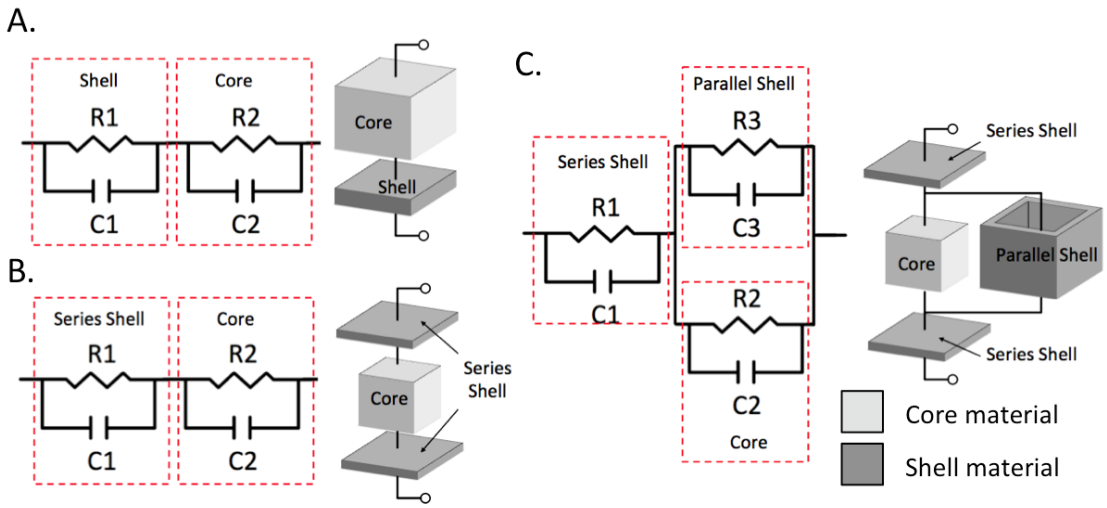

Fig. 4. *Equivalent circuits and the physical microstructures they represent for (A) the SLM, (B) SBLM and (C) PBLM.*

The SLM and SBLM result in two parallel RC circuits in series, whilst the PBLM requires an additional RC circuit for the parallel shell. Derivations for the impedance responses of the dual and triple RC circuits are given in *appendices one* and *two,* respectively. A summary of intercepts, plateaus and their meanings is given in figure 5 and table 2, respectively. The possible arc diameters, plateaus and Debye frequencies provide 12 extracted values to consider for each impedance response. This data was obtained for the FEM simulations and each of the three equivalent circuit spectra. These four plots of the impedance data are functions of the same parameters but weight the data differently. As discussed in the theory section (Chapter 1), for different combinations of material properties certain formalisms will not display all responses within the system whilst others will. Obtaining the intercepts and plateaux for more than one formalism will increase the accuracy of fully characterising the system in question.

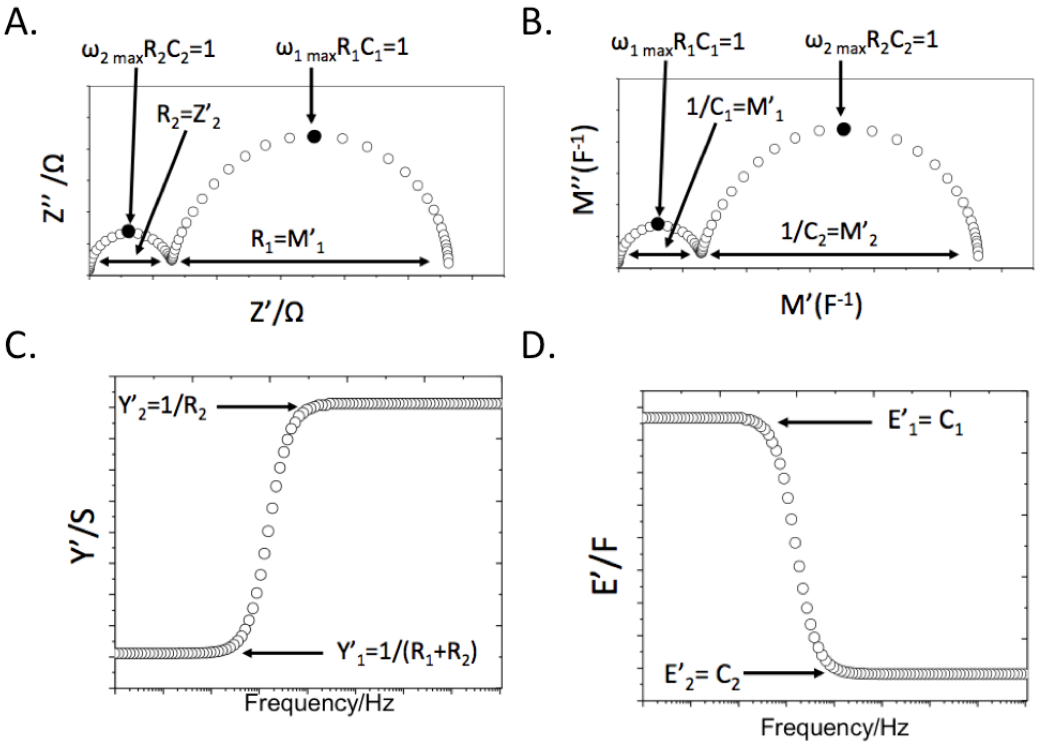

Fig. 5. *Intercepts and plateaus for (A) Z* Nyquist plot, (B) M* Nyquist plot, (C) Y' spectroscopic plot and (D) E' spectroscopic plot. Subscripts one and two denote the low and high frequency response, respectively. Note that the plateaus for (C) and (D) are approximations that hold if $R_1 >> R_2$ and $C_1 >> C_2$, see appendix one.*

Table. 2. *Table of impedance spectra intercepts and plateaus with their physical meaning for the double and triple RC circuits shown in fig. 4. Subscript s-shell is a series shell, subscript p-shell is a parallel shell and subscript core is core.*

Intercept/Plateau	Dual RC	Triple RC
R_1	$R_{s\text{-shell}}$	$R_{s\text{-shell}}$
C_1	$C_{s\text{-shell}}$	$C_{s\text{-shell}}$
R_2	R_{core}	$1/(R_{core}^{-1} + R_{p\text{-shell}}^{-1})$
C_2	C_{core}	$(C_{core} + C_{p\text{-shell}})$

6.2.3. Finding the best equivalent circuit

In order to select the best equivalent circuit for a given set of material properties, a comparison of the twelve impedance values extracted was made between the FEM spectra and each equivalent circuit. For each comparison, the root mean squared (RMS) deviation was calculated using:

$$D_{rms} = \sqrt{(x_{EC} - x_{FEM})^2} \tag{6.1}$$

where D_{rms} is the RMS deviation, x_{EC} is the response from the equivalent circuit value and x_{FEM} is the extracted FEM value. We assume that an equivalent circuit should fit the impedance spectra in all formalisms, thus if an equivalent circuit

does not have the same number of impedance responses for a given formalism, that equivalent circuit was deemed invalid. If the FEM spectra and an equivalent circuit fit had the same number of impedance responses the D_{rms} values were calculated and used to calculate a mean value of D_{rms} where the equivalent circuit with the lowest value of D_{rms} was chosen as the best equivalent circuit for the given set of material properties. This process is summarised in fig. 6.

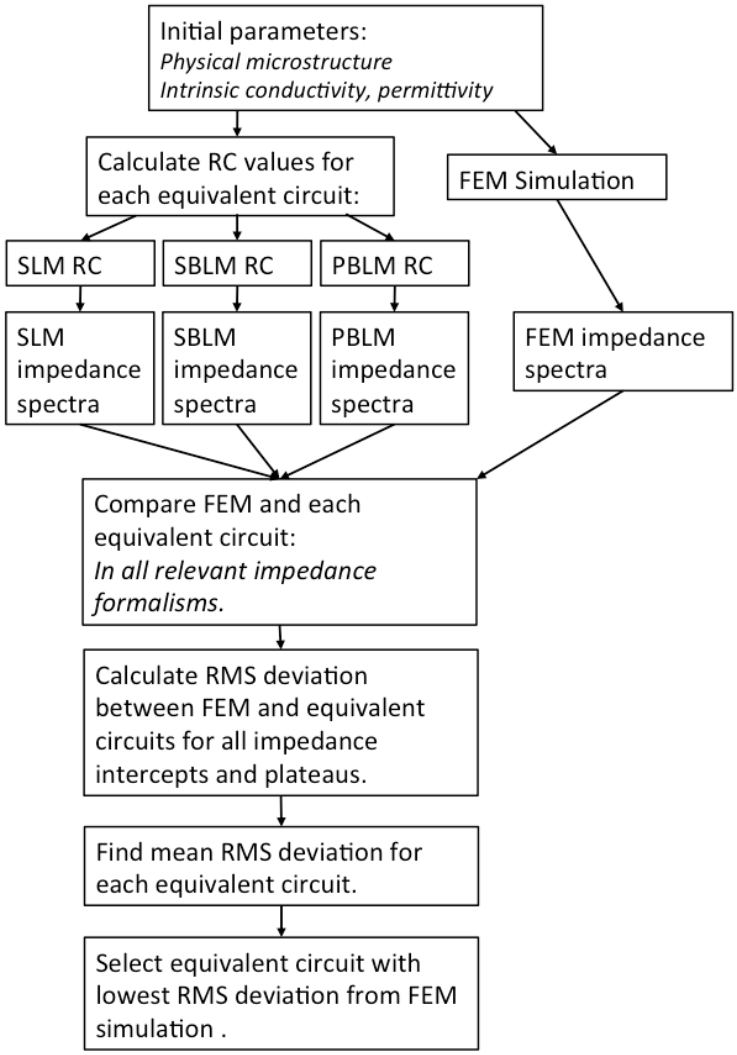

Fig. 6. *Flowchart showing how the equivalent circuit that best represents the FEM simulated impedance spectra is selected.*

As the collecting of all key values for different impedance formalisms was performed by hand, a protocol was established to ensure that data was collected in a repeatable manner. For the case of the Z* and M* Nyquist plots it would be expected that there would be one or two arcs present depending on how similar the core and shell time constants were. To ensure consistency, when the arcs were merged so that there were no intermediate minima (for an example of this see fig. 7A) it was defined that only one response was present. It is possible to fit semicircles to merged spectra (see fig. 7B), however this adds additional uncertainty to the analysis and, depending on how you fit the semicircles, a variety

of arc diameters can be achieved. The presence of a minimum provided a simple criterion for accepting the presence of two measurable arcs (see fig. 7C).

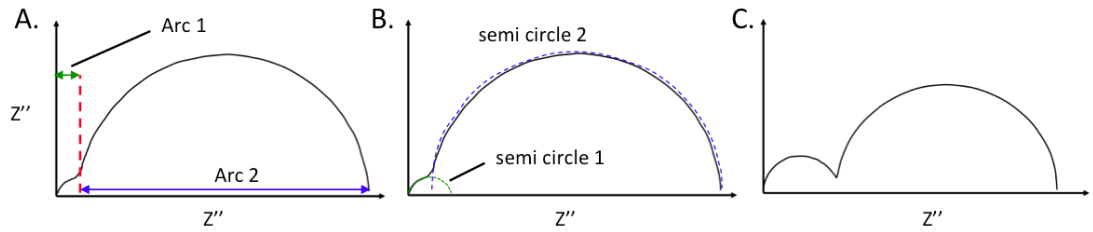

Fig. 7. *(A) Schematic of Z* Nyquist plot with two merged arcs, (B) same plot with semicircles fitted, note the uncertainty of the overlap of the semi circles and (C) Z* Nyquist plot with two arcs with separation defined by a minimum in Z''.*

Another issue arises when extracting data from Y' spectroscopic plots. A limitation of the FEM code is an artefact in the Y' spectrum caused by the reference layer (see fig. 8). The reference layer is a purely resistive layer included for the finite element calculation (covered in in chapter 3). The material properties of the reference layer are chosen so that it has a minimal influence on the simulated impedance spectra but the effect is most pronounced when viewing the data in Y'. The resulting dispersion can completely dominate the high frequency Y' spectroscopic plateau meaning that this impedance response is not recorded. As this dispersive effect is not present in the equivalent circuits, it would cause the equivalent circuits to be deemed inadequate and as such, the high frequency plateau of Y' would be removed from the selection criteria.

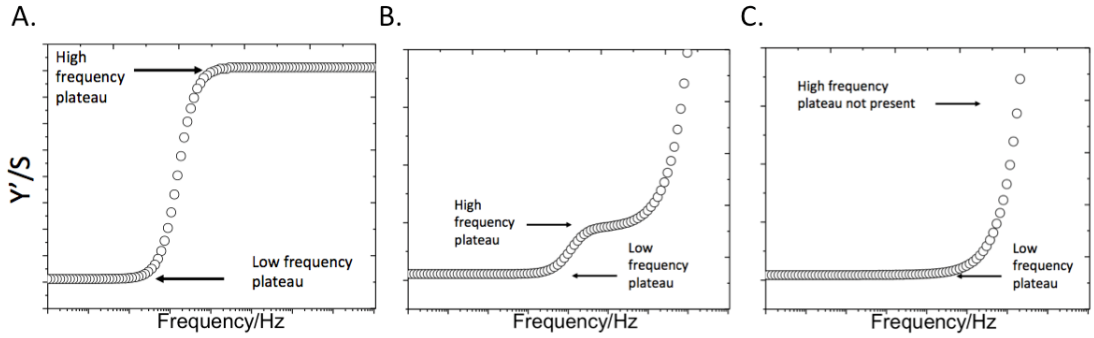

Fig. 8. *Schematics of Y' spectroscopic plots for: (A) an equivalent circuit simulation with two plateaus and no dispersion, (B) a FEM simulation with two plateaus and a resistive dispersion term and (C) a FEM simulation where only the low frequency plateau is present as the high frequency plateau has been swamped by the dispersion. Note the change in scale from (A) to (B) to show the dispersion in (B), the plateau heights are the same.*

Once the best equivalent circuit for given material properties is identified, we must investigate the core and shell time constants so that we assign core and shell responses to the correct part of the impedance spectra. Time constants are detailed in chapter one. We recall that a material with a larger time constant will have a Debye response at a lower frequency than a material with a smaller time constant. In chapter four it was found that, for an encased model with a core

volume fraction of 0.8, the core time constant did not vary significantly due to curved conduction pathways forming through the core[8]. From this result, it will be assumed that the core time constants in this chapter are geometry independent. The analytical time constants (τ) were calculated with:

$$\tau = \frac{\varepsilon_0 \varepsilon_r}{\sigma} \tag{6.2}$$

Using equation (6.2) to calculate the core and shell time constants for each point on the material property space so the core and shell responses were correctly assigned to the low or high frequency parts of the impedance spectra. Whichever material had the larger time constant was assigned to the low frequency response and the material with the smaller time constant was assigned the high frequency response.

Values of σ and ε_r can now be extracted for the core and shell materials. For the SLM and the SBLM equivalent circuits, the low frequency resistance and capacitance values (R_1 and C_1) and the high frequency resistance and capacitance values (R_2 and C_2) are substituted into equations (2.1) and (2.2), respectively. These values can be then compared to the known (inputted) values. The process is the same for the low frequency shell properties of the PBLM, but the high frequency resistance and capacitance values are a composite of the core and the parallel shell properties. Since the shell properties are already known from the low frequency data, substituting the best values for the shell conductivity into equation (2.1) and (2.2) gives:

$$\sigma_2 = \frac{1}{G_2}\left(\left(\frac{1}{R_2}\right) - (\sigma_1 G_3)\right) \tag{6.3}$$

$$\varepsilon_{r2} = \frac{1}{G_2 \varepsilon_0}\left(C_2 - (\varepsilon_0 \varepsilon_{r1} G_3)\right) \tag{6.4}$$

where G_2 the geometric factor of the core (area over length), G_3 is the geometric factor of the parallel shell material, R_2 is the high frequency resistance, σ_1 is the shell conductivity, σ_2 is the core conductivity, ε_{r1} is the shell permittivity, ε_{r2} is the core permittivity and C_2 is the high frequency capacitance.

Once the high and low frequency intrinsic values have been calculated for each formalism, it is possible to map out the most accurate intrinsic values that can be obtained from impedance data under these conditions and identify which formalism(s) is needed to obtain it. This process is summarised in fig. 9. Due to the large number of data points, a computer program was written to automate the calculation of intrinsic values and comparisons of the equivalent circuits and possible impedance formalisms.

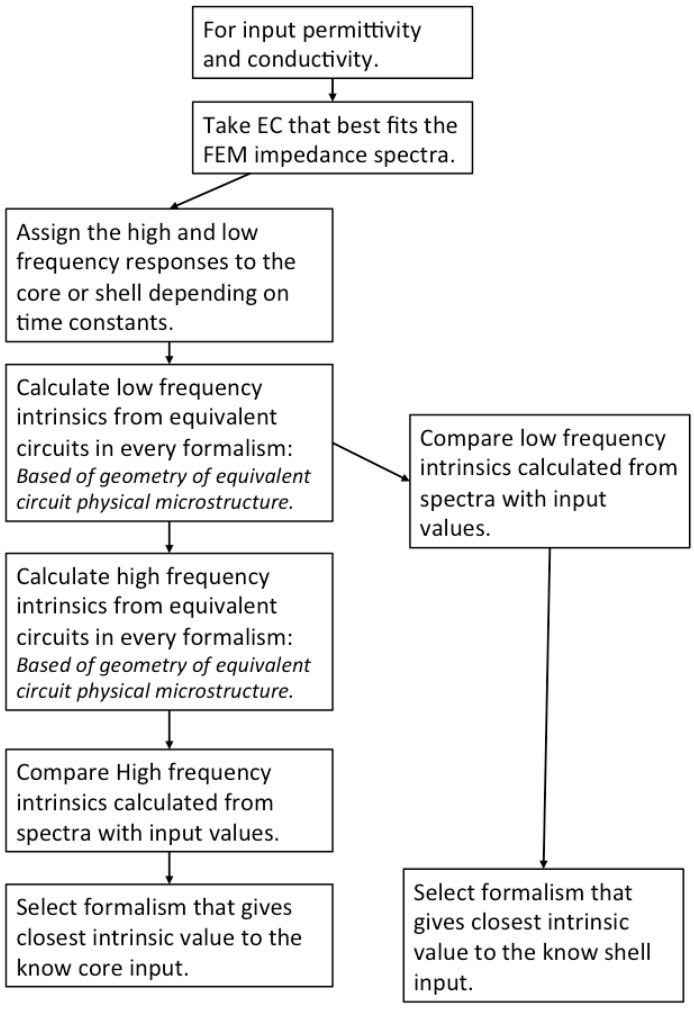

Fig. 9. *Flowchart showing how the impedance formalism that is most accurate for obtaining intrinsic values from impedance spectra is selected.*

6.3. Results

6.3.1. Optimal Equivalent Circuit

To find the optimal equivalent circuit, a large range of material property combinations were simulated using FEM along with the equivalent circuits using the Zview program[11]. Using the methodolgy previously outlined, a measure of how well each equivalent circuit fitted the FEM-simulated impedance data was obtained. For the SLM, the deviation was higher than for the SBLM and PBLM for all combinations of material properties (see fig. 10A); its size rising from ±34 to ±163%. There were also large regions where the SLM completely failed to replicate the impedance response of the FEM simulation. This occurred where the shell permittivty or conductivity was very different to that of the core.

Both the SBLM and the PBLM did better that the SLM (see fig. 10B and C, respectively). For the SBLM, the deviation ranged from ±0.7 to ±20% and for the PBLM from ±0.55 to ±20%. There were some combinations of material properties that the SBLM failed to replicate. However, the PBLM produced the same number of impedance responses in all formalisms as the FEM data. Typically the SBLM was

better for scenarios where the conductivity and permittivity for the core and shell were very different (see fig. 10D region i). For regions where the material properties were similar, the PBLM generally was found to be the best equivalent circuit (see fig. 10D region ii). However when the permittivity of the shell was lower than that of the core, both regions had a similar conductivty and the PBLM worked well (see fig. 10D region iii). Also when the conductivity of the core and shell were very different but the permittivities were similar, again the PBLM was superior (see fig. 10D region iii). This is shown by a plot of which equivalent circuit had the lowest value of deviation (see fig. 10D). It should be noted that, when the SBLM provided the best fit, the minimum and maximum absolute differences between the deviations of the PBLM and SBLM are ±0.03 to ±0.4%. The difference is more significant when the PBLM is the best fit where the minimum and maximum absolute differences are ±0.01 to ±14.22%, where the greatest difference is where the core and shell have matching or close to matching permittivity and conductivity.

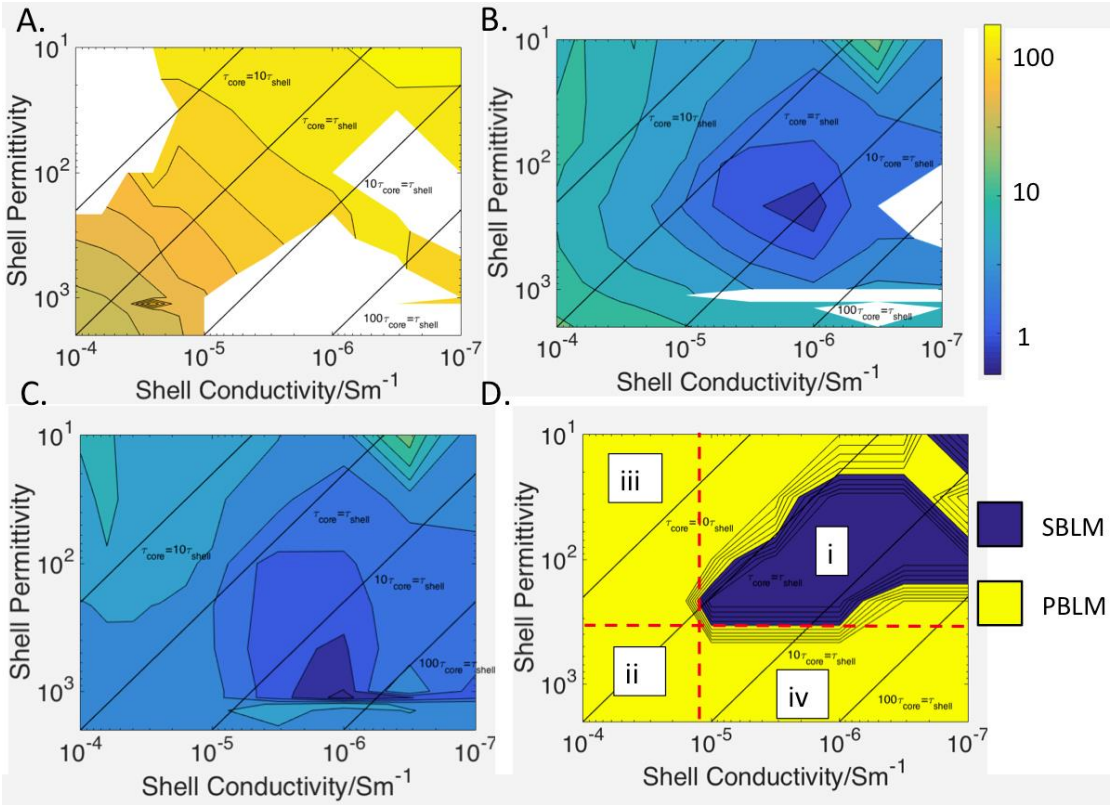

Fig. 10. *Plots of the RMS deviation of (A) the SLM, (B) the SBLM and (C) the PBLM compared to the FEM-simulated results for all simulated combinations of material properties. The deviation uses a log scale; white spaces show areas where an equivalent circuit did not have the same number of impedance responses as the FEM simulation and is considered invalid. (D) shows which equivalent circuit has the lowest RMS deviation and is considered to be the best fit. This depends on material properties and the dashed lines enclose several regions (i to iv) that are discussed in the text. The straight lines plotted on top of the contours show the ratio between the theoretical core and shell time constants.*

From the map showing which equivalent circuit provides the best fit of the FEM data, several points of interest were selected to examine the equivalent circuit fits in the four impedance formalisms (see fig. 11). These points were selected to show how the impedance spectra differed for the region where the SBLM provided the best fit of the FEM data and several points in the region where the PBLM was selected as the best fit. A summary of the material properties of the four points of interest is given in table 3 along with reasons for their selection. Table 4 gives the RMS deviation for each equivalent circuit at the four points of interest.

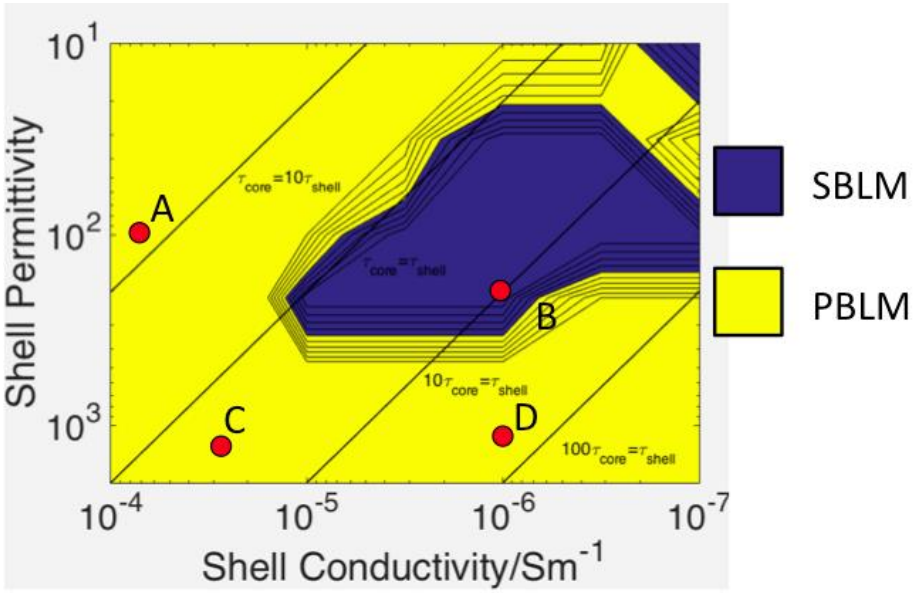

Fig. 11. *Four points of interest on the material properties plots showing where the SBLM or PBLM fitted the FEM simulated impedance spectra best.*

Table. 3. *Material properties of points of interest A to D with reasons for selection.*

Position	Shell ε_r	Shell σ/Sm^{-1}	Comment
A	100	6.31E-5	Low shell ε_r and high σ.
B	215	1E-6	Lowest deviation of SBLM from FEM results.
C	1260	2.51E-5	High shell ε_r and high σ.
D	1122	1e-6	High shell ε_r and low σ.

Table. 4. *RMS deviation values for each equivalent circuit at points of interest A to D. Note N/A indicates that an equivalent circuit did not have the same number of intercepts as the FEM simulation and was discarded from selection.*

Position	Shell ε_r	Shell σ/Sm^{-1}	RMS deviation/%		
			SLM	SBLM	PBLM
A	100	6.31E-5	N/A	9.49	5.43
B	215	1E-6	117.44	0.72	1.12
C	1260	2.51E-5	44.41	9.57	3.45
D	1122	1e-6	N/A	N/A	4.04

At point A, where the shell permittivity was 100 and its conductivity was 0.0631 mSm^{-1}, the PBLM provided the best fit. Comparing the three equivalent circuits with the FEM spectra (plotted as impedance Nyquist plots, see fig. 12A) showed that the SLM overestimates the total resistance by over 50%. The PBLM and SBLM were much closer to the FEM spectra, overestimating the total resistance by 10 and 20%, respectively. A modulus Nyquist plot (see fig. 12B) showed the SLM underestimating the total capacitance by over 100%. The SLM also did not have a definable minimum between the core and shell arcs, discarding its fit from selection. The SBLM and PBLM fitted the FEM data exactly. Spectroscopic plots of the real admittance (fig. 12C) and real capacitance (fig. 12D) again showed that SLM provided the worst fit whereas the SBLM and PBLM plateaus tended to the same value at high and low frequency. Although it was not included in the selection criteria, the PBLM provided a much closer fit for the transitions between the high and low frequency plateaus, particularly for the real capacitance.

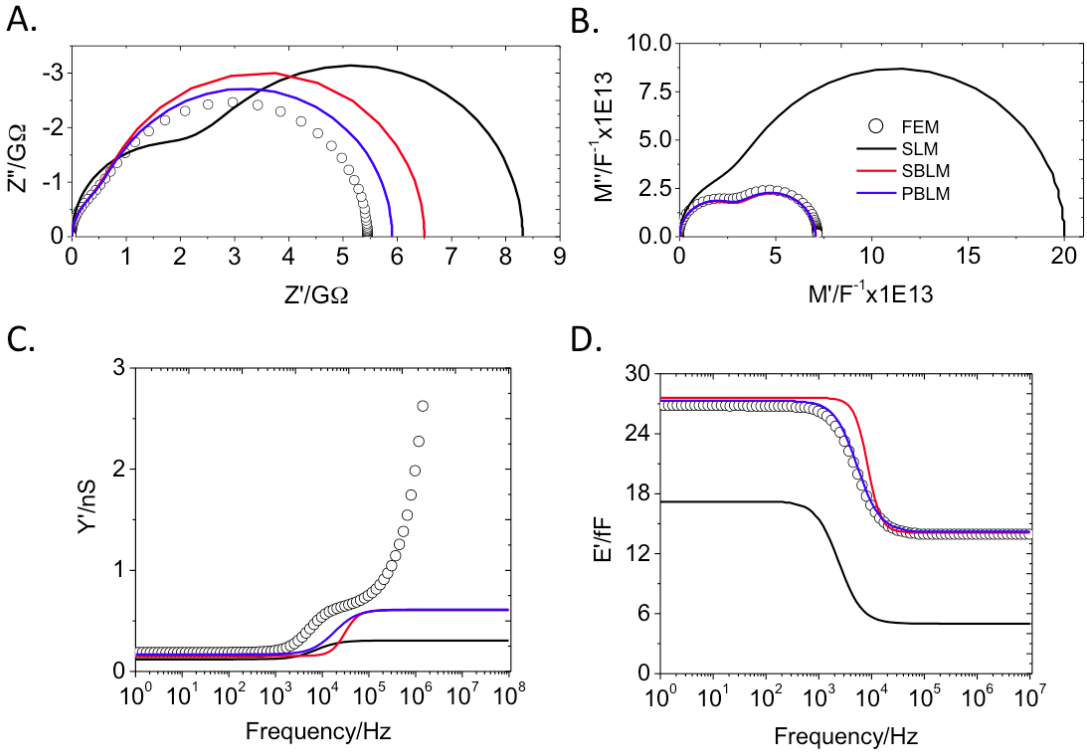

Fig. 12. *Comparison of the impedance response simulated with FEM (circles) with the three equivalent circuits fits (solid lines) for position A: (A) Impedance Nyquist plot, (B) modulus Nyquist plot, (C) real admittance spectroscopic plot and (D) real capacitance spectroscopic plot.*

For point B, where the shell permittivity was 215 and its conductivity was 1 μSm^{-1}, the SBLM provided the best fit but was not a significant improvement over the PBLM. For impedance Nyquist plots (see fig. 13A) the SLM overestimated the total resistance by 300% whereas the SBLM and PBLM matched the FEM spectrum well. A modulus Nyquist plot (see fig. 13B) showed that the SLM overestimated the M* arc diameters by over 100%. The SLM also did not predict the position of a minimum between the core and shell arcs correctly whereas the SBLM and PBLM did.

The SLM underestimated the position of the low and the high frequency plateaus of a real admittance spectroscopic plot (see fig. 13C). The SBLM and PBLM predicted the low frequency Y' plateau but underestimated the height of the high frequency plateau. Finally, for a spectroscopic plot of the real capacitance (see fig. 13D) the SLM underestimated both plateaus whereas the PBLM and SBLM gave good agreement with the FEM data. The main contribution to the difference in RMS deviation between the PBLM and the SBLM was in the M* arcs and the high frequency E' plateau with a difference in the deviations of ~1% each. Despite the SBLM giving the lowest average RMS deviation, it should be noted that the PBLM gave a much better fit for the transition between the high frequency and low frequency plateaus for E' and Y'.

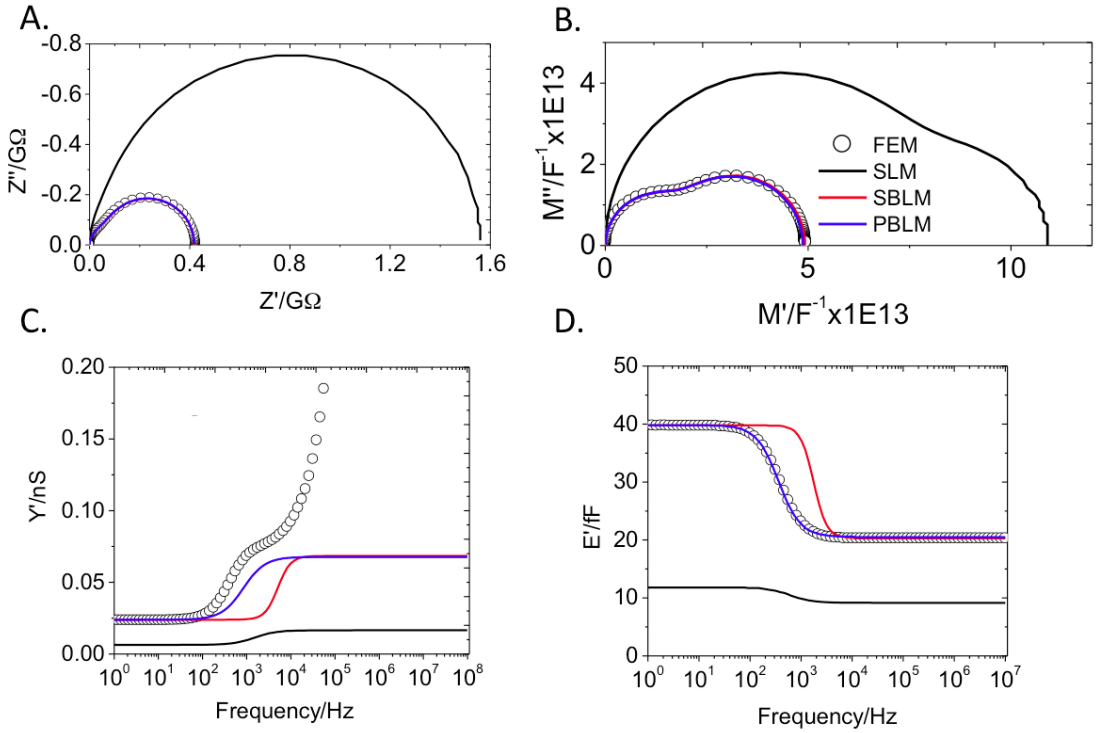

Fig. 13. *Comparison of the impedance response simulated with FEM (circles) with the three equivalent circuit fits (solid lines) for position B. (A) Impedance Nyquist plot, (B) modulus Nyquist plot, (C) real admittance spectroscopic plot and (D) real capacitance spectroscopic plot.*

The impedance response of point C (permittivity of 1260 and conductivity of 25.1 μSm^{-1}) showed significant merging of the two regions' responses, which is not surprising given the proximity of the core and shell time constants. Here the PBLM was the most effective equivalent circuit. Nyquist plots of impedance (see fig. 14A) and modulus (see fig. 14B) showed a single arc for all equivalent circuits. The diameters of both the Z* and M* arcs were significantly overestimated (by ~100 and ~50% respectively) by the SLM. The SBLM fitted the arcs within 10% and the PBLM provided the best fit. For spectroscopic plots of Y' and E' (see figs. 14C and D, respectively), all equivalent circuits underestimated the heights of the low and high frequency plateaus in both cases. The SLM provided the worst fit, followed by the SBLM, whilst the PBLM provided the best fit.

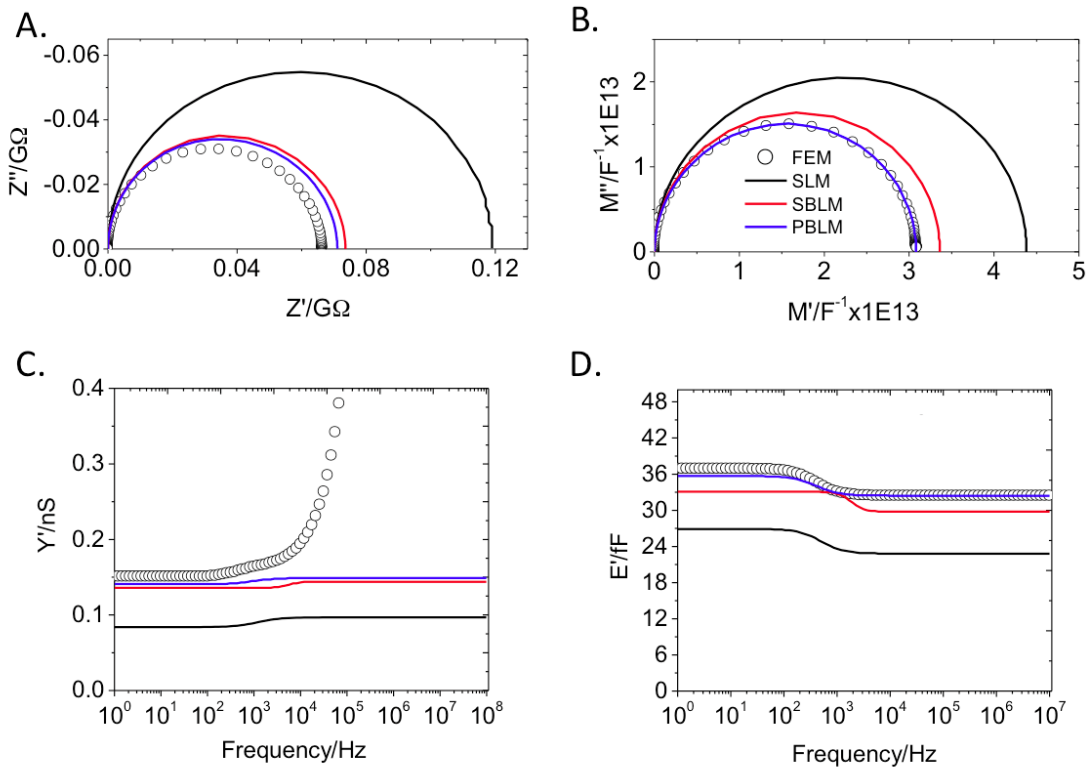

Fig. 14. *Comparison of the impedance response simulated with FEM (circles) with the three equivalent circuits fits (solid lines) for position C. (A) Impedance Nyquist plot, (B) modulus Nyquist plot, (C) real admittance spectroscopic plot and (D) real capacitance spectroscopic plot.*

The final point of interest, D with a conductivity of 1 μSm^{-1} and permittivity of 1122 was fitted best by the PBLM. Once again the SLM overestimated the total resistance as seen in an impedance Nyquist plot (see fig. 15A) where the total arc diameter was out by nearly 300%. Here the PBLM and SBLM proved to be excellent fits of the FEM data. For a modulus Nyquist plot (see fig. 15B) the SLM predicted a minimum between the core and shell arcs that did not exist for the FEM spectrum and overestimated the M* arc diameters. The PBLM and SBLM both fitted the low frequency M* arc but the SBLM overestimated the high frequency arc in contrast to the near exact fit of the PBLM.

Spectroscopic plots of the real admittance (see fig. 15C) showed that the SLM underestimated the heights of the low and high frequency plateaus. The SBLM and PBLM provided a near exact fit of the low frequency plateau and both underestimated the high frequency plateau by a lesser degree than the SLM. Finally, spectroscopic plots of the real capacitance (see fig. 15D) showed that the PBLM provided the best fit to the FEM data for the plateau heights and the low to high frequency transition. The SBLM fitted the plateau heights but did not correctly predict the transition frequency. The SLM underestimated both the E' plateau heights.

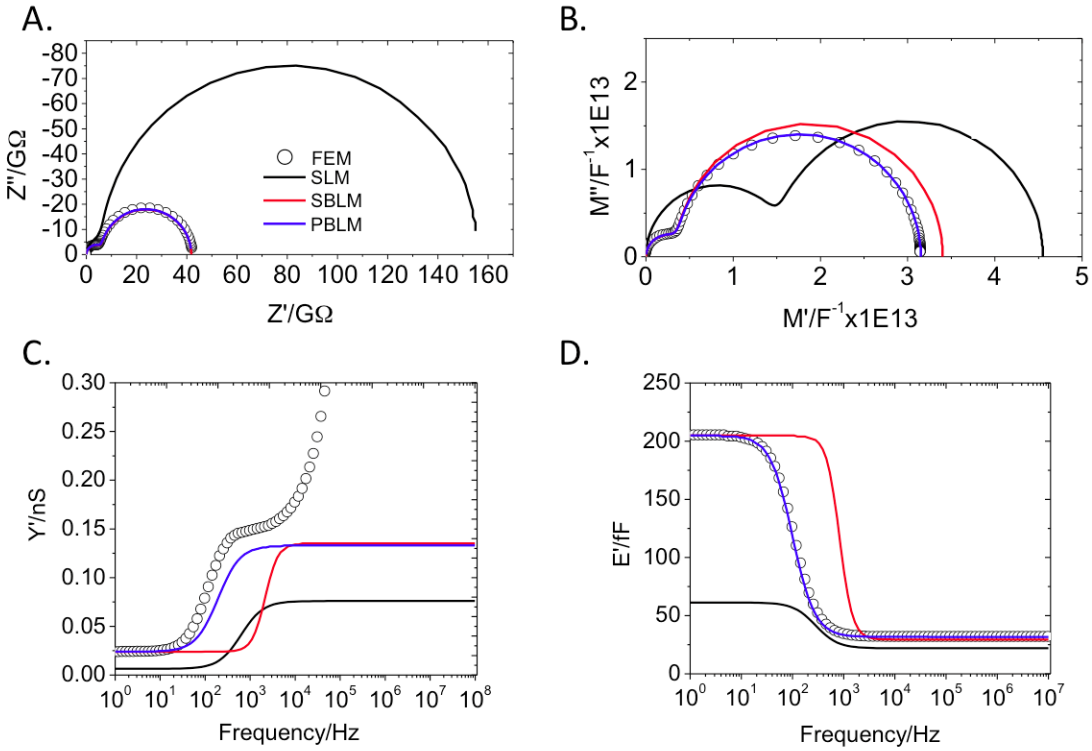

Fig. 15. *Comparison of the impedance response simulated with FEM (circles) with the three equivalent circuits fits (solid lines) for position D. (A) Impedance Nyquist plot, (B) modulus Nyquist plot, (C) real admittance spectroscopic plot and (D) real capacitance spectroscopic plot.*

All three equivalent circuits overestimate the high frequency real admittance plateau leading to an overall better fit of the capacitances present in the FEM data than the resistances. The PBLM provides the best fit for the transition between low and high frequency plateaus for E' and Y' spectroscopic plots for all points of interest. There are several cases where the SLM predicts behaviour that is very different to the FEM data.

6.3.2. Extracting Shell Conductivity

Using the best equivalent circuit, values for the conductivity and permittivity could be extracted using equations (2.1), (2.2), (6.3) and (6.4). These equations require a value of capacitance or resistance (for a permittivity or conductivity, respectively) that can be obtained from a range of impedance formalisms. Using the methods detailed in section 6.2.2 it is possible to find the impedance formalism that gives the most accurate value for a given intrinsic material property. The different methods for obtaining resistance and capacitance, with the shorthand notation used to define them, are summarised in table 5. Diagrammatic examples of which parts of the spectra the short hand notations refer to are given in fig. 16.

Table. 5. *Table defining notation for different impedance formalisms to find resistance and capacitance values for extracting intrinsic property values.*

Notation	Conductivity or permittivity extracted from:
M'1	Capacitance from low frequency M* arc diameter.
M'W1	Resistance from low frequency M* arc diameter and Debye frequency using RCω=1.
M'2	Capacitance from high frequency M* arc diameter.
M'W2	Resistance from high frequency M* arc diameter and Debye frequency using RCω=1.
Z'1	Resistance from low frequency Z* arc diameter.
Z'W1	Capacitance from low frequency Z* arc diameter and Debye frequency using RCω=1.
Z'2	Resistance from high frequency Z* arc diameter.
Z'W2	Capacitance from high frequency Z* arc diameter and Debye frequency using RCω=1.
E'LF	Capacitance approximated from low frequency E' spectroscopic plateau.
E'HF	Capacitance approximated from high frequency E' spectroscopic plateau.
Y'LF	Conductivity approximated from low frequency E' spectroscopic plateau.
Y'HF	Conductivity approximated from high frequency E' spectroscopic plateau.

A plot of the RMS deviation of the shell conductivity extracted using the formalism that gave the lowest value is shown in fig. 17A. This shows that it is more accurate to extract the shell conductivity when the difference between the core and shell conductivity is larger or the difference between the core and shell permittivity is larger. The shell conductivity can be extracted with less than ±10% RMS deviation from the input value when the shell conductivity falls below 3.16 μSm^{-1} or the permittivity is less than or equal to 31.6. Two regions are not covered by the previous statement. The first region, for conductivities of 0.1 mSm^{-1} to 63.1 μSm^{-1}, extends the region where the shell conductivity can be extracted to within ±10% to shell permittivities of 100. The second region, where the shell permittivity is 2000 to 1122, extends the resolvable region to 15.8 μSm^{-1}. A schematic showing which impedance formalism was best for extracting the shell resistance and hence giving the most accurate shell conductivity is given in fig. 17B. Regions where the extracted conductivity has deviated by ±25% from the known value have been discarded as being too inaccurate. The geometric factor used to convert resistance to conductivity is based upon the equivalent circuit that offered the best fit of the FEM data for the given material properties as discussed in section 6.2.2.

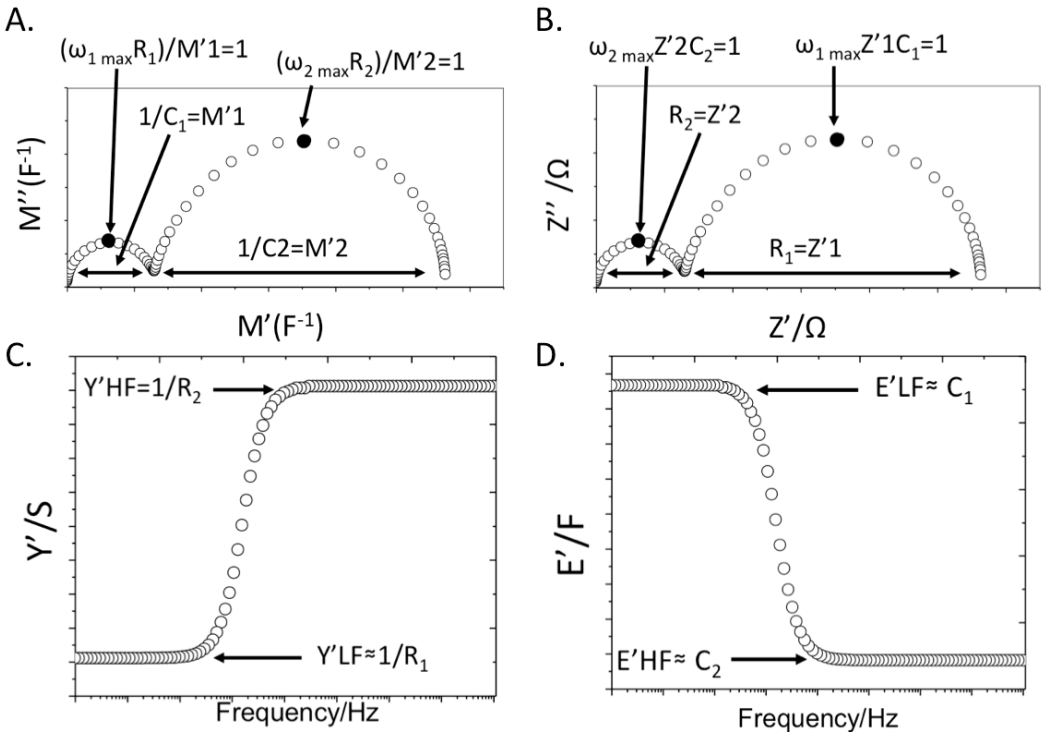

Fig. 16. *Schematics of impedance data annotated with abbreviations used for the intercepts. (A) Modulus Nyquist plot where the shell and core capacitances are extracted from inverse arc diameters are defined as M'1 and M'2, respectively. Resistances extracted from the Debye angular frequencies (ω_{max}) and capacitances are defined as M'W1 and M'W2 (for the shell and core). (B) Impedance Nyquist plot where the shell and core resistances are extracted from inverse arc diameters are defined as Z'1 and Z'2, respectively. Capacitances extracted from the Debye angular frequencies (ω_{max}) and capacitances are defined as Z'W1 and Z'W2 (for the shell and core). (C) Admittance spectroscopic plot where the shell and core resistances extracted from the low and high frequency plateaus are defined as Y'LF and Y'HF, respectively. (D) Capacitance spectroscopic plot where the shell and core capacitances extracted from the low and high frequency plateaus are defined as E'LF and E'HF, respectively. These plots assume that the shell time constant is greater than the core time constant.*

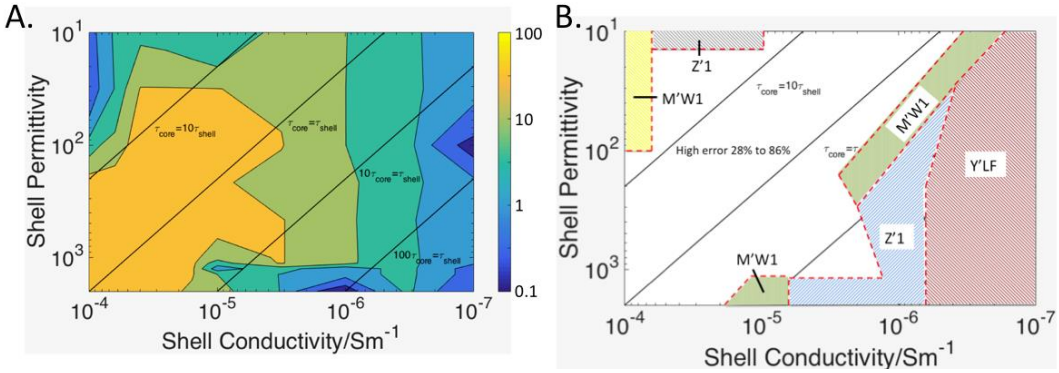

Fig. 17. *(A) Plot of the lowest RMS deviation when extracting the shell conductivity using the optimal equivalent circuit and impedance formalism. Note the scale is logarithmic. (B) Schematic showing which impedance formalism gave the lowest deviation for the combinations of material properties. Note: Regions with an RMS deviation of over 25% from the input shell conductivity have been discarded leaving white space.*

Fig. 17B shows that there are distinct regions of material properties where certain impedance formalisms are best for extracting the shell conductivity. An enlargement of fig. 17B is shown in fig. 18 with the addition of several (blue) lines corresponding to regions of interest that will be examined in further detail (regions i to iv). In region i, where the shell conductivity varies from 0.1 mSm^{-1} to 63.1 μSm^{-1} and the shell permittivity varies from 10 to 100, the resistance calculated from the shell imaginary modulus Debye frequency (M'W1) gives the most accurate value for the shell conductivity. In region ii, where the shell permittivity is 10 and shell conductivity ranges from 39.8 μSm^{-1} to 1 μSm^{-1}, Nyquist low frequency arc diameters of impedance (Z'1) are the best. Region iii is a diagonal band between where the shell time constant is equal to the core time constant (τ_{core} and τ_{shell}, respectively) and $\tau_{shell} = 10\tau_{shell}$. Here M'W1 is best. Finally, for region iv, there is a transition from Z'1 to where the shell real admittance plateau (Y'LF) gives the best value as the shell conductivity decreases from 1 μSm^{-1} to 0.1 μSm^{-1}.

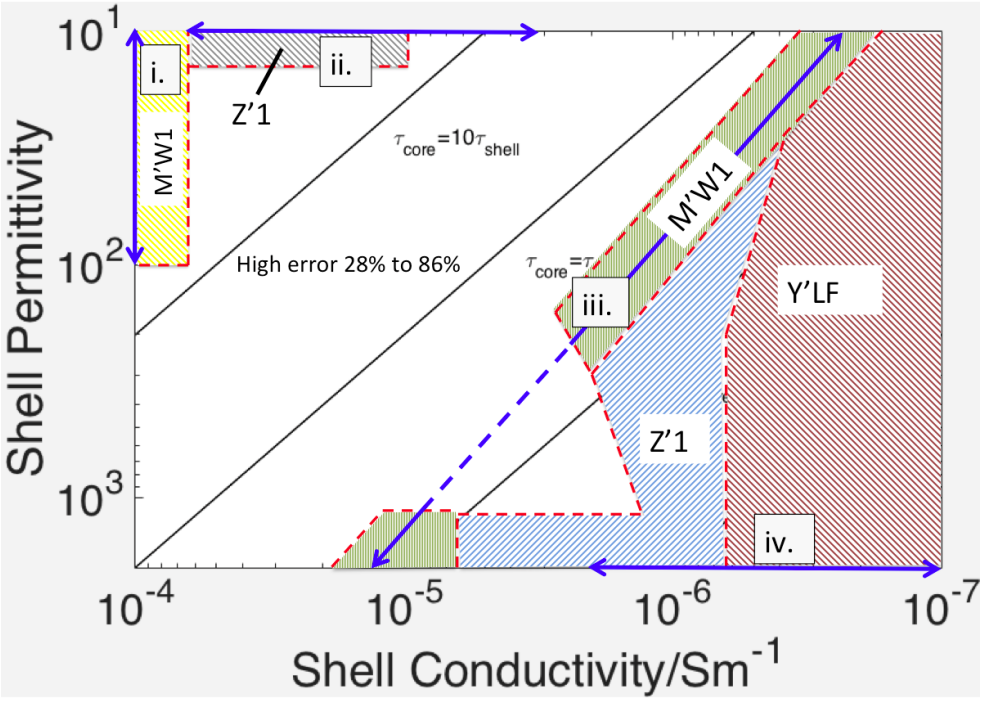

Fig. 18. *Schematic showing which regions of interest (blue lines, labelled i to iv) are examined to find why different formalisms are better for extracting the shell conductivity.*

Since the shell conductivity is being extracted, there are four impedance plots that are significant: spectroscopic plots of admittance which will allow the Y'LF to be taken from the shell plateau; impedance Nyquist plots which give Z'1 from the shell arc diameter; and a combination of spectroscopic plots of the imaginary modulus and modulus Nyquist plots which give a Debye frequency and capacitance respectively, allowing the calculation of M'W1. For region i these plots are given in fig. 19.

Due to the material properties within region i, the shell time constants calculated analytically are smaller than the core time constant (which is fixed). This means that the shell response occurs at a higher frequency than the core

response and so the high frequency arcs and plateaus are assigned to the shell. Spectra studied in region i have the same conductivity as the core (0.1 mSm^{-1}) and their permittivities vary from 10 to 100. Despite the fact that the conductivity of the core and shell is the same, a spectroscopic plot of the real admittance shows (see fig. 19A) high frequency plateaus that vary with the shell permittivity. Hence in region i the admittance is not suitable for extracting the shell conductivity. The high frequency arcs of impedance Nyquist plots (see fig. 19B) were merged with the low frequency arc making extraction of a value unreliable or impossible. Spectroscopic plots of the imaginary modulus (see fig. 19C) had well-defined high frequency peaks where the shell Debye frequency could be obtained and modulus Nyquist plots (see fig. 19D) had high frequency arcs where a diameter could be obtained. Despite the merging of the modulus arcs at higher shell permittivity values, the shell conductivity calculated using M'W1 proved to be the most accurate, giving values within ±0.5 to ±6% of the value inputted into the FEM package.

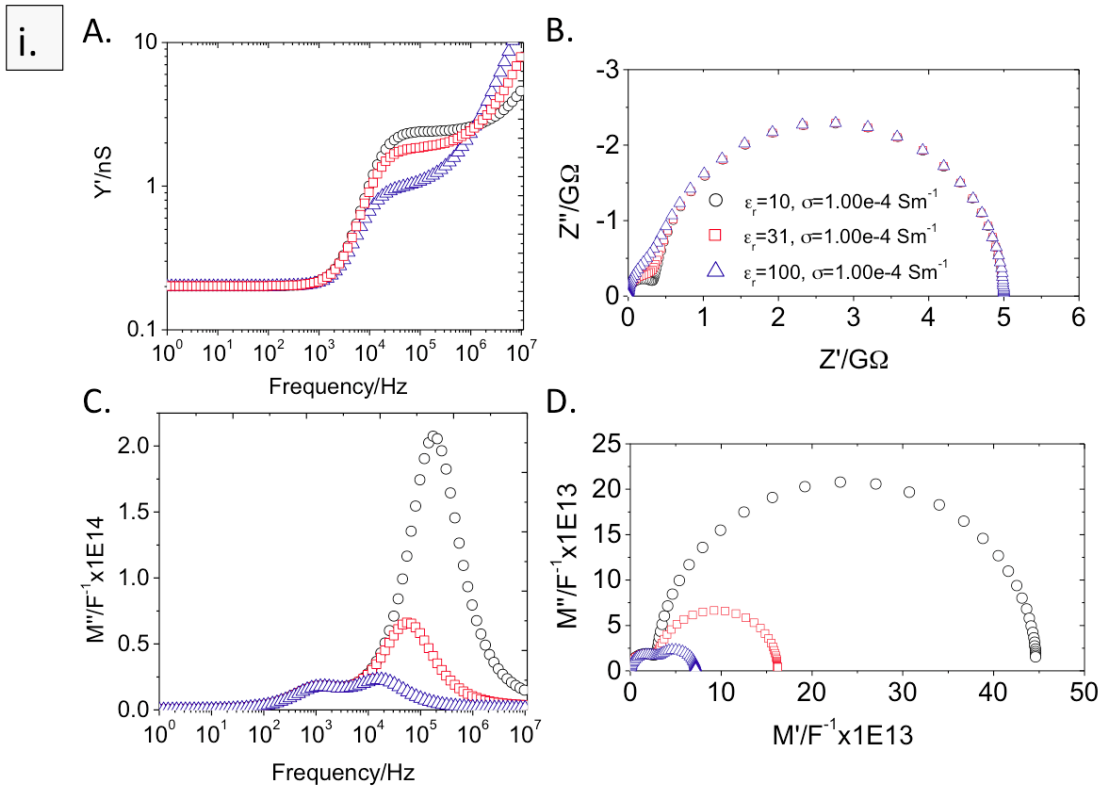

Fig. 19. *Impedance response for region i for extracting the shell conductivity plotted as: (A) real admittance spectroscopic, (B) impedance Nyquist, (C) imaginary modulus spectroscopic and (D) modulus Nyquist.*

For region ii, where Z'1 had performed the best, M'W1 did not work as well. This is because the arcs of modulus Nyquist plots (see fig. 20A) were too merged to give a reliable capacitance for calculating M'W1 despite the well-defined peaks present in spectroscopic plots of the imaginary modulus (see fig. 20B). It is possible that, despite being well defined, the imaginary modulus peaks are a merged response of both the core and shell. The shell plateaus of spectroscopic plots of the real admittance (see fig. 20D) give less accurate values for shell

conductivity, roughly ±13% than impedance Nyquist plots (see fig. 20C). When the shell impedance arc is well-defined (see fig. 20E), the deviation in extracting the shell conductivity from Z'1 can be as little as ±4%. As the shell conductivity decreases further, the low shell conductivity dominates the arc giving an accurate resistance.

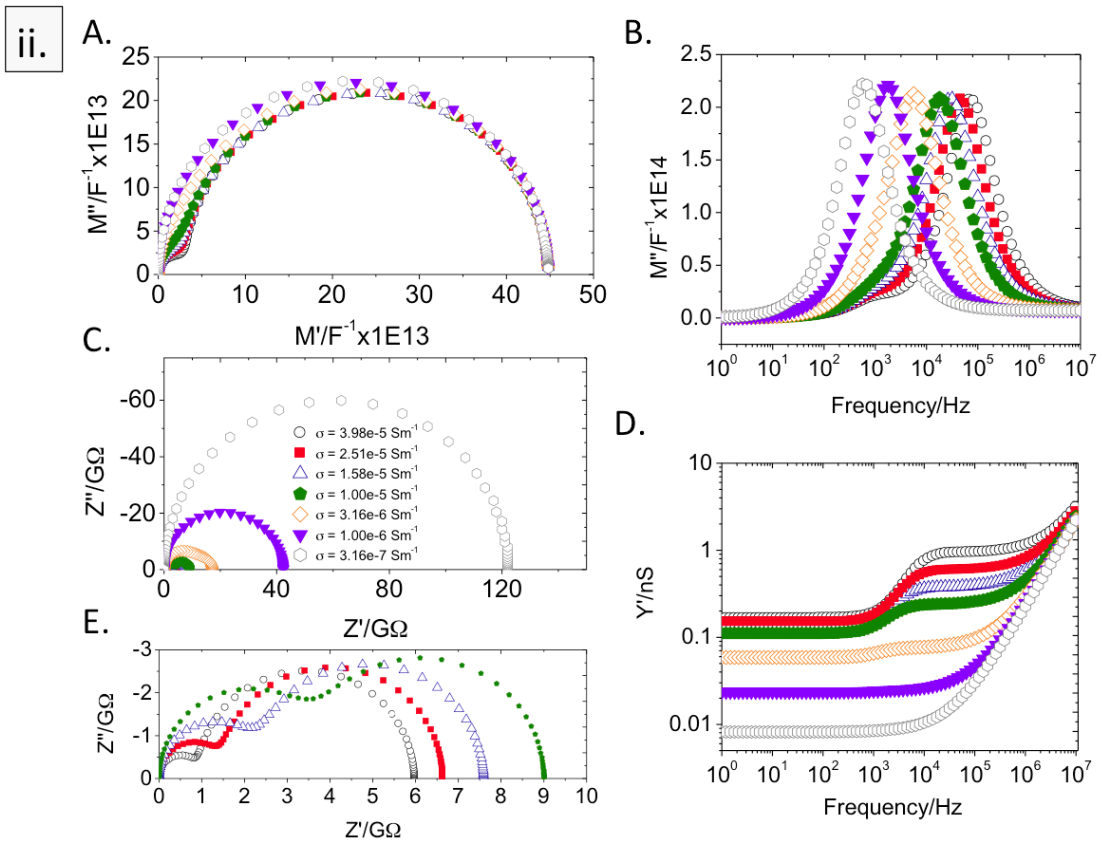

Fig. 20. *Impedance response for region ii for extracting the shell conductivity plotted as: (A) modulus Nyquist, (B) imaginary modulus spectroscopic, (C) impedance Nyquist, (D) real admittance spectroscopic and (E) impedance Nyquist (enlargement of origin of plot C's origin). The shell permittivity is 10 for all plots.*

In region iii, M'W1 gave the most accurate shell conductivity values. The reader should note that a portion of region iii was discarded, as the lowest possible deviation was unacceptably high where the shell conductivity was ~3.16 μSm^{-1} and shell permittivity ~464. The shell time constant is always larger than that of the core for region iii. Hence the low frequency response is assigned to the shell here. As the magnitude of τ_{shell} is less than an order of magnitude greater than τ_{core} the approximation that the high and low frequency plateaus of admittance spectroscopic plots tend to separate resistance values is not valid here. Fig. 21A shows that the Y' spectroscopic plateaus are merged and unsuitable for extracting Y'LF.

Imaginary modulus spectroscopic plots (see fig. 21B) show single peaks. Nyquist plots of modulus and impedance (see figs. 21C and D, respectively) show a single arc. An enlargement of the spectroscopic plots of the imaginary impedance and imaginary modulus (see figs. 22A and B, respectively) to show the high shell permittivity peaks reveals that the impedance Debye peaks contain a shoulder at low frequency. This indicates a composite response of multiple time constants and

is not (visibly) present in the M'' peaks. For both Z'1 and M'W1 in region iii, the deviation was greatest for higher shell conductivity (±70.11 and ±24.21%, respectively), decreasing at low shell conductivity to ±7.03 and ±4.32%, respectively. The gains in accuracy are more significant at higher shell conductivities. It is likely that the modulus response is slightly more dominated by the shell and hence M'W1 gives more accurate values than Z'1 for region iii.

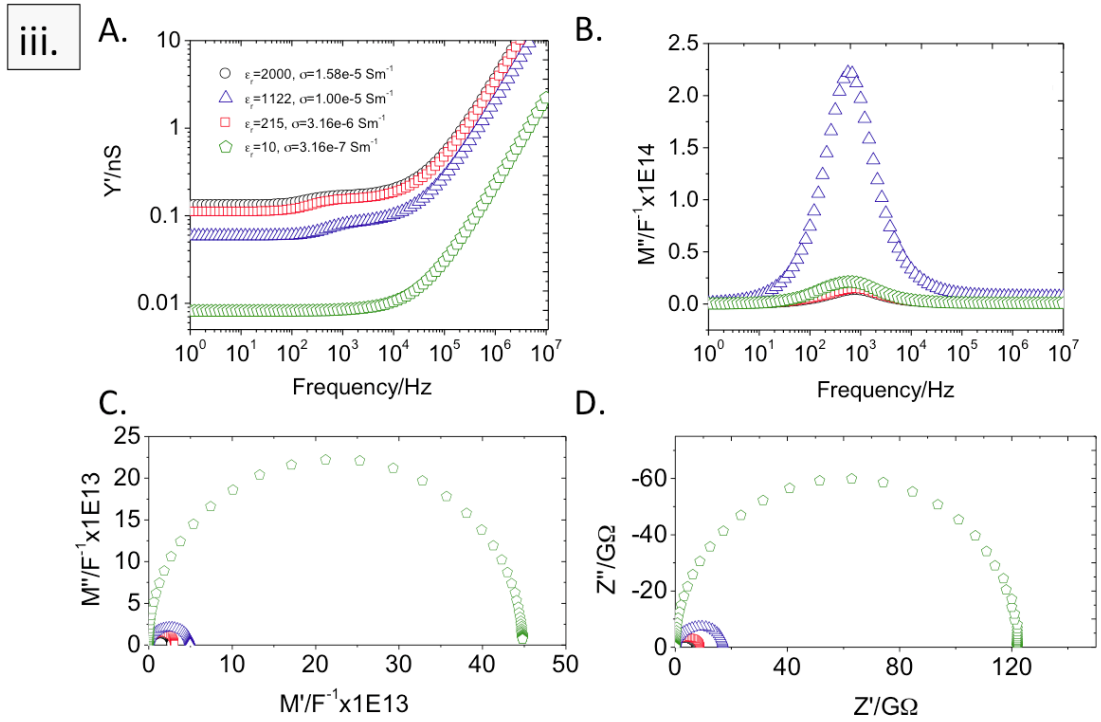

Fig. 21. *Impedance response for region iii for extracting the shell conductivity plotted as: (A) real admittance spectroscopic, (B) imaginary modulus spectroscopic, (C) modulus Nyquist and (D) impedance Nyquist.*

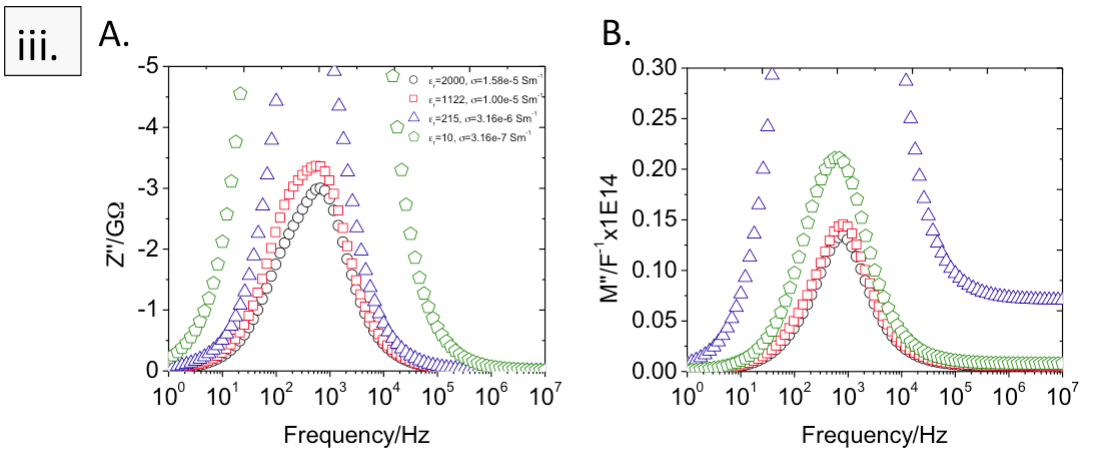

Fig. 22. *Enlargements of the imaginary spectroscopic plots of (A) impedance and (B) modulus. Note the decrease in symmetry of the impedance peaks for shell ε_r = 2000 and 1122.*

Region iv is the remaining property space. It is surrounded by region iii as τ_{shell} becomes increasingly larger than τ_{core}, hence the low frequency response is assigned to the shell. Here the best formalism for extracting the shell conductivity changes from Z'1 to Y'LF as the conductivity falls below 1 μSm^{-1}. Here modulus Nyquist and M'' spectroscopic plots (see figs. 23A and B, respectively) either do not have low enough frequency to resolve the Debye peak or are too merged to successfully use M'W1 to obtain the shell conductivity. Likewise, the low frequency Z* Nyquist arc (see fig. 23C) cannot be resolved for shell conductivities of 0.316 μSm^{-1} or lower with the frequency range used in this study. Where the frequency is sufficiently low to resolve the Z* arcs, Z'1 provides the most accurate value of shell conductivity (±3.39 to ±7.03% deviation for the Z'1 versus ±15.06 to ±33.54% deviation for Y'LF as shell conductivity decreases). When the Z* arcs cannot be resolved, Y' spectroscopic plots (see fig. 23D) are the only alternative and Y'LF is the best formalism for extracting the shell conductivity, giving values with deviations of ±4.05 and ±0.35% for shell conductivities of 0.316 and 0.1 μSm^{-1} respectively.

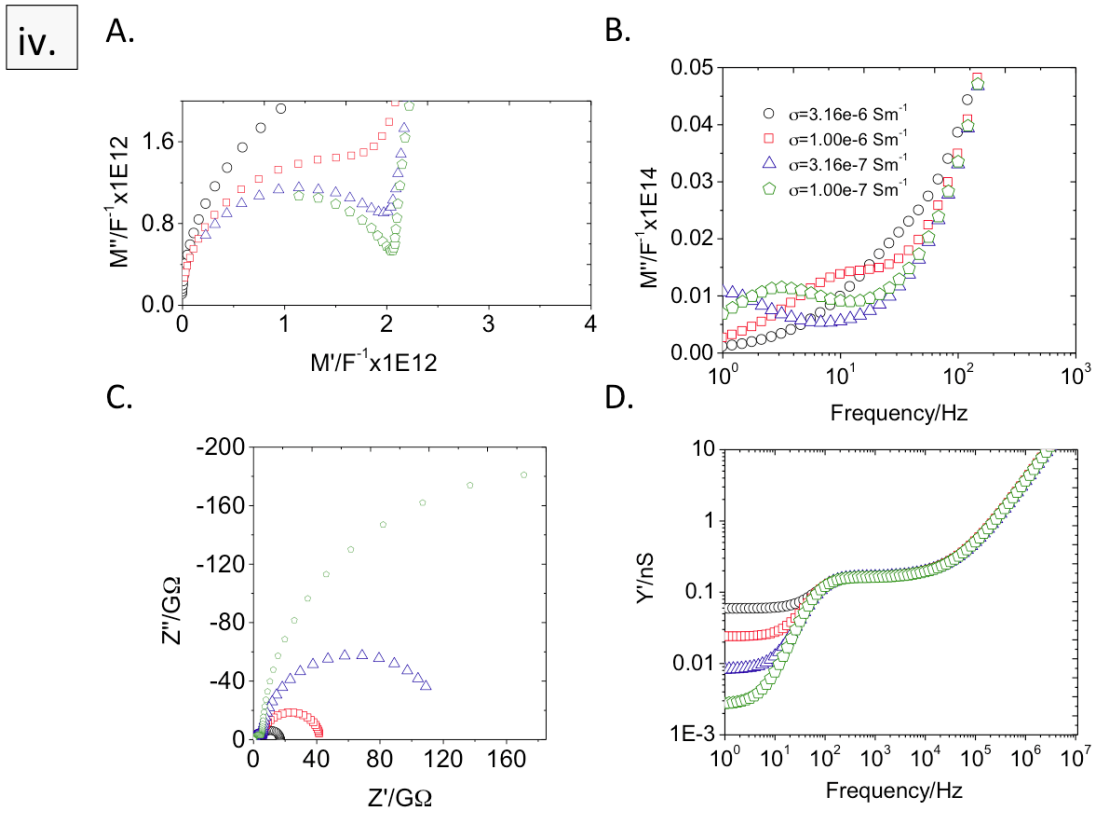

Fig. 23. *Impedance response for region iv for extracting the shell conductivity plotted as: (A) modulus Nyquist, (B) Imaginary modulus spectroscopic, (C) impedance Nyquist and (D) real admittance spectroscopic. Note (A) and (B) have been enlarged to show the low frequency shell response. The shell permittivity is 2000 in all plots.*

6.3.3. Extracting Shell Permittivity

The methods used to extract the shell permittivity in this study are: the shell arc diameter of a modulus Nyquist plot (M'1); the shell plateau of a spectroscopic plot of the real capacitance (E'LF); and using the diameter of the shell arc of an impedance Nyquist plot with the Debye frequency obtained from a spectroscopic

plot of the imaginary impedance (Z'W1). A plot of the lowest possible RMS deviation from the known values of shell permittivity when using the best equivalent circuit and formalism for a range of material properties is given in fig. 24A. Similar to the extraction of shell conductivity, the extraction of the shell permittivity becomes more accurate as the shell permittivity becomes more different to that of the core or the shell conductivity becomes more different to that of the core. Generally, the deviation is less than ±10% when the shell conductivity is less than 3.16 μSm^{-1} or the shell permittivity is less than 80. This is expanded to a shell permittivity of 100 when close to the permittivity axis (for shell conductivities of 0.1mSm^{-1} to 63.1 μSm^{-1}) and to conductivities as high as 10 μSm^{-1} close to the conductivity axis from shell permittivities of 2000 to 1122. A schematic of what formalism is best for extracting the shell permittivity for varied shell properties is given in fig. 24.

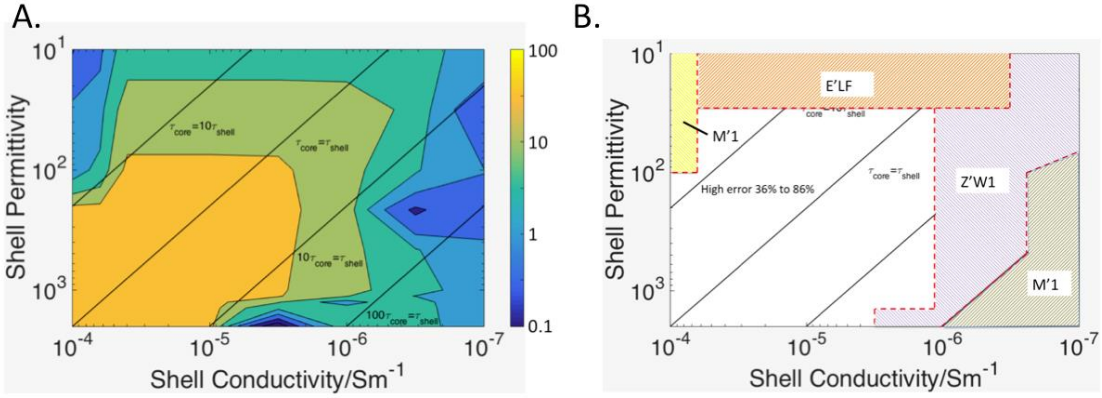

Fig. 24. *(A) Plot of the lowest RMS deviation when extracting the shell permittivity using the optimal equivalent circuit and impedance formalism. Note the scale is logarithmic. (B) Schematic showing which impedance formalism gave the lowest deviation for the combinations of material properties. Note: regions with an RMS deviation of over 25% from the input shell permittivity have been discarded leaving white space.*

An enlargement of fig. 24B is given in fig. 25 with blue lines to show regions of interest selected for further study. There are distinct regions where certain formalisms are better than others for extracting the shell permittivity. Regions where the shell permittivity cannot be extracted to within ±25% of the true value have been discarded. Region i, similarly to the plot for low frequency conductivity, is a region where the modulus formalism works well. Modulus Nyquist plots can be used to find the shell capacitance (M'1). This area is for shell permittivities between 10 and 100 and shell conductivities between 0.1 mSm^{-1} and 63.1 μSm^{-1}.

Region ii, where the shell conductivity varies from 63.1 to 0.316 μSm^{-1} and the shell permittivity varies from 10 to 31.6 gives the most accurate values for shell permittivity when using the shell plateaus in spectroscopic plots of the real capacitance. The majority of the remaining property space where shell conductivity is lower than 1 μSm^{-1} is split between region iii, where extracting shell permittivity from the Debye frequency of spectroscopic plots of the imaginary impedance is best and region iv, where it is best to use the shell arc diameters of the modulus Nyquist plots. Region iii also extends to shell conductivities increasing to 3.16 μSm^{-1} for shell permittivities greater than 1410.

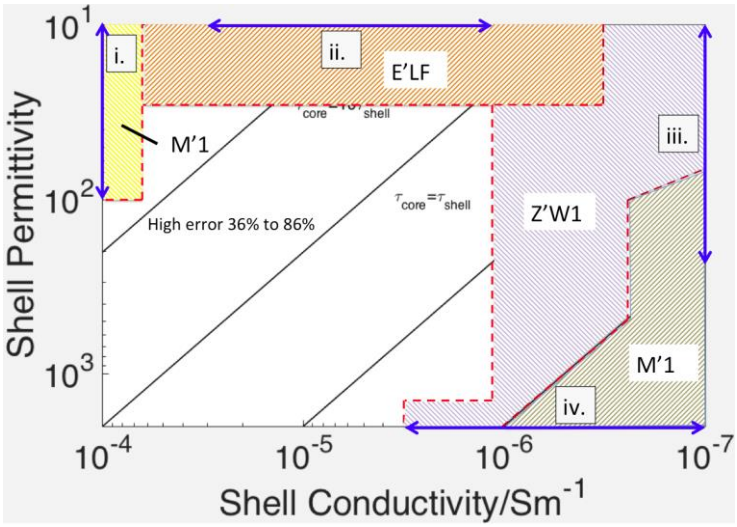

Fig. 25. *Schematic showing which regions of interest (blue lines, labelled i to iv) are examined to find why different formalisms are better for extracting the shell permittivity.*

In region i τ_{core} is greater than τ_{shell}, hence the high frequency response is assigned to the shell. Spectroscopic plots of E' (see fig. 26A) give distinct plateaus but, due to the proximity of the core and shell time constants, values of extracted shell permittivity were between ±10 to ±44% off the true value. The high frequency response of Nyquist plots of impedance and spectroscopic plots of the imaginary impedance (see figs. 26B and C, respectively) were too well-merged to extract resistances and Debye frequencies to calculate the shell permittivity from Z'W1. Modulus Nyquist plots (see fig. 26D) showed a distinct high frequency arc that could be used to extract the shell permittivity with deviation from the true value of ±8%, reducing to ±4% as the shell permittivity reduced to 10. This is due to the M* arc diameter increasing, which reduces the uncertainty arising from the merging between the low and high frequency arcs.

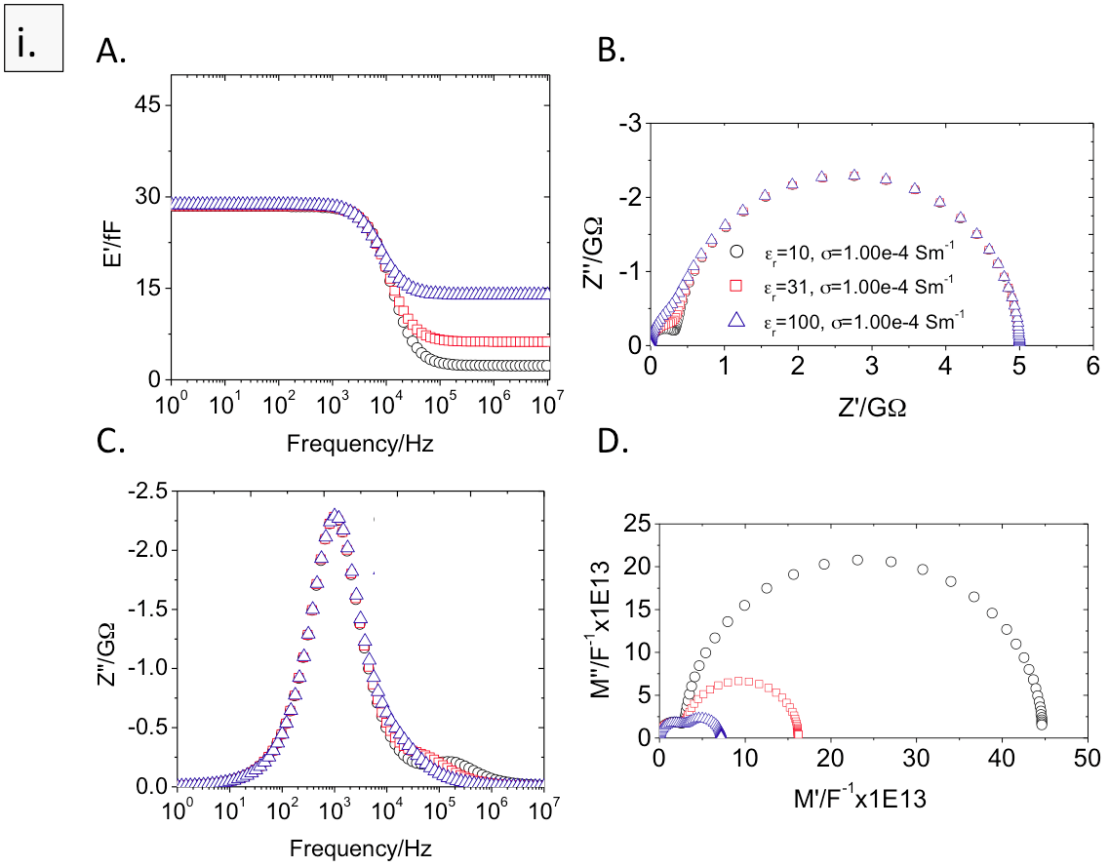

Fig. 26. *Impedance response for region i for extracting the shell permittivity plotted as: (A) real capacitance spectroscopic, (B) impedance Nyquist, (C) imaginary impedance spectroscopic and (D) modulus Nyquist.*

For region ii, E'LF was the best method for extracting the shell permittivity. Here τ_{core} is greater than τ_{shell}, hence the high frequency response is assigned to the shell. Both a modulus Nyquist plot and a spectroscopic plot of the imaginary impedance (see figs. 27A and B, respectively) showed merged responses making extraction of the shell permittivity using M'1 or Z'W1 unreliable. The most viable method studied was to use spectroscopic plots of E' (see fig. 27C) that had a high frequency plateau with a value of 2.23 fF giving the shell permittivity to within ±10% of the true value.

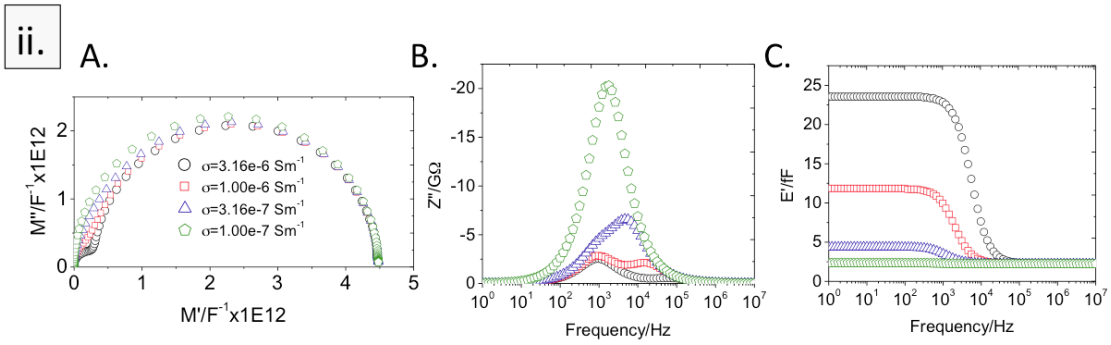

Fig. 27. *Impedance response for region ii for extracting the shell permittivity plotted as: (A) modulus Nyquist, (B) imaginary impedance spectroscopic and (C) real capacitance spectroscopic. The shell permittivity is 10 for all plots.*

Region iii examines the transition between Z'W1 and M'1 for a fixed shell conductivity of 0.1 μSm^{-1} as the shell permittivity increases. Here τ_{shell} is greater than τ_{core} and so the low frequency response is assigned to the shell. At shell permittivities of 10 to 31, the modulus Nyquist arcs are merged (see fig. 28A) making extraction of the shell capacitance using M'1 unreliable. As the shell permittivity increases beyond 100 the modulus Nyquist arcs become distinct for the shell and core (see fig. 28B for an enlargement of the high shell permittivity arcs) permitting reliable use of M'1. Conversely, as the permittivity increases, impedance Nyquist arcs do not have low enough frequency to be resolved (see fig. 28C). Spectroscopic plots of the imaginary impedance (see fig. 28D) have well-defined peaks allowing the shell Debye frequency to be extracted. The impedance Nyquist plots show only one arc. However these are dominated by the low conductivity of the shell in region iii allowing accurate measurement of the shell resistance when the frequency is low enough to resolve it. When the shell permittivity is low enough to resolve the impedance Nyquist arcs the shell resistance and Debye frequency can be used to calculate the shell permittivity accurately using Z'W1. Spectroscopic plots of E' (see fig. 29) have well-defined plateaus for the core and shell. This formalism consistently extracts the shell permittivity in region iii with a deviation of ~±6%. E'LF is not selected over M'1 or Z'W1 because, in the permittivity range where these formalisms work well, the deviation is as low as ~±2 and ~±3% respectively.

iii.

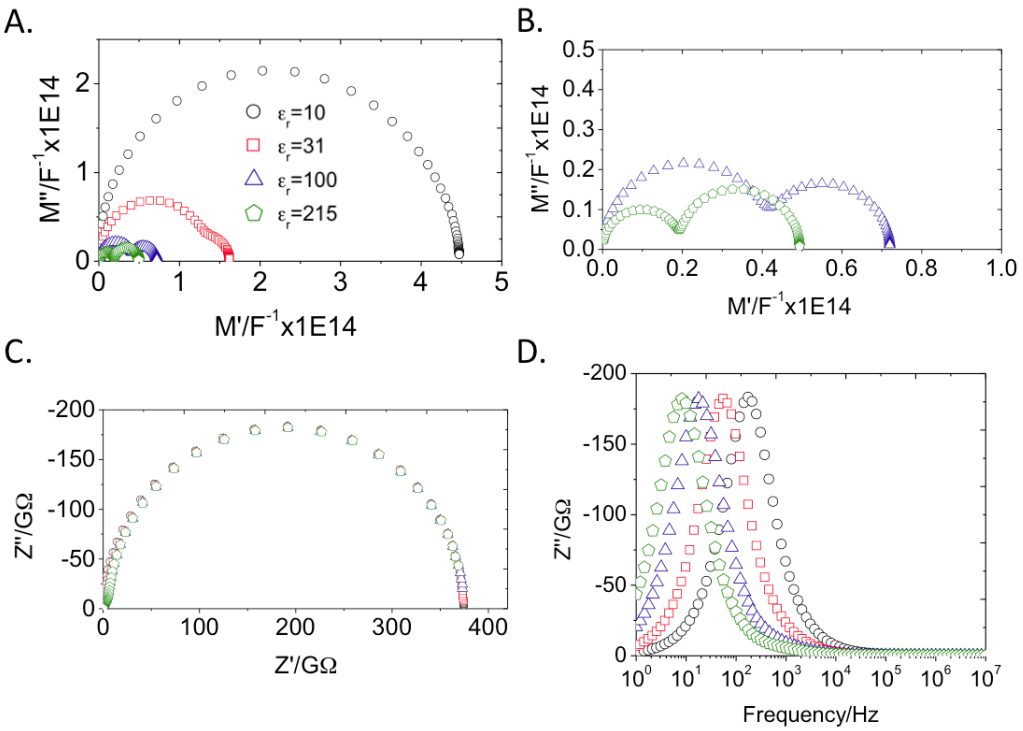

Fig. 28. *Impedance response for region iii for extracting the shell permittivity plotted as: (A) modulus Nyquist, (B) enlargement of origin of (A), (C) impedance Nyquist and (D) imaginary impedance spectroscopic. Note the shell conductivity for all plots is 0.1* μSm^{-1}.

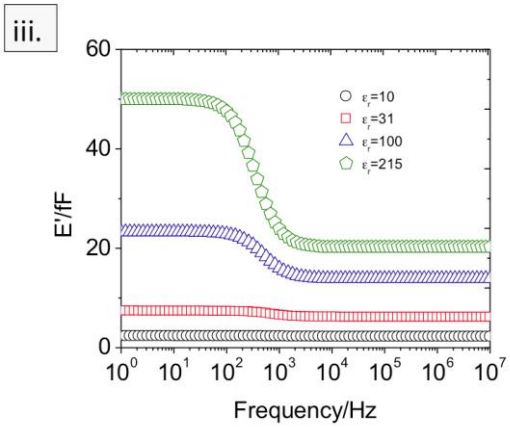

Fig. 29. *Real capacitance spectroscopic plot of region iii for extracting the shell permittivity.*

Region iv examines the transition between the Z'W1 and M'1 methods for a fixed shell permittivity of 2000. Between shell conductivities of 3.16 μSm^{-1} and 1 μSm^{-1} Z'W1 is the best method for extracting the shell permittivity with a deviation of ±0.04 and ±5.78%, respectively. As the conductivity decreases to first 0.316 μSm^{-1} and then 0.1 μSm^{-1}, M'1 provides the most accurate shell permittivity with deviations of ±5.97 and ±1.17%, respectively. Here the low frequency response is assigned to the shell. Modulus Nyquist plots (see fig. 30A) showed distinct arcs for lower shell conductivities, hence M'1 could be used for the more resistive shells. Conversely, impedance Nyquist plots (see fig. 30B) only had low enough frequencies to resolve the higher shell conductivities.

Spectroscopic plots of the imaginary impedance (see fig. 30C) had extractable Debye peaks for all but the lowest shell conductivity. In order to calculate the shell permittivity using Z'W1, well resolved Z* Nyquist arcs are required; hence Z'W1 is only usable for higher shell conductivities. Spectroscopic plots of E' (see fig. 30D) showed low frequency plateaus that appeared to vary with shell conductivity, given that the shell permittivity was fixed. E'LF gave the shell permittivity to within ~±6% for a shell conductivity of 0.1 μSm^{-1}. However, this increased to ~±54% for a shell conductivity of 3.16 μSm^{-1} making the extraction of shell permittivity by E'LF increasingly unreliable.

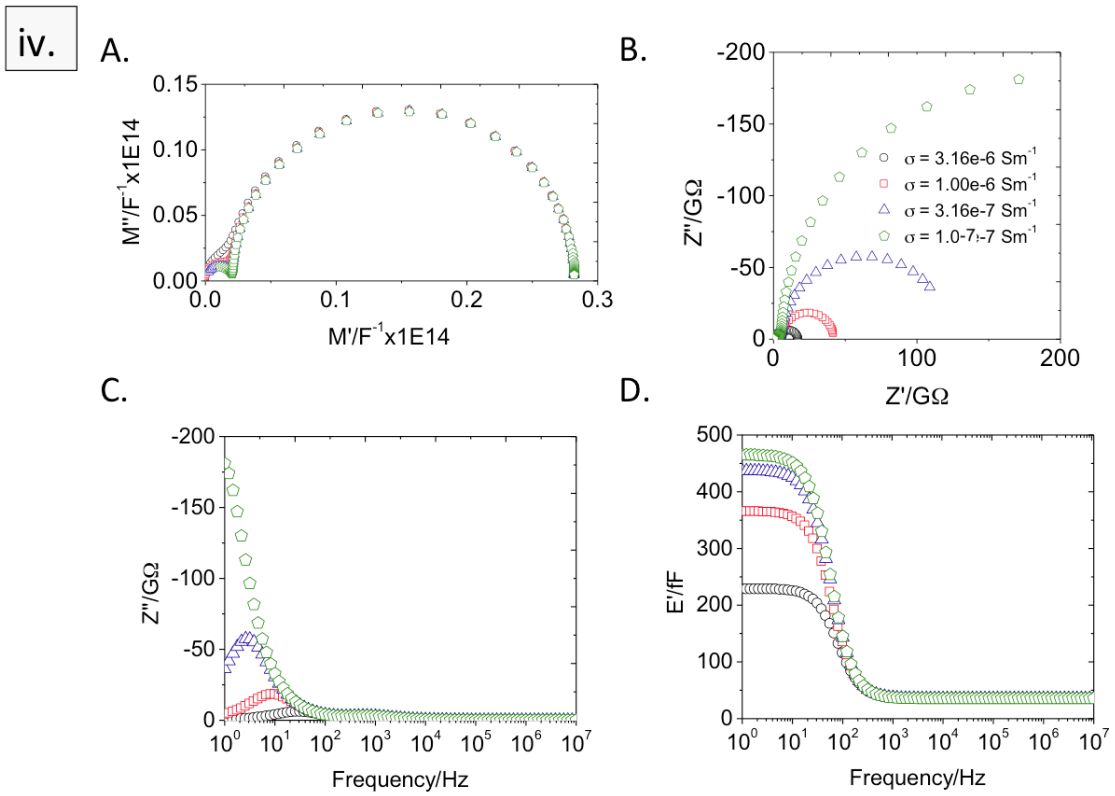

Fig. 30. *Impedance response for region iv for extracting the shell permittivity plotted as: (A) modulus Nyquist, (B) impedance Nyquist, (C) impedance spectroscopic and (D) real capacitance spectroscopic. Shell permittivity is 2000.*

6.3.4. Extracting the core conductivity

This study employs three methods to calculate the core conductivity: resistances taken from impedance Nyquist core arcs (Z'2); the core plateau of real admittance spectroscopic plots (Y'HF); resistances calculated by the capacitance and Debye frequency of modulus Nyquist and imaginary spectroscopic plots, respectively (M'W2). Where the PBLM was selected as the best fit of the FEM impedance data, the core response also contains the parallel shell component. This means that extraction of the core conductivity requires the shell conductivity. In this work, the extracted best value of conductivity is substituted into equations (6.3) and (6.4) to obtain the core conductivity.

A plot of the lowest deviation possible for extracting the core conductivity is given in fig. 31A. The extraction of the core conductivity became less reliable when the shell had significantly different conductivity and permittivity to the core. The core conductivity could be extracted to within a deviation of ±10% when the shell conductivities were less than 10 μSm^{-1} or shell permittivities were greater than or equal to 1000. There was an extension to the low deviation region for shell conductivities below 1 μSm^{-1} and shell permittivities greater than 100. A schematic of what formalisms were best for extracting the core conductivity for varied shell properties is given in fig. 31B.

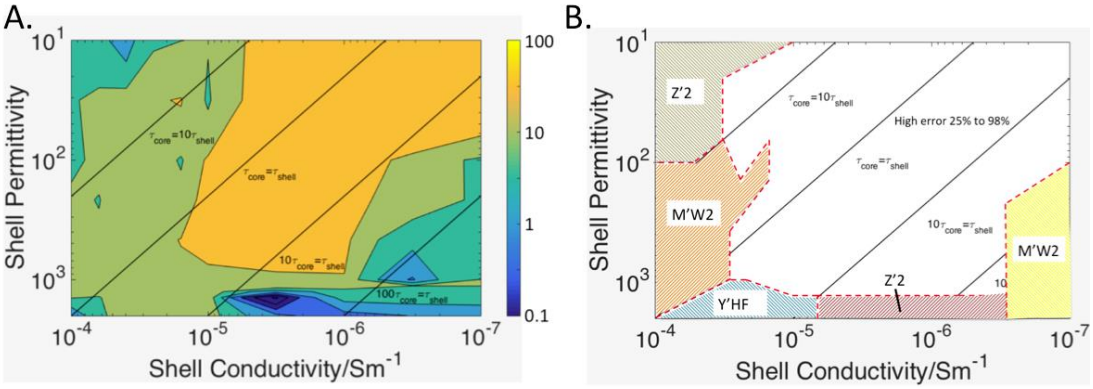

Fig. 31. *(A) Plot of the lowest RMS deviation when extracting the core conductivity using the optimal equivalent circuit and impedance formalism. Note the scale is logarithmic. (B) Schematic showing which impedance formalism gave the lowest deviation for the combinations of material properties. Note: regions with an RMS deviation of over 25% from the input core conductivity have been discarded leaving white space.*

Several distinct areas where specific formalisms are best for extracting the core conductivity exist. An enlargement of fig. 31B is given in fig. 32. Here several lines (blue) have been plotted to show regions (i to iii) for further study. Region i has a fixed core and shell conductivity of 0.1 mSm^{-1} and the shell permittivity varies from 10 to 2000. Here the best formalism changes from Z'2 to M'W2 as the shell permittivity increases to 100. Region ii is centred on the transition of Y'HF to Z'2 along the conductivity axis for shell conductivities of 39.8 μSm^{-1} to 3.16 μSm^{-1}. Finally, region iii examines a region where M'W2 out-performs Z'2 and Y'HF as the shell permittivity increases for a fixed shell conductivity of 0.1 μSm^{-1}.

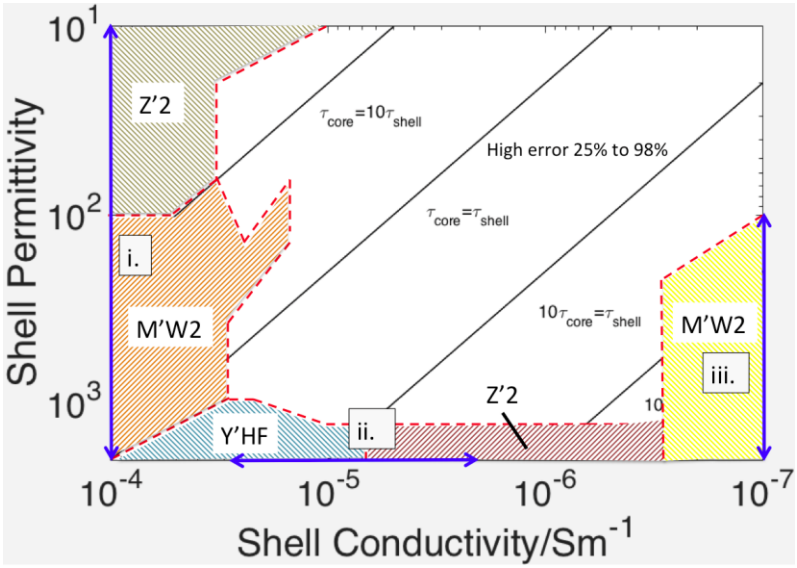

Fig. 32. *Schematic showing which regions of interest (blue lines, labelled i to iii) are examined to find why different formalisms are better for extracting the core conductivity.*

In region i, τ_{core} is greater than τ_{shell}. Hence the low frequency response is assigned to the core except when the core properties are the same as the shell. When the shell permittivity is low, Nyquist plots of impedance (see fig. 33A) reveal

two separate arcs allowing for the shell conductivity to be extracted accurately using Z'2. For a shell permittivity of 10 the extracted core conductivity only deviated by ±8.53%. As the impedance Nyquist arcs become more merged as the shell permittivity increases, the high frequency shell arc disappears in modulus Nyquist plots (see fig. 33B) leaving a single arc that permits extraction of the core capacitance. Combining the core capacitance with a Debye frequency taken from spectroscopic plots of the imaginary modulus (see fig. 33C) allowed more accurate calculation of the core conductivity for shell permittivities of 1000 to 2000 using M'W2 within ±14.32% (for a shell permittivity of 1000). Spectroscopic plots of Y' (see fig. 33D) show a single plateau for shell permittivities of 1000 and 2000. Here τ_{core} and τ_{shell} are of the same magnitude making the extraction of the core conductivity by Y'HF unreliable.

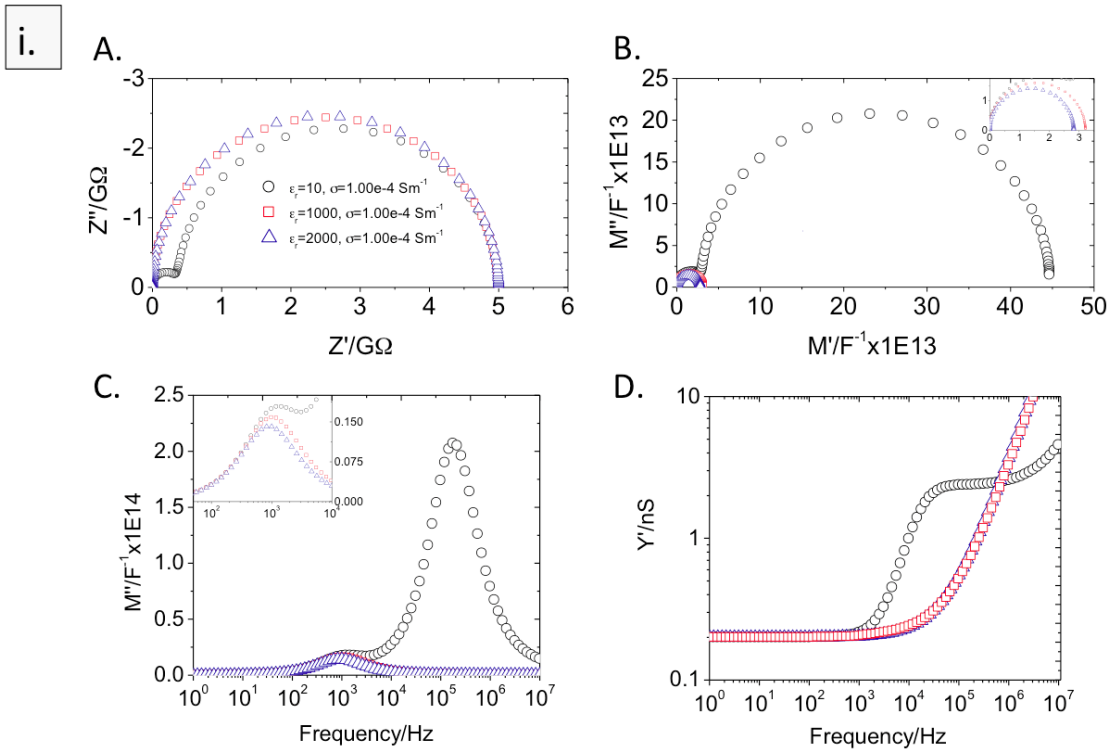

Fig. 33. *Impedance response for region i for extracting the core conductivity plotted as: (A) Impedance Nyquist, (B) modulus Nyquist, (C) imaginary modulus spectroscopic and (D) real admittance spectroscopic. Note the inset graphs for (B) and (C).*

Region ii examines the transition of Y'HF to Z'2 at a shell conductivity of ~10 μSm^{-1} where the shell permittivity is 2000. In this region $\tau_{shell} > \tau_{core}$, hence the high frequency response is assigned to the core. Modulus Nyquist plots (see fig. 34A) show merged arcs making the extraction of core capacitances unreliable. This means that it was not possible to combine the core capacitance with core Debye frequencies from spectroscopic plots of the imaginary modulus (see fig. 34B) and so it was not possible to calculate the core conductivity from M'W2. Impedance Nyquist plots (see fig. 35C) had discrete core and shell arcs at lower shell conductivities. This means that core resistances could only be measured for more resistive shell conductivities, allowing the core conductivity to be calculated using Z'2. For shell conductivities of 3.16 and 1 μSm^{-1}, the Z'2 method extracted core

conductivities with a deviation of ±1.65 and ±0.52%, respectively. Spectroscopic plots of Y' (see fig. 34D) always had a high frequency plateau in region ii. As the shell conductivity decreased from 39.8 to 1 μSm^{-1} the deviation increased from ±14.23 to ±21.52%. For the models where the difference between the shell and core conductivity was much less than an order of magnitude, Y'HF was selected as it was the only method that could give a value for the core conductivity.

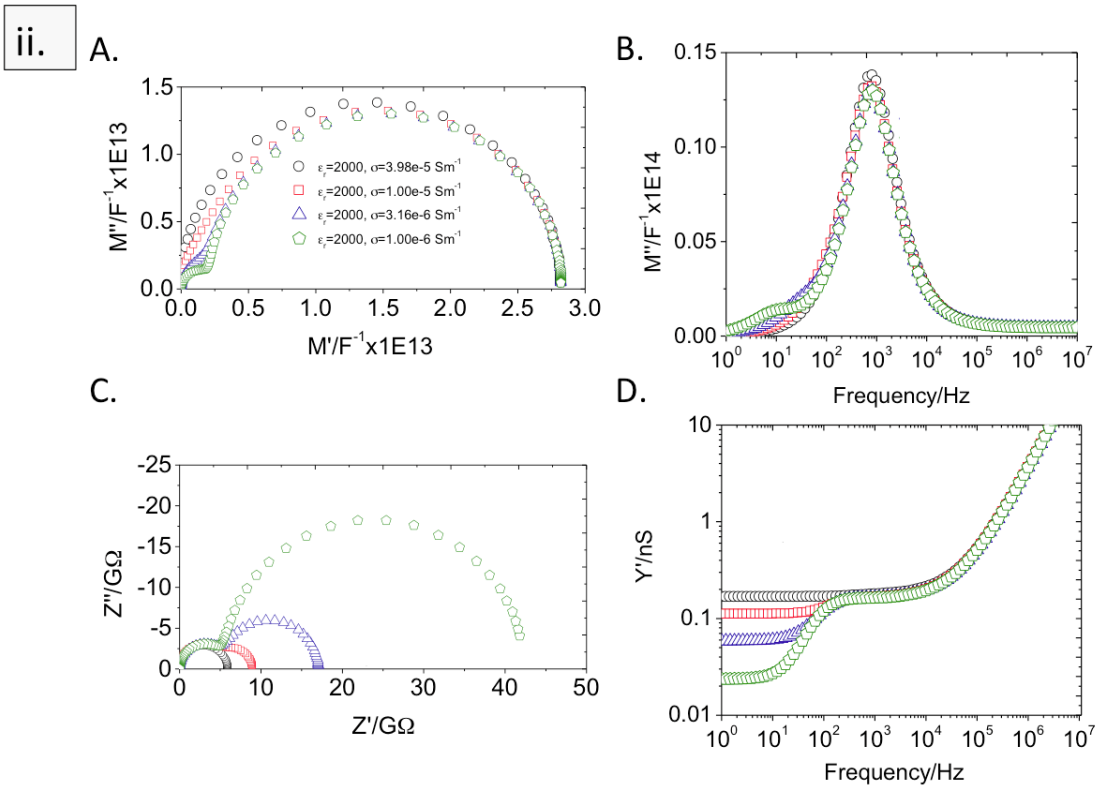

Fig. 34. *Impedance response for region ii for extracting the core conductivity plotted as: (A) modulus Nyquist, (B) imaginary modulus spectroscopic, (C) impedance Nyquist and (D) real admittance spectroscopic plot.*

Region iii describes a region where M'W2 performs best for fixed shell conductivity of 0.1 μSm^{-1} as the shell permittivity decreases. Here $\tau_{shell} > \tau_{core}$, hence the high frequency response is assigned to the core. Nyquist impedance plots (see fig. 35A) showed merged arcs. An enlargement of the origin of the impedance Nyquist plots (see fig. 35B) revealed that, despite the merging of the core and shell arc, at higher permittivities the core arc could be made out. This allowed the core conductivity to be extracted using Z'2 for shell permittivities of 1260 and 2000 but with deviations of ±26.12 and ±15.31%, respectively. M'W2 works the best for extracting core conductivity because there are well-defined modulus Nyquist arcs (see fig. 35C) and imaginary modulus spectroscopic Debye peaks (see fig. 35D), allowing the calculation of the core conductivity using M'W2. Deviations in region iii ranged between ±0.96 to ±7.82% for M'W2. Spectroscopic plots of Y' showed that, despite the shell conductivity being fixed, the core plateau heights varied with shell permittivity (see fig. 35D). This shows the accuracy of approximating the core conductance to the high frequency plateau decreases as τ_{shell} and τ_{core} become more similar in magnitude. As the shell permittivity increased, the deviation in Y'HF varied from ±80.62 to ±12.22% in region iii.

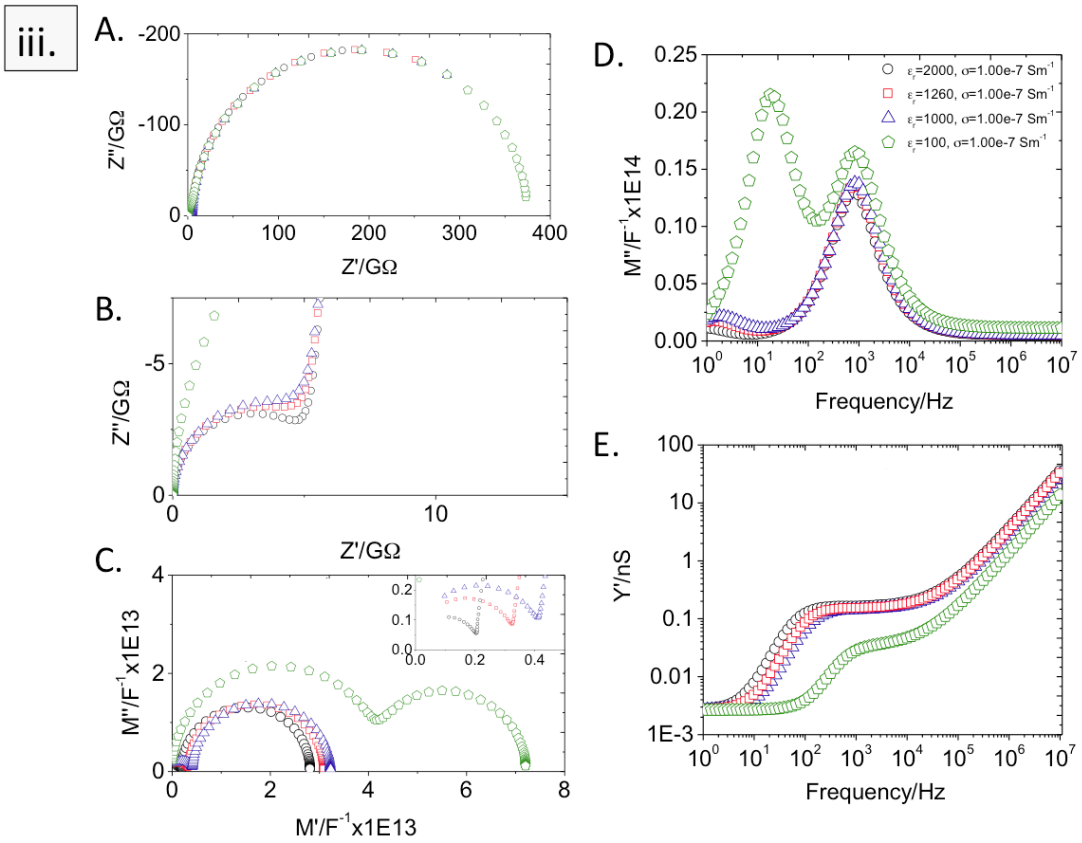

Fig. 35. *Impedance response for region iii for extracting the core conductivity plotted as: (A) Impedance Nyquist, (B) enlargement of the origin of (A), (C) modulus Nyquist, (D) imaginary modulus spectroscopic and (E) real admittance spectroscopic.*

6.3.5. Extracting the core permittivity

The three methods used to calculate the core permittivity in this work were: extracting the capacitance from modulus Nyquist arc diameters (M'2); using the core plateau of the real capacitance (E'HF); calculating the core capacitance from impedance Nyquist arc diameters and the core Debye frequency from the imaginary component of impedance (Z'W2). A plot of the lowest RMS deviation when extracting the core permittivity is given in fig. 36A. Similar to the core conductivity, the core permittivity could be extracted with greater accuracy if the core and shell conductivity were similar or the core and shell permittivity were more similar. The core permittivity could be extracted with less than ±10% deviation when the shell conductivity is greater than 25.1 μSm^{-1} or a shell permittivity less than 215. The low deviation region was extended to shell conductivities as low as 10 μSm^{-1} at low shell permittivities (10 to 31) and for shell permittivities as low as 100 for shell conductivities between 1 and 0.1 μSm^{-1}. A plot of the impedance formalisms that were most successful in extracting the core permittivity is given in fig. 36B.

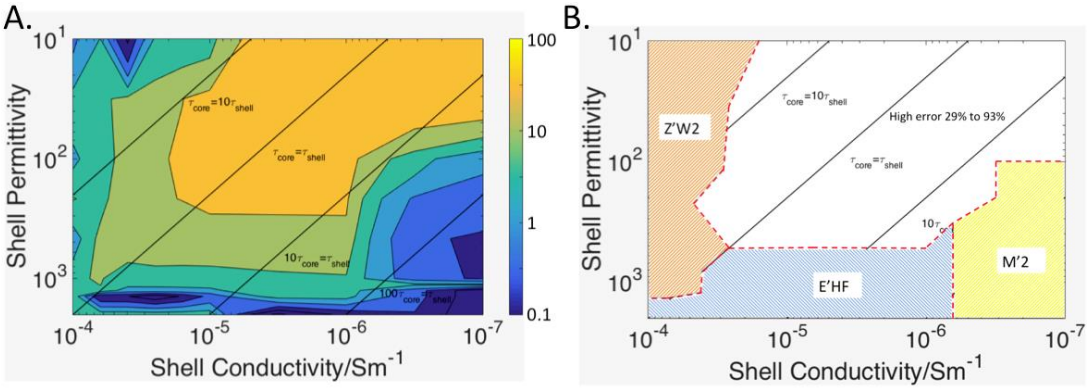

Fig. 36. *(A) Plot of the lowest RMS deviation when extracting the core permittivity using the optimal equivalent circuit and impedance formalism. Note the scale is logarithmic. (B) Schematic showing which impedance formalism gave the lowest deviation of the combinations of material properties. Note: regions with an RMS deviation of over 25% from the input core permittivity have been discarded leaving white space.*

The three methods used to extract the core permittivity occupied distinct areas of the material property space (see fig. 37 for enlargement of fig. 36B). Z'W2 performed best for shell conductivities greater than 39.8 μSm^{-1} and shell permittivities less than ~1260. M'2 worked for shell conductivities lower than 0.316 μSm^{-1} and shell permittivities greater than 100. For the remaining material property space where shell permittivity was greater than ~464, E'HF was the best. Two regions where Z'W2 and M'2 met the space occupied by E'HF (regions i and ii, respectively) were considered for further study to see why the preferred formalism changed at this point. Region i had a fixed core and shell conductivity of 0.1 mSm^{-1}. Region ii had a fixed core and shell permittivity of 2000.

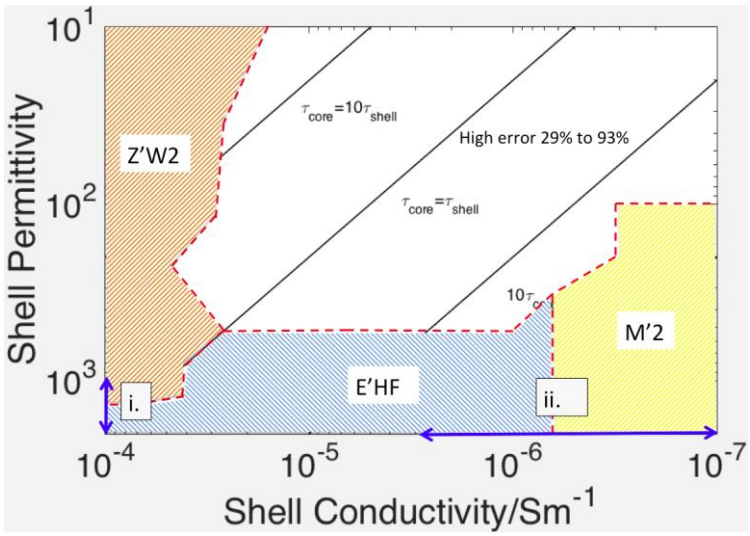

Fig. 37. *Schematic showing which regions of interest (blue lines, labelled i and ii) are examined to find why different formalisms are better for extracting the core permittivity.*

For region i, impedance Nyquist plots (see fig. 38A) and spectroscopic plots of the imaginary impedance (see fig. 38B) had merged responses that gave spectra consistent with a encased model composed of only core material with a

conductivity of 0.1 mSm^{-1} and permittivity of 2000. The measured Debye frequency of the composite response changed from 950 Hz (when the shell permittivity was 2000) to 1000Hz for the other three models. Hence the change in shell permittivity could not be resolved accurately. It was assumed that the core response dominated the impedance Nyquist and imaginary impedance spectroscopic plots. Modulus Nyquist plots (see fig. 38C) gave merged arcs where a difference in shell permittivity could be resolved but, as this was a highly composite response, accurate values of the core permittivity could not be obtained.

Spectroscopic E' plots showed two plateaus (see fig. 38D) for all but the model with a shell permittivity of 2000. When two plateaus were present it was assumed that the core plateau was at lower frequency, as its time constant was larger than that of the shell. Both the high and low frequency plateaus were significantly affected by the reduction in shell permittivity. The transition of E'HF to Z'W2 is probably due to the model with equal core and shell properties having a single plateau in E' that gives better values for the core permittivity. As soon as multiple time constants are present in the model the plateaus for E' become composites of the core and shell properties, making the extraction of the core permittivity unreliable. Then the core-dominated response of the Impedance Nyquist and spectroscopic plots became preferable to use for analysis.

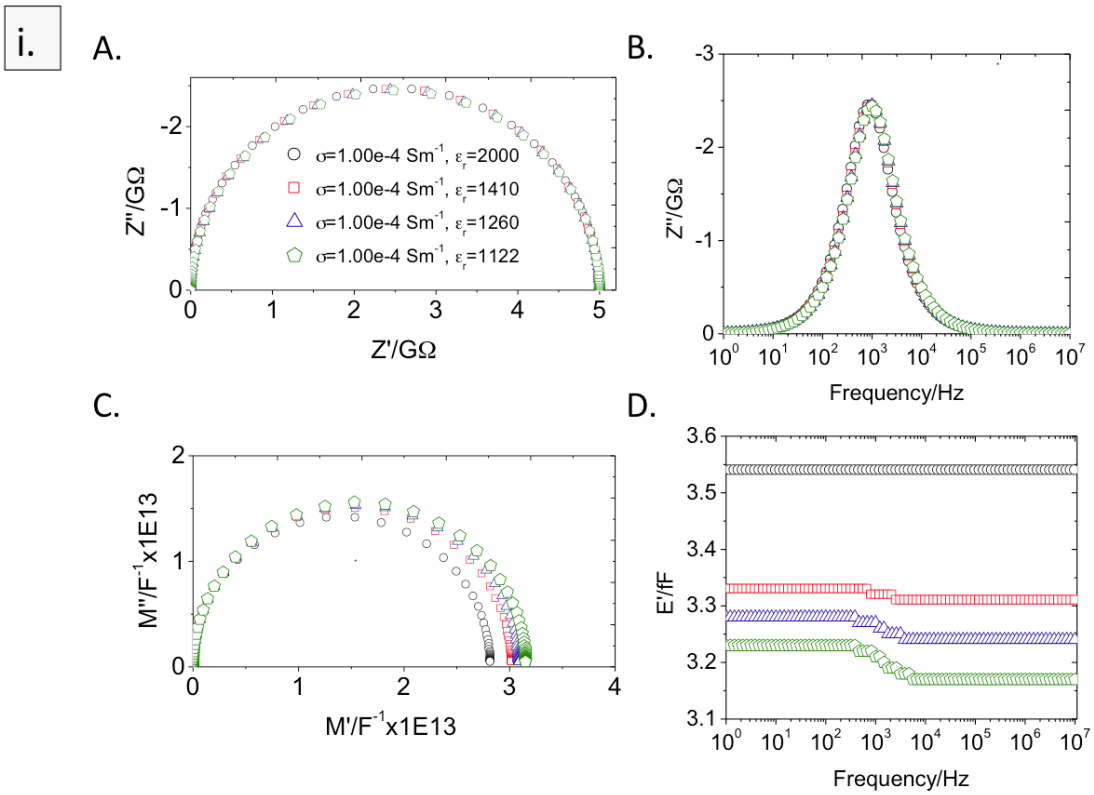

Fig. 38. *Impedance response for region i for extracting the core permittivity plotted as: (A) Impedance Nyquist, (B) imaginary impedance spectroscopic, (C) modulus Nyquist, (D) real capacitance spectroscopic.*

For region ii, the core response occurs at high frequency as $\tau_{shell} > \tau_{core}$. Here M'2 performs best at low shell conductivities and E'HF is best for higher shell conductivities. At low shell conductivities, the high frequency arcs of modulus Nyquist plots (see fig. 39A) are well resolved, allowing the core permittivity to be calculated from M'2. Models with shell conductivities of 0.1 and 0.316 μSm^{-1} have deviations for extracting the core permittivity with M'2 of ±0.22 and ±1.34%, respectively. As the shell conductivity increases beyond 1 μSm^{-1} the modulus Nyquist arcs are too well merged to obtain the core capacitance reliably. The impedance Nyquist core arcs (see fig. 39B) are distinguishable for shell conductivities of 0.1 to 3.16 μSm^{-1} but are always merged, making Z'W2 unreliable. For spectroscopic plots of imaginary impedance (see fig. 39C) high frequency peaks are merged and are not always usable due to a lack of impedance Nyquist arc diameters. Finally, E' spectroscopic plots had well defined plateaus for the core and shell. Here, as soon as the modulus Nyquist plots became too merged to extract data, the approximation offered by the E' plateaus becomes the most accurate way to extract the core permittivity. For shell conductivities of 1 and 3.16 μSm^{-1}, E'HF gave deviations in the extracted core permittivity of ±0.02 and ±0.12%, respectively.

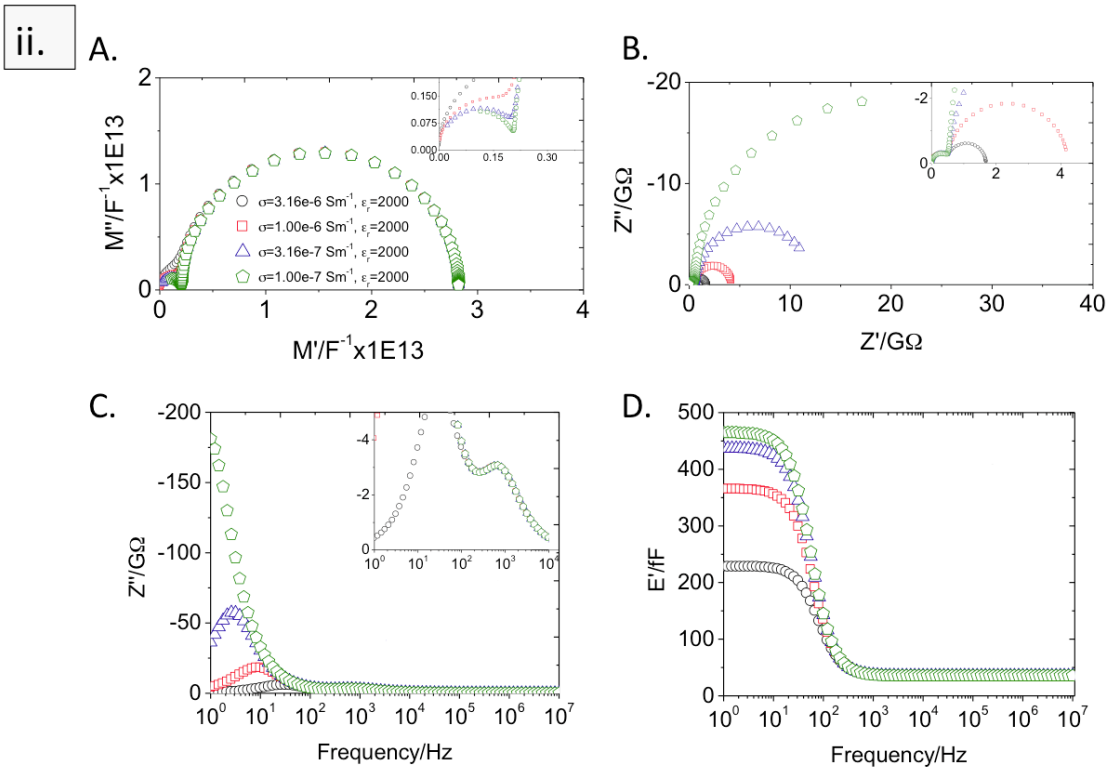

Fig. 39. *Impedance response for region ii for extracting the core permittivity plotted as: (A) modulus Nyquist, (B) impedance Nyquist, (C) imaginary impedance spectroscopic, (D) real capacitance spectroscopic.*

6.4. Discussion

In this chapter, the fits provided by several equivalent circuits for an encased model with fixed core properties and varied shell properties were compared. It is important to note that the resistances and capacitances were derived from the geometries associated with the hypothetical microstructures associated with the three equivalent circuits (see fig. 4) and the intrinsic conductivity and permittivity values inputted into the finite element simulation. No additional refinements were made. The equivalent circuit fits are purely analytical. If an analytical fit such as these equivalent circuits can model the impedance response of a finite element simulation in all four impedance formalisms, there is a strong indication that the equivalent circuit in question offers a good representation of the physical behaviour of FEM simulation.

Of the three equivalent circuits the SLM performed the worst. Comparing the impedance response in the four different formalism plots gave a minimum average deviation of ±34% and a maximum of ±163%. There were large regions of the material property space where the SLM completely failed to replicate the FEM simulated data. This was defined as the equivalent circuit not having the same number of arcs or plateaus as the FEM simulation. The majority of the material regions where the SLM failed were when the core and shell time constants differed by greater than an order of magnitude (see fig. 40). As the SLM assumes purely serial connectivity, all the material in each layer experiences a homogenous current flow and will contribute to the electrical response equally. As the core and shell time constants become closer in value the impedance response of the SLM will be similar to a electrically homogenous cube of materal. However, for the encased model, as the core and shell permittivity and conductivity values become increasingly different, it will be possible for additional conductive or capacitative pathways to form through the microstructure (as observed in chapters 4 and 5). This means that the encased model increasingly deviates from the SLM at lower shell conductivities and permititivies.

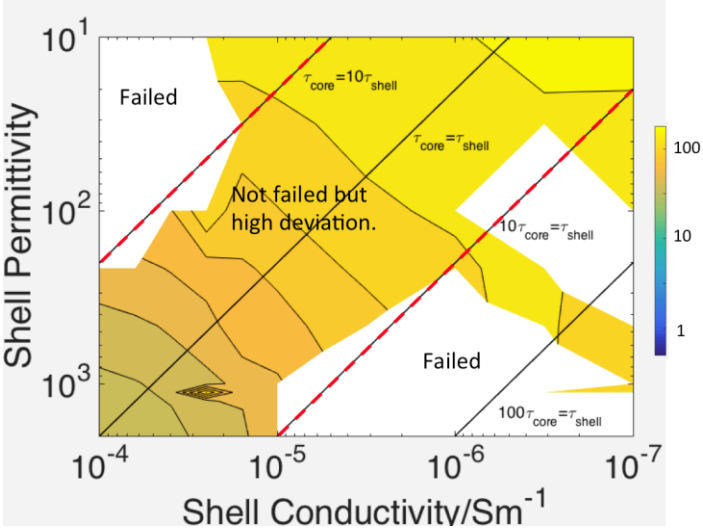

Fig. 40. *Plots of the RMS deviation of the SLM compared to the FEM simulated results for all simulated combinations of material properties with dashed lines seperating the regions where the SLM fails completely and the region where the values of the core and shell time constants are close enough for the SLM to work but not effectively. Note the deviation uses a log scale, white spaces show areas where an*

equivalent circuit did not have the same number of impedance responses as the FEM simulation and is therefore considered invalid. Note the straight lines plotted on top of the contours show the ratio between the theoretical core and shell time constants.

Both the SBLM and PBLM provided a better fit of the FEM simulation than the SLM, both with a maximum deviation of ±20%. The SBLM provided a marginally better fit (maximum difference beween SBLM and PLBM of ±0.4%) in material regions where the core and shell had very different properties (see fig. 41A). Here there is only a small difference between the SBLM and PBLM because the additional parallel pathways through the PBLM are not favourable enough to attract sufficient current to significantly affect the impedance response. The regions where the SBLM could not replicate the FEM data (white spaces) were due to the SBLM predicting minima between the core and shell impedance Nyquist arcs that were not present in the FEM data (see fig. 42). This instance is a borderline case where an equivalnet circuit has failed the selection criteria but still predicts a similar form to the FEM data. The PBLM was most favourable when either the shell and core permittiviy or conductivity were very similar (see fig. 41B). Here the difference in deviation from the FEM data for the PBLM and SBLM was ±14%. It is easy to understand why the PBLM works well when the shell conductivty is close to that of the core (0.1 mSm^{-1}) as the conduction pathways through the parallel shell become increasingly favourable in good agreement with the literature[6, 7, 12].

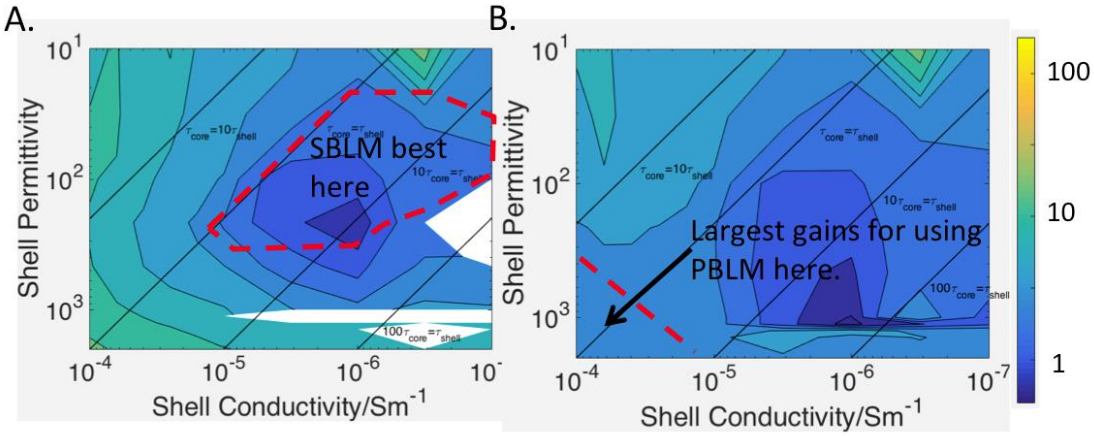

Fig. 41. *Plots of the RMS deviation of (A) the SBLM and (B) the PBLM compared to the FEM simulated results for all simulated combination of material properties. Note the deviation uses a log scale, white spaces show areas where an equivalent circuit did not have the same number of impedance response as the FEM simulation and is considered invalid. Note the straight lines plotted on top of the contours show the ratio between the theoretical core and shell time constants.*

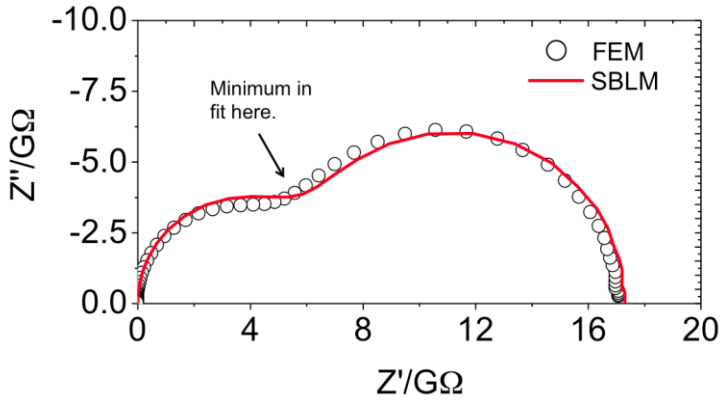

Fig. 42. *Impedance Nyquist plot of an encased model with a shell conductivity of 3.16 μSm^{-1} and shell permittivity of 1122 with corresponding SBLM equivalent circuit fit.*

It is harder to see why the PBLM performs well when the shell permittivity is the same as or close to the core permittivity of 2000 and the shell conductivity is lower than that of the core. Here it would be expected that the current would flow preferentially through the core, producing an electrical microstructure that resembles the SBLM[8]. It is possible that, since the high shell permittivty means that the capacitance of the parallel shell will have a lower impedance than its resistance at a lower frequency, leading to an increase in current flow through the parallel shell. A current density plot taken at the core Debye frequency for an encased model with a shell conductivity of 0.1 μSm^{-1} and permittivity of 2000 showed that the current density was 0.02 Am^{-2} in the series shell and 0.05 Am^{-2} in the parallel shell (see fig. 43A and B). Given that the core current density was 5.3 Am^{-2} it is surprising that this very small difference in current density would have any significance but the PBLM did fit the FEM data better here with a deviation of ±3.25% versus ±8.59% for the SBLM. Further work should be undertaken to clarify why the PBLM performs better here.

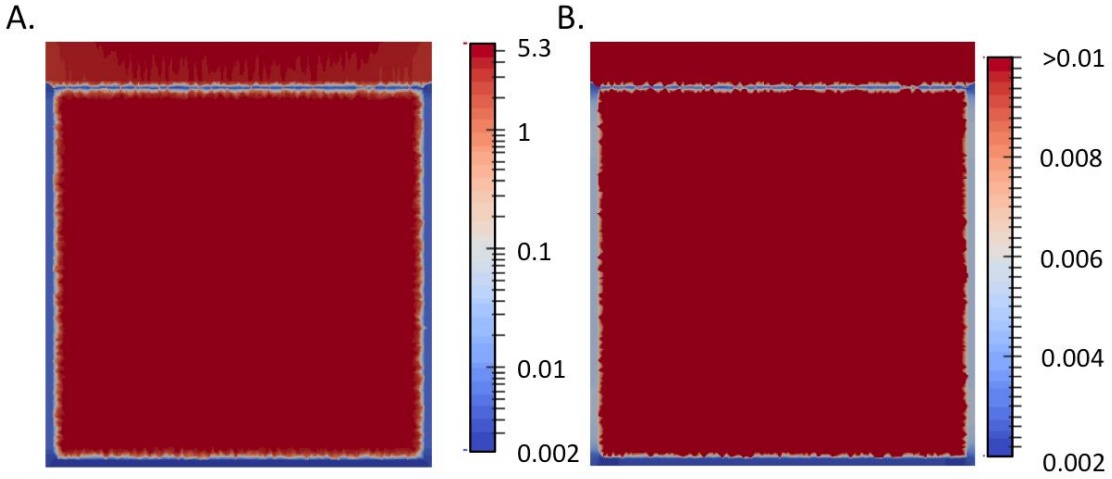

Fig. 43. *Current density plots of an encased model with a shell conductivity of 0.1 μSm^{-1} and permittivity of 2000 where (A) shows the full range of current densities on a logarithmic scale and (B) shows only the lower current densities on a linear scale; note the higher current denisty in the parallel shell region. Units are Am^{-2}.*

When extracting values of permittivity and conductivity for the shell and core regions, several patterns were revealed (see fig. 44). For the shell properties

the most accurate values were obtained when the shell had lower conductivity or permittivity than the core (see figs. 44A and B). Here the difference in shell properties allows reliable (less than ±10% deviation) extraction of the shell conductivity or permittivity at shell conductivities lower than 3.16 μSm or shell permittivities lower than 31.6. This is true even for material regions where the theoretical core and shell time constants are the same. It is possible that the measured time constant is changing due to geometry effects similar to what was observed in chapter four.

When extracting the core intrinsic properties the trends observed with the shell properties are reversed somewhat (see figs. 44C and D). When the core and shell permittivities or conductivities are similar the extracted values are more accurate. This could simply be due to the fact that, as the core volume fraction is 0.8, when the core and shell properties are very similar the core response will dominate since there is more of it. Both the SBLM and PBLM assume the same cubic geometry for the core, so extracting a response that is merged from the core and shell is only undestimating the volume by 20%.

It is important to consider that, when the core properties are extracted using the PBLM, the shell conductivity or permittivity is required for equations (6.3) and (6.4) adding an additional uncertainty to the process. In this work the most accurate value is obtained for the shell intrinsic properties is inputted to equations (6.3) and (6.4), which from figs. 44A and B, can be a factor of two out from the actual value. This suggests that there could have been some favourable cancelling of errors when using incorrect values of the shell intrinsic properties to calculate the core properties. Finally, there are regions where either the shell conductivity is the same as or close to the core value but the shell and core permittivities are very different or both permittivities are the same and the conductivities are different. As seen in chapters four and five, when the permittivity of the core and shell is fixed to the same value and the conductivity varied, conduction pathways form and alter the impedance response. Likewise, when there is a difference in permittivity but conductivity is fixed, capacitive pathways form. This behaviour causes extensions to the region of low deviation along the conductivity and permittivity axes for the core and shell intrinsic propeties.

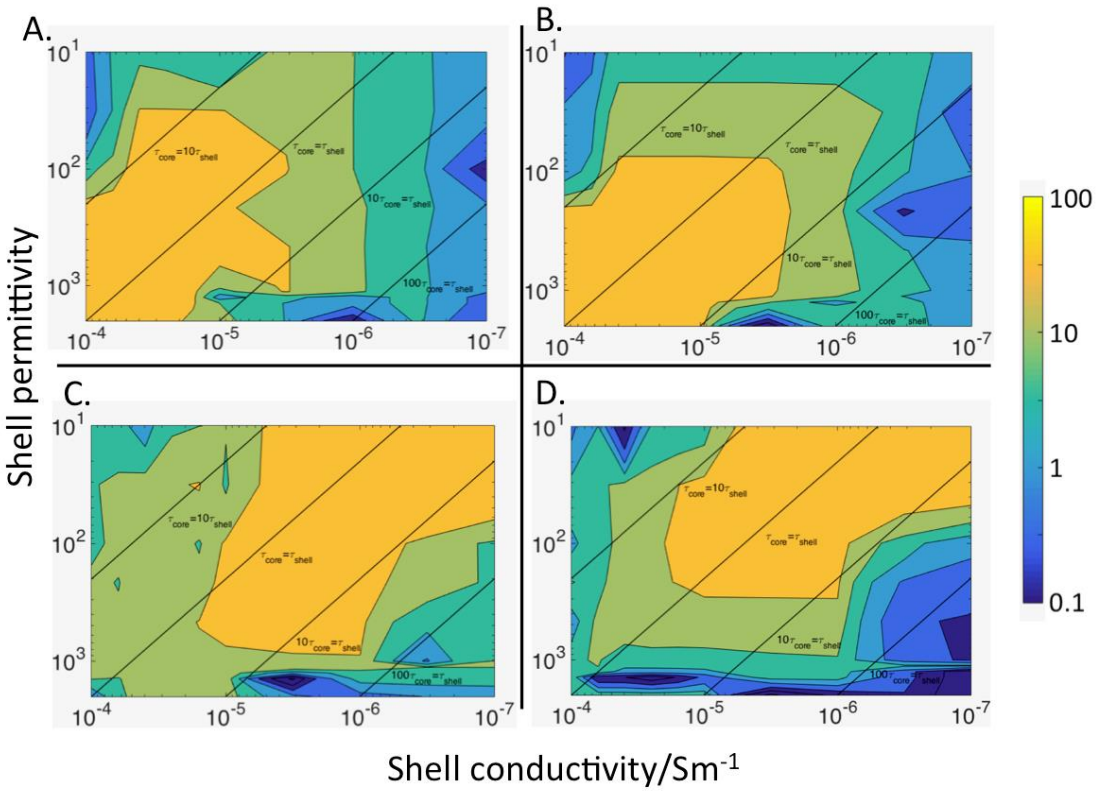

Fig. 44. *(A) Plot of the lowest RMS deviation when extracting intrinsic material properties using the optimal equivalent circuit and impedance formalism. (A) Shell conductivity, (B) shell permittivity, (C) core conductivity and (D) core permittivity. Note the scale is logarithmic.*

When examining which impedance formalism could be used to extract the extrinsic shell and core resistances and capacitances that gave the most accurate values of conductivity and permittivity, it was found that there were distinct regions where certain formalisms performed better than others. For the shell intrinsic properties, there were similarities between the formalisms used in extraction of shell conductivity and permittivity. These were divided into five regions (see fig. 45). In region i the arc diameters of Nyquist plots of impedance and modulus provided the most accurate values for conductivity and permittivity, respectively. As the shell time constant was over 100 times greater than the core time constant, the Nyquist arcs were well defined. There were instances where there was no data at low enough frequencies to resolve the low frequency arcs. Here spectroscopic plots of Y' and E' could be used. However, if Nyquist plots included low enough frequencies they provided slightly more accurate intrinsic values.

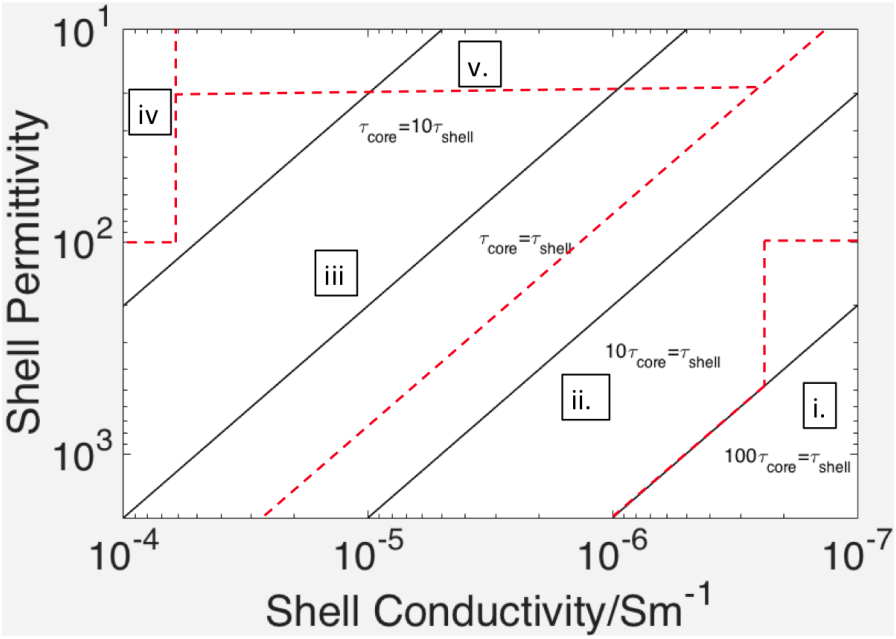

Fig. 45. *Schematic of regions where specific formalisms obtain the shell intrinsic material properties more accurately.*

For region ii, the core and shell time constants become closer in magnitude. Hence Nyquist plots become merged and the plateaus of E' and Y' spectroscopic plots produce increasingly composite values of the core and shell properties. Here spectroscopic plots of the imaginary components of impedance and modulus performed best. These spectroscopic plots gave a Debye frequency that had to be combined with a resistance or capacitance (for a permittivity or conductivity respectively, see table 3) acquired from Nyquist plots. Although the Nyquist plots were merged, it is likely that the merged arcs were dominated by the shell properties or that there was favourable cancelling of errors.

Region iii had deviations from ±28 to ±86% and hence was discarded as a region. It cannot be resolved with the limitations of impedance spectroscopy. Region iv could be resolved using the modulus formalism with Nyquist arc diameters to calculate the shell permittivity and spectroscopic plots of the imaginary modulus to find the shell conductivity. The modulus formalism is sensitive to small capacitances (arc diameters equal to inverse capacitances, see chapter one) and has worked well here because the shell permittivity is low (10 to 100) and hence has a low capacitance.

Finally, for region v when the shell permittivity is 10, impedance Nyquist plots provide the best shell conductivities. For extracting shell permittivity, E' spectroscopic plots are the best and can be used while the shell permittivity is 100 or less. Y' spectroscopic plots and modulus Nyquist plots are too merged to be useful.

Finding the best formalisms to extract the core properties also gave regions that were shared between conductivity and permittivity. Fig. 46 shows the four regions identified. In region i it was found that the Debye peaks of spectroscopic plots of impedance and modulus allowed the most accurate calculation of the core permittivity and conductivity. However, for shell permittivities less than 100, the core conductivity was extracted most accurately using impedance Nyquist arcs. When the shell permittivity was greater than 100 the Nyquist arcs and imaginary

Debye peaks (Z* and M*) only showed one impedance response. Given the larger volume fraction of the core material, it would be expected that resolving a merged response would give intrinsic properties weighted towards the core. Spectroscopic plots (of Y' and E') do not work here because their high and low frequency plateaus become functions of both the core and shell properties making extraction of individual properties difficult.

Region ii was discarded for having too high deviation (from ±25 to ±98%). Region iii varied in what formalism worked best. For the core permittivity, spectroscopic plots of E' provided the most accurate values, as E' is sensitive to the large capacitance of the core. For the core conductivity, the best formalism changed from Y' at high shell conductivities to impedance Nyquist plots at low shell conductivities. This is due to impedance Nyquist arcs giving exact resistances when the arcs are not merged. Otherwise the admittance is the only remaining option.

In region iv the modulus formalism provides the best values for core conductivities and permittivities. Here the core and shell arcs were less merged than in impedance Nyquist plots (see figs. 35A to C and 39A to B). As the Nyquist plots are required for calculation using the Debye peaks of M'' and Z'' spectroscopic plots, the modulus formalism was best for calculating the core conductivity. Spectroscopic plots of Y' and E' gave good values but were typically a few per cent out when compared to the modulus.

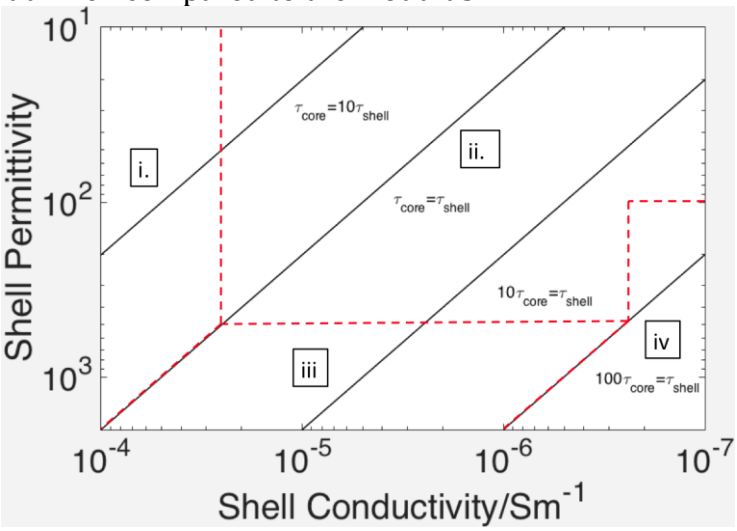

Fig. 46. *Schematic of regions where specific formalisms obtain the core intrinsic material properties more accurately.*

There are several limitations in the work presented in this chapter that could be improved upon in future work. Firstly, there are a few additional methods of data collection that could be used. The imaginary components of admittance and capacitance have a Debye peak that correlates with a parasitic capacitance (see chapter one). It is also possible to approximate the Nyquist arc diameters by doubling the height of an imaginary spectroscopic Debye peak. These methods could be added to the comparison. The frequency range studied could also include lower frequencies, down to 0.1 Hz, allowing the impedance spectra for some of the more resistive models to be fully resolved. Finally, to keep the size of this study reasonable, several parameters were kept fixed. By increased automation of data

collection, it would be feasible to vary core-shell volume fractions and the properties of the core as well.

6.5. Conclusions

In this chapter, the impedance response of an encased model approximation of a core-shell microstructure was simulated using FEM. The core volume fraction, conductivity and permittivity values were fixed to 0.8, 0.1 mSm^{-1} and 2000, respectively. The shell properties varied with conductivities from 0.1 mSm^{-1} to 0.1 μSm^{-1} and relative permittivities from 10 to 2000. Three equivalent circuits were compared to the FEM data to assess which provided the best fit. Using the best equivalent circuit, the intrinsic conductivities and permittivities of the core and shell regions were extracted using four impedance formalisms. The extracted values were compared to the values originally inputted into the finite element program, allowing the most accurate impedance formalism for a given situation to be established (for the range of properties investigated). Key findings are:

- The SLM is inadequate for fitting the encased model simulated in this chapter; the SBLM or PBLM should be used instead.
- The SBLM provided the best fit when both the core and the shell properties (permittivity and conductivity) have a difference of at least an order magnitude.
- When either the conductivity or permittivity of the shell is within an order of magnitude of the core value, the PBLM is the best equivalent circuit for the case studied.
- Multi-formalism analysis of impedance data is vital to extract the most accurate properties for the microstructure investigated and the limitations of a given study.
- Extracting intrinsic properties from the shell of a core-shell microstructure is most accurate when either the shell conductivity or shell permittivity is significantly different to those of the core.
- Extracting the intrinsic properties of the core of a core-shell microstructure is most accurate when either the shell conductivity or shell permittivity is very similar to that of the core.

6.6. References

1. Z. Zhao, V. Buscaglia, M. Viviani, M. T. Buscaglia, L. Mitoseriu, A. Testino, M. Nygren, M. Johnsson, and P. Nanni, "Grain-size effects on the ferroelectric behavior of dense nanocrystalline BaTiO3 ceramics," *Physical Review B,* 70[2] (2004).

2. A. R. West, D. C. Sinclair, and N. Hirose, "Characterization of electrical materials, especially ferroelectrics, by impedance spectroscopy," *Journal of Electroceramics,* 1[1] 65-71 (1997).

3. D. C. Sinclair and A. R. West, "Impedance and Modulus Spectroscopy of Semiconducting $BaTiO_3$ Showing Positive Temperature-Coefficient Of Resistance," *Journal of Applied Physics,* 66[8] 3850-56 (1989).

4. E. J. Abram, D. C. Sinclair, and A. R. West, "A strategy for analysis and modelling of impedance spectroscopy data of electroceramics: Doped lanthanum gallate," *Journal of Electroceramics,* 10[3] 165-77 (2003).

5. J. E. Bauerle, "Study of Solid Electrolyte Polarization by a Complex Admittance Method," *Journal of Physics and Chemistry of Solids,* 30[12] 2657-2670 (1969).

6. H. Nafe, "Ionic-Conductivity of ThO_2-Based And ZrO_2-Based Electrolytes Between 300-K and 2000-K," *Solid State Ionics,* 13[3] 255-63 (1984).

7. J. H. Hwang, D. S. McLachlan, and T. O. Mason, "Brick layer model analysis of nanoscale-to-microscale cerium dioxide," *Journal of Electroceramics,* 3[1] 7-16 (1999).

8. J. P. Heath, J. S. Dean, J. H. Harding, and D. C. Sinclair, "Simulation of Impedance Spectra for Core-Shell Grain Structures Using FiniteElement Modeling," *Journal of the American Ceramic Society,* 98[6] 1925-31 (2015).

9. J. C. Maxwell, "A Treatise on Electricity and Magnetism.″ Cambridge University Press, (2010).

10. D. C. Sinclair, "Characterization of Electro-materials using ac Impedance Spectroscopy," *Bol. Soc, Esp. Cerám. Vidrio,* 34[2] 55-65 (1995).

11. S. Associates, "http://www.scribner.com/software/general-electrochemistry/68-general-electrochemistr/376-zview-for-windows." in, Vol. 2016.

12. N. J. Kidner, N. H. Perry, T. O. Mason, and E. J. Garboczi, "The brick layer model revisited: introducing the nano-grain composite model," *Journal of the American Ceramic Society,* 91[6] 1733-46 (2008).

Chapter 7: Conclusions and Future Work

Motivated by the large market for dielectric ceramics the effect of physical microstructure on the electrical microstructure has been studied using finite element modelling. The finite element package used allows the generation and simulation of polycrystalline materials. Possible microstructural features that can be generated include bulk material, grain boundaries, pores and secondary phases, allowing for variable grain size and phase volume fractions. In this work core-shell microstructures have been the focus. During electrical characterisation, particularly by impedance spectroscopy, measurements are defined by the electrical microstructure. If the electrical microstructure does not resemble the physical microstructure, correlating the electrical characterisation to the physical microstructure becomes unreliable. Here the effects of paths of least impedance have been investigated to find under what conditions capacitive and conduction pathways form. This can be due to a change in the physical microstructure and/or the material properties.

7.1. Conclusions

In chapters four and five it has been shown that, if the conductivity or permittivity of a material varies with position within a physical microstructure, the configuration of the physical microstructure can influence the resulting electrical microstructure even if the volume fractions of different material regions are constant. Three physical microstructures were investigated: the series layer model (SLM, see fig. 1A); the parallel layer model (PLM, see fig. 1B); and the encased model (see fig. 1C). The SLM and PLM are the series and parallel variants of Maxwell's layered condenser model[1]. These models are useful as they are equivalent to two parallel resistor-capacitor elements connected in series (for the SLM, see fig. 1D) or parallel (for the PLM, see fig. 1E) and describe pure serial and parallel connectivity, respectively. The SLM and PLM can be solved analytically, therefore allowing validation of equivalent finite element simulations. Simulations that have more complex microstructures, such as the encased model, can be compared to the SLM and PLM to find out whether serial or parallel connectivity is dominant in a given model. The encased model is a nested cube approximation of a core-shell microstructure. In chapters four and five it was found that the encased model could not be modelled by the SLM accurately when the core volume fraction was less than 0.7 (see fig. 1F). This was due to the electrical microstructure.

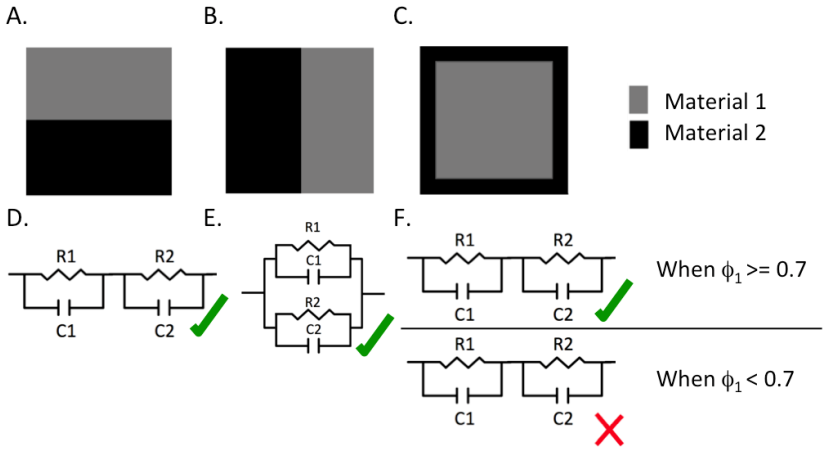

Fig. 1. *Schematics of the physical microstructures of (A) the SLM, (B) the PLM and (C) the encased model. (D) and (E) show equivalent circuits for the SLM and PLM, respectively. (F) The approximate equivalent circuit for an encased model when the core volume fraction (ϕ_1) is greater than 0.7. This approximation assumes that either the permittivity of the core and shell is fixed and the core is less resistive than the shell (chapter 4) or the conductivity of the core and shell is fixed and the core permittivity is greater than the shell (chapter 5).*

A change in electrical microstructure will alter the resultant impedance spectra and can have ramifications for any further analysis of the impedance data. This is evidenced by the change in the impedance response when changing the physical microstructure from an encased model to a series layer model (SLM), where the core and shell regions of the encased model and the layers of the SLM have different properties. In chapter four, the two materials had a fixed permittivity and a core material that was less resistive than the shell[2]. These material properties could be applied to $CaCu_3Ti_4O_{12}$ ceramics that were found to have semi conductive grains with resistive grain boundaries[3]. In chapter five, the conductivity was fixed and the permittivity was greater in the core region. This could be applied to $BaTiO_3$ nano-powders that have suppressed ferroelectricity at the particle surfaces due to a transition from a tetragonal (ferroelectric) to cubic (paraelectric) crystal structure[4]. The work in this thesis could be applied to many electrical composite materials but these examples demonstrate some of the applications in the field of functional oxides. In both chapters, the impedance response was altered with a reduced contribution from the shell. This was due to the formation of conduction or capacitive pathways (in chapters four and five, respectively) forming within the microstructure. Given the interplay between capacitive and conduction effects it is simpler to think of these preferable pathways as paths of least impedance.

The difference between the SLM and the encased model's impedance response varied with the volume fraction of the core region (ϕ_{core}), with the difference between the two models increasing as the core became smaller. This is due to pathways of least impedance forming in the region of the shell parallel to the core as the shell thickness become similar to the core. The current density was less in these parallel pathways and hence did not affect the magnitude of the shell's impedance response but could cause broadening of the Debye peaks in spectroscopic plots of the imaginary component of the electric modulus. In chapter six, it was observed that an equivalent circuit that modelled the parallel shell with

an additional parallel resistor-capacitor branch fitted the transition between high and low frequency plateaus of spectroscopic plots of real admittance and real capacitance, showing that parallel pathways can alter the form of an impedance response.

There are many instances in this thesis where the advantages of using multiple formalisms to analyse impedance data is demonstrated. In chapter four, the impedance response of core and shell regions was better resolved using the electric modulus formalism than by using the impedance because the more resistive shell dominated the impedance response. Conversely in chapter five, for a similar encased structure, the electric modulus formalism was dominated by the low permittivity of the shell and the impedance provided better resolution of the core and shell responses. In chapter six, when evaluating the fits of several equivalent circuits it was observed that in some cases an equivalent circuit would fit the finite element simulation very well in some formalisms but less well in other formalisms. This shows that it is not adequate to fit an equivalent circuit to just one formalism. A summary of key results is presented below:

- Application of the brick layer model to core-shell microstructures becomes increasingly unreliable as ϕ_{core} decreases. The error in estimating volume fractions from capacitance (or resistance) ratios exceeds 25% when ϕ_{core} is lower than 0.70 for the parameters used in this study. This effect is present when the conductivity of the core is greater than the shell for a fixed permittivity and when the permittivity of the core is greater than the shell for fixed conductivity (chapters four and five, respectively).
- Non-ideality in impedance spectra can be influenced by heterogeneous current flow that is a result of physical microstructure and is independent of a distribution of relaxation times caused by a variation in material properties (chapter four).
- When a material has regions with different permittivities but the same conductivity, the electrical microstructure can be affected by the configuration of the physical microstructure. This is caused by capacitive pathways forming between the regions that are electrically active at a given frequency due to their time constants (chapter five).
- It is more effective to extract volume fractions from resistance ratios than from capacitance ratios when permittivity varies and conductivity is fixed (chapter five).
- The series layer model is inadequate for fitting the encased model simulated in chapter six; the series brick layer model or parallel brick layer model should be used instead.
- Multi-formalism analysis of impedance data is vital to extract the most accurate properties for the microstructure investigated and to assess the limitations of a given study.

7.2. Future Work

There are several areas which future work should investigate:

- In this study, plots of the electrical microstructure are taken at the maximum current or voltage on an AC sinusoid for a given frequency. This approach has worked well for the material properties studied in chapter

four but became more complex in the later chapters. Additional work should be undertaken to find when the most representative electrical microstructure occurs on a current or voltage sinusoid at any given frequency.

- In chapter four, the series brick layer model could fit the encased model simulations only at high ϕ_{core} values. At lower ϕ_{core} values the existence of parallel pathways was established. It should therefore be investigated whether the parallel brick layer model provides a better fit in these circumstances.
- The quantitative analysis of the electrical microstructure used in chapter four should be extended to probe the distribution of capacitive pathway lengths present in the encased models in chapter five.
- The material property space studied in chapter six should be extended to include variable core properties and multiple volume fractions of the encased model.
- The simulations in chapter six should have all measured time constants calculated to investigate whether they have any geometry dependence.
- It has been shown that both conduction and capacitive pathways can form alternate routes for current to flow through a model (e.g. through the encased model's parallel shell component) if the conductivity or permittivity varies with position through the microstructure. Further work should investigate under what circumstances conduction or capacitive pathways are more dominant.
- Additional microstructural features such as porosity and interface roughness should be simulated and their effect on impedance spectroscopy characterised.
- At present, all conductivity and permittivity values assigned to a model are constant during the simulation. Additional work should be undertaken to study the frequency and electric field dependency of material properties and how this may alter the electrical response as measured by impedance spectroscopy.

7.3. References

1. J. C. Maxwell, "A Treatise on Electricity and Magnetism." Cambridge University Press, (2010).

2. J. P. Heath, J. S. Dean, J. H. Harding, and D. C. Sinclair, "Simulation of Impedance Spectra for Core-Shell Grain Structures Using FiniteElement Modeling," *Journal of the American Ceramic Society,* 98[6] 1925-31 (2015).

3. D. C. Sinclair, T. B. Adams, F. D. Morrison, and A. R. West, "$CaCu_3Ti_4O_{12}$: One-step internal barrier layer capacitor," *Applied Physics Letters,* 80[12] 2153-55 (2002).

4. C. Baek, J. E. Wang, S. Moon, C. H. Choi, and D. K. Kim, "Formation and Accumulation of Intragranular Pores in the Hydrothermally Synthesized Barium Titanate Nanoparticles," *Journal of the American Ceramic Society,* 99[11] 3802-08 (2016).

Appendix

A.1. Derivations for the impedance response of two parallel resistor capacitor elements connected in series

Here we will consider the impedance response of two parallel resistor capacitor elements connected in series (see fig. A1) which will be referred to as circuit A1. The impedance response of this circuit will be derived for all four impedance formalisms to the final equations that were then manipulated to find the intercepts and plateaus in chapter one. Hence appendix one gives the derivation of equations (1.47) for the impedance (Z*), (1.55) for the electric modulus (M*), (1.63) for the admittance (Y*) and (1.74) for the complex capacitance (E*).

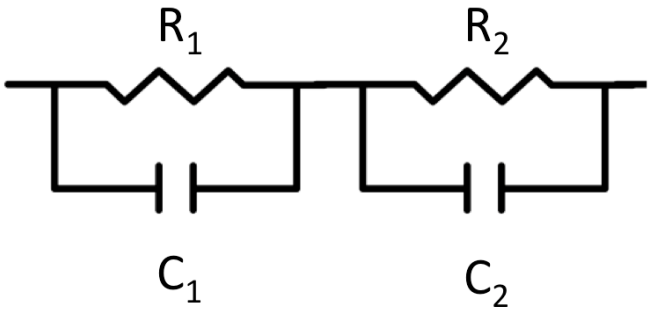

Fig. A1. *Schematic of two parallel resistor capacitor elements connected in series.*

Consider *Z**:

Since *Z** adds in series the total impedance of circuit A1 is simply the addition of the impedance response of two parallel resistor capacitor elements. Equation (1.39) gives the impedance response of a parallel resistor capacitor element as:

$$Z^* = \frac{R - j\omega R^2 C}{1 + (\omega RC)^2} \tag{1.39}$$

Addition of (1.39) with itself with R_1, C_1, R_2 and C_2 substituted into the two equations gives:

$$Z^* = \frac{R_1 - j\omega R_1^2 C_1}{1 + (\omega R_1 C_1)^2} + \frac{R_2 - j\omega R_2^2 C_2}{1 + (\omega R_2 C_2)^2} \tag{1.47}$$

Consider *M**:

Take the M* response for a single parallel resistor capacitor element given in (1.44):

$$M^* = \frac{1}{C}.\frac{\omega^2 R^2 C^2}{1 + (\omega RC)^2} + j\frac{1}{C}.\frac{\omega RC}{1 + (\omega RC)^2} \tag{1.44}$$

Add the real and imaginary part of (1.44):

$$M^* = \frac{1}{C}.\frac{\omega^2 R^2 C^2 + j\omega RC}{1 + (\omega RC)^2} \qquad (A.1)$$

Addition of (A.1) with itself with R_1, C_1, R_2 and C_2 substituted into the two equations gives:

$$M^* = \frac{1}{C_1}.\frac{\omega^2 R_1^2 C_1^2 + j\omega R_1 C_1}{1 + (\omega R_1 C_1)^2} + \frac{1}{C_2}.\frac{\omega^2 R_2^2 C_2^2 + j\omega R_2 C_2}{1 + (\omega R_2 C_2)^2} \qquad (1.55)$$

Consider Y^*:

Given the total impedance (Z^*) of circuit A1 is the addition of the impedance of the two parallel resistor capacitor elements (Z^*_1 and Z^*_2 respectively):

$$Z^* = Z_1^* + Z_2^*$$

The admittance is the inverse of impedance, therefore:

$$Y^* = \frac{1}{Z_1^* + Z_2^*} \qquad (A.2)$$

Substitute the admittance of parallel resistor capacitor elements R_1C_1 and R_2C_2 (Y^*_1 and Y^*_2, respectively) into equation (A.2).

$$Y^* = \frac{1}{\frac{1}{Y_1^*} + \frac{1}{Y_2^*}} \qquad (A.3)$$

Multiply top and bottom of equation (A.3) by $Y^*_1Y^*_2$:

$$Y^* = \frac{Y_1^* Y_2^*}{Y_2^* + Y_1^*} \qquad (A.3)$$

The admittance for a single parallel resistor capacitor element is given in equation (1.36), substituting into (A.3) gives:

$$Y^* = \frac{\left(\frac{1}{R_1} + j\omega C_1\right)\left(\frac{1}{R_2} + j\omega C_2\right)}{\left(\frac{1}{R_1} + j\omega C_1\right) + \left(\frac{1}{R_2} + j\omega C_2\right)}$$

$$Y^* = \frac{\left(\left(\frac{1}{R_1 R_2}\right) + j\omega\left(\frac{C_1}{R_2} + \frac{C_2}{R_1}\right) - \omega^2 C_1 C_2\right)}{\left(\frac{1}{R_1} + \frac{1}{R_2}\right) + j\omega(C_1 + C_2)} \qquad (A.4)$$

Multiply top and bottom of (A.4) by the complex conjugate of the denominator of (A.4) giving equation (1.63):

$$Y^* = \frac{\left(\left(\frac{1}{R_1R_2}\right) + j\omega\left(\frac{C_1}{R_2} + \frac{C_2}{R_1}\right) - \omega^2 C_1 C_2\right)\left(\left(\frac{1}{R_1} + \frac{1}{R_2}\right) - j\omega(C_1 + C_2)\right)}{\left(\frac{1}{R_1} + \frac{1}{R_2}\right)^2 + \omega^2(C_1 + C_2)^2} \quad (1.63)$$

Consider E^*:

The relation between E* and Y* is:

$$E^* = \frac{Y^*}{j\omega} \quad (A.5)$$

Substitute equation (1.63) into (A.5) to derive E^* for circuit A1 to give equation (1.74):

$$E^* = \frac{\left(\left(\frac{1}{R_1R_2}\right) + j\omega\left(\frac{C_1}{R_2} + \frac{C_2}{R_1}\right) - \omega^2 C_1 C_2\right)\left(\left(\frac{1}{R_1} + \frac{1}{R_2}\right) - j\omega(C_1 + C_2)\right)}{j\omega\left(\frac{1}{R_1} + \frac{1}{R_2}\right)^2 + j\omega^3(C_1 + C_2)^2} \quad (1.74)$$

A.2. Derivation for the Parallel Brick Layer Model equivalent circuit

Here the impedance response of the Parallel Brick Layer Model (PBLM) is derived for all four impedance formalisms. First consider the sub circuit consisting of two parallel resistor capacitor elements connected in parallel in isolation (see fig. A2).

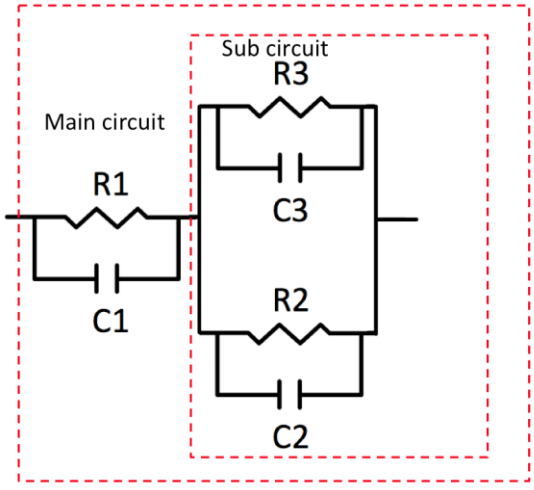

Fig. A2. *Schematic of the PBLM equivalent circuit separating the sub circuit consisting of two parallel resistor capacitor elements connected in parallel in isolation.*

Consider Y*:

For a single RC element the impedance response is given by equation (1.38):

$$Z^* = R + \frac{1}{j\omega C} \tag{1.38}$$

Considering admittance (Y*) is the inverse of impedance (Z*) and adds in parallel, for the sub circuit:

$$Y^* = \frac{1}{Z^*} = \frac{1}{R_2} + \frac{1}{R_3} + j\omega C_2 + j\omega C_3 \tag{A.6}$$

Giving the real (Y') and imaginary (Y'') component of (A.6) as:

$$Y' = \frac{1}{R_2} + \frac{1}{R_3} \tag{A.7}$$

$$Y'' = \omega C_2 + \omega C_3 \tag{A.8}$$

Consider E*:

The relation between E* and Y* is given by equation (A.5). Substituting (A.6) into (A.5) gives:

$$E^* = C_2 + C_3 + \frac{1}{j\omega R_2} + \frac{1}{j\omega R_3} \tag{A.9}$$

The real and imaginary components of (A.9):

$$E' = C_2 + C_3 \tag{A.10}$$

$$E'' = -\frac{1}{\omega R_2} - \frac{1}{\omega R_3} \tag{A.11}$$

Consider Z*:

Writing equation (A.6) as:

$$Y^* = \left(\frac{1}{R_2} + \frac{1}{R_3}\right) + j\omega(C_2 + C_3) \tag{A.12}$$

Then divide both sides by the bracketed resistance term:

$$\frac{Y^*}{\left(\frac{1}{R_2}+\frac{1}{R_3}\right)} = 1 + j\omega\frac{(C_2+C_3)}{\left(\frac{1}{R_2}+\frac{1}{R_3}\right)} \qquad (A.13)$$

Take the inverse of equation (A.13) and divide by the reciprocal resistance term:

$$Z^* = \frac{1}{\left(1 + j\omega\frac{(C_2+C_3)}{\left(\frac{1}{R_2}+\frac{1}{R_3}\right)}\right)} \cdot \frac{1}{\left(\frac{1}{R_2}+\frac{1}{R_3}\right)} \qquad (A.14)$$

Multiply top and bottom of (A.14) by the complex conjugate of the denominator:

$$Z^* = \frac{\frac{1}{\left(\frac{1}{R_2}+\frac{1}{R_3}\right)}}{\left(1 + j\omega\frac{(C_2+C_3)}{\left(\frac{1}{R_2}+\frac{1}{R_3}\right)}\right)} \cdot \frac{\left(1 - j\omega\frac{(C_2+C_3)}{\left(\frac{1}{R_2}+\frac{1}{R_3}\right)}\right)}{\left(1 - j\omega\frac{(C_2+C_3)}{\left(\frac{1}{R_2}+\frac{1}{R_3}\right)}\right)} \qquad (A.15)$$

Giving:

$$Z^* = \frac{\frac{1}{\left(\frac{1}{R_2}+\frac{1}{R_3}\right)} - j\omega\frac{(C_2+C_3)}{\left(\frac{1}{R_2}+\frac{1}{R_3}\right)^2}}{1 + \left(\omega\frac{(C_2+C_3)}{\left(\frac{1}{R_2}+\frac{1}{R_3}\right)}\right)^2} \qquad (A.16)$$

Consider the real component (Z') of (A.16):

$$Z' = \frac{\frac{1}{\left(\frac{1}{R_2}+\frac{1}{R_3}\right)}}{1 + \left(\omega\frac{(C_2+C_3)}{\left(\frac{1}{R_2}+\frac{1}{R_3}\right)}\right)^2} \qquad (A.17)$$

Consider the frequency limits of (A.17)

Low frequency $\omega \to 0$:

$$Z' \to \frac{\frac{1}{\left(\frac{1}{R_2}+\frac{1}{R_3}\right)}}{1 + (0)^2}$$

$$Z' \rightarrow \frac{1}{\left(\frac{1}{R_2}+\frac{1}{R_3}\right)} \qquad (A.18)$$

High frequency $\omega \rightarrow \infty$:

$$Z' \rightarrow \frac{\frac{1}{\left(\frac{1}{R_2}+\frac{1}{R_3}\right)}}{1+(\infty)^2}$$

$$Z' \rightarrow 0 \qquad (A.19)$$

Consider the imaginary component (Z'') of (A.16):

$$Z'' = \frac{\omega \frac{(C_2+C_3)}{\left(\frac{1}{R_2}+\frac{1}{R_3}\right)^2}}{1+\left(\omega \frac{(C_2+C_3)}{\left(\frac{1}{R_2}+\frac{1}{R_3}\right)}\right)^2}$$

$$Z'' = \frac{1}{\left(\frac{1}{R_2}+\frac{1}{R_3}\right)} \frac{\omega \frac{(C_2+C_3)}{\left(\frac{1}{R_2}+\frac{1}{R_3}\right)}}{1+\left(\omega \frac{(C_2+C_3)}{\left(\frac{1}{R_2}+\frac{1}{R_3}\right)}\right)^2} \qquad (A.20)$$

Consider the frequency limits of (A.20):

At low frequency $\omega \rightarrow 0$:

$$Z'' \rightarrow \frac{1}{\left(\frac{1}{R_2}+\frac{1}{R_3}\right)} \frac{(0)}{1+(0)^2}$$

$$Z'' \rightarrow 0 \qquad (A.21)$$

At high frequency when $\omega \rightarrow \infty$:

$$Z'' \rightarrow \frac{1}{\left(\frac{1}{R_2}+\frac{1}{R_3}\right)} \frac{\infty}{1+(\infty)^2}$$

$$Z'' \rightarrow 0 \qquad (A.22)$$

Consider the Debye function present in (A.20) when:

$$\omega \frac{(C_2+C_3)}{\left(\frac{1}{R_2}+\frac{1}{R_3}\right)} = 1 \qquad (A.23)$$

Substitute equation (A.23) into (A.20):

$$Z'' = \frac{1}{\left(\frac{1}{R_2}+\frac{1}{R_3}\right)} \frac{1}{1+(1)^2}$$

$$Z'' = \frac{1}{\left(\frac{1}{R_2}+\frac{1}{R_3}\right)} \frac{1}{2} \qquad (A.24)$$

Consider *M**:

*M** is related to *Z** by:

$$M^* = j\omega Z^* \qquad (A.25)$$

Hence multiply equation (A.16) by $j\omega$:

$$j\omega Z^* = j\omega \frac{\frac{1}{\left(\frac{1}{R_2}+\frac{1}{R_3}\right)} - j\omega \frac{(C_2+C_3)}{\left(\frac{1}{R_2}+\frac{1}{R_3}\right)^2}}{1+\left(\omega \frac{(C_2+C_3)}{\left(\frac{1}{R_2}+\frac{1}{R_3}\right)}\right)^2}$$

$$M^* = \frac{\omega^2 \frac{(C_2+C_3)}{\left(\frac{1}{R_2}+\frac{1}{R_3}\right)^2} + j\omega \frac{1}{\left(\frac{1}{R_2}+\frac{1}{R_3}\right)}}{1+\left(\omega \frac{(C_2+C_3)}{\left(\frac{1}{R_2}+\frac{1}{R_3}\right)}\right)^2} \qquad (A.26)$$

Consider the real component (M') of (A.26):

$$M' = \frac{\omega^2 \frac{(C_2+C_3)}{\left(\frac{1}{R_2}+\frac{1}{R_3}\right)^2}}{1+\left(\omega \frac{(C_2+C_3)}{\left(\frac{1}{R_2}+\frac{1}{R_3}\right)}\right)^2} \qquad (A.27)$$

Consider the frequency limits of (A.27):

Low frequency ω→0:

$$M' \to \frac{(0)^2 \frac{(C_2 + C_3)}{\left(\frac{1}{R_2} + \frac{1}{R_3}\right)^2}}{1 + (0)^2}$$

$$M' \to 0 \qquad (A.28)$$

High frequency when ω→∞:

$$M' \to \frac{\infty^2 \frac{(C_2 + C_3)}{\left(\frac{1}{R_2} + \frac{1}{R_3}\right)^2}}{1 + \infty^2 \frac{(C_2 + C_3)^2}{\left(\frac{1}{R_2} + \frac{1}{R_3}\right)^2}}$$

$$M' \to \frac{1}{(C_2 + C_3)} \qquad (A.29)$$

Consider the imaginary component (M'') of (A.26):

$$M'' = \frac{\omega \frac{1}{\left(\frac{1}{R_2} + \frac{1}{R_3}\right)}}{1 + \left(\omega \frac{(C_2 + C_3)}{\left(\frac{1}{R_2} + \frac{1}{R_3}\right)}\right)^2} \qquad (A.30)$$

Multiply equation (A.30) by the capacitive term over its self:

$$M'' = \frac{\omega \frac{1}{\left(\frac{1}{R_2} + \frac{1}{R_3}\right)}}{1 + \left(\omega \frac{(C_2 + C_3)}{\left(\frac{1}{R_2} + \frac{1}{R_3}\right)}\right)^2} \cdot \frac{(C_2 + C_3)}{(C_2 + C_3)}$$

$$M'' = \frac{\omega \frac{(C_2 + C_3)}{\left(\frac{1}{R_2} + \frac{1}{R_3}\right)}}{(C_2 + C_3)\left(1 + \left(\omega \frac{(C_2 + C_3)}{\left(\frac{1}{R_2} + \frac{1}{R_3}\right)}\right)^2\right)} \qquad (A.31)$$

Consider the frequency limits of (A.31):

At low frequency ω→0:

$$M'' \rightarrow \frac{(0)}{(C_2 + C_3)(1 + (0)^2)}$$

$$M'' \rightarrow 0 \qquad (A.32)$$

At high frequency ω→∞:

$$M'' \rightarrow \frac{(\infty)}{(C_2 + C_3)(1 + (\infty)^2)}$$

$$M'' \rightarrow 0 \qquad (A.33)$$

Consider the Debye function present when equation (A.23) holds, substitute (A.23) into (A.31):

$$M'' = \frac{1}{(C_2 + C_3)(1 + (1)^2)}$$

$$M'' = \frac{1}{(C_2 + C_3)(2)} \qquad (A.34)$$

Considering the total resistance (R_t) and capacitance (C_t) for the sub circuit. Equation (A.7) gives the Y' conductance plateau as $1/R_2 + 1/R_3$. Equations (A.18) and (A.24) gives an impedance Nyquist plot arc of diameter $1/(1/R_2 + 1/R_3)$ and height $1/2(1/R_2 + 1/R_3)$, respectively. From these two results the total resistance for the sub circuit is:

$$R_t = \frac{1}{\frac{1}{R_2} + \frac{1}{R_3}} \qquad (A.35)$$

Equation (A.10) gives an E' capacitance plateau of $C_2 + C_3$. Equations (A.29) and (A.34) gives an modulus Nyquist plot arc of diameter $1/(C_2 + C_3)$ and height $1/2(C_2 + C_3)$, respectively. From these two results the total capacitance for the sub circuit is:

$$C_t = C_2 + C_3 \qquad (A.35)$$

Consolidating these values as a single RC element allows the main circuit to be simplified into a dual RC circuit where one time constant is the product of R_1C_1 and the other R_tC_t.